Electric field determination and magnetic topology optimization in Hall thrusters

Julien Vaudolon

Centre Val de Loire UNIVERSITÉ
Spirit of the Loire Valley

UNIVERSITÉ D'ORLÉANS

UNIVERSITE D'ORLEANS

ÉCOLE DOCTORALE
ENERGIE, MATERIAUX, SCIENCES DE LA TERRE ET DE L'UNIVERS

Institut de Combustion Aérothermique Réactivité et Environnement
CNRS Orléans

THÈSE présentée par :

Julien VAUDOLON

soutenue le : **1er octobre 2015**

pour obtenir le grade de : **Docteur de l'université d'Orléans**

Discipline : **Physique**

Electric field determination and magnetic topology optimization in Hall thrusters

THÈSE DIRIGÉE PAR :

M. Stéphane MAZOUFFRE	Directeur de recherche, ICARE, CNRS Orléans

RAPPORTEURS :

M. Yevgeny RAITSES	Principal Research Physicist, PPPL, Princeton University
M. Jean-Pierre BŒUF	Directeur de recherche, LAPLACE, CNRS Toulouse

JURY :

Mme. Carole HÉNAUX	Maître de Conférences, LAPLACE, Université de Toulouse
M. Jean-Pierre BŒUF	Directeur de recherche, LAPLACE, CNRS Toulouse
M. Dunpin HONG	Professeur, GREMI, Université d'Orléans
M. Stéphane MAZOUFFRE	Directeur de recherche, ICARE, CNRS Orléans
M. Yevgeny RAITSES	Principal Research Physicist, PPPL, Princeton University
M. Jean-Marcel RAX	Professeur, LOA, Ecole Polytechnique
M. Nicolas ARCIS	Docteur, CNES
M. Stéphan ZURBACH	Docteur, Snecma

Acknowledgements

My guitar has six strings capable of capturing the harmony and the vastness of music. Likewise, each of the six chapters of my thesis is meant to examine a specific aspect of the physics of Hall thrusters, to build a coherent ensemble (fortunately I am not good enough to play on twelve strings). Having committed to this research may be the smartest thing I've ever done so far, and I would like to express my deep and sincere thanks to those who have supported this research these last three years.

First, and foremost, I owe a major Thank You to my advisor, Stéphane Mazouffre, for his unfailing support and considerable expertise in electric propulsion. I feel extremely lucky to have had the chance to work with such a talented person. You gave me your trust three and a half years ago, to work on a PhD concerned with Hall thrusters, even though I did not really know what a plasma was like at that time. The countless hours we have spent together talking about physics, but also about the life that finally does exist after research, have often constituted milestones that guided my work. I hope we will further collaborate to propel spacecrafts farther and faster.

This research has been made possible by the joint funding of CNES and Snecma. I thank Nicolas Arcis and Claude Boniface of the CNES for our discussions. Great thanks to Antoine Caratgé, Jean-Marie Lonchard and Stéphan Zurbach who answered my questions (which may have seemed naïve) in 2011 on electric propulsion activities in France. Thanks to David, Thierry and Joël for the PPS-FLEX testing in Vernon.

I couldn't have gotten as far with my thesis if it weren't for a bunch of very smart people who preceded me. My sincere gratitude to Käthe Dannenmayer, Guillaume Bourgeois and Aurélien Lejeune who first introduced me to the various experimental tools at my disposal (vacuum chambers, thrusters, diagnostics). Your experience as PhD candidates and postdoctoral fellow was a beacon of light in the darkness of my ignorance. I also feel really indebted to Raphaël Vilamot and Damien Gawron. Although we never met, you guys have made at least 50 % of this dissertation possible.
This experimental work could not have been performed if it wasn't for the many collaborations that have occurred. I am grateful for the challenging but successful three test campaigns I had the opportunity to perform in the PIVOINE facility. The G^2 task force and Sisouk's ability to react promptly was appreciated. Part of these tests have used the PPS-FLEX Hall thruster, a marvelous tool to optimize the magnetic topology. Great thanks to Raphaël Vilamot, Carole Hénaux, Dominique Harribey and Alberto Rossi of the LAPLACE in Toulouse for this architecture. Thanks also to Laurent Garrigues of LAPLACE for your simulations and your cheerful nature. I will always remember the ice hockey game (let's spot the cow!). Many thanks to Jacek Kurzyna of IPPLM in Poland for his EMD algorithm, which has been a crucial tool for analyzing the fluorescence photons time series. Finally, I thank the electric propulsion team at ESA, in the Netherlands, for two months of testing.

Thanks to all the people close by with whom I have collaborated and/or experienced the funniest parts of my life lately. Sedina, your invaluable knowledge is remarkable and the stimulating discussions we have had have imparted momentum to my work. However, your way of tying ropes still gives me nightmares. And beware Sarah, you may dislocate it! Dennis, thanks for getting me out of the lab to meet people. I admired your self-control when you faced the vagaries of research. Denis, y'en avait assez! Thanks buddy

for the good times, I'm sure there will be plenty more. Thierry, besides your abilities in computer science that helped me a lot, I enjoyed our guitar jams. I may not be as relaxed and skilled as you are, but I'm working on it. I appreciated our common interest for good meals. I cannot forget to mention my great pal Lahib! You always leave an indelible mark wherever you go. The few months we spent on the time-resolved LIF measurements, and our running sessions, were among the greatest times of my PhD. Guillaume, the week-long flatshare in the Netherlands was exhausting. Not only because of the rocket-engine-like beer flow rate we had (but also the alarm...).
We had a number of trainees, for better or worse. Benjamin, you participated in important breakthroughs for my research by writing Matlab routines. Other students I wasn't in charge of are memorable. Audrey, on sait que c'est toi qui a tagué Harry! Florian's willingness to save us from work is now legendary.

Guillaume told me that there were more open questions after his PhD than before he started it. I hope to have brought insights into some of the features of Hall thrusters. Yet, many unknowns remain and there's still a tremendous amount of work to be done. I wish good luck to you Lou. I have no doubt your contribution will help the EP community (with or without a gas lighter).

Great thanks to the laboratory administrative and technical staff: Laurent and Eric for not only building me quality parts, but for teaching me a thing or two about fabrication at the same time, Marine, Murielle, Corinne and Vincent for the administrative stuff, Nicolas and Fabrice for electronic problems and Yann for software glitches.

Most importantly, I thank my mum for her unending love and unwavering support in my endeavors. Your commitment to my education and manners is how I came to be what I am today, and what allows me to orient my professional life as I see fit. Thanks 

Julien Vaudolon
Orléans, France
June 2015

A ma mère,

A l'équipe PE de l'ICARE.

– John Aaron: Try SCE to AUX
– Gerald Carr: What the hell's that?
– Gerry Griffin: SCE to Off?
– Gerald Carr: Apollo 12, Houston, try SCE to Auxiliary, over
– Pete Conrad: FCE to Auxiliary, what the hell's that? NCE to Auxiliary?
– Gerald Carr: S-C-E, S-C-E to Auxiliary
– Alan Bean: SCE to AUX

Communication between Mission Control and Apollo 12, after a lightning bolt had struck the Saturn V, 36 s *after lift-off from Cape Canaveral, 16:22 UTC, November 14 1969*

Contents

List of Figures

List of Tables

Nomenclature

Constants

m_e	electron mass, 9.1094×10^{-31}	kg
m_i	xenon ion mass, 2.1802×10^{-25}	kg
e	electron charge, 1.6022×10^{-19}	C
k_B	Boltzmann's constant, 1.3807×10^{-23}	$\mathrm{J/K}$
g_0	gravitational acceleration, 9.80665	$\mathrm{m/s^2}$
μ	standard gravitational parameter of Earth, 3.9860×10^{14}	$\mathrm{m^3/s^2}$

Variables

$\mathbf{B} = (B_r, B_\theta, B_z)$	magnetic field	T
B_r	radial magnetic field	T
D	probe collector diameter	m
$\mathbf{E} = (E_r, E_\theta, E_z)$	electric field	$\mathrm{V/m}$
E_i	ionization losses	V
I_b	ion beam current	A
I_d	discharge current	A
I_{sp}	specific impulse	s
$L_{_B}$	width at half-maximum of B_r profile	m
i	orbit inclination	$^\circ$
j_i	ion current density	$\mathrm{mA/cm^2}$
$\mathbf{k}$	wave vector	$\mathrm{m^{-1}}$
L_i	length of the ionization zone	m
m_i	initial mass	kg
$\dot{m}_p$	propellant mass flow rate	$\mathrm{kg/s}$
n	plasma number density	$\mathrm{m^{-3}}$
p_{res}	background pressure	Pa
(r, θ, z)	cylindrical coordinate system	
(r, θ, ϕ)	spherical coordinate system	
R	probe distance from the thruster inner pole	m
S	collection area	$\mathrm{m^2}$
T	thrust	N
T_e	electron temperature	eV
t	time	s
$\mathbf{u} = (u_r, u_\theta, u_z)$	electron velocity	$\mathrm{m/s}$
U_{acc}	accelerating potential	V
U_d	discharge voltage	V
$\mathbf{v} = (v_r, v_\theta, v_z)$	ion velocity	$\mathrm{m/s}$

V_{CRP}	cathode potential relative to ground	V
V_d	$\mathbf{E} \times \mathbf{B}$ drift velocity	$\mathrm{m/s}$
V_p	plasma potential	V
v_p	propellant effective exhaust velocity	$\mathrm{m/s}$
$\mathbf{w_n}$	$\mathrm{n^{th}}$ order moment of the IVDF	$(\mathrm{m/s})^n$
ΔV	velocity increment	$\mathrm{m/s}$
δ	uncertainty	A
ε	electron energy	eV
η_a	anode efficiency	1
η_i, α	ionization efficiency	1
θ_{div}	ion beam divergence half-angle	$^\circ$
λ	wavelength	m
λ_D	Debye length	m
λ_i	ionization mean free path	m
ν_i	ionization frequency	Hz
ξ	payload mass fraction	1
ξ_i	ion current fraction	1
τ	atom residence time in the magnetized region	s
ϕ, Φ, U, V	potential	V
ϕ_a	anode mass flow rate	$\mathrm{mg/s}$
ω	pulsation	$\mathrm{rad/s}$

Acronyms

CEX	Charge-EXchange
CNES	Centre National d'Etudes Spatiales
CNRS	Centre National de la Recherche Scientifique
DC	Direct Current
EMD	Empirical Mode Decomposition
EP	Electric Propulsion
EPL	ESA Propulsion Laboratory
ESA	European Space Agency
FEMM	Finite Element Method Magnetics
FFT	Fast Fourier Transform
GDR	Groupement De Recherches
GEMaC	Groupe d'Etudes de la Matière Condensée
GEO	Geosynchronous Equatorial Orbit
GOCE	Gravity field and steady-state Ocean Circulation Explorer
GTO	Geostationary Transfer Orbit
HT	Hall thruster
ICARE	Institut de Combustion, Aérothermique, Réactivité et Environnement
IEDF	Ion Energy Distribution Function
IMF	Intrinsic Mode Function
ITT	Ion Transit Time
IVDF	Ion Velocity Distribution Function
JPL	Jet Propulsion Laboratory
LAPLACE	LAboratoire PLAsma et Conversion d'Energie
LIF	Laser-Induced Fluorescence
MIREA	Moscow State Institute of Radio Engineering Electronics and Automation

ML	Modèle de Laboratoire
MS	Magnetic Shielding
NASA	National Aeronautics and Space Administration
NExET	New Experiments on Electric Thrusters
PIC	Particle-In-Cell
PIVOINE	Propulsion Ionique pour les Vols Orbitaux, Interprétations et Nouvelles Expériences
PMT	PhotoMultiplier Tube
PPI	Petit Propulseur Innovant
PPS	Propulseur Plasma Stationnaire
RPA	Repulsing Potential Analyzer
RF	Radio Frequency
SMART-1	Small Missions for Advanced Research in Technology-1
SPF	Small Plasma Facility
SPT	Stationary Plasma Thruster
TR	Time-Resolved
TTL	Transitor-Transitor Logic
VUV	Vacuum UltraViolet
WL	Wall-Less
XUV	Extreme UltraViolet

Concepts and preliminaries

Getting off world: elements of space propulsion

THE physical means by which a thruster operates, be it airbreathing, chemical, electric, or otherwise, is all about imparting momentum to a propellant mass that is expelled from the system. In return, thrust is applied to the vehicle and serves its acceleration. The aim usually consists in converting the chemical energy stored in the propellant bounds into kinetic energy through combustion. There is, however, one exception to that rule: plasma propulsion[1]. Electric Propulsion (EP) differs fundamentally from other propulsive concepts. The energy used for the propellant acceleration is not embarked on board the spacecraft, but harvested in the vacuum of space. This feature makes EP advantages but it is also its main drawbacks.

To date, space propulsion system capabilities can be categorized in two independent spots: low and high thrust-to-mass ratios. Conventional systems, that lift-off rockets for instance, fall into the large thrust-to-mass ratio category. The principles of chemical propulsion have been known and used for millennia, the first reference to gun powder going back to the Han Dynasty in 206 BC. Reactants are mixed in a combustion chamber, then ignited (in case of hypergolic fluids these two steps occur simultaneously). Thrust is generated by expanding the combustion gases in a convergent-divergent nozzle which converts thermal energy into kinetic energy. The unbalanced pressure forces exerted on the walls at the nozzle exit generates thrust.
Electric propulsion devices can generate thrust in several ways: either by heating a gas, using an electric field or relying on the Lorentz force. This technology currently displays low thrust-to-mass ratios. While chemical systems are oft-cited as energy-limited due to the finite amount of energy stored in the reactants, electric systems are primarily bound to the limits of the power processing unit. Other considerations may appear, depending on the technology. For instance, the current that can pass through a planar sheath is limited by space-charged effects and sets the maximum achievable thrust for a gridded ion engine. Thrust is rigorously expressed in different ways for chemical and electric systems. However, a common expression can be derived in the form of (1) by considering the fundamental process of momentum exchange under which these system operate

$$T = \dot{m}_p v_p, \tag{1}$$

where $\dot{m}_p$ is the propellant mass flow rate and v_p its effective exhaust velocity. The most powerful single-nozzle liquid-fueled rocket engine ever developed, the F-1, exhibits an oxidizer and fuel combined flow rate of approximately 3,000 $\mathrm{kg/s}$, an exhaust velocity of about 2.5 $\mathrm{km/s}$ and develops 680 metric tons of thrust. On the other hand, the PPS-20k Hall thruster (the most powerful electric thruster tested in Europe) is nominally operated at 43 $\mathrm{mg/s}$ of xenon. The ion velocity is 23 $\mathrm{km/s}$ and the thrust equals 1 N. Exhaust velocities between chemical and electrical systems are separated by one order of magnitude,

[1] Solar sails and laser systems are excluded from the discussion since they do not accelerate a propellant.

while the flow rates differ by $\sim 10^8$! Therefore, while the thrust linearly scales with the propellant velocity and flow rate, its amplitude is mostly determined by $\dot{m}_p$.
However, mechanics states that v_p is the prominent factor to tune in order to deliver a useful mass fraction at destination. The change in vehicle's velocity ΔV, the payload mass fraction ξ and v_p are linked through the rocket equation (2), appropriately named after Konstantin Tsiolkovski who derived it at the beginning of the 20$^{\text{th}}$ century.

$$\xi = \exp\left(-\frac{\Delta V}{v_p}\right). \tag{2}$$

Comparisons between propulsive systems are usually made in the form of (3), which introduces the specific impulse I_{sp}. It is expressed in seconds, and represents the total impulse per unit weight of propellant (it is a measure of how effectively propellant is converted into useful thrust).

$$I_{sp} = \frac{\int T dt}{g_0 \int \dot{m}_p dt}. \tag{3}$$

If the thrust and mass flow rate are assumed constant over the thrust time,

$$I_{sp} = \frac{T}{g_0 \dot{m}_p} = \frac{v_p}{g_0}. \tag{4}$$

As a result of equations (2) and (4), v_p is the main performance indicator used to compare space propulsion systems between each other.

Rewriting equations (1) and (2), the critical parameters of a space mission design (mass consumption and trip time) can be highlighted as a function of the two key parameters of a space engine (thrust and specific impulse)

$$\begin{cases} \Delta m_p = m_i \left(1 - \exp\left[-\dfrac{\Delta V}{g_0 I_{sp}}\right]\right), \\ \Delta t = \dfrac{g_0 I_{sp} \Delta m_p}{T}. \end{cases} \tag{5}$$

In the end, reducing trip time or mass, i.e. developing high thrust or I_{sp}, is a choice that must be made in light of the overall mission needs. Usually a trade must be made and it is up to the designer's discretion to choose the system that best suits the mission.

Orbital mechanics for electric and chemical propulsion systems

Having orbital maneuvers performed by electric thrusters, a chemical propulsion system, or a combination of both, has crucial implications on the vehicle design and operation. For instance, chemically-propelled communication satellites reach their operational orbit in a matter of days, but delivers only a small payload mass fraction at destination. On the contrary, electric thrusters' low fuel consumption results in a high payload mass fraction, at the expense, yet, of months of transfer towards the proper orbit.
However, mechanics applies the same way, whatever the propulsion system. The prime quantity that describes the energy required to perform a maneuver is the ΔV, i.e. the change in magnitude or direction of the velocity vector, or both. This quantity must be carefully planned to maximize the payload mass carried aloft. This section is concerned with the illustration of chemical and electric propulsion performance when dealing with

a textbook case: the transfer trip from a GTO to a GEO orbit. The problem can be constrained in many ways. In this work, we set the vehicle's initial mass and compute the final mass at destination. The transfer time is a free parameter and the trajectory is not optimized to maximize the payload mass fraction delivered in the final orbit, so that the problem is actually under constrained. We assume that the satellite is either equipped with the Daimler-Benz 5400/2 chemical thruster, or with a pair of 5 kW-like Hall thrusters. Their performance are reported in table 1. Their burn period being short compared with the coasting time, chemical maneuvers are considered impulsive, and will be dealt with analytically. The coasting duration in between burns are computed using Kepler's third law. Electric propulsion trajectories cannot be processed the same way and require a much more detailed computation. In this work, the Earth's oblateness, atmospheric drag, luni-solar perturbations and solar eclipses have been considered. The time step is set constant and equal to 100 s.
Let us consider a 4 t satellite, put into a standard 250x36000 km GTO parking orbit by an Ariane 5 rocket launched from the French Guiana Spaceport. The initial inclination of the orbit is 6° and the argument of perigee is 180° for placing the apogee at the ascending node. These injection parameters are those most typically met by Ariane 5 in GTO[1]. Three successive phases are considered: increase of the semimajor axis (only for EP), reduction of the inclination and circularization. Notice that the super-GTO orbit is usually preferred for electric satellites owing to its higher apogee. However, the standard GTO is herein considered for the purpose of the comparison.

Phase 1: Increasing the semimajor axis

The first phase consists in increasing the semimajor axis of the parking orbit to reach that of the final orbit. This operation is first required when using EP for limiting the number of orbits that cross the Van Allen radiation belts. The thrust vector direction is set perpendicular to the position vector in the local orbital plane. The trajectory is shown in figure 1.1. Continuous thrust portions are shown in green. The ballistic eclipse phases, in which the thrusters do not operate, are shown in black.

Phase 2: Reducing the orbit inclination

Chemically-propelled satellite Out-of-plane maneuvers are fuel-consuming and the thrust strategy must be optimized. In order to modify only the orbit inclination, the chemical bursts should occur along the orbit nodal line. Additionally, the spacecraft velocity V_0 should be minimized, since the required ΔV is written

$$\Delta V_{inclination} = 2V_0 \sin\left(\frac{i_f - i_i}{2}\right), \tag{6}$$

where i_i and i_f are the initial and final inclinations, respectively. The argument of perigee, i.e. the angle between the nodal line and the perigee, has been set to 180° for both these reasons.

Electrically-propelled satellite The continuous low-thrust trajectories of electric spacecrafts make it impossible to change the inclination only. Dealing with this phenomenon, however, is well out the scope of this study. The thrust vector is normal to the orbital plane. The trajectory is shown in figure 1.2. The color code is similar to that used in figure 1.1.

Table 1: Performance of chemical and electric propulsion systems for carrying a satellite from GTO to GEO.

		Chemical	**Electric**
	Thruster	1 5400/2, Daimler-Benz	Pair of 5 kW Hall thrusters
	T, N	400	2×0.325
	I_{sp}, s	317	1,730
Phase 1	ΔV_1, m/s		1,234
	m_p, kg		281
	ξ_1		0.930
	duration		89 days
Phase 2	ΔV_2, m/s	167	470
	m_p, kg	209	102
	ξ_2	0.948	0.904
	duration	11 hours	31 days
Phase 3	ΔV_3, m/s	1,473	1,137
	m_p, kg	1,430	234
	ξ_3	0.590	0.846
	duration	24 hours	80 days
Global	ΔV, m/s	1,640	2,841
	m_p, kg	1,639	617
	ξ	0.590	0.846
	duration	35 hours	200 days

Phase 3: Circularization

The orbit must now be circularized for the communication satellite to achieve the GEO.

Chemically-propelled satellite A chemical burst is made at apogee to raise the perigee. The required ΔV reads

$$\Delta V_{circularization} = \sqrt{\frac{\mu}{r_2}} - \sqrt{\frac{2\mu r_1}{r_2\left(r_1 + r_2\right)}}, \tag{7}$$

where r_1 is the initial perigee, r_2 the initial apogee and μ is the standard gravitational parameter of Earth.

Electrically-propelled satellite The electric propulsion thrust is continuous, provided the satellite solar arrays are able to collect sun light. The thrust vector angle is determined from the Gauss form of the Lagrange planetary equations in the case of an in-plane maneuver, thus allowing the most efficient reduction of eccentricity over time[2]. The perigee altitude is raised more quickly than the apogee is decreased. Therefore, there are portions close to the apogee were the thrusters are off while thrust phases near the perigee are still necessary. These portions are indicated in red in figure 1.3.

The Hare and The Tortoise

Chemical systems are the hares, electric thrusters are the tortoises. Yet the moral "slow and steady wins the race" must be nuanced. The performance of both for sending communication satellites in GEO is presented in table 1. Maneuvers are generally more

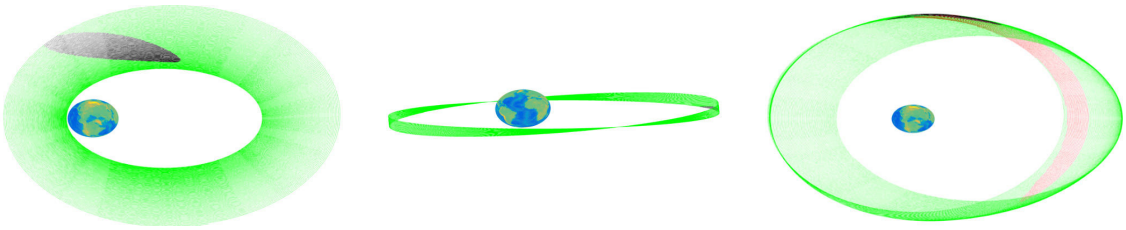

1.1: Phase 1: increase of semimajor axis. 1.2: Phase 2: correction of inclination. 1.3: Phase 3: circularization of the orbit.

Figure 1: Example of a three-phases thrust strategy for an EP-propelled satellite. Continuous thrust portions are shown in green. The ballistic eclipse phases, in which the thrusters do not operate, are shown in black. Red phases are balistic due to the particular nature of the thrust strategy that has been proposed.

challenging to perform for electrically-propelled spacecrafts, in terms of ΔV (i.e. energy required). However, the ions expelled by plasma accelerators shoot out into space with a high velocity, which lowers the fuel consumption compared to chemical devices. The mass budget at destination is therefore more favorable to the payload. Despite some reduction in problem complexity, the coasting time presented in table 1 is close to that computed for real and optimized trajectories. One must then be up for months of transfer trip before starting a commercial use, but it does not seem to deflect the wind beneath the wings of electric propulsion, given its current attractiveness on the satellite market.
This textbook case reflects the global caracteristics of electric and chemical propulsion systems. It also highlights their complementarity. Both could be used in different phases of a single mission, to break free of a planet pull before thrusting continously, for instance. On the contrary, chemical and electric thrusters can be used separately. Based on table 1, electric propulsion is clearly suited for orbit transfer, exploration into deep space and low-altitude missions. Very low-altitude orbits can even be tempted owing to EP unique abilities, like the GOCE mission.

Background and context of this work

Electric thrusters are categorized into three groups, according to their means of generating thrust: electrothermal, electrostatic and electromagnetic. Countless descriptions of these families have already been made by EP fellows[3–5]. **This thesis is concerned with the physics, and the performance, of Hall thrusters[2].**

Electric propulsion applications have been confined to orbit maintenance-like operations since the earliest flights in the 1960's. However, the substantial mass savings allowed by Hall thrusters (HT) yield benefits to a number of Earth orbital and interplanetary missions that other electric propulsion technologies do not provide.
Research and engineering endeavors to develop high-efficiency flight models began in Europe with the fall of the Soviet bloc. Since then, the use of electric propulsion has grown steadily worldwide. Notably, French and American successes have recently demonstrated that EP is not only able to meet earth-orbiting mission requirements, but also to permit exploration in deep space through the SMART-1 and Dawn missions, among others. The developments made by France and the U.S. now span the power range from 0.2 to 100 kW. Still, some major issues arise, and must be overcome, as ever more ΔV is required: the ion bombardment on the channel walls limits the operational lifetime of HT to about 10,000 h and current designs only achieve 55-60 % of efficiency during operation.

[2]Hall thrusters can be said both electrostatic and electromagnetic: ions are accelerated by an electric field, which is generated by means of a magnetic field…

Is there a way to do better?
Recently, the launch of two lightweight satellites based on the Boeing 702SP bus has marked the debut of a new era. As demonstrated in table 1, half of the weight of chemical communication satellites is taken up with fuel. Having the large tank in the bus core removed has made the all-electric satellite producing cycle shorten. Added the increased payload delivered at destination and the launch cost reduced (the main driver for using EP), going all-electric appears as an interesting alternative to conventional systems for telecom operators. In response to Boeing, Airbus Defence and Space has unveiled its own electric propulsion design. Two satellites are slated to launch in 2017 on the Ariane 5 launcher. More contracts are about to be awarded for all-electric platforms. A commercial war has just begun, which is going to determine the future of electric propulsion. Should commercial fleet operators meet the expected cost savings, the number of electric thrusters sell worldwide might soar. Which manufacturer is going to keep the market pace is unknown though.

Research outline

Magnetic topology The channel geometry and the magnetic topology are the most prominent aspects when designing a HT. A focused research program to investigate the consequence of modifying the channel width was started in 2009 within the framework of the CNRS/CNES/Snecma joint-research program GDR 3161. The 200 W Hall thruster known as the PPI (French acronym for *Petit Propulseur Innovant*) was used to vary the channel width while keeping its mean diameter constant. The wall losses have been shown to decrease when enlarging the channel width, resulting in higher ionization efficiency[6]. However, modifying the channel geometry also changes the magnetic field radial gradients and its near-wall amplitude. A detailed study concerning the magnetic field was left to be done.

A central theme of this research is concerned with the influence of the magnetic topology on the performance of HT. The magnetic field confines the plasma, and acts as the support structure that transmits the thrust to the vehicle. The present work focuses on two research axes:

- The role of the magnetic field configuration was first investigated by G. Bourgeois on the PPI and on the PPS®1350-ML[7]. The experiments have shown the dramatic impact of the magnetic field amplitude on the ion acceleration. The magnetic exploration was however limited, due to the lack of flexibility of standard magnetic circuits.
  A new and versatile magnetic structure has been developed by R. Vilamot et al. at the LAPLACE laboratory, which is free from the physical constraints of an usual design[8]. The magnetic structure has been mounted on a dedicated thruster based on the PPS®1350-ML architecture. The prototype is named PPS-Flex, as it appears to be extremely flexible in terms of magnetic field configurations[9]. The objectives of the research program involving the PPS-Flex thruster are manifold, namely: to better understand the influence of the magnetic field, to investigate unexplored operating conditions, and to optimize the B field shape for high-efficiency operation and long lifetime. The vacuum chambers used for the four test campaigns with the PPS-Flex, and the PPS-Flex itself are described hereinafter. The results of the tests are discussed in Chapter 5.

- Modern B field designs have been optimized for HT operation with xenon. However, its scarcity and the large price swings that occur on the rare gas market con-

stitute black spots that make relevant the study of alternative propellants. In search for solutions, a variety of alternatives can be proposed[10–12]. The simplest solution is to substitute another rare gas for xenon, since it would not change the overall architecture of the propulsion system radically. Setting radon aside for safety reasons as it is radioactive, krypton is therefore the next logical choice after xenon in the rare gas family. The performance penalty incurred by utilizing helium, neon or argon would be more significant than with krypton, but specific impulse would increase. It is about 13 times more prevalent than xenon in the air and can currently be produced at a cost fraction of one-tenth that of xenon.
Initial measurements with the PPI operated with krypton have revealed that the acceleration efficiency is not fundamentally altered when using krypton instead of xenon[13]. The higher ionization potential, however, lowers the ionization efficiency of the krypton-fueled discharge. Based on the results of the first attempts with krypton, the ICARE Laboratory has devoted a significant effort in the past two years in designing a Hall thruster to test optimization paths for krypton: the PPI-Mag. The thruster is described in the following sections. The results of the test campaign, conducted in the NExET test bench, are presented in Chapters 4 and 5.

Laser-Induced Fluorescence spectroscopy Aside from the performance and magnetic field analysis, this dissertation is motivated by better understanding the Hall thruster physics. Laser-Induced Fluorescence (LIF) measurements on the XeII ion have been made, prominently along the PPI channel centerline, in the NExET vacuum chamber. The experimental results are presented in Chapters 1, 2 and 3 and shed light on some of the ion flow properties. Accessing the time-averaged and time-varying ion velocity distribution function allows the comparison with PIC codes, that certainly delves deep into the physics, but still require experimental data nonetheless. The research has been particularly focused on two axes:

- A new technique to perform time-resolved LIF measurements has been implemented and investigated. The measurement branch is based on a photon-counting method[14]. Since a statistical photon accumulation appears necessary, a specific set-up that ensures time-coherence is required. Fast power cuts of the plasma have been used in the past. In this case, repeatable conditions are achieved through a periodic reignition of the plasma. This inherently transient regime does not match a natural operation, and more precisely, the time-averaged IVDF departs from the unperturbed regime[14]. Instead, a potential modulation on a floating electrode placed near the cathode exhaust is applied. A resonance with the thruster natural regime of low-frequency oscillation can be found on a narrow modulation frequency band. The temporal evolution of electronic properties have been previously recorded in the far-field plume of the PPI with this system[15]. As we will see, the time-averaged behavior of the thruster is not modified by the driving of the cathode, and validates the technique.
  Time-resolved measurements have been made in the near-field plume of the PPI. Ionization and ion transit time-like oscillations have been observed and analyzed. Features of these modes are discussed and new insights into the Hall thruster physics are gained.

- The electric field is a prime quantity to describe creation and transport of species. Its determination from a LIF data set, however, necessitates a model equation. The time-averaged energy-, fluid- and kinetic-based approaches are examined and compared in the near-field ion flow of the PPI. The physical accuracy and description must be assessed in light of experimental and theoretical requirements. The shortcomings of

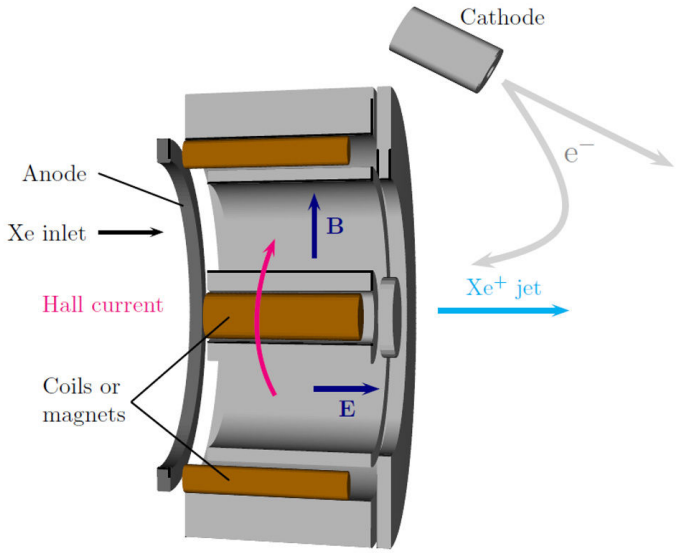

Figure 2: Cross-sectional schematic of a Hall thruster. The neutral propellant is injected into the discharge chamber and collides with electrons trapped by the radial magnetic field to create ion-electron pairs. The ions are accelerated by the axial electric field. Part of the electrons coming from the cathode neutralizes the ion beam.

the models are discussed. Conclusions and recommendations are drawn for a proper computation of the electric field.

The Hall thruster

A Hall thruster is a low-pressure $\mathbf{E}\times\mathbf{B}$ DC discharge maintained between an external cathode and an anode. The ceramic walls of the discharge chamber house the anode, which is placed at the upstream end of the channel, and often serves as a gas injector. Hall thrusters have been fed with a multitude of propellant gas[16]. Xenon is usually preferred for its high atomic mass and low ionization energy. Coils or magnets are strategically placed behind the inner and outer ceramics in a symetrical manner, and imprisoned by iron parts that act as screens that drive the magnetic flux to shape a two-pole pieces architecture. The magnetic topology is complex, and often reduced to a purely radially-directed field along the channel centerline, peaking at the thruster exhaust. The magnetic field strength is chosen strong (respectively weak) enough to make the electron (ion) Larmor radius much smaller (larger) than the thruster discharge chamber sizes. A simple picture, that does not take the anomalous electron transport into account, states that the high electron resistivity induced by the magnetic field generates a sharp potential drop that extends on both sides of the $\mathbf{B}$ field maximum. The resulting axial electric field drives a large electron azimuthal drift, the Hall current, which is responsible for the efficient ionization and acceleration of the gas. The ion beam is neutralized by a fraction of electrons emitted from the cathode. Modern Hall thrusters deliver a thrust-to-power ratio in excess of 50 $\mathrm{mN/kW}$, far above what is produced by gridded ion engines, with an efficiency around 60 %. The specific impulse is nevertheless moderate with a typical value of 2,000 s under normal operating conditions.

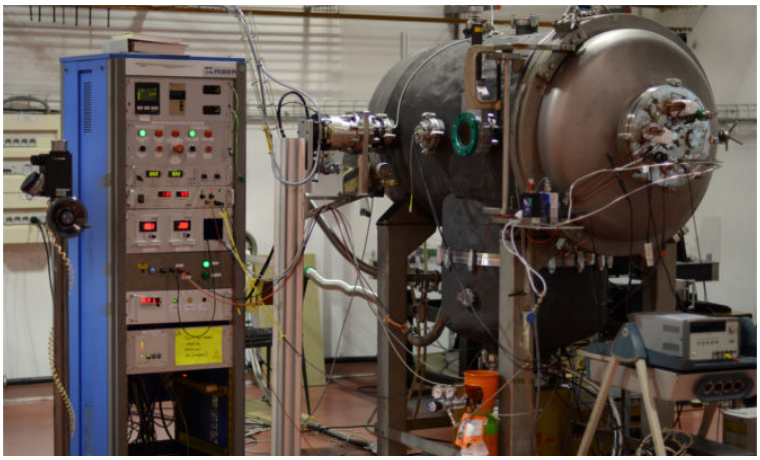

Figure 3: The NExET vacuum chamber.

Overview of test benches

NExET

The NExET (New Experiments on Electric Thrusters) cryogenically-pumped vacuum vessel is dedicated to plasma space propulsion research. This facility has been commissioned at the ICARE laboratory in November 2008 and is used in conjunction with the PIVOINE-2g installation. All the PPI and PPI-Mag experiments have been performed in the NExET vessel. NExET is based on a 1.8 m in length and 0.8 m in diameter stainless steel cylinder. Primary pumping is ensured by a dry pump that evacuates 400 $\mathrm{m^3.h^{-1}}$. A turbomolecular pump is capable of further evacuating NExET to 10^{-6} mbar-N_2, by absorbing light gases such as N_2, O_2, H_2O and H_2 at a rate of 350 $\mathrm{l.s^{-1}}$. The cryogenic pump absorbs gases such as SF_6, Xe and Kr. The pumping speed is 8,000 $\mathrm{l.s^{-1}}$ when the 0.5 $\mathrm{m^2}$ cold plate is sustained at 35-40 K. This pump warrants background pressure as low as 2.10^{-5} mbar-Xe during operation, when backed by the turbomolecular pump. The heavy particle momentum exchange mean free path is thus on the order of the vessel length, ensuring a negligible impact of the residual gas on the measurements. The ion flux is indeed conserved, as demonstrated in Chapter 4. The pump is also capable of absorbing moderate mass flow rates of krypton.
A large water-cooled screen covered with graphite tiles is mounted at the back of the chamber. It absorbs a part of the ion beam energy, therefore reducing the thermal load onto the cryogenic surface. Several observation windows are mounted, as well as multiple vacuum feed-throughs for diagnostics. A large front door enables the access within the vessel.

PIVOINE-2g

Measurements with the SPT100-ML, and part of the PPS-Flex experiments, have been conducted at the PIVOINE-2g ground test facility. The vacuum tank can be seen in figure 4.1. The vessel is 2.2 m in diameter, and 4 m long. Two-stage primary pumping can evacuate PIVOINE to a rough vacuum, before cryogenic pumping is started. PIVOINE is equipped with 10 single-stage cryoheads, surrounded by liquid nitrogen cooled baffles, that pump xenon, and a two-stage cryopump to evacuate light gases such as air, achieving a pumping capability of 200,000 $\mathrm{l.s^{-1}}$ of xenon. A residual pressure of 5.10^{-6} mbar-Xe (1.10^{-5} mbar-Xe) is provided with the 10 (4) cryoheads activated, for a 1.5 kW Hall

4.1: The PIVOINE-2g chamber.

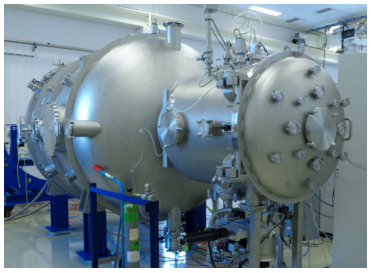

4.2: SPF and CORONA chambers at ESA Propulsion Laboratory.

Figure 4: Vacuum vessels at PIVOINE-2g and ESA ground test facilities.

thruster operating at a flowrate of 4.8 $\mathrm{mg/s}$.
PIVOINE is equipped with an inverted pendulum thrust stand that has proven suited for spanning the 10 mN - 1 N range. A rotating arm is placed inside the vessel with 11 unguarded planar probes to scan the ion current density profile in the plume, at approximately 70 cm downstream the thruster exit plane. The Faraday probe distribution has been modified during the fourth PPS-Flex test campaign in order to evaluate the influence of the probe geometry on the ion current measurements. Another holder, which is able to place diagnostics anywhere in the equatorial plane of the plume, is mounted perpendicularly to the thruster axis. Windows are located at various points on the vessel for performing optical measurements. The thruster can be positionned at multiple positions on the axis of the vessel thanks to a hollow translator that is capable of passing cables and optical fibers through. Finally, the chamber is fitted with numerous tools for monitoring and recording the thruster parameters.

SPF

The Small Plasma Facility (SPF) vacuum vessel[3], located at the European Space Agency (ESA), has hosted the PPI for a series of experiments in June 2013. The objectives were to design and validate a Retarding Potential Analyzer for performing measurements in the backflow of Hall thrusters, where the plasma density is on the order of 10^{12} $\mathrm{m^{-3}}$. These experiments have been made as part of a contract between ICARE and ESA. The results are not included in this dissertation.

CORONA

The third test campaign with the PPS-Flex occurred in the CORONA test bench at ESA Propulsion Laboratory. CORONA is mainly dedicated to electric propulsion thrusters testing activities. The size of the main vessel is 2 m in diameter and 4 m in length, the hatch size is 1 m in diameter and 1.5 m in length. The total volume is about 16 $\mathrm{m^3}$. The pumping speed was measured to be 49,000 $\mathrm{l.s^{-1}}$-Xe at a massflow of 5.0 $\mathrm{mg/s}$.
CORONA is equipped with monitoring devices for both the test bench and thruster operation. As diagnostic tools, CORONA possesses two thrust stands (for measuring thrusts levels inferior or exceeding 10 mN), and three rotating arms that can be fitted with electrostatic probes.

[3]SPF hatch is a 1 m $\times\varnothing$ 1 m stainless steel cylinder. The length and the diameter of the main chamber are equal to 2 m. The nominal pumping capacity is 67,000 $\mathrm{l.s^{-1}}$-$\mathrm{N_2}$.

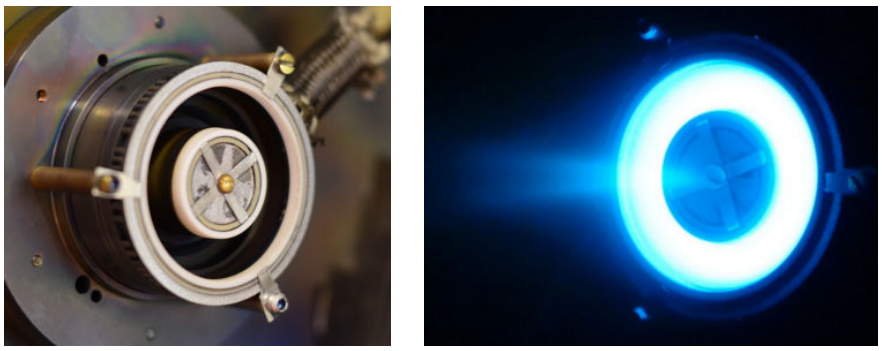

Figure 5: The PPI Hall thruster (left), operating in the SPF vacuum vessel (right).

Hall thrusters used in this work

The Hall thrusters herein described have been operated with an orificed hollow cathode built at the ICARE Laboratory, and based on a MIREA design. Xenon is passed over a lanthanum haxaboride (LaB_6) thermionic emitter, which is constantly heated by a tungsten filament. The heating current ranges from 12 A to 17 A. A keeper electrode is placed near the cathode orifice and initiates the plasma breakdown. The normal operation is then keeperless, except when the discharge is modulated (see Chapter 1). The massflow has been set to 0.2 $\mathrm{mg/s}$ for the PPI and PPI-Mag thrusters, and to 0.4 $\mathrm{mg/s}$ for operating the PPS-Flex and SPT100-ML. The cathode and the thruster are electrically floating, the discharge being grounded by the negative pole of the cathode heating circuit. Its potential has been kept constant and equal to -20 V during testing.

PPI

The PPI is named after a French acronym for *Petit Propulseur Innovant*. The thruster was originally designed by the GEMaC team in Versailles[17,18]. A picture of the PPI HT is shown in figure 5. This thruster exhibits three interesting features that make it highly versatile. First, the magnetic field is generated by way of miniature SmCo magnets brought together inside rings located on either side of the channel walls. A soft iron magnetic circuit with a back gap drives the magnetic flux in order to obtain the desired topology. No magnetic screen is used. The magnetic field strength can easily be modified by varying the number of magnets. Second, the propellant gas is injected homogeneously inside the channel using a porous ceramic instead of a classical metal hollow gas injector. A stainless-steel ring placed at the back of the channel serves as anode. Third, a central copper heat drain is employed to evacuate the heat flux towards a radiator placed behind the thruster. During operation at 200 W, the inner magnet steadystate temperature is 200 $^{\circ}\mathrm{C}$, well below the Curie point.
A special version of the thruster was designed in which the channel width h can be easily modified while keeping the mean diameter d unchanged. Three channel widths were realized by installing three sets of ceramic rings, such that the channel cross-section area is either S_0, two times S_0 or three times S_0, wherein $S_0 = \pi h_0 d_0$ corresponds to the value of standard HT. The three channel geometries are labelled S_0, $2S_0$ and $3S_0$, respectively.
The PPI has been equipped with alumina and boron nitride ceramics during this research. The influence of the wall material on the electric field distribution is briefly discussed in Chapter 1. The magnetic research work is not concerned with this engine, which has been used for studying the physics of Hall thrusters, notably through laser-induced fluorescence measurements.

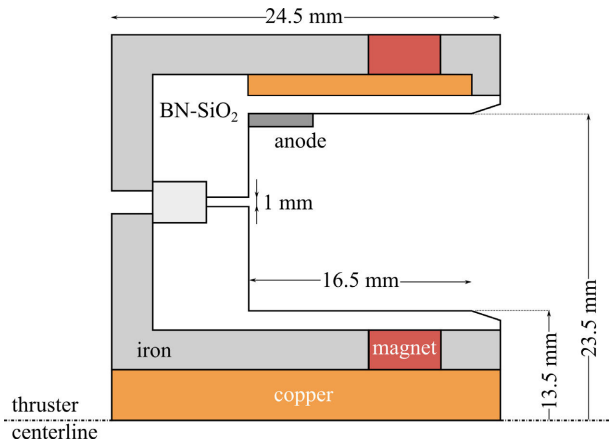

Figure 6: Cross-section schematics of the PPI-Mag.

PPI-Mag

The PPI-Mag is a 200 W Hall thruster that has been used to investigate the influence of a specific magnetic field parameter. Its design has been largely inspired from that of the PPI. The channel geometry is $2S_0$ and cannot be modified. Boron nitride ceramics have been used. A cross-section schematics of the PPI-Mag is shown in figure 6.
Sets of pure iron and AlNiCo magnet rings can be inserted for shaping different magnetic field topographies. The maximum radial B field amplitude and gradients along the channel axis are kept constant between the three configurations that have been tested. However, the width at half-maximum of the radial magnetic field profile, L_B, can be varied. The standard magnetic field configuration is similar to that of the PPI. The aim of the design is to increase the ionization efficiency when krypton is used as a propellant, to reach that of xenon, by enlarging L_B compared to the standard configuration. Details concerning the magnetic field profiles are provided further in Chapter 5.
The PPI-Mag has been operated at various operating points, in xenon and krypton. Measurements in the plume using planar and Langmuir probes have been completed by thermal imagery. The planar probes, the mechanical rotating system and the control software have been designed for the purpose of the measurements and are described in Chapter 4.

PPI-MS

The PPI-MS is a 200 W Hall thruster which possesses a magnetic shielding **B** field configuration[19]. The ceramics are that of the PPI-Mag Hall thruster to allow comparisons between a standard and wall-shielded operation. The magnetic field is generated by small SmCo magnets, and the flux is conducted through an Armco® circuit. Numerous simulation iterations have been made using the free software FEMM, which is able to perform non-linear magnetostatic calculations, in order to design a circuit capable of generating a magnetic shielding topology[20]. Additionally, the magnetic circuit shape and dimension have been optimized to comply with standard machining procedures and tolerances. A photograph of the PPI-MS is shown in figure 7. The design of the thruster magnetic circuit is described in details in Chapter 6.

PPS-Flex

The PPS-Flex is a unique prototype to study the influence of the magnetic topology on the performance of Hall thrusters[9,21]. The PPS-Flex has been designed by Raphaël

Figure 7: Photograph of the PPI-MS.

Vilamot et al. at the LAPLACE laboratory, with the prospect of controlling the B field parameters in independent, versatile and broad manners. The number of magnetizing coils is significantly higher than in standard HT. As can be seen in figure 8, the magnetic circuit of the PPS-Flex is divided into four stages. Four external coils located around the outer wall of the channel and one internal coil wrapped around the central core constitute one stage. Each stage is powered independently. The stage number results from a trade-off between performance, dimensions, complexity, weigth and cost. Each stage provides degrees of freedom for controlling the magnetic topology. The magnetic assembly includes the 20 coils previously described and shown in figure 8. In addition, 2 complementary coils are located behind the back wall of the channel. They allow to better control the zero-field region near the anode as well as the internal gradients. With this configuration, the number of degrees of freedom is 10: 4 internal coils, 4 external stages, each with 4 coils connected in series, and the two back coils. The PPS-Flex operation therefore requires to control independently 10 power supplies just for the B field generation.
The thruster channel geometry is based on that of the PPS®1350. However, both the channel and magnetic assembly have been lengthened. An external conic part, visible in figure 8, has been added. The coils and the ferromagnetic parts that make this last section are necessary to control the magnetic field gradients outside the channel. In order to protect those coils from the thermal heat flux and from ion bombardment, the additional section is shielded with a ceramic piece. The conic shape is such that the ceramic screen has a limited interaction with the plasma downstream the annular channel. Notice that the additional section can be removed. In that case the PPS-Flex channel becomes similar to that of the PPS®1350-ML, at the expense, however, of magnetic flexibility.
In view of the complexity of the magnetic circuit, a sophisticated control interface is necessary to properly operate the PPS-Flex thruster. The process is divided in two parts. A Matlab display permits the definition of the magnetic topology inside the channel, for computation of the necessary currents in each coil and for visualization of the resulting magnetic field map. The computed currents are loaded in a scalar array. A Labview display permits the control of the coil power supplies. The scalar array obtained in the Matlab interface can be directly pasted into a window in the Labview interface, which then automatically configures the power units. This interface also allows a direct control of the power supplies.
Four test campaigns have occurred with the PPS-Flex, in three different vacuum cham-

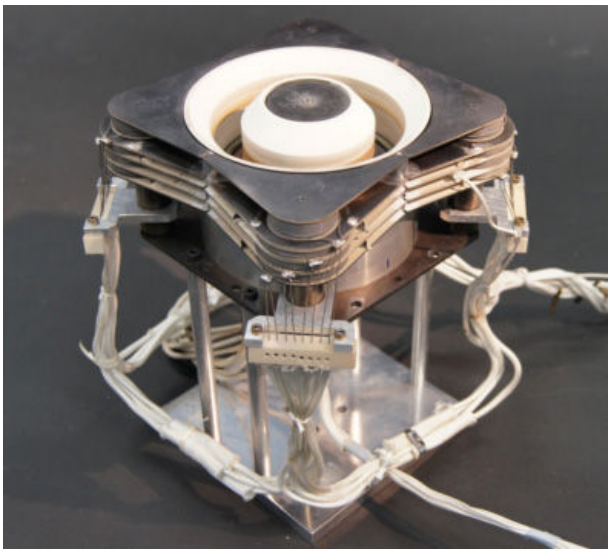

Figure 8: Photograph of the PPS-Flex Hall thruster without the external cathode.

bers: LIC (Snecma, Vernon), PIVOINE-2g (ICARE, CNRS Orléans) and CORONA (EPL, ESA, The Netherlands). The unique abilities of this thruster and its associated controls have made it possible to study the independent influence of the plasma lens, upstream and downstream axial gradients of the radial magnetic field component, B field amplitude...

SPT100-ML

The SPT100-ML is a 1.5 kW Hall thruster which delivers a thrust of about 80 mN at 350 V and 4.8 $\mathrm{mg/s}$ of xenon mass flow rate. The thruster rear plate has been drilled and can be used for shinning a laser beam close to the channel centerline. A slit has been made on both the magnetic circuit and outer ceramic, which allows to observe the channel perpendicularly. Laser-induced fluorescence measurements have been made to derive the axial electric field profile. These results have been used to compare LIF and electrostatic probe outcomes. The results are given in a separate test report[22].

Organization of this thesis

This dissertation is organized in two major parts: Chapters 1 - 3 discuss the physics of Hall thrusters, while Chapters 4 - 6 characterize the performance of Hall thrusters.
In Chapter 1, the laser-induced fluorescence diagnostic tool is presented. The novel method that has been employed for performing time-resolved measurements is exposed and validated in the time-averaged domain. Some quantities of interest for this research that can be deduced from LIF measurements are presented. Chapter 2 presents several models and their respective assumptions that are used to infer time-averaged electric field values from LIF measurements. This discussion is exemplified through measurements in the PPI. A time-resolved characterization of the electric field and ion velocity oscillations is proposed in Chapter 3, using the discharge stabilization technique described in Chapter 1.
Theoretical considerations for accurate probe measurements are presented in Chapter 4. The development of a rotating arm for the NExET vacuum chamber is reported, and measurements in the far-field plume of the PPI-Mag Hall thruster are discussed. The influence of the magnetic topology on the performance of Hall thrusters is analyzed and discussed

Figure 9: Photograph of the SPT100-ML Hall thruster. The magnetic circuit and outer ceramic ring have been machined to allow LIF measurements in the discharge channel. The fluorescence collection optical assembly is shown, and is aligned on the slit to pinpoint the channel axis.

in Chapter 5. The PPS-FLEX and PPI-Mag test campaigns are described, and partial results are presented. Some Hall thruster advanced designs are proposed and discussed in Chapter 6. Finally, the major conclusions from this dissertation are summarized and suggestions for future works are proposed.

References

[1] Edouard Perez. *Ariane 5 User's Manual*. Arianespace, 2011.

[2] A. Ruggerio, P. Pergola, S. Marcuccio and M. Andrenucci. Low-thrust maneuvers for the efficient correction of orbital elements. In Proceedings of the 32nd International Electric Propulsion Conference, Wiesbaden, Germany, IEPC-2011-102, 2011.

[3] D.L. Brown. *Investigation of low discharge voltage Hall thruster characteristics and evaluation of loss mechanisms*. PhD thesis, University of Michigan, 2009.

[4] J. A. Linnell. *An evaluation of krypton propellant in Hall thrusters*. PhD thesis, University of Michigan, 2007.

[5] L. Garrigues. *Modélisation d'un propulseur à plasma stationnaire pour satellites*. PhD thesis, Université Paul Sabatier, 1998.

[6] S. Mazouffre, G. Bourgeois, K. Dannenmayer and A. Lejeune. Ionization and acceleration processes in a small, variable channel width, permanent-magnet Hall thruster. *J. Phys. D: Appl. Phys.*, 45(185203), 2012.

[7] G. Bourgeois. *Influence de la topologie magnétique, de la cathode et de la section du canal sur l'accélération des ions dans un propulseur à effet Hall*. PhD thesis, Université d'Orléans, 2012.

[8] R. Vilamot. *Optimisation de la configuration magnétique d'un propulseur à effet Hall par résolution du problème magnétostatique inverse*. PhD thesis, Université de Toulouse, 2012.

[9] S. Mazouffre, G. Bourgeois, J. Vaudolon, L. Garrigues, C. Hénaux, D. Harribey, R. Vilamot, A. Rossi, S. Zurbach and D. Le Méhauté. Development and testing of Hall thruster with flexible magnetic field configuration. *J. Propul. Power*, 31:1167–1174, 2015.

[10] R.A. Dressler. Propellant alternatives for Ion and Hall effect thrusters. 47th AIAA/ASME/SAE/ASEE Joint Propulsion Conference & Exhibit, San Diego, California, AIAA 2011-5809, 2000.

[11] A. Kieckhafer, L.B. King. Energetics of propellants option for high-power Hall thruster. *J. Propul. Power*, 23(1), 2007.

[12] J. Szabo, B. Pote, S. Paintal, M. Robin, A. Hillier, R.D. Branam, R. Huffman. Performance evaluation of an iodine-vapor Hall thruster. *J. Propul. Power*, 28(4), 2012.

[13] S. Mazouffre, K. Dannenmayer, G. bourgeois, A. Lejeune. Performances of a variable channel width Hall thruster operating with xenon and krypton. In Proceedings of the 3rd Space Propulsion Conference, Bordeaux, France, 2012.

[14] S. Mazouffre and G. Bourgeois. Spatio-temporal characteristics of ion velocity in a Hall thruster discharge. *Plasma Sources Sci. Technol.*, 19(065018), 2010.

[15] K. Dannenmayer. *Scaling laws and electron properties in Hall effect thrusters*. PhD thesis, Université d'Orléans.

[16] R. R. Hofer. *Development and characterization of high-efficiency, high-specific impulse xenon Hall thrusters*. PhD thesis, University of Michigan, 2004.

[17] M. Guyot, P. Renaudin, V. Cagan, C. Boniface. Patent FR 0705658, 2007.

[18] M. Guyot et al. New Concepts for Magnetic Field Generation in Hall Effect Thrusters. Proceedings of the 5th International Spacecraft Propulsion Conference, Heraklion, Greece, 2008.

[19] I.G. Mikellides, I. Katz and R.R. Hofer. Design of a Laboratory Hall Thruster with Magnetically Shielded Channel Walls, Phase I: Numerical Simulations. 2011.

[20] D. Meeker. *Finite Element Method Magnetics, User's Manual*, 2010.

[21] Stéphane Mazouffre, Julien Vaudolon, Guillaume Largeau, Carole Hénaux, Alberto Rossi and Dominique Harribey. Visual evidence of magnetic shielding with the PPS-Flex Hall thruster. *IEEE Transactions on plasma science*, 42(10), 2014.

[22] A. Pétin, J. Vaudolon and S. Mazouffre. Mesures de sonde émissive dans le canal du SPT100-ML et du PPS®1350-ML. Technical report, PE-R-06-2015, ICARE, CNRS, 2015.

Chapter 1

Laser-Induced Fluorescence on Hall thrusters[1]

Contents

THE Hall thruster has benefited from considerable experimental and theoretical research since the 1960's earliest designs. The physical processes that govern its operation remain, however, ill-understood despite the numerous developments worldwide. Plasma/wall interactions, electron transport, influence of the magnetic topology and utilization of alternative propellants rank among the central issues currently investigated. This situation has hindered the construction of novel architectures and predictive models. The fine examination of ion transport in this magnetized plasma source is an important way to access the underlying physics in details. The transport properties of xenon and krypton ions can be examined through the measurement of a statistical quantity, the Ion Velocity Distribution Function (IVDF). Laser-induced fluorescence (LIF) spectroscopy is a non-intrusive way to probe the xenon and krypton IVDF (these two elements being the most common propellants used at this time).

Time-averaged experiments have been extensively performed on Hall thrusters[1–4]. The discharge of a Hall thruster, however, is highly non-stationary, and exhibits a rich spectrum of fluctuations in plasma properties[5]. Current and plasma fluctuations from $\sim$10 kHz up to $\sim$100 MHz play a major role in ionization, diffusion and acceleration. While some studies characterizing the existence and possible control of these oscillations were published in the mid 60's to mid 70's they have received attention recently as there

[1] Adapted from:
J. Vaudolon, L. Balika and S. Mazouffre, *Rev. Sci. Instrum.*, **84**, 073512 (2012)

is a growing need to extend and enhance the performance of these thrusters for a broader range of space missions.
The investigation of the discharge properties naturally requires time-resolved measurements at the oscillation time scale. The time-dependent IVDF is accessible by means of time-resolved laser-induced fluorescence (TR-LIF) on the ion population. In order to achieve time-resolved measurements, a specific set-up is necessary. Phase-sensitive detection has been used by N.A. MacDonald, C.J. Durot and A. Diallo at Standford, Michigan and Princeton universities, respectively, in time- and frequency-domain[6–8]. This system, however, requires large discharge current oscillation amplitudes, and cannot be used to study high frequency oscillations that are superimposed on a low-frequency oscillating background. It also implies to hold the level of a periodic signal from the plasma. Instead, we propose a photon-counting method which does not require the wave pattern to be known in advance over the measurement time period, provided, however, that repeatable conditions can be achieved at some point for trigerring another scan, hence preserving time coherence. This strategy requires some experimental conditions to be met. Firstly, the occurence frequency of fluorescence events must be below the maximum pulse counting rate of the detection system to stay within a linear regime. Secondly, the detection apparatus must be able to distinguish between LIF photons and background noise, and to accumulate over several oscillation cycles. Third, a temporal resolution much below the oscillation time period is required. Finally, and most critical, reproducible measurement conditions imply temporal coherence of the oscillations. This is possible, for instance, with a quasi-periodic behavior of the plasma parameters. Notice, however, that periodic discharge disruption and damping can be observed with this system, which constitutes another option for time-resolved measurements[9].
In Sec. 1.1, LIF basic principles are described. The determination of the Xe II $5d^4F_{5/2} \rightarrow 6p^2D_{5/2}$ and Kr II $4d^4F_{7/2} \rightarrow 5p^2D_{5/2}$ transitions wavelength are reported in Sec. 1.2. Sec. 1.3 depicts the optical bench to perform time-averaged measurements. The photon-counting set-up and the discharge modulation system necessary to undertake TR-LIF are presented in Sec. 1.4. Finally, quantities relevant for this dissertation that can be computed from LIF measurements are presented. Conclusions are drawn in Sec. 1.6.

1.1 Principles

LIF spectroscopy is a non-invasive diagnostic tool that allows the determination of the velocity of probed particles along a laser beam direction by measuring the Doppler shift of absorbed photons[2]. Ions at velocity $\mathbf{v}$ having an electronic transition frequency ω_0 may be driven to an excited state provided they satisfy the required Doppler shift

$$\omega_L - \mathbf{k_L}.\mathbf{v} = \omega_0, \tag{1.1}$$

where ω_L is the frequency and $\mathbf{k_L}$ the wave vector of the laser beam. Scanning the laser frequency yields the one-dimensional distribution function. As indicated by the above equation, ion velocity components along the two axes perpendicular to $\mathbf{k_L}$ are not preferentially selected by the laser. Thus, the measured distribution is

$$f(\mathbf{x}, v_z, t) = \iint f(\mathbf{x}, \mathbf{v}, t) d^2\mathbf{v}, \tag{1.2}$$

where in this case we have taken the laser beam to be along the z direction.

Time-averaged and time-resolved LIF have been extensively used to measure the characteristics of the electric field in Hall thrusters[9,10]. Ion velocity measurements using

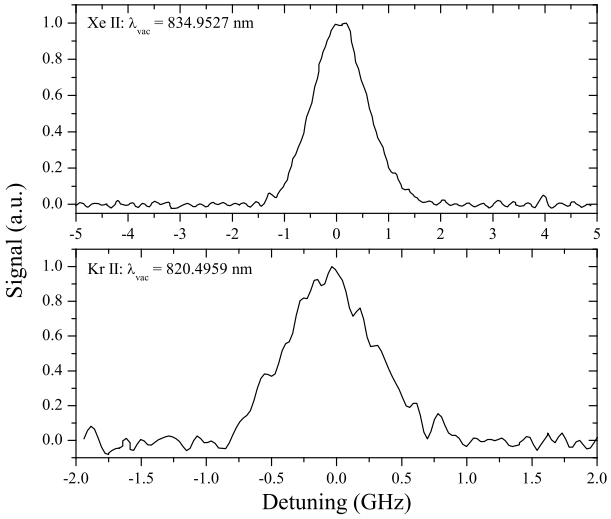

1.1.1: IVDF of Xe and Kr in the RF cell.

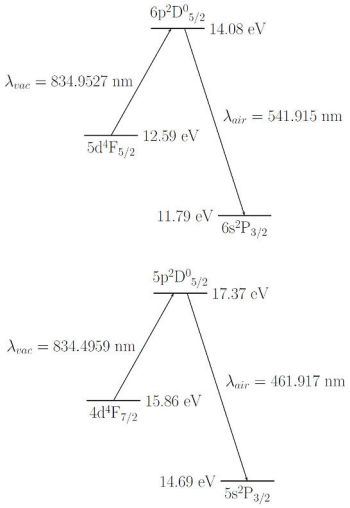

1.1.2: Simplified energy diagrams of xenon (top) and krypton (bottom) ions.

Figure 1.1: Normalized fluorescence spectra as a function of the laser detuning for the xenon and krypton metastable states at room temperature. λ_{vac} is the vacuum wavelength of the transition measured in the RF cell, and corresponds to a 0 GHz detuning.

LIF are extremely accurate, being subjected to the wave-meter resolution and Zeeman effect which can be deconvolved. The Zeeman effect is characterized by a splitting of the energy levels into manifold sub-levels in presence of a magnetic field, which can lead to a broadening of the IVDF. Fortunately, the IVDF width is maximum near the peak magnetic field. In the worst case scenario, the Zeeman broadening would range in the GHz, while the IVDF width is on the order of 10 GHz. The Zeeman effect has therefore been neglected. Since LIF does measure the ion velocity instead of the local plasma potential like an emissive probe would, direct evaluation of the potential drop used for acceleration is made. It however implies to compute the electric field using an appropriate physical model. The IVDF is a quantity that can also be used to compute many parameters which range from fundamental plasma properties to thruster performance.

1.2 Xe II and Kr II transitions

Laser-induced fluorescence examination of xenon and krypton ion ground-states necessitates transition schemes in the XUV or VUV range[2]. However, the large electron density and temperature encountered in the Hall thruster discharge usually allows to assume that low-energy metastable states are directly populated by electron impact, either from the neutral state during ionization, or from the ion ground-state. This feature makes the IVDF of excited states resemble that of ground-state and simplifies considerably the experimental requirements.

The fluorescence spectral line shape is the convolution of the IVDF with the absorption line shape and the laser frequency profile. The laser linewidth is below 1 MHz and can be considered a Dirac delta function. Broadening mechanisms of the ion line shape - isotopic shift, hyperfine structure, Doppler effect and Zeeman splitting - have been studied previously and can be neglected for the transitions considered in this work[2,4,11]. The raw fluorescence spectra presented in this dissertation are therefore considered to correspond to the IVDF.

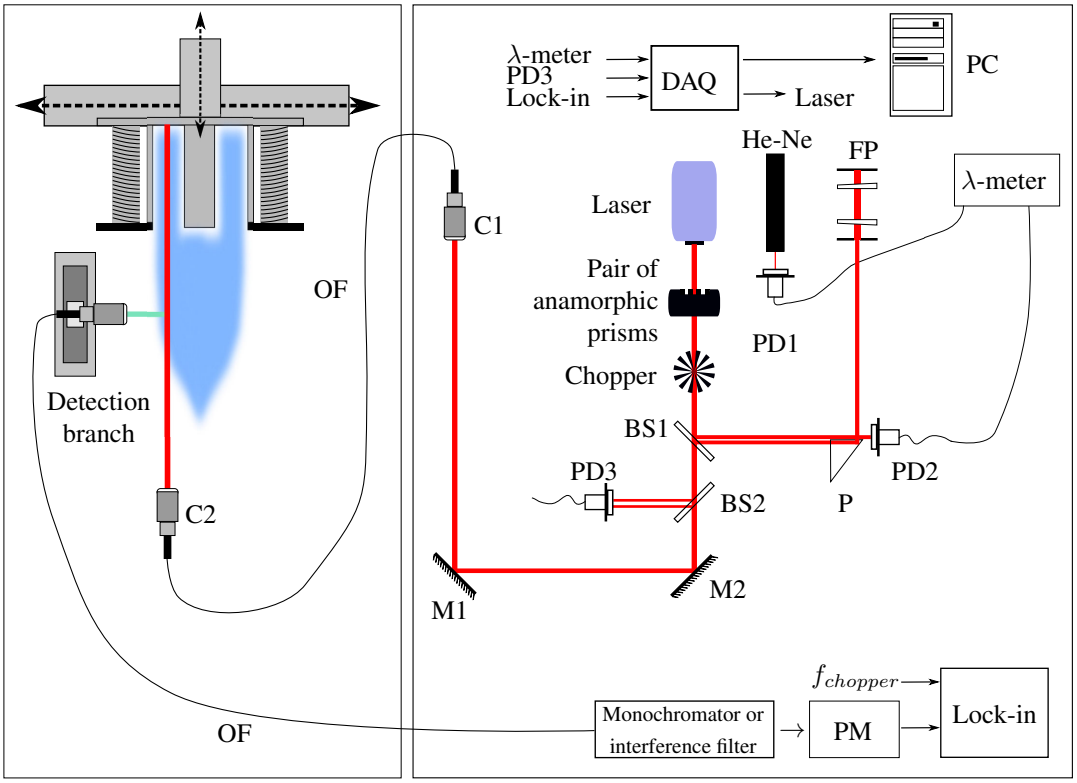

Figure 1.2: LIF optical bench for time-averaged measurements. OF: optical fiber, BS: beam splitter, P: prism, M: mirror, PD: photodiode, C: collimator, FP: Fabry-Perot. The thruster is mounted onto two perpendicular translation stages.

The vacuum wavelengths λ_{vac} of the Xe II and Kr II transitions probed in this research, presented in figure 1.1.1, have been accurately measured by means of LIF spectroscopy in a low-pressure cylindrical RF cell. The optical train is presented in 1.3. The laser beam is injected on both sides of the cell to cancel out any drift effect. The detection branch has been placed at 90° with respect to the laser beam axis. The transition schemes are presented in figure 1.1.2. The xenon $5d^4F_{5/2}$ metastable state at 12.6 eV has been probed at $\lambda_{vac} = 834.9527$ nm. Other contributions report a similar value[11]. The fluorescence is collected at $\lambda_{air} = 541.9$ nm. The large population and the favorable branching ratio of this transition leads to high signal-to-noise ratio[12,13]. The krypton $4d^4F_{7/2}$ metastable state at 15.9 eV has been probed at $\lambda_{vac} = 834.4959$ nm. This value is lower than that found in the literature[14]. The lower signal-to-noise ratio observed in krypton is related to the high energy of the metastable state and to a higher ionization energy compared to xenon. The fluorescence is collected at $\lambda_{air} = 461.9$ nm. The wavelengths values presented in figure 1.1.1 have been used in this work as null velocity references to determine ion Doppler shifts.

1.3 Optical bench for time-averaged measurements

The LIF optical assembly is presented in figure 1.2. The xenon and krypton transitions are probed by an amplified tunable single-mode external cavity laser diode able to deliver up to 600 mW in the near infrared around 800 nm. A pair of anamorphic prisms circularize the laser beam. Beam splitters are used to divide the initial beam into secondary beams. The wavelength is accurately measured by a calibrated 60 m/s pre-

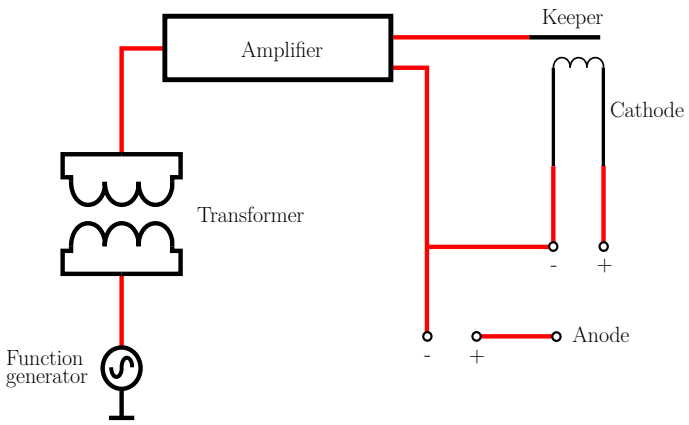

Figure 1.3: Electrical set-up of the keeper modulation.

cision wave-meter. A high finesse Fabry-Perot interferometer is used to check the laser stability and detect mode-hops. The primary laser beam is modulated by a mechanical chopper at a frequency $\sim$1 kHz before being coupled into a single-mode optical fiber of 5 µm core diameter. The laser beam propagates along the center of the discharge channel. The typical laser power density is 10 $\mathrm{mW/mm^2}$ within the measurement volume, which guarantees a sufficient signal-to-noise ratio and a limited saturation of the transition[4]. A collection branch made of a 40 mm focal lens focuses the light onto a 200 µm core diameter optical fiber. The magnification ratio is 1, meaning spatial resolution in the axial direction is 200 µm. The fluorescence light is focused onto the entrance slit of a 20 cm focal length monochromator that isolates the fluorescence line from the background. A photomultiplier tube (PMT) serves as a light detector. For time-averaged LIF measurements, a lock-in amplifier operating at the chopper frequency is used to distinguish the fluorescence light from the intrinsic plasma emission.

1.4 Time-resolved acquisitions

1.4.1 Stabilization technique

At low-pressure, i.e. in low density discharges, the fluorescence signal is made of a few photons per oscillation period. A statistical accumulation appears necessary, even though the fluorescence events could be increased by working in a strongly saturated regime. The core of the optical fiber which collects the fluorescence may also be enlarged, at the expense of spatial resolution yet, a critical point when strong gradients do exist. A temporal coherence of the discharge oscillations is therefore required to perform such an accumulation.

In order to stabilize the discharge, a sinusoidal frequency-tunable potential oscillation is applied between a floating electrode in the vicinity of the cathode (referred to as the keeper) and the negative pole of the cathode. A schematic view is presented in figure 1.3. Such a modulation has been used in a previous work to perform probe measurements in the far-field plume of Hall thrusters[15]. This active harmonic system has two interesting features: firstly, the modulation signal is a clock reference, and has been used as a triggering signal for starting the counting card scans (see 1.4.2). Secondly, the frequency content is fairly the same at any time, which warrants reproducible measurements conditions. Short discharge power cuts have been used in the past to actively perform TR-LIF experiments[9]. This technique has been shown, however, to perturb the time-averaged dis-

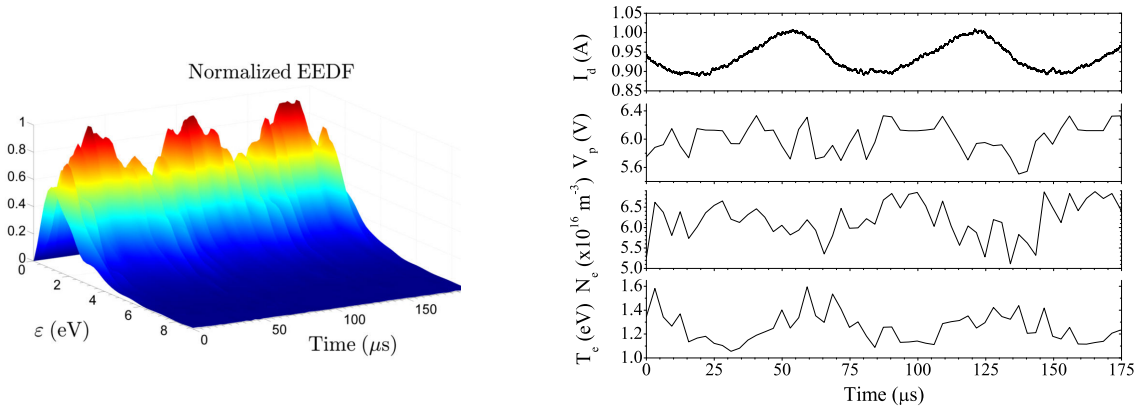

Figure 1.4: (Left) Temporal evolution of the normalized electron energy distribution function (EEDF). The width of the EEDF does not fluctuate much, but its peak amplitude changes over time. (Right) From top to bottom: time-resolved profiles of the discharge current, plasma potential, electron density, and electron temperature.

charge behavior.
The modulation frequency cannot be chosen randomly but corresponds to a characteristic frequency of the system. In this work, resonance has been reached with the low-frequency ionization oscillation known as the *breathing mode*[16]. The discharge current oscillation amplitude is monitored as the frequency is adjusted in order to maximize the plasma response to the excitation. The current driven through the keeper is relatively small and represents approximately 6 % of the discharge current. The potential stimulation peak-to-peak amplitude equals 120 V.
Time-resolved Langmuir probe measurements have been performed at 6 mm away from a heated hollow cathode exhaust, along its centerline. The Langmuir probe tip is made of a 2.5 mm long, 200 µm in diameter pure tungsten wire. The cathode is based on a MIREA design, and is similar to that used to perform the measurements presented in this dissertation, and notably the TR-LIF measurements presented in Chapter 3. The cathode was operated with the PPI thruster at 200 V of discharge voltage and 1.0 mg/s of xenon anode flow rate. The cathode flow rate was 0.2 mg/s. The temporal evolution of the Electron Energy Distribution Function (EEDF) is presented in figure 1.4 (left). The electron energy is denoted ε. The EEDF has been computed using equation (4.16). The width of the EEDF does not appear to fluctuate much, compared to the oscillation of the peak amplitude. Figure 1.4 (right) portrays the evolution of the discharge current, plasma potential, electron number density and electron temperature. There is no discernible coherent evolution of the plasma potential. The electron density variates by 25 %, while the electron temperature oscillates by almost 60 %. Notice that these two oscillations are in phase opposition. Further studies that lie outside the frame of this research could be performed to diagnose the internal cathode plasma.

1.4.2 Modification to the time-averaged bench configuration

Unlike the phase-sensitive detection system used for time-averaged experiments, our strategy for performing time-resolved acquisitions relies on a photon-counting technique. This method has been applied in the past to diagnose oscillating and pulsed discharges[17,18]. However, this is the first time this technique is applied to the remotely-stabilized plasma of a Hall thruster.

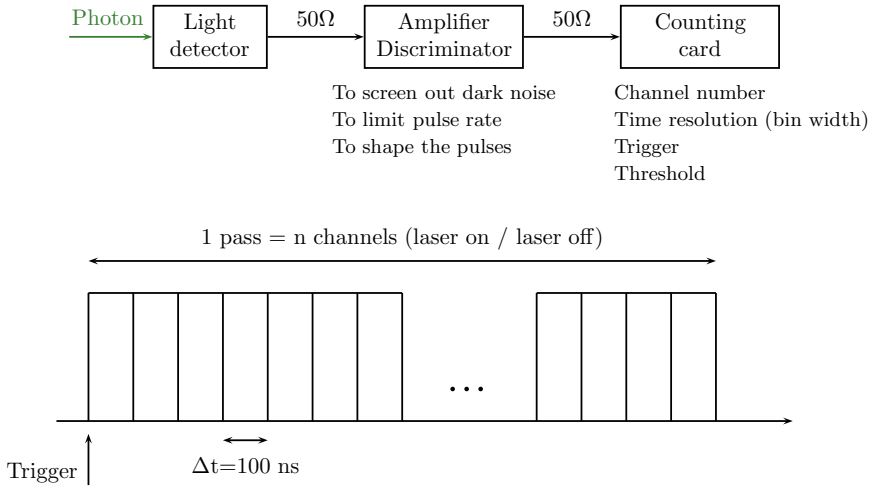

Figure 1.5: Schematic of the detection branch. Photon events are amplified and selected according to their energies. The counting card accumulates the events over n channels of 100 ns length each. Both laser-on and laser-off acquisitions are made to screen out the noise and reveal the fluorescence.

The chopper is removed from the optical bench presented in figure 1.2. This is the only modification to the optical train before injecting the laser into the optical fiber. The detection branch is sketched in figure 1.5. Photons are detected by means of a high gain low dark noise Hamamatsu R7518P photomultiplier tube. A fast amplifier and discriminator 9302 module from Ortec is used to screen out the noise from the PMT. This has two advantages. Firstly, the count rate is limited to avoid the pulse counter saturation. Secondly, any incoming photon is converted into a TTL signal. Each photon pulse can be distinguished from the background noise by an appropriate setting of the discriminator threshold. The pulses are counted by a MCS-PCI multichannel scaler from Ortec, composed of 65,535 channels. The saturation occurs for pulse trains whose frequency exceeds 150 MHz. The direct observation of the discriminator output pulse train by an oscilloscope has made it possible to estimate the count rate to about 10 MHz during our experiments. The modulation signal acts as a trigger which starts the counting of the incoming photon events over a few oscillations period, which warrants perfect reproducibility for each pass. The channel width (the temporal resolution) is 100 ns. Hundreds of thousands of passes are necessary to obtain a suitable LIF signal-to-noise ratio. The laser wavelength is kept constant through a feedback loop, the uncertainty being that of the wavemeter. The fluorescence signal (typically a hundred photons per minute) is extracted by subtracting laser off measurements from laser on acquisitions. As highlighted earlier, the entire period of the oscillation can be recorded instead of being reconstructed by an external device over several oscillation periods. Moreover, any wave shape can be recorded with this technique.

1.4.3 Validation of the technique

Influence of the plasma modulation: discharge current waveform

Figure 1.6 shows the effect of the modulation system on the discharge current. The modulation is set to 16.5 kHz. The resonance with the breathing mode occurs over a 2 kHz band. The monitoring of the maximum discharge current amplitude allows the proper calibration of the modulation frequency. The discharge current mean value remains

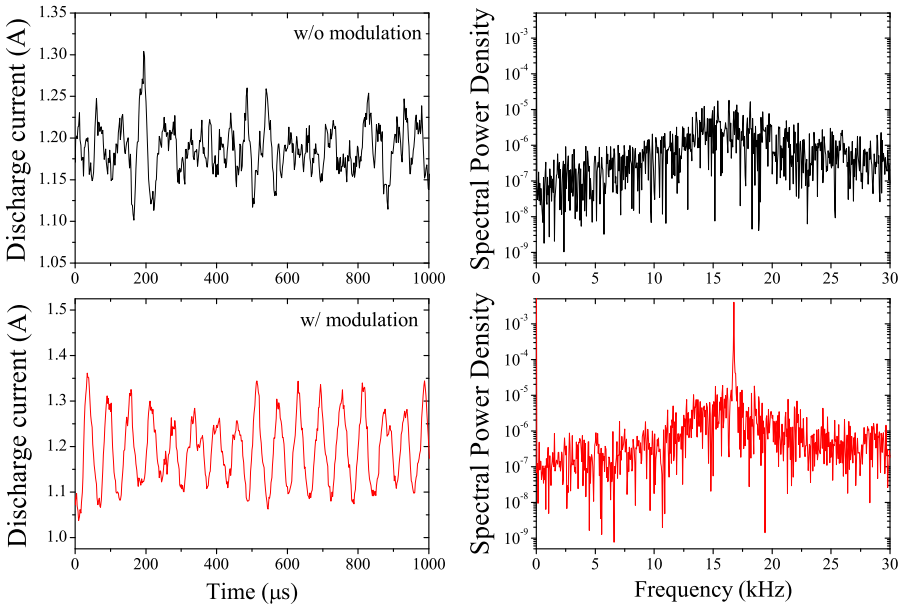

Figure 1.6: Impact of the potential modulation on the discharge current waveforms. A peak response of the plasma has been reached at a modulation frequency of 16.5 kHz.

unchanged, which is mandatory to conserve the thruster time-averaged behavior (the same feature has been observed on the cathode potential relative to ground). The discharge current is also phase-locked, which ensures temporal coherence throughout all measurement scans. A peak is observed on the discharge current Fourier transform at the frequency of the modulation, which reveals an efficient transfer of energy at a particular frequency. The modulated and unmodulated discharges exhibit similar harmonics elsewhere, which tends to indicate that energy remains located in the low-frequency mode. This is however far from certain, as we shall see in Chapter 3.
The possibility of modulating the discharge is related to the ratio of the input power of the modulation amplifier to the power of the system to be modulated. The current driven through the keeper is about 60 mA, which is an additional 2 % input power in the discharge. This value allows an efficient stabilization and does not disturb the thruster average behavior (see figures 1.7 and 1.8). A similar modulation system has been successfully built and tested on a 1.5 kW Hall thruster[15]. In order to achieve a proper control of the breathing mode, a higher amplification was necessary. Similar characteristics of the plasma parameters were observed, meaning this technique is sizeable.

Time-averaged IVDF

Several IVDFs have been acquired along the channel axis of the PPI, at various operating points and locations, to evaluate the influence of the discharge stabilization on the time-averaged ion properties. Figure 1.7 shows the IVDF obtained with and without use of the modulation system, at 5 mm downstream the thruster exit plane. The discharge voltage is set to 200 V, the anode flow rate is 1.2 mg/s and the channel walls are made of BN-SiO_2. The spectra match each other at almost every ion velocity. A slight difference on the low velocity tail of the main peak is noticeable. The velocity gap, however, is close to the measurement error. The discrepancy likely originates from the thruster thermal drift since it is also observed on two successive measurements performed on a discharge free from the stabilization apparatus.

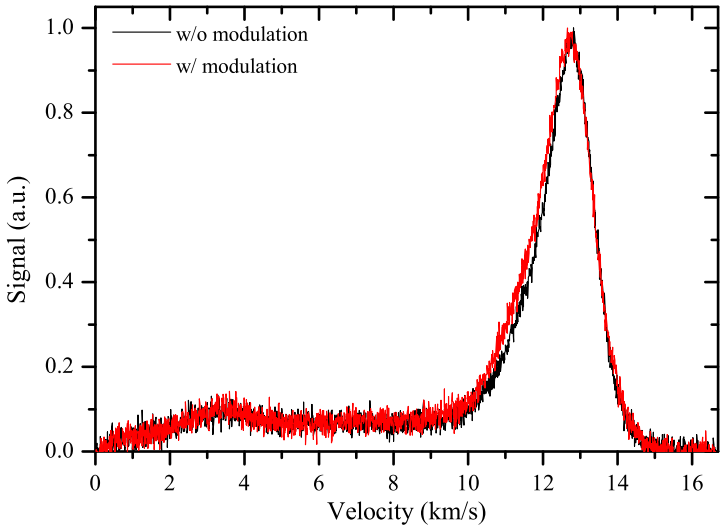

Figure 1.7: Time-averaged IVDF of the modulated and unmodulated discharge, at 5 mm downstream the thruster exit plane.

Reconstruction of time-averaged IVDFs

Time-averaged LIF profiles can be reconstructed from time-resolved measurements. This is a way to determine whether the statistical accumulation is able to properly extract the LIF signal with the current parameters. Examples of time-resolved IVDF, as well as typical measurement parameters, can be found in Chapter 3. Figure 1.8 presents the reconstruction of the time-averaged IVDF from the time-resolved data. The signals have been normalized for the purpose of the comparison. The raw time-averaged LIF profile obtained with a lock-in detection technique is shown in black. The temporal means of the photon time series, plotted in red squares, perfectly match the time-averaged measurements, which validates our approach. Several positions have been examined inside and outside the discharge channel. A perfect agreement between time-resolved and time-averaged LIF has been observed at each location along the channel axis.

1.5 Quantities deduced from LIF measurements

Numerous quantities can be inferred from LIF measurements. Quantities of interest for the purpose of this dissertation are presented in the following sections through the analysis of some measurements. Notice, however, that other parameters can be computed, such as the IVDF standard deviation, of which axial profile highlights, for instance, the typical overlapping of the ionization and acceleration areas in Hall thrusters[4].

1.5.1 Ion velocity distribution

In our conditions, laser-induced fluorescence directly accesses the (3D,1V) IVDF in a non-intrusive manner by measuring the ion Doppler shift. Since our LIF test bench has not been calibrated, there is no possible way of measuring absolute ion densities. The signal is therefore expressed in arbitrary units.
The ion velocity distribution has been acquired in the plume of the PPI, along the channel centerline, at nominal operating point: 200 V discharge voltage, 1.0 $\mathrm{mg/s}$ anode flow rate. The $2S_0$ channel was equipped with alumina ceramics. Measurements have been performed from 6 mm inside the channel up to 100 mm downstream the ion flow. The

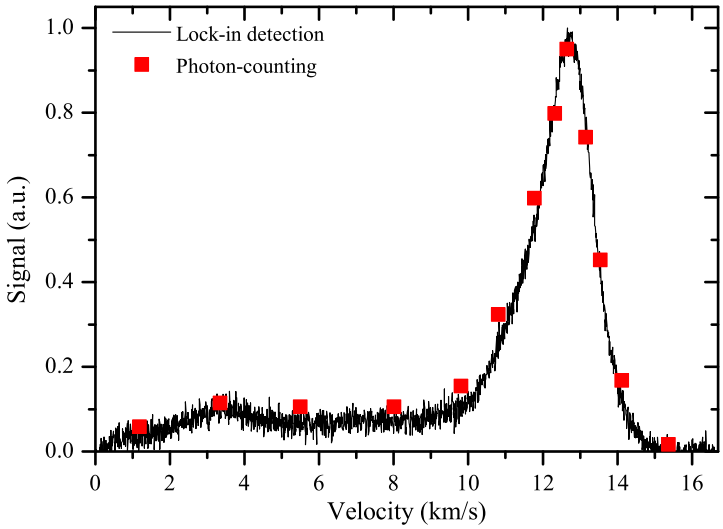

Figure 1.8: Comparison between the raw IVDF obtained through time-averaged LIF and the profile inferred from the photon-counting technique, at 5 mm downstream the thruster exit plane.

mapping of axial IVDFs in the 1D-phase space is presented in figure 1.9. The colorbar magnitude corresponds to the normalized signal. The main accelerating pattern is labelled (1), and corresponds to the most probable ion group accelerated by the electric field. Since LIF measures the ion velocity component projected on the laser wave vector direction, and because of the finite beam divergence angle, ions leaving the channel from the diametrically opposed location appear as slow velocity ions in group (2). Assuming a monokinetic ion population that diverges from a point source localized on the mean diameter, the velocity vector projection geometrically scales with $\cos\left(\tan^{-1}\left(1/z\right)\right)$, where z is the distance from the thruster exit plane, hence the curvature of group (2)[19]. Groups (3) and (4) could result from local ionization or from charge-exchange collisions, see the collision mean free paths in table 2.1.
This mapping was previously made in the plume of the PPI, but the measurement range did not extend inside the channel. Despite that several hundred hours of thruster operation and a year separate the two series of measurements, the velocity groups that appear on the map are similar to those previously observed[19]. The thruster was also operated with two different cathodes, however based on the same design. The similarities in the IVDF mapping therefore indicates that the ceramics wearing mechanisms do not modify the physical processes that generate these velocity groups.

1.5.2 Electric field and ionization frequency profiles

The local electric field amplitude can be computed using a model. Three time-averaged approaches are proposed in Chapter 2. Additionally, the time-averaged ionization frequency profile can be obtained from the Boltzmann equation. Weak assumptions on this equation lead to the separation of ionization and acceleration contributions, even if these processes are physically linked.

1.5.3 Electron temperature

Langmuir probe measurements are usually used to compute the electron temperature. Deriving this quantity from LIF measurements is more intricate and experimentally-

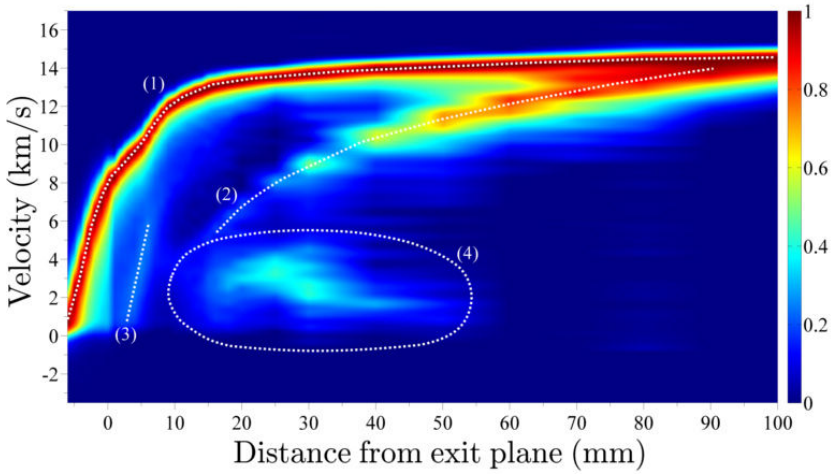

Figure 1.9: Normalized map in a 1D-phase space representation of xenon ion axial velocity distributions. The position 0 mm refers to the PPI channel exit plane.

requiring. Firstly, several IVDFs need to be acquired with a spatial step small enough to ensure a suitable resolution when computing the ionization frequency from the Boltzmann equation, see Chapter 2. The experimental signal-to-noise ratio is a quantity which plays a major role on the final computation, and must be maximized. Secondly, the ion density profile is obtained in arbitrary unit from the IVDF integration. Assuming a quasi-neutral plasma, a single Langmuir probe measurement can be used to infer the electron density at some location in the plume, in order to obtain the absolute density profile, without resort to the optical assembly calibration[2]. The ionization rate is therefore known and can be used to determine the electron temperature[20]. This is an interesting manner to evaluate the electron temperature with a non-invasive technique. The probe perturbation can indeed be limited by measuring the I-V characteristic in the far-field plume, yet not to far for the LIF signal-to-noise ratio to be acceptable.

Comparison of electron temperatures deduced from emissive probe and LIF measurements has been made in the near-field plume of the PPI operating under nominal conditions[21]. No electron density measurement has been made to obtain the absolute density profile. Instead, we have appropriately chosen the ion density to equal 6.10^{17} m^{-3} at the exit plane.

The heated emissive probe has been effective in measuring the plasma potential Φ_{hp} in a wide variety of plasmas, from RF discharges to tokamaks. In this work, we have considered the floating point technique[22]. The heaterless probe has been used to measure the floating potential Φ_{cp}. Assuming a constant ion flux in the sheath, and that ions enter the sheath at the Bohm velocity, the difference between the floating potential Φ_{fl} of the filament and the plasma potential Φ_{pl} scales linearly with the electron temperature. We have assumed that $\Phi_{fl} = \Phi_{cp}$. Due to the space charge limited regime of the emissive sheath, the floating potential saturates at $\alpha \mathrm{T_e}/e$ below the plasma potential. More precise measurements using the inflection point method, and PIC simulation predictions have revealed that $\alpha \sim 1.5$[22]. Therefore, we have assumed that $\Phi_{pl} = \Phi_{hp} + 1.5T_e$.

The electron temperature values inferred from emissive probe and LIF measurements are presented in figure 1.10. The small electron temperature deduced from LIF measurements at locations downstream 10 mm does not seem physical. An appropriate setting

[2]The density profile is rigorously that of the metastable state that is probed. However, since we assume the IVDF to resemble that of the ground state, we implicitly suppose that any quantity derived from it mimics the ground state dynamics.

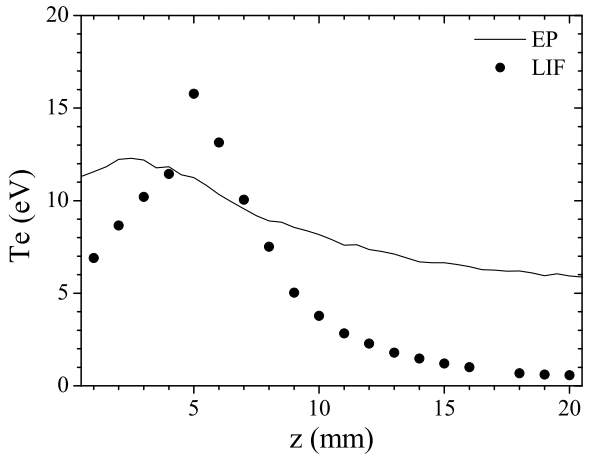

Figure 1.10: Electron temperature profiles deduced from emissive probe and LIF measurements.

of the density profile baseline, an improved signal-to-noise ratio to compute the ionization frequency evolution, or LIF-calibrated measurements of the Xe II ground-state, may provide a more accurate evaluation of the electron temperature.

1.6 Conclusion

The basic principles of laser-induced fluorescence spectroscopy have been briefly presented. The xenon and krypton transitions used in this thesis have been probed at rest, and reference vacuum wavelengths have been obtained. These values have been used to compute the ion velocity from LIF measurements in Chapters 2 and 3. The optical train and the detection branches used for time-averaged and time-resolved measurements have been described.

The photon-counting technique has been validated as a diagnostic technique, provided the discharge oscillations can be maintained in a quasi-harmonic regime. A potential modulation on a floating electrode placed in close proximity of the cathode exhaust has proven to be capable of injecting energy in a narrow frequency band, thus achieving resonance with the discharge. Temporal coherence has been achieved by synchronizing the measurements and the discharge oscillations. The association of both the modulation and the pulse-counting techniques appears to be very effective to perform time-resolved measurements. This technique is able to examine the discharge oscillations, in an almost natural regime, without modifying the time-averaged behavior of the plasma parameters.

Laser-induced fluorescence allows the determination of the local electric field, a key quantity that controls ionization, transport, and in the case of Hall thrusters, the overall performance. Yet its computation appears abstruse, and relies on a physical model. Time-averaged LIF is used in Chapter 2 to clarify the models that can be considered in an experimental work (and to pinpoint their limits), while a time-resolved investigation of the electric field and of the ion flow is made in Chapter 3.

References

[1] D.H. Manzella. Stationary plasma thruster ion velocity distribution. AIAA 1994-3141.

[2] S. Mazouffre. Laser-induced fluorescence diagnostics of the cross-field discharge of Hall thrusters. *Plasma Sources Sci. Technol.*, 22(013001), 2013.

[3] W.A. Hargus and C.S. Charles. Near exit plane velocity field of a 200-watt Hall thruster. *J. Propul. Power*, 24(1), 2008.

[4] G. Bourgeois. *Influence de la topologie magnétique, de la cathode et de la section du canal sur l'accélération des ions dans un propulseur à effet Hall*. PhD thesis, Université d'Orléans, 2012.

[5] E.Y. Choueiri. Plasma oscillations in Hall thrusters. *Phys. Plasmas*, 8(1411), 2001.

[6] N. A. MacDonald, M. A. Cappelli and W. A. Hargus. Time-synchronized continuous wave laser-induced fluorescence on an oscillatory xenon discharge. *Rev. Sci. Instrum.*, 83(113506), 2012.

[7] C. J. Durot, A. D. Gallimore and T. B. Smith. Validation and evaluation of a novel time-resolved laser-induced fluorescence technique. *Rev. Sci. Instrum.*, 85(013508), 2014.

[8] A. Diallo, S. Keller, Y. Shi, Y. Raitses and S. Mazouffre. Time-resolved ion velocity distribution in a cylindrical Hall thruster: Heterodynebased experiment and modeling. *Rev. Sci. Instrum.*, 86(033506), 2015.

[9] S. Mazouffre and G. Bourgeois. Spatio-temporal characteristics of ion velocity in a Hall thruster discharge. *Plasma Sources Sci. Technol.*, 19(065018), 2010.

[10] J. Vaudolon, B. Khiar and S. Mazouffre. Time evolution of the electric field in a Hall thruster. *Plasma Sources Sci. Technol.*, 23(022002), 2014.

[11] E. Pawelec, S. Mazouffre and N. Sadeghi. Hyperfine structure of some near-infrared Xe I and Xe II lines. *Spectrochimica Acta Part B*, 66:470–475, 2011.

[12] S. Zielinska, L. Bratasz and K. Dzierzega. Absolute transition rates for transitions from $5p^4(^3P)6p\ ^4P_{5/2}$, $^4P_{3/2}$, $^4D_{7/2}$ and $^2D_{5/2}$ levels of Xe II. *Physica Scipta.*, 66:454–457, 2002.

[13] K. Dzierzega, U. Griesmann, G. Nave and L. Bratasz. Absolute transition rates for transitions from 5p levels in Kr II. *Physica Scipta.*, 63:209–218, 2001.

[14] See http://www.nist.gov/pml/data/asd.cfm for NIST atomic spectra database.

[15] K. Dannenmayer. *Scaling laws and electron properties in Hall effect thrusters*. PhD thesis, Université d'Orléans.

[16] J.P. Bœuf and L. Garrigues. Low frequency oscillations in a stationary plasma thruster. *J. Appl. Phys.*, 84, 1998.

[17] B. Pelissier and N. Sadeghi. Time-resolved pulse-counting lock-in detection of laser induced fluorescence in the presence of a strong background emission. *Rev. Sci. Instrum.*, 67(3405), 1996.

[18] S. Mazouffre, D. Gawron and N. Sadeghi. A time-resolved LIF study on the ion velocity distribution function in a Hall thruster after a fast current disruption. *Phys. Plasmas*, 16(043504), 2009.

[19] A. Lejeune, G. Bourgeois and S. Mazouffre. Kr II and Xe II axial velocity distribution functions in a cross-field ion source. *Phys. Plasmas*, 19(073501), 2012.

[20] G.J.M. Hagelaar and L.C. Pitchford. Solving the Boltzmann equation to obtain electron transport coefficients and rate coefficients for fluid models. *Plasma Sources Sci. Technol.*, 14:722, 2005.

[21] J. Vaudolon, A. Pétin and S. Mazouffre. Evaluation of different methods for determining the electric field profile in a Hall thruster. Proc. of the 4th Space Propulsion Conference, SP2014-2979732, 2014.

[22] J.P. Sheehan, Y. Raitses, N. Hershkowitz, I. Kaganovitch and N.J. Fisch. A comparison of emissive probe techniques for electric potential measurements in a complex plasma. *Phys. Plasmas*, 18(073501), 2011.

Chapter 2

How to compute the electric field from LIF measurements?[1]

Contents

THE electric field distribution plays a fundamental role in the dynamics, the physical processes and the organization of plasma discharges. It governs the species transport, wave structures, ionization phenomena and sheath properties and its precise determination is therefore key[1–4]. Different techniques have been developed to measure macro and microfields in low-pressure discharges. Intrusive methods such as Langmuir and emissive probes are widely used[5,6]. A Langmuir probe can provide the plasma potential from its I-V curve with a reasonable uncertainty. An emissive probe is a quick and easy way to access the local plasma potential using the floating point technique, provided the sheath potential is significantly reduced to limit the error on the measurement[7]. More sophisticated methods are available for properly extracting the plasma potential from the current-voltage trace[8]. Langmuir and emissive probes, however, suffer from a variety of intricate uncertainties, such as the theory used to derive the plasma quantities, contamination issues and their inherent invasive nature.

In contrast, optical methods have the advantage of being non-intrusive. Unlike probes, optical techniques also do not require complex apparatus to compensate for the strong oscillations of the discharge. The Stark shift of high Rydberg states of the hydrogen, helium, argon, krypton and xenon gases has been successfully measured by a technique called fluorescence dip spectroscopy, with high spatial and temporal resolution[9–13]. In short, this technique excites atoms from their ground state to a short-lived intermediate state with one or two photons coming from a first laser. The fluorescence

[1] Adapted from:
J. Vaudolon and S. Mazouffre, *Phys. Plasmas*, **21**, 093505 (2014)

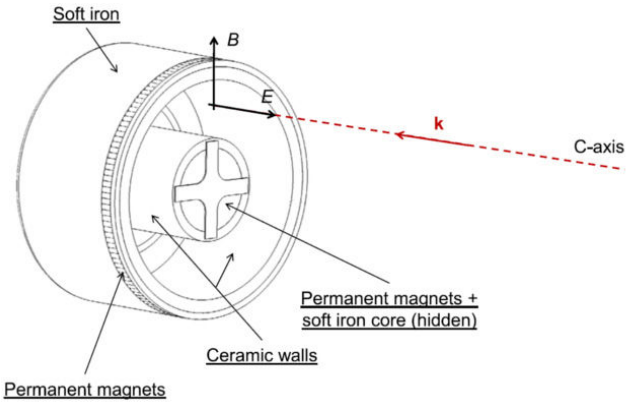

Figure 2.1: Layout of the PPI ; the laser propagates axially. **k** is the laser wave vector, either oriented in the radial or axial directions in this work.

light from this intermediate state is then depleted when a second step excitation is resonant with a Rydberg state. In highly-excited Rydberg states, the electrons are on large orbits and the electric field of the core is relatively weak. Thus, small external fields can be detected with a great accuracy. The minimum detectable field is mostly limited by the finite bandwidth of the laser radiation and is on the order of 1 $\mathrm{V/cm}$[13]. Fluorescence dip spectroscopy is accurate but cumbersome and expensive since it requires solid-state lasers and complex optical trains.

Laser-Induced Fluorescence on a metastable ion state is affordable with laser diodes and is less complicated, provided that the metastable state properties can image the ground state dynamics. As described in Chapter 1, this technique allows the direct measurement of the IVDF with high spatial and temporal resolution[14]. The determination of the local electric fields, however, is indirect and requires the use of a physical model. The purpose of this part is to evaluate the applicability of different methods for computing the electric field distribution from LIF measurements. The vast set of results available, the complex electric and magnetic cross-field topology, the kinetic regime of the discharge and the partial overlapping of the ionization and acceleration zones make the Hall thruster plasma particularly interesting for this study. LIF measurements can require several days, possibly even weeks, of experiments for the derivation of a full electric field profile. For this reason, the choice of the physical model which best describes the problem at stake, and an evaluation of the practical possibilities for reducing the number of acquisitions are important issues.

The method we suggest to compare various ways of extracting the electric field is based on LIF experiments, performed in the PPI Hall thruster. The PPI is depicted in figure 2.1. The electric and magnetic field directions are given. The measurements have been performed along the channel axis (red line). The laser wave vector used for the LIF measurements is designated as $\mathbf{k}$. $\mathbf{k}$ has been oriented in radial and axial directions to measure the concomitant IVDF. We use an (r, θ, z) cylindrical coordinate system to account for the annular shape of the source. Azimuthal contributions are neglected[15].

Sec. 2.1 presents the theoretical models that can be used to derive the electric field profile from LIF measurements. Sec. 2.2 describes the experiments and examines the results. Finally, conclusions and recommendations are discussed in Sec. 2.3.

Table 2.1: Ionization, charge-exchange and momentum exchange collision mean free paths[16,17]. The Xe neutral density is assumed constant and equal to 10^{18} m^{-3}. Momentum transfer and ionization collisions can be neglected in the acceleration zone. Charge-exchange may however occur locally. The ionization mean free path is far greater than that in the discharge channel, since the neutral density at the anode is at least an order of magnitude higher.

	Cross-section, m^2	**Mean free path,** m
Momentum transfer, e-Xe	10^{-22}	10,000
Momentum transfer, Xe^+-Xe	10^{-20}	100
Charge-exchange, Xe^+-Xe	6.10^{-17}	0.02
Ionization, e-Xe	4.10^{-20}	25

2.1 Methods for determining the E field using LIF data

Since LIF measures the ion velocity instead of the local plasma potential as an emissive probe does, a direct evaluation of the ion kinetic energy is made. An appropriate physical model, however, is required, in order for the electric field to be computed. The energy conservation, the fluid and Boltzmann equations that have been considered in the present work are now described.

2.1.1 Energy conservation

Since the ionization and acceleration regions partially overlap in a Hall thruster, the locally-created ions, with a null mean velocity, also contribute to the overall mean velocity value of the IVDF. Such low-velocity ions can be seen on the axial IVDF presented in figure 2.3 for instance. The consideration of the ion mean velocity (first order moment of the IVDF) will therefore result in an underestimation of the true local axial electric field.

The simplest way to evaluate the electric field using a LIF data set is to compute the ion potential energy using the most probable ion velocity. Ions travelling at this velocity have been generated at the beginning of the ionization zone, where the electrostatic acceleration has not been experienced yet. The most probable ion velocity group subsequently flows out of the entire acceleration domain at the measurement point. In this approach, we neglect the ionization, charge-exchange and momentum exchange collisions. However, the collision mean free paths presented in table 2.1 show that charge-exchange collisions are highly-probable in the near-field plume[16,17]. The ion group labelled (4) in figure 1.9, located 20 to 30 mm downstream the PPI exit plane, may well originate from CEX collisions with the residual gas.

The evaluation of the potential then simply reduces to the energy conservation equation for a particle in a static electric field. This viewpoint differs from an ensemble average perspective reached when considering the ion mean velocity. Use of the latter is further addressed in the fluid model. Under these considerations, the energy conservation therefore reads

$$\frac{1}{2} m_i v^2 = eU, \tag{2.1}$$

where notations have their usual meaning. The mixed spatial derivatives have been neglected. The radial and axial accelerating electric fields thus read

$$\begin{aligned} E_r &= \frac{m_i}{2e}\frac{dv_r^2}{dr}, \\ E_z &= \frac{m_i}{2e}\frac{dv_z^2}{dz}, \end{aligned} \tag{2.2}$$

where in this case, v_r and v_z respectively refer to the radial and axial most probable ion velocities.

2.1.2 Fluid equations

The fluid electric field is expressed in the steady-state and non-stationary cases. The time-averaged model is used in this chapter. Chapter 3 makes use of the non-stationary equation.
We consider the continuity and momentum conservation equations for unmagnetized ions, in the case of negligible charge-exchange and momentum-exchange collisions, which give

$$\begin{cases} \dfrac{dn}{dt} + \nabla.\left(n\mathbf{w_1}\right) = \nu_i n, \\ \dfrac{dn\mathbf{w_1}}{dt} + \nabla.\left(n\mathbf{w_1}\otimes\mathbf{w_1}\right) = \dfrac{e}{m_i}n\mathbf{E} + \nu_i n\mathbf{u_n} - \dfrac{1}{m_i}\nabla\mathbf{P}, \end{cases} \tag{2.3}$$

where n is the plasma density, ν_i the ionization frequency, $\mathbf{u_n}$ the neutral velocity, $\mathbf{w_1} = (w_{1,r}, w_{1,z})$ the ion mean velocity, which is given by the first order moment of the IVDF, and $\mathbf{P}$ the pressure tensor. No strong shear stresses are expected in the region of the ion flow investigated by the fluid model in our work. Off diagonal elements of the pressure tensor are therefore set to zero. The collisionless medium and the strong anisotropy of the plasma flow however implies to distinguish the radial and axial pressure terms.

Steady-state case

The continuity equation is inserted in the momentum balance equation. The neutral mean velocity is assumed to be zero. The one dimensional case has been studied only, since none of our analysis consider the mixed spatial derivatives. The time-averaged electric fields thus read

$$\frac{eE_r}{m_i} = w_{1,r}\frac{dw_{1,r}}{dr} + \nu_i w_{1,r} + \frac{1}{nm_i}\frac{dP_{rr}}{dr}, \tag{2.4}$$

$$\frac{eE_z}{m_i} = w_{1,z}\frac{dw_{1,z}}{dz} + \nu_i w_{1,z} + \frac{1}{nm_i}\frac{dP_{zz}}{dz}. \tag{2.5}$$

Time-varying electric field

Under the same assumptions, system (2.3) can be rewritten to obtain the temporal evolution of the electric field

$$\frac{eE_z}{m_i} = \frac{1}{n}\frac{dnw_{1,z}}{dt} + \frac{w_{1,z}}{n}\frac{dnw_{1,z}}{dz} + w_{1,z}\frac{dw_{1,z}}{dz} + \frac{1}{nm_i}\frac{dP_{zz}}{dz}. \tag{2.6}$$

The ionization and pressure gradient terms need to be considered for the electric field profile to be computed. However, measuring these terms is a demanding task. In order to distinguish the acceleration and ionization contributions, the Boltzmann equation can be used.

2.1.3 Boltzmann equation

The Boltzmann model is presented in the time-averaged case only. The 1D1V time-resolved electric field and ionization frequency equations have been presented in a previous work[18].
The Boltzmann equation uses the IVDF directly inferred from LIF measurements. Neglecting charge-exchange collisions, momentum-exchange collisions and the neutral gas temperature compared to the ion energy, the Boltzmann equation reads

$$\mathbf{v}.\nabla_{\mathbf{r}} f + \mathbf{a}.\nabla_{\mathbf{v}} f = \nu_i f_0, \tag{2.7}$$

where $\nabla_{\mathbf{r}}$ and $\nabla_{\mathbf{v}}$ stand for the space and velocity gradients, $\mathbf{a}$ is the acceleration and f_0 is the distribution of the neutrals, approximated by a Dirac Delta function[19]. The use of the Boltzmann equation has two main advantages. Firstly, it considers the kinetic nature of the plasma processes. Secondly, the ionization and acceleration terms can be evaluated independently, even though these processes appear to be intimately linked in the discharge.
The 1D1V expression of the axial electric field has been developed by Pérez et al.[19] and reads

$$\frac{eE_z}{m_i} = \frac{w_1 w_2}{2w_1 - w_3}\frac{dw_3}{dz}, \tag{2.8}$$

where

$$\begin{cases} u_m = \dfrac{\int v_z^m f dv_z}{\int f dv_z}, \\ w_m = \dfrac{u_m}{u_{m-1}}, m \geq 2, w_1 = u_1. \end{cases} \tag{2.9}$$

Similarly, we have derived the radial 1D1V expression

$$\frac{eE_r}{m_i} = \frac{w_1 w_2}{2w_1 - w_3}\frac{dw_3}{dr}. \tag{2.10}$$

w_i in this radial case has been evaluated by integration of the radial velocity components with their respective distributions. The general case that considers collisions and a Maxwellian neutral gas distribution has been derived by Pérez-Luna et al.[19].

The 2D2V radial and axial electric field expressions have been derived by Spektor[20]. Adopting the notation introduced by Pérez-Luna et al.[19], we define

$$\begin{cases} u_{i,r}u_{j,z} = \dfrac{\iint v_r^i v_z^j f dv_r dv_z}{\iint f dv_r dv_z}, \\ w_{m,l} = \dfrac{u_{m,l}}{u_{m-1,l}}, \end{cases} \tag{2.11}$$

where $l = r, z$. In order to simplify the electric field expressions, we use the notation

introduced by Spektor[20]. Let us write

$$\begin{cases} z_r = \dfrac{\xi_2\gamma_1 + \gamma_2}{1 - \xi_1\xi_2}, \\ z_z = \dfrac{\xi_1\gamma_2 + \gamma_1}{1 - \xi_1\xi_2}, \\ \xi_1 = -\dfrac{w_{1,r}}{w_{3,z}}\dfrac{2w_{1,z} - w_{2,z}}{2w_{1,z} - w_{3,z}}, \\ \xi_2 = -\dfrac{w_{1,z}}{w_{3,r}}\dfrac{2w_{1,r} - w_{2,r}}{2w_{1,r} - w_{3,r}}, \\ \gamma_1 = \dfrac{dw_{3,z}/dz}{2w_{2,z} - w_{3,z}} - \dfrac{1}{w_{2,z}}\dfrac{2w_{1,z} - w_{2,z}}{2w_{1,z} - w_{3,z}}\dfrac{dw_{1,r}}{dr} - \dfrac{dw_{1,z}w_{2,z}/dz}{w_{1,z}w_{2,z}}, \\ \gamma_2 = \dfrac{dw_{3,r}/dr}{2w_{2,r} - w_{3,r}} - \dfrac{1}{w_{2,r}}\dfrac{2w_{1,r} - w_{2,r}}{2w_{1,r} - w_{3,r}}\dfrac{dw_{1,z}}{dz} - \dfrac{dw_{1,r}w_{2,r}/dr}{w_{1,r}w_{2,r}}. \end{cases} \tag{2.12}$$

The radial and axial electric field expressions therefore read

$$\frac{eE_r}{m_i} = \frac{w_{1,r}w_{2,r}}{2w_{1,r} - w_{3,r}}\frac{dw_{3,r}}{dr} + \frac{w_{2,r} - w_{3,r}}{2w_{1,r} - w_{3,r}}\left(z_z w_{1,r}w_{1,z} + w_{1,r}\frac{dw_{1,z}}{dz}\right), \tag{2.13}$$

$$\frac{eE_z}{m_i} = \frac{w_{1,z}w_{2,z}}{2w_{1,z} - w_{3,z}}\frac{dw_{3,z}}{dz} + \frac{w_{2,z} - w_{3,z}}{2w_{1,z} - w_{3,z}}\left(z_r w_{1,r}w_{1,z} + w_{1,z}\frac{dw_{1,r}}{dr}\right). \tag{2.14}$$

The ionization frequency can be written as

$$\nu_i = z_r w_{1,r} + z_z w_{1,z} + \frac{dw_{1,r}}{dr} + \frac{dw_{1,z}}{dz}. \tag{2.15}$$

The use of such expressions requires 2D LIF measurements. Although the experimental determination of $f(\mathbf{x}, v_r, t)$ and $f(\mathbf{x}, v_z, t)$ is not an issue, measuring $f(\mathbf{x}, v_r, v_z, t)$ is a time-consuming process. The assumption that $f(\mathbf{x}, v_r, v_z, t) = f(\mathbf{x}, v_r, t) \times f(\mathbf{x}, v_z, t)$ is valid as long as f is isotropic. In a Hall thruster, however, the on-channel axis radial IVDF is close to a Maxwellian distribution, while the axial IVDF departs from its initial Maxwellian shape due to several processes, the prominent contribution being the overlapping of the ionization and acceleration zones. The above field expressions nonetheless assume that the local 2D IVDF is the product of the radial and axial IVDFs. To account for the proper IVDF, one may use the optical tomography technique described by Koslover and McWilliams[21]. Tomography allows for the unambiguous determination of the complete ion velocity distribution using multiple 1D measurements on the velocity space. Computing the complete IVDF with this technique, however, requires the determination of a significative number of one dimensional IVDFs, resulting in a prohibitively long measurement period.

Notice that our 2D2V equations are not identical to those of Spektor[20]. Since only radial, respectively axial, IVDFs have been measured at locations 1, 2 and 3, respectively 2, 4 and 5, depicted in figure 2.2, we implicitly assumed that $\dfrac{dw_{(1,2),(r,z)}}{d(z,r)} \equiv 0$, resulting in the present simplified expressions.

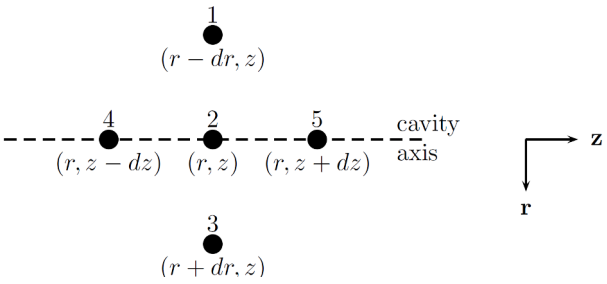

Figure 2.2: Molecule representing 2D LIF measurement locations. This molecule has been moved at 5 different positions along the channel axis.

2.2 LIF experiments

The discharge parameters are first presented. Section 2.2.2 then compares the outcomes of the different models presented in section 2.1, by focusing on a particular portion of the electric field profile presented in 2.2.3, in the case of the $2S_0$ channel geometry equipped with alumina ceramics. Section 2.2.3 illustrates the application of the electric field computation through a practical case: the evaluation of the influence of the PPI channel width and wall material, on the axial electric field profile, along the channel axis.

2.2.1 Plasma discharge

The PPI has been used in this work, with a magnetic topology that resembles that of the SPT100. The **B** field maximum is 250 G and located at the thruster exit plane. The operating conditions are similar both in section 2.2.2 and in section 2.2.3. The potential difference between the anode and the cathode is constant and equal to 200 V. The cathode potential relative to ground is constantly monitored and remains stable at -20 V. The anode xenon mass flow rate is set at 1.0 mg/s, and the cathode mass flow rate is 0.2 mg/s. Under these operating conditions, the discharge current mean value is 0.9 A. The experiments have been performed in the NExET vacuum chamber.

2.2.2 Comparison of the different methods

Experimental procedure

The optical bench and the detection apparatus have been presented in figure 1.2. The data set includes axial and radial LIF measurements. The measurement points are sketched by a molecule whose central point is aligned on the channel axis. The position $z = 0$ refers to the thruster exit plane. The molecule is depicted in figure 2.2. The molecule central point (location 2) is moved at z =4, 6, 8, 10 and 15 mm. Radial measurements are performed at locations 1, 2 and 3, while axial IVDF have been acquired at locations 2, 4 and 5. Radial and axial spatial steps, namely dr and dz, are both equal to 0.5 mm. This data set allows the evaluation of the axial and radial velocity gradients. The small bump that can be observed at 3 km/s on the radial IVDF shown in figure 2.3 originates from the hyperfine structure of the xenon optical transition at 834 nm. This structure is located at 4 GHz from the main peak and has been observed in previous studies[18,22]. It has also been observed on several radial IVDF profiles recorded in the same conditions, at various locations along the channel axis.

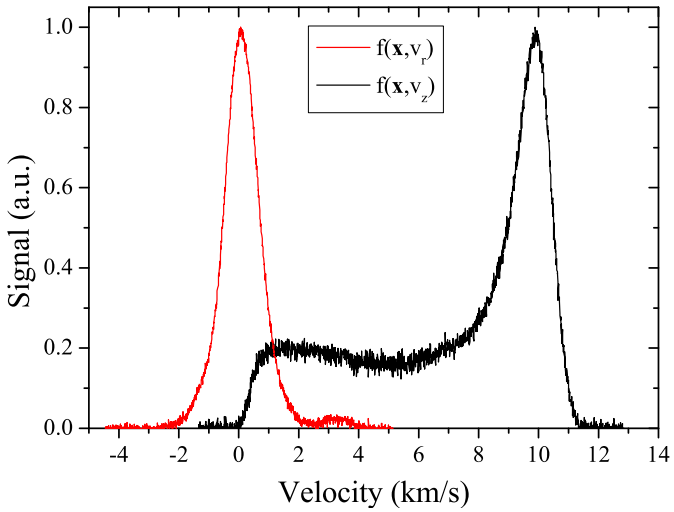

Figure 2.3: Raw traces of the radial (in red) and axial (in black) time-averaged IVDFs at 4 mm downstream the exit plane ($2S_0$ channel geometry and alumina ceramics are used).

Results and discussions

In this section, we investigate the radial and axial electric field profiles obtained on the cavity axis through the application of different theories. The error bars which appear on the figures have been evaluated by adding a moderate level of white Gaussian noise to the LIF measurements which accounts for 5% of the IVDF amplitude. The error bar amplitudes result from the comparison between the clean and noisy IVDF computations. The presented error bars represent the total error lower bound since the influence of the velocity uncertainty on the computations is not considered. Owing to the fact that only radial, respectively axial, IVDFs have been measured at locations 1, 2 and 3, respectively 2, 4 and 5, we implicitly assumed that radial, respectively axial, quantities do not vary axially, respectively radially, considering that the (dr, dz) spatial steps are small enough for this assumption to be valid. Any azimuthal component contribution is neglected in the assumption of unmagnetized ions. Notice, however, that previous work on the same source revealed that a low azimuthal velocity component does exist[15]. The azimuthal velocity of the ions is driven not only by the magnetic deflection; the cathode influence must also be considered. For a more precise determination of the axial electric field, the azimuthal components must be taken into account.

Under these assumptions, the 2D radial and axial fluid equations reduce to their 1D expression. Since accessing the ionization frequency is a non-trivial task, this term is omitted in many experimental works. However, in a Hall thruster, the ionization term is larger than the inertial term by approximately one order of magnitude at the beginning of the acceleration zone which is located inside the channel. The pressure term is similarly neglected in many studies. Figure 2.4 presents the z evolution of the inertial, ionization and pressure gradient terms in the 1D axial fluid model, i.e. equation (2.5), in our conditions. The inertial and ionization terms appear to be of similar importance. The pressure is however much lower by approximately 5 orders of magnitude. The ionization contribution therefore needs to be carefully evaluated.

The ionization frequency profile can be assessed using LIF and probe measurements, or using calibrated LIF alone, which then allows the determination of the ion density. One might think that fast measurements of the ionization frequency using probes (typically a few seconds with a fast translation stage) could be paired with the simple fluid model.

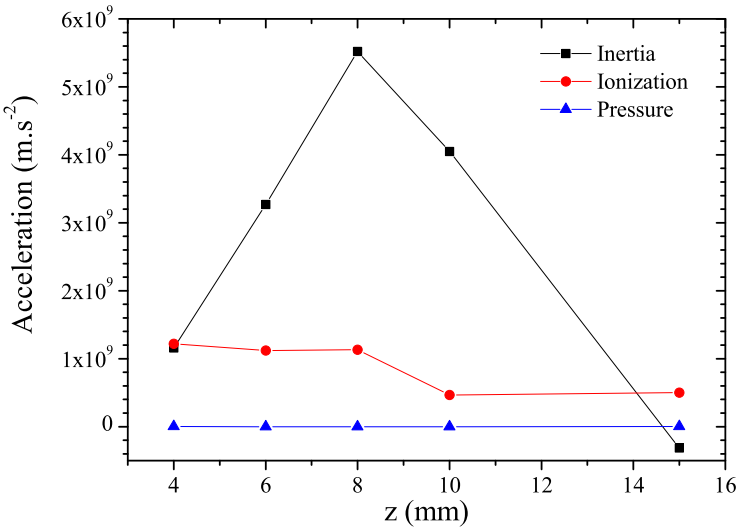

Figure 2.4: Profiles of the inertial, ionization and pressure terms which appear in the fluid equation (2.5).

The ion mean velocity used in the fluid model, however, requires the LIF measurement of the complete IVDF. For this reason, the electric field computation using a fluid approach is as demanding as using the kinetic approach. With the latter, the ionization and acceleration terms are evaluated separately. At low pressure, the fluid model is unsuitable for describing the ion flow which exhibits large Knudsen numbers. The fluid approach is therefore of little interest in an experimental work which aims at determining the **E** field profile at low pressure, provided the experimental signal-to-noise ratio is sufficient to use more advanced models for which the computation is more intricate. At moderate Knudsen numbers, both kinetic and fluid methods are expected to provide similar results.

The energy conservation equation, in which the most probable velocity is considered, can be used to assess the electric field profile. This will result in the overestimation of the local field, especially where the ionization and acceleration zones overlap, but the measurement time is greatly reduced since only the most probable ion velocity group is probed.

The Boltzmann equation is a powerful tool for computing the local electric field and ionization term. The independent evaluation of the accelerating electric field and the ionization frequency is possible under certain conditions[19]. The z 1D1V and (r, z) 2D2V equations have been used to compute the electric field and ionization frequency profiles. The w_i computation using equations (2.9) and (2.11) is extremely noise-sensitive and special care must be taken during the measurements to keep the final error bar as small as possible.

The results of the calculation is presented in figure 2.5. The outside peak in the electric field profile is clearly visible and distinguished by the four methods (see figure 2.7 for the complete axial electric field profile). The error bar tends to be larger with the 2D2V model, because of the finite signal-to-noise ratio and numerical errors. The field values are lower with the 2D2V computation since a small fraction of the total energy is lost in the radial component instead of being used for acceleration. The 3D3V model would further decrease the accelerating **E** field because of the ion azimuthal drift. The error bars globally tend to widen when the distance from the thruster increases due to the reduction in the signal-to-noise ratio level. Finally, the fluid model provides acceptable values of the electric field and reveals its structure. The regime of the ion flow can therefore be

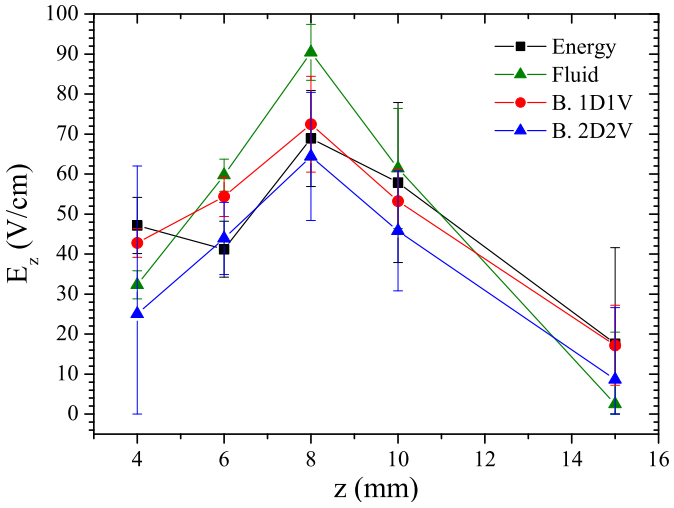

Figure 2.5: Axial electric field profiles calculated with the energy conservation, the fluid, the Boltzmann 1D1V and 2D2V models.

described using kinetic and fluid approaches, in this region at least.
The ionization frequency profile given in figure 2.6 has been computed using the two Boltzmann models presented in 2.1.3. Although the curve trends are similar, the 2D2V formulation leads to strong numerical constraints using experimental data, and the error bar widens.

The radial electric field has been computed using the energy conservation and the 2D2V models. Since the ion velocity vector is purely axial on the channel axis, a zero net radial electric field is expected. However, similarly to the observation of Spektor[20], the 2D2V Boltzmann equation leads to a non-zero radial electric field directed towards the thruster centerline. We evaluate in table 2.2 the rr and zz pressure tensor components contribution to the electric field values by computing $w_{2,(r,z)}/w_{1,(r,z)}$, since

$$u_{2,(r,z)} = u_{1,(r,z)}^2 + P_{(rr,zz)}. \tag{2.16}$$

From this expression we can conclude that whenever the pressure tensor can be ignored $u_{2,(r,z)}/u_{1,(r,z)} \sim u_{1,(r,z)}$ and thus $w_{2,(r,z)} \sim w_{1,(r,z)}$. The pressure indeed plays an important role in the radial direction, since the IVDF width is much larger than the ion radial mean velocity, but this may not be the reason for the observation of a radial electric field. The error bar associated with the E_r computation has been evaluated and ranges from 45 $\mathrm{V/cm}$ at 4 mm up to 150 $\mathrm{V/cm}$ at 10 mm. These values are well over the 6 $\mathrm{V/cm}$ estimation that is computed by the 2D2V approach. Such an electric field would accelerate the ions towards a radial velocity of approximately 800 $\mathrm{m/s}$ on the dr step we used for the measurements. Depending on the axial position, radial velocities at location 1 range from 100 $\mathrm{m/s}$ to 300 $\mathrm{m/s}$. These values are however coherent with the radial electric field values computed by the energy equation, which has been found to vary from -1 $\mathrm{V/cm}$ up to 3 $\mathrm{V/cm}$. Notice that the same inability to produce coherent values of the radial electric field has been observed with the 1D1V Boltzmann radial equation. Azimuthal effects as well as distortion of the absorption line shape, due to the hyperfine structure and Zeeman effect, need to be considered for conclusive arguments to be made. The use of argon instead of xenon would be of interest in this matter since argon does not possess any abundant isotope, rendering the line profile simpler. However, the higher ionization potential of argon would lower the fluorescence signal and therefore decrease the signal-to-noise ratio.

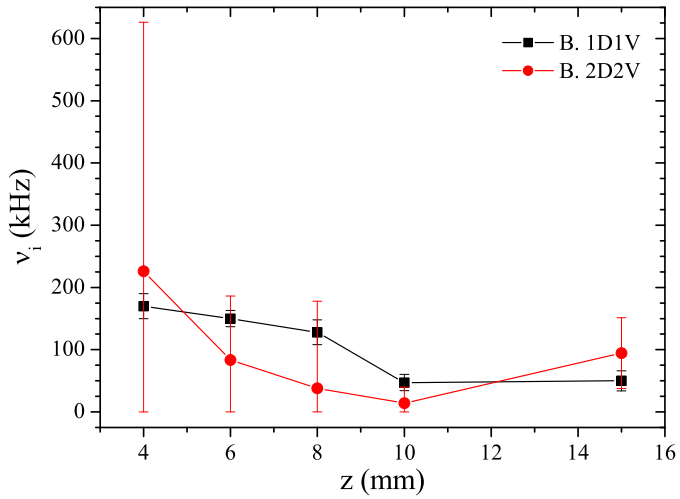

Figure 2.6: Ionization frequency profile calculated using the Boltzmann 1D1V and 2D2V models.

Table 2.2: Effect of the rr and zz pressure tensor components at various locations along the channel axis.

z, mm	4	6	8	10	15
$w_{2,z}/w_{1,z}$	1.19	1.17	1.14	1.10	1.14
$w_{2,r}/w_{1,r}$	32.8	7.59	163	9.30	2.21

2.2.3 Application: Influence of the channel width and wall material on the electric field profile

Experimental procedure

The most probable ion velocity group of the axial IVDF is probed every 1 mm along the channel axis, from 11 mm upstream up to 30 mm downstream the exit plane. The axial electric field amplitude is computed using equation (2.2). The S_0 and $2S_0$ channel geometries have been used with alumina ceramics. Additionally, the channel has been equipped with boron nitride walls in the $2S_0$ geometry to study the influence of the ceramic material.

Electric field profiles

The accelerating electric field profiles are presented in figure 2.7. The traditional vision that sets the maximum electric field amplitude close to the magnetic field peak does not apply to measurements made with alumina ceramics (as a reminder, the magnetic field peak is located at the thruster exit plane). The wide configuration exhibits, with alumina walls, a peculiar two-peak structure that has also been revealed by time-averaged and time-resolved LIF experiments, as well as emissive probe measurements of the plasma potential[7,23]. It is well known that unstable modes of the plasma can contribute to transport. A possible link between a high-frequency azimuthal mode and electron transport has been highlighted by PIC simulations[24]. For wavenumbers inferior to the reciprocal Debye length, the growth rate of this instability is directly linked to the $\mathbf{E} \times \mathbf{B}$ electron azimuthal drift velocity amplitude: the higher the velocity drift, the higher the growth rate[25]. The drift velocity V_d is produced by the combination of the crossed radial magnetic field and axial electric field, so that $V_d \approx E/B$. At these scales, and outside the channel, the unstable mode is thus more likely to be triggered in regions of strong electric field (it has

been checked that the magnetic field monotonical decay is not steep enough to modify the ordering of the electric and magnetic field contributions). It is therefore possible to assume, or predict, that unstable regimes are intense at 8 mm downstream the channel exit plane, when alumina ceramics are used as a wall material. Additionally, $V_d = 530\ \mathrm{km/s}$ in the $2S_0$ geometry, and $V_d = 1,080\ \mathrm{km/s}$ in the S_0 configuration, which suggests a higher instability amplitude with a narrow channel. This reasoning can be linked to recent experiments on microturbulence performed by means of collective Thomson scattering[26] with the PPI thruster, which have clearly shown the impact of the chamber geometry. The microturbulence level 8 mm outside the channel is found to decrease when the channel width increases, suggesting that the electron current due to microturbulence decreases, and possibly electron transport[24]. The resulting increase in the plasma resistivity for a wide configuration leads to a strong electric field outside the channel, in agreement with our LIF data. This description, however, contradicts the observations of Raitses et al, who observed an increase in plasma resistivity inside the channel when the channel was widened[27]. The role of turbulence and wall interactions on transport is an active topic of research and no definitive conclusions can yet be drawn concerning which mechanism is responsible for the double peak in the electric field.

The ion energy at 30 mm away from the exit plane is higher with the wide channel channel configuration: 127 eV versus 115 eV. Thus the acceleration efficiency is estimated to be 71% with the large channel configuration compared to 64% with the narrow channel[2]. This difference could originate in increased wall losses and decreased magnetic mirror effects as the channel narrows[28].

The electric field profile in the $2S_0$ channel geometry, equipped with boron nitride ceramics, is similar to numerous profiles reported in the literature which peak at the location of maximum magnetic field. The ion energy at the exit plane is similar to that measured with alumina ceramics. The boron nitride ceramics have, however, shown far greater erosion rates than alumina. This statement is supported by observations with the naked eye. A cone-like shape was clearly visible on the boron nitride inner and outer ceramics after 100 h of firing, while the alumina walls remained unchanged after 600 h of operation. The sole ion energy value cannot be considered a determining factor, and the ion flux should be measured to draw conclusive arguments. Ultimately the erosion rate can be assessed experimentally.

The ion energy at 30 mm is 150 eV, thus 23 eV higher compared to the case of alumina ceramics. The acceleration efficiency is estimated to be 83%, 12% over that of an alumina-wall configuration. Hall thrusters equipped with BN-SiO_2 ceramics are known to be more efficient than those equipped with alumina ceramics. Without performing any measurement, it is however clear from the observation reported in the previous paragraph that the erosion rate of alumina walls is much lower than that of BN-SiO_2. In case of application to flight hardware, a trade-off between performance and lifespan would eventually set the wall material that best suit the mission requirements.

2.3 Conclusions

Several methods that can be used to derive the time-averaged axial electric field using LIF have been investigated. The fluid approach appears to be of little interest in a very low pressure experimental work when ionization occurs locally, but has been able to describe the intermediate ion flow regime of the thruster. The model's simplicity is

[2]The acceleration efficiency is the ratio of the effective ion kinetic energy to the maximum energy they can possibly reach. The maximum energy is the anode potential, minus the far-field plasma potential, which has been assumed to be null for drawing orders of magnitudes, but usually equals a few volts.

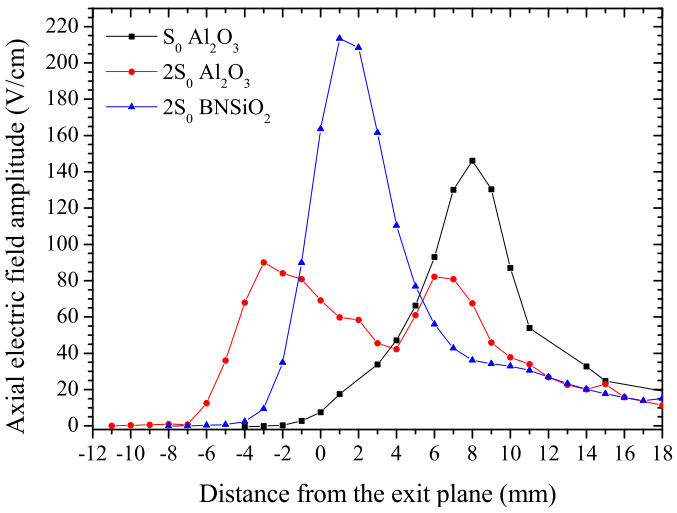

Figure 2.7: Axial electric field profiles along the PPI channel centerline, for different channel geometries and wall material. Discharge voltage is 200 V ; anode flow rate is 1.0 mg/s.

however counterbalanced by the experimental requirements. The energy and Boltzmann equations can be used, provided special experimental and numerical care are taken. A trade-off between physical meaning and complexity makes the 1D1V Boltzmann equation preferable where ionization occurs. The ionization frequency can also be derived from the Boltzmann approach. The 2D2V formulation leads to a large error bar which makes the proper evaluation of the electric field profile and ionization term difficult. The radial electric field has also been calculated. Although its values were expected to be small, the 2D2V computation gives a non-zero radial field directed towards the source centerline, which is inconsistent with the zero mean ion radial velocities that have been measured. The large values of the error bar do not permit conclusions to be made concerning precise radial electric field values. The energy equation is, in this case, more suitable and provides meaningful results.

The energy conservation model has been used to analyze various electric field profiles in the plume of the PPI Hall thruster. The influence of the wall material, and channel geometry, has been briefly discussed. Increase in wall losses with the channel narrowing corroborate a previous work on the same thruster[28]. The research shows the complex nature of the electric field shape, that is not determined only by the magnetic field profile. This work should be completed by probe measurements. While it is true that probes are invasive, measurements can be quite fast. A consequent number of operating conditions may therefore be explored in a matter of days. The technique can be validated by comparing the electric field profiles inferred by the probe measurements to the spatial evolutions presented in figure 2.7.

This work has been performed for time-averaged quantities. The time-resolved investigation is more complex, yet of great interest for revealing the time-dependent balance between the different processes which together are used to describe the electric field profile.

References

[1] M.A. Lieberman and A.J. Lichtenberg. *Principles of Plasma Discharges and Materials Processing*. John Wiley and Sons, 2nd edition, 2005.

[2] F.F. Chen. *Introduction to plasma physics*. Plenum Publishing Corp., 2nd edition, 1984.

[3] J.M. Rax. *Physique des plasmas*. 2005.

[4] P. Chabert and N. Braithwaite. *Physics of Radiofrequency Plasmas*. 2011.

[5] K. Dannenmayer and S. Mazouffre. Electron flow properties in the far-field plume of a Hall thruster. *Plasma Sources Sci. Tecnol.*, 22(035004), 2013.

[6] J.P. Sheehan and N. Hershkowitz. Emissive probes. *Plasma Sources Sci. Tecnol.*, 20(063001), 2011.

[7] J. Vaudolon and S. Mazouffre. Evaluation of different methods for determining the electric field profile in a Hall thruster. In Proceedings of the 4th Space Propulsion Conference, Cologne, Germany, SP2014-2979732, 2014.

[8] J.P. Sheehan, Y. Raitses, N. Hershkowitz, I. Kaganovitch and N.J. Fisch. A comparison of emissive probe techniques for electric potential measurements in a complex plasma. *Phys. Plasmas*, 18(073501), 2011.

[9] U. Czarnetzki, D. Luggenhölscher and H.F. Dobele. Sensitive Electric Field Measurement by Fluorescence-Dip Spectroscopy of Rydberg States of Atomic Hydrogen. *Phys. Rev. Lett.*, 81(4592), 1998.

[10] U. Czarnetzki, D. Luggenhölscher and H.F. Dobele. Space and time resolved electric field measurements in helium and hydrogen RF-discharges. *Plasma Sources Sci. Tecnol.*, 8(230), 1999.

[11] K. Takizawa, K. Sasaki and A. Kono. Sensitive measurements of electric field distributions in low-pressure Ar plasmas by laser-induced fluorescence-dip spectroscopy. *Appl. Phys. Lett.*, 84(185), 2004.

[12] T. Kampschulte, J. Schulze, D. Luggenholscher, M.D. Bowden and U. Czarnetzki. Laser spectroscopic electric field measurement in krypton. *New J. Phys.*, 9(18), 2007.

[13] U. Czarnetzki and K. Sasaki. Ultra-Sensitive Measurement of Sheath Electric Fields by Laser-Induced Fluorescence-Dip Spectroscopy. *J. Plasma Fusion Res.*, 83(215), 2007.

[14] J. Vaudolon, L. Balika and S. Mazouffre. Photon counting technique applied to time-resolved laser-induced fluorescence measurements on a stabilized discharge. *Rev. Sci. Instrum.*, 84(073512), 2013.

[15] G. Bourgeois, S. Mazouffre and N. Sadeghi. Unexpected transverse velocity component of Xe^+ ions near the exit plane of a Hall thruster. *Phys. Plasmas*, 17(113502), 2010.

[16] Phelps and Hayashi cross-section databases. www.lxcat.net, retrieved on May 5, 2015.

[17] R.A. Dressler and Y. Chiu. Quantifying Plasma Collision Processes in Xenon Powered Electric Propulsion Systems. 27th Internation Symposium on Rarefied Gas Dynamics. AIP Conference Proceedings, Volume 1333, pp. 1065-1072, 2011.

[18] G. Bourgeois. *Influence de la topologie magnétique, de la cathode et de la section du canal sur l'accélération des ions dans un propulseur à effet Hall*. PhD thesis, Université d'Orléans, 2012.

[19] J. Pérez-Luna, G.J.M. Hagelaar, L. Garrigues and J.P. Boeuf. Method to obtain the electric field and the ionization frequency from laser induced fluorescence measurements. *Plasma Sources Sci. Tecnol.*, 18(034008), 2009.

[20] R. Spektor. Computation of two-dimensional electric field from the ion laser induced fluorescence measurements. *Phys. Plasmas*, 17(093503), 2010.

[21] R. Koslover and R. McWilliams. Measurement of multidimensional ion velocity distributions by optical tomography. *Rev. Sci. Instrum.*, 57(2441), 1986.

[22] E. Pawelec, S. Mazouffre and N. Sadeghi. Hyperfine structure of some near-infrared Xe I and Xe II lines. *Spectrochimica Acta Part B*, 66:470–475, 2011.

[23] W.A. Hargus and M.A. Cappelli. Interior and exterior laser-induced fluorescence and plasma measurements within a Hall thruster. *J. Propul. Power*, 18:159–68, 2002.

[24] J. C. Adam, A. Heron, and G. Laval. Study of stationary plasma thrusters using two-dimensional fully kinetic simulations. *Phys. Plasmas*, 11:295, 2004.

[25] J. Cavalier. *Modèles cinétiques et caractérisation expérimentale des fluctuations électrostatiques dans un propulseur à effet Hall*. PhD thesis, Université de Lorraine, 2013.

[26] S. Tsikata, N. Lemoine, V. Pisarev, and D. M. Gresillon. Dispersion relations of electron density fluctuations in a Hall thruster plasma, observed by collective light scattering . *Phys. Plasmas*, 16(033506), 2009.

[27] Y. Raitses, D. Staack, M. Keidar and N.J. Fisch. Electron-wall interaction in Hall thrusters. *Phys. Plasmas*, 12(057104), 2005.

[28] S. Mazouffre, G. Bourgeois, K. Dannenmayer and A. Lejeune. Ionization and acceleration processes in a small, variable channel width, permanent-magnet Hall thruster. *J. Phys. D: Appl. Phys.*, 45(185203), 2012.

Chapter 3

Ionization and transit time oscillations[1]

Contents

LOW-PRESSURE cross-field plasma sources, such as Hall thrusters, are characterized by a broad family of oscillatory phenomena[1]. Despite decades of research, many properties of these oscillations are still poorly-understood[2]. However, knowledge of the instability characteristics is key for describing plasma processes, such as the anomalous electron transport, ionization and ion acceleration. Many experimental and numerical studies have focused on ionization instabilities in the kHz range and on electron turbulence in the MHz range[3–6], but experimental work on the intermediate frequency band instabilities remains rare. While a wide variety of models has been developed, no experimental validation supports their outcomes[7,8]. In cross-field plasmas, this intermediate range of oscillations between $100\ \mathrm{kHz}$ and $1\ \mathrm{MHz}$ is often referred to as the ion transit time (ITT) instability, because the typical time period is on the order of the ion time-of-flight through the acceleration region. The practical difficulty of accessing the ion dynamics over a very short time scale, without perturbing the plasma, has made knowledge of the fundamental properties of the ITT difficult to obtain. This chapter reports on the first and direct experimental

[1] Adapted from:
J. Vaudolon, B. Khiar and S. Mazouffre, *Plasma Sources Sci. Technol.*, **23**, 022002 (2014)
J. Vaudolon and S. Mazouffre, *Plasma Sources Sci. Technol.*, **24**, 032003 (2015)

characterization of the ITT instability in a Hall thruster. The measurements, associated with a two-fluid model of the plasma, reveal a complex physics which is dependent on the magnetic field profile, and possibly on the low-frequency ionization mode.
The processing technique of the non-linear time-resolved signals is first described. A simple case is examined to highlight the crucial impact of the spectral analysis method on the frequency spectrum computations. The temporal evolution of some ion velocity groups is exemplified in section 3.2 to present the measurement outcomes. The time evolution of the electric field and ion mean velocity are inferred from the time-resolved data. The low and high frequency oscillation of the electric field are investigated in section 3.3, while 3.4 characterizes the long-observed-but-still-mysterious ion transit time regime of oscillation. Conclusions are presented in section 3.5.

3.1 Hilbert-Huang transform

The stochastic nature of the Hall thruster discharge oscillations has been known and dealt with for decades[1]. Many of the oscillations originate from the complex distribution of the electric and magnetic fields, as well as from the plasma/wall interaction. Natural modes of Hall thrusters are though to be self-excited by the plasma to regulate the particle production and diffusion[9,10]. Early measurements of the plasma floating potential revealed in the 1970's two oscillating regimes which account for most of the energy content below 1 MHz[11]. The low frequency ionization mode, referred to as the *breathing mode*, has notably been extensively studied ever since[5,12].

Spectra analysis techniques such as the Fourier transform are well-suited to organize stationary waveforms into a collection of harmonics. Still, non-stationary signals inherently possess time- and frequency-varying properties. A simple picture is that of a pendulum with a variable spring constant. In this simple, yet instructive example, the differential equation describing the pendulum position u can be written in the form of $\ddot{u} + \omega u = F$, where F is a periodic forcing function and ω the oscillation frequency. In the stationary case, ω is constant. On the contrary, a variable spring constant yields ω to depend on u. The frequency of u thus changes from location to location, and time to time, even within one oscillation cycle. As Huang et al. pointed out, this intra-frequency frequency variation is the hallmark of non-linear systems[13].
Suitable theoretical tools for studying the properties of Hall thruster oscillatory regimes are therefore necessary. Most of non-stationary signal processing methods rely on *a priori* considerations, which assume that any signal, be it stochastic, can be projected on a predetermined decomposition basis. For instance, the Short Time Fourier Transform applies the Fourier Transform to the original signal, multiplied by a window function. The width of the window function is such that the signal to be processed can be considered stationary over the time period that is examined. However, the width and the shape of the window are fixed: a large (respectively narrow) window will not allow the detection of the high (low) frequency content. Moreover, the finite time representation of the window function generates additional harmonics that modify the frequency spectrum. The Wavelet Transform addresses some of the short time Fourier transform issues. The signal is projected on a mother wavelet in the time-scale domain. The wavelet scale can be varied to follow the signal evolution: the wavelet is dilated to capture low frequency oscillations, and compressed to reveal higher frequency modes. The low frequency modes are therefore resolved in details in the frequency domain, and high frequency oscillations are precisely described in the time domain. Unfortunately, the mother wavelet will significantly influence the result of the analysis, as the basic functions of wavelet transformation are

fixed and do not necessarily match the shape of the considered data series in every instant in time. Both the windowed Fourier transform and the Wavelet transform underlies the Heisenberg-Gabor uncertainty principle, indicating that a time- or frequency-dependent information cannot be classified by the same accuracy simultaneously[14].
In this dissertation, we propose the application of a recent technique: the Hilbert-Huang transform. This processing tool is based on an adaptive basis, which departs from the a priori methods described above. The process is appropriately deemed *empirical*, since the modes are directly built from the signal itself through an iterative procedure. There is no technical assumption concerning the nature of the time series. Besides, the limitations of the classical time-frequency joint analysis do not apply, since the spectral properties are not deduced from standard convolution operations. The technique has been recently developed by Huang et al.[13]. This method has been used in the last years to study monochromatic and transient water waves[15]. Its first utilization in the field of plasma physics goes back in 2004 by Terradas et al.[16]. The method has been applied to floating potential time series measured in the exhaust of the SPT100-ML Hall thruster in 2005[17].
The following two subsections present the two-step processing procedure. The simple example of a two-tone non-stationary signal acts as a guiding thread to accompany and exemplify the theoretical developments.

3.1.1 Empirical Mode Decomposition

The Empirical Mode Decomposition (EMD) decomposes a multimodal time series into a superposition of monomodal components, each of which is called an Intrinsic Mode Function (IMF)[13]. As we shall see, the IMFs are computed by means of an iterative scheme called the *Huang's sifting algorithm*. The sifting process is subjected to a stopping criterion which guarantees that each IMF satisfies two requirements: the difference between the number of local maxima of the oscillation and the number of zero crossings is at most one, and the mean of the upper and lower envelopes of the oscillation is zero. The definition of the stopping criterion is given in the following paragraphs.

Let $\mathbf{X} = \{X_t\}_{t\geqslant 0}$ be a real, discrete and stochastic process, and $x = (X_i)_{i=[\![1..N]\!]}$ be a realization of $\mathbf{X}$ in $\mathbb{R}^{\mathrm{N}}$. We set $i = 1$, $j = 1$ and $r_0 = x$ as an initialization step. The EMD computes the IMFs of x using the following sifting algorithm:

1. Identification of the local extrema of r_{i-1}.
2. Computation of the mean of the upper and lower envelopes of r_{i-1}, denoted $\bar{e}$.
3. Determination of the local fluctuation, $h_i^j = r_{i-1} - \bar{e}$.
4. If h_i^j does not comply with the two requirements an IMF must meet, then the algorithm goes to step 1 with $r_{i-1} = h_i^j$ and j is incremented. In practice, the mean of h_i^j is never zero, and the sifting process stops when the stopping criterion SD_j, i.e. the standard deviation between h_i^{j-1} and h_i^j defined by equation (3.1), drops below a threshold value Δ
$$SD_j = \int \frac{\left|h_i^{j-1} - h_i^j\right|^2}{\left(h_i^{j-1}\right)^2} dt \leqslant \Delta. \tag{3.1}$$
5. If h_i^j is an IMF, the i$^{\text{th}}$ IMF of x is $m_i = h_i^j$, and the i$^{\text{th}}$ residual is $r_i = x - m_i$. The algorithm then increments i and restarts from step 1, as long as extrema can be found.

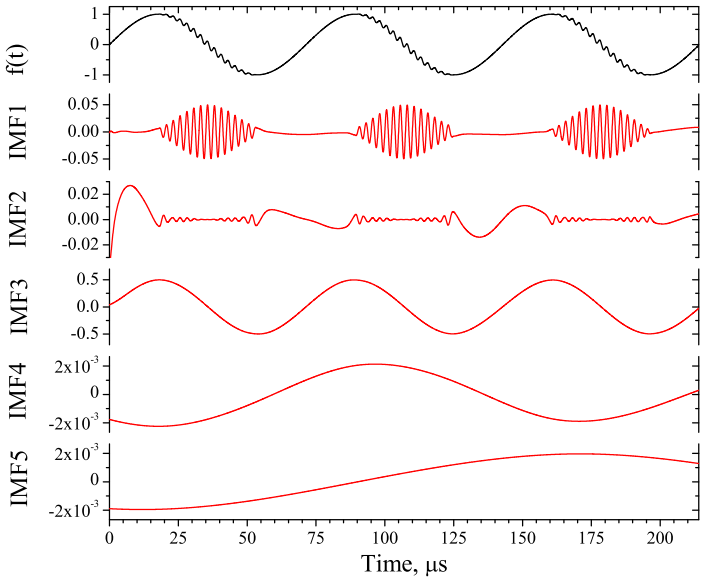

Figure 3.1: Decomposition of the signal $f(t)$ into intrinsic mode functions. The original signal (black) is plotted atop the figure. The IMFs (red) are represented below. IMFs 1 and 3 show the powerful ability of the EMD to extract the intermittent characteristics of the signal.

We denote by n the largest index for which m_i is defined. Then,

$$x = \sum_{i=1}^{n} m_i + r_n. \tag{3.2}$$

Laser-induced fluorescence time series are broadband signals, for which it has been shown that, typically, $n \approx \ln N$[18]. This relation provides the number of modes than can be expected from the decomposition of photon time series.

As an example, let us consider a two-tone harmonic signal, for which the high frequency tone occurs solely on the descending phase of the lower tone. The signal is defined by f, such as

$$f : \left| \begin{array}{ccc} \mathbb{R}_+ & \longrightarrow & \mathbb{R} \\ t & \longmapsto & \sin(2\pi f_1 t) + 0.1 \sin(2\pi f_2 t) \times g(t), \end{array} \right. \tag{3.3}$$

where f_1 and f_2 are the two tones of the signal and g is a window function defined by $g : t \longmapsto \cos(2\pi f_1 t) \times \mathrm{sgn}(\cos(2\pi f_1 t) - 1)$. The cosine operator ensures smooth transitions between increasing and decreasing phases of the background oscillation, and the sign function is used to make the low-amplitude tone appear only on the decreasing slopes. This example mimics the discharge current waveforms computed by Coche and Garrigues, which revealed transit time oscillations on the decreasing portions of the breathing mode oscillations[9].

The function f has been discretized in 10,000 points, from 0 µs to 350 µs. The two frequencies f_1 and f_2 are respectively equal to 14 kHz and 400 kHz to represent the breathing and transit time oscillations[2]. The EMD algorithm has been applied to f with $\Delta = 10^{-4}$. Cubic spline interpolations have been used to compute the residual envelopes.

The signal together with the IMFs are presented in figure 3.1. Firstly, it can be seen that the amplitude of IMFs 1 and 3 is 0.1 and 1, respectively, while the four others exhibit

[2]The breathing and notably transit time instabilities are not localized on a specific frequency, but the physical picture is simplified for the purpose of this example.

much lower amplitudes. The global picture is coherent with the definition of f. Secondly, IMF 1 reveals the intermittent nature of the signal high-frequency content, and the background support is adequatly represented by IMF 3. Thirdly, five IMFs have been extracted during the sifting process. Issues are therefore raised concerning the physical relevance of some modes, since only two were expected to accurately retrieve the original time series. Several reasons can be invoked, see 3.1.3.

Concluding, the EMD is an adaptative scheme, guided and controlled by the data, that decomposes a signal into IMFs. An IMF is an oscillatory mode of the signal, as a counterpart to the harmonic function. But its nature is much more general, owing to a time-dependent frequency content. In order to extract the non-stationary features of each mode (amplitude, frequency and phase), a novel method was proposed recently, relying on the function itself[13]. This method is now examined.

3.1.2 Hilbert spectral analysis

In contrast to Fourier and wavelet analysis, the spectral properties of the signals are defined on an *a posteriori* basis, since the amplitude, frequency and phase of the oscillatory components are obtained from the IMFs. The process is thus entirely controlled by the data.
The instantaneous frequency of a signal is defined as the derivative of the phase. The instantaneous frequency of any real-valued signal is thus zero. The original signal is therefore continued to a complex analytic function denoted z:

$$z = x + iy. \tag{3.4}$$

The complex part y can be defined in many ways. However, the construction of y is based on some requirements which make its uniqueness:

- First, defining z by a unique function, e.g. the data, is more suitable. Then y must depend on x.
- Analytic continuation on the complex plane sets the uniqueness of y. Condition for uniqueness is demonstrated by integrating the convolution of z with $1/\alpha$ on a closed contour of $\{\gamma \in \mathbb{C} | \operatorname{Im}(\gamma) > 0\}$, in a neighborhood of $\alpha \in \mathbb{R}_+$ to corroborate with $x(t) = 0$ for $t < 0$. Two conditions are thus obtained on z, namely $z(\alpha) = x(\alpha) + iy(\alpha)$ and $z(\alpha) = i\mathscr{H}[x](\alpha) - \mathscr{H}[y](\alpha)$, where $\mathscr{H}$ is the Hilbert transform. Since $\mathscr{H}^2[x] = -x$, $y = \mathscr{H}[x]$.
- Most of the time, x is in the space of square integrable functions on $\mathbb{R}$. Thus its Hilbert transform is in the same space and therefore real-valued[19]. Choosing $y = \mathscr{H}[x]$ ensures that $\operatorname{Re}(z) = x$.

The Hilbert transform is applied to each IMF to determine its amplitude and frequency time series. The original signal can be retrieved by the computation of

$$x(t) = \operatorname{Re}\left(\sum_{i=1}^{n} a_i(t) \exp\left[i\left\{\int \omega_i(t)dt + \phi_i(t)\right\}\right]\right) + r_n, \tag{3.5}$$

where a_i, ω_i and ϕ_i are the amplitude, frequency and phase of the i$^{\text{th}}$ IMF. This expansion is more general than the Fourier form in which the coefficients are constant over time. This variable amplitude-frequency representation in time domain is the Hilbert spectrum

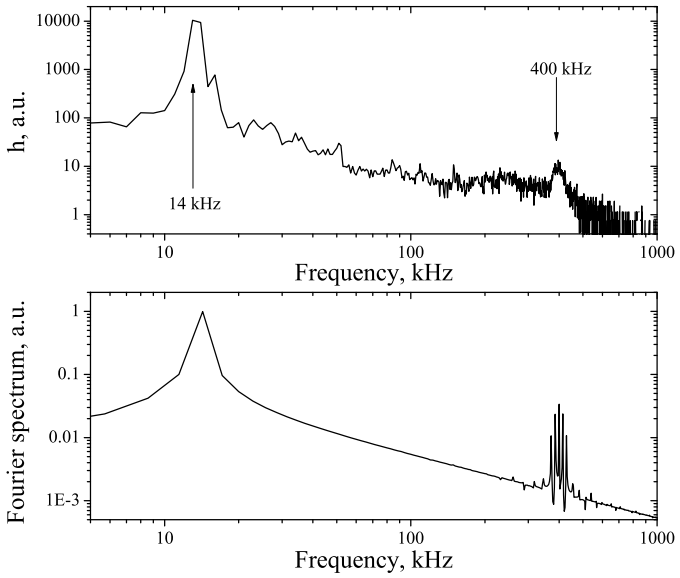

Figure 3.2: Hilbert marginal (top) and Fourier frequency spectra (bottom) of f.

denoted $H(\omega, t)$. Yet this approach can reveal quite complex to interpret. The number of variables can be reduced by defining the Hilbert marginal spectrum h

$$h(\omega) = \int H(\omega, t)\, dt \tag{3.6}$$

At first glance, the marginal spectrum simplifies the problem. Does it? Not much, since its interpretation can be tricky, especially considering the stochastic nature of the signals we intend to process. The marginal spectrum is a measure of the contribution from each frequency to the total energy, on a probabilistic sense. In other words, the more energy appears at a particular frequency, the more likely such a wave may have appeared somewhere in the whole time span of the data. In Fourier analysis, the existence of energy means that a trigonometric function has been part of the signal in a deterministic manner. The marginal and Fourier frequency spectra of the signal f are presented in figure 3.2. It can be seen that both spectra present peaks located at the tones of the signal. There is, however, a ratio 1,000 between the peak amplitudes in h, and a ratio 36 in the Fourier spectrum. These ratios are linked to the previous discussion, in the sense that Fourier harmonics persist over time, while IMF 1 only accounts for half of the time in the Hilbert total energy content. The energy of each tone, $\int |x(t)|^2 dt$, has been computed over one time period. The energy of the low-frequency tone is 400 times higher than that of the high-frequency mode, which makes the marginal spectrum closer to the true ratio. The Fourier spectrum also reveals numerous harmonics that have been generated to reproduce the original trace of the signal. In vain, though, since this technique is inherently not able to retrieve the original form.

3.1.3 Ongoing research

Most of the progress in using the Hilbert-Huang Transform has been in its application, but the mathematical background is not yet fully developed. Several problems remain to be treated, and concepts to be more accurately described on a physical point of view. Here are some of the issues tackled at the present time.

Boundaries The data interpolation and the determination of extrema are problematic at the boundaries of the time series. A common practice consists in duplicating the data in order to extend the time window. The interpolation is thus possible on the original time period of interest. This is the prediction of a non-linear and non-stationary evolution of a stochastic process, which is inherently inadequate. This is why, in practice, the first and last oscillation time periods are often omitted when analyzing the data.

Interpolation Cubic spline interpolations have been used in this work. The interpolation technique that best suits the data is yet to be examined, and should depend on the signal itself. Most real-life signals are smooth, and must be represented by differentiable functions. This is why linear interpolations are excluded. Cubic spline interpolation represents a good alternative but interpolating the extremes can cause overshooting or crossing of the signal.

Convergence Is there a guarantee that a signal can always be decomposed into a finite number of IMFs? From the general experience, this seems to be true, but there is no mathematical background that demonstrates the existence an IMF set for any signal, and the number of IMF sets that can be computed eventually. This issue is related to the sifting process parameters and to a more rigorous definition of the IMF. Fortunately, the experience shows that even the vague definition given by Huang et al. is satisfying, in the sense that the results are similar when the parameters are varied[13].

Stopping criterion The question remains as to how small Δ should be to ensure that h_i^j is an IMF.

Miscellaneous Many statistical problems are still to be addressed, like the confidence limit of the results, the relevance of the instantaneous frequency, influence of the signal length, sampling issues, variations of the sifting process...

3.2 Time-resolved experiments

3.2.1 Experimental conditions

An extensive LIF study in the time-averaged domain has been reported in the first two chapters. The complete axial IVDF profiles have been measured in the plume of the PPI, on the channel axis, at the nominal operating point: $U_d = 200\ V$ and $\phi_a = 1.0\ mg/s$. The PPI was equipped with alumina ceramics, in the $2S_0$ geometry, see Chapter 2. The IVDF mapping has already been presented in figure 1.9. Based on these measurements, fifteen points that represent characteristic trends of the time-averaged IVDF profile have been chosen at each location along the channel centerline. The temporal evolution of each ion velocity group has been recorded during approximately 5 min, through 176,000 acquisitions on 7,150 bins of the counting card, to yield the time-resolved IVDF. The operating conditions are those reported in 1.5.1.
The modulation apparatus was used to operate in a time-coherent regime. The resonance with the breathing mode was found to be maximum at a potential modulation frequency of 14 kHz. Since each counting card bin width is 100 ns, the record length encompasses 10 breathing oscillation time periods.

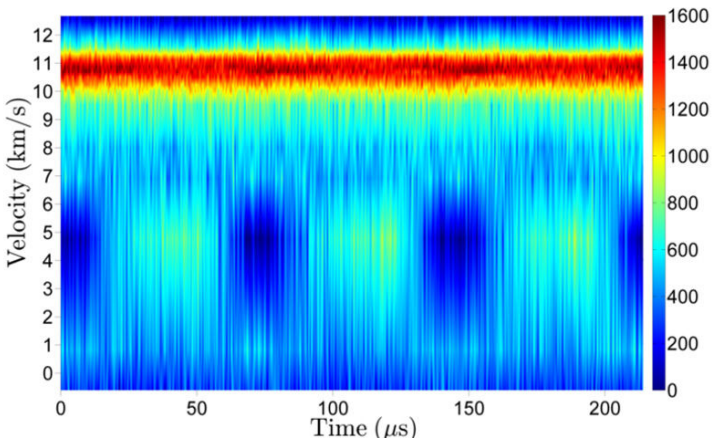

Figure 3.3: Axial ion velocity distribution at 4 mm away from the discharge channel as a function of time. The window spans 3 breathing oscillations. The colorbar represents the number of fluorescence photons. Low-velocity ions are created during the replenishment of the channel by neutrals.

3.2.2 Time-varying IVDFs

Time-resolved ion velocity distributions $f(\mathbf{x}, v_z, t)$ have been measured using the LIF optical train presented in figure 1.2, with some modifications to the detection branch presented in subsection 1.4.2. The IVDF obtained at 4 mm downstream the thruster exit plane is represented in figure 3.3 for illustrating the measurement outcome. The IMFs oscillating above 1 MHz have been removed from the raw data. The number of fluorescence photons is presented as a function of both the ion velocity and time during three breathing oscillations. The number of photons of the most probable velocity group at 11 $\mathrm{km/s}$ is phased with the discharge current waveform[20], meaning that the low-velocity tail of the distribution is periodically populated during the replenishment of the channel by neutral species[5]. This group can be seen in the time-averaged plume mapping in figure 1.9. Charge-exchange collisions or the back-and-forth movement of the ionization area can be invoked to explain the presence of slow ions. Typical charge-exchange cross sections for singly-charged xenon ions lies around 6.10^{-17} m^2, and the neutral density is close to 10^{18} m^{-3}, which make the mean free path on the order of 2 cm. Therefore, it seems quite unlikely that this group originates from CEX collisions.

Several oscillation regimes can be observed in figure 3.3, notably the low frequency ionization mode, which is relatively narrow-band, and a superposition of high-frequency oscillations that cannot be precisely characterized in the present form. The marginal spectra of four velocity groups are presented in figure 3.4. The corresponding ion velocity is indicated within the frame of each plot. The general trend in amplitude is similar, i.e. the breathing mode is carrying most of the energy, and one or two oscillations are observed at higher frequencies. The breathing mode amplitude for the low-velocity group at 4.8 $\mathrm{km/s}$ is much higher than that of the others, which is perceptible in figure 3.3. Structures that contain a significant amount of energy are observed above 100 kHz while the time coherence is based on stabilizing a low frequency mode of the discharge at 14 kHz. Whether the link between the low and high frequency oscillations happens naturally in Hall thrusters, or is influenced by the oscillatory driving of the discharge remains unknown though. The results of figure 3.4, and examples of coherent structures obtained through the Hilbert-Huang analysis that can be found in Ref.[20], show that the ion dynamics in the [100 kHz;1 MHz] band is either controlled and stabilized by the breathing mode, or influenced by the modulation apparatus.

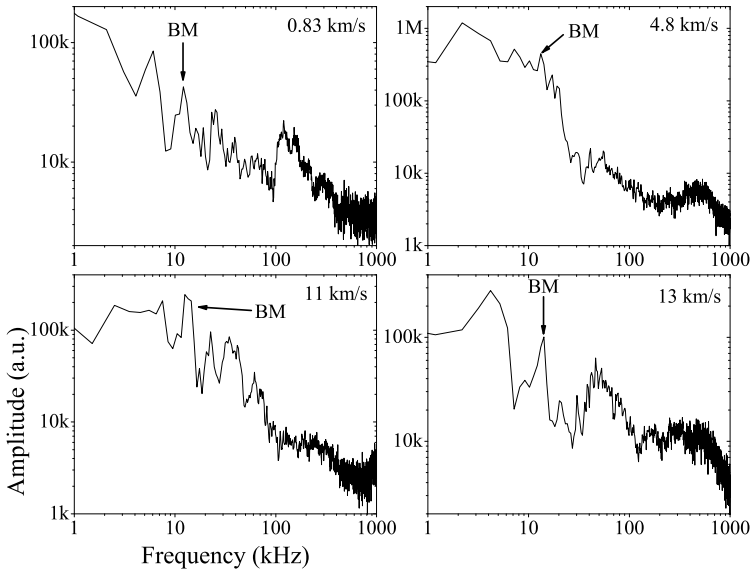

Figure 3.4: Marginal spectra of ion velocity groups present on the axial IVDF at 4 mm downstream the exit plane. The breathing mode frequency (BM) is identified at the modulation frequency. Oscillations with frequencies ranging far above the breathing mode can be observed.

3.3 Temporal evolution of macroscopic quantities

In this section, the ion density n and ion mean velocity w_1 are presented, and correspond to the zeroth and first order moments of the axial IVDFs that have been scanned

$$n(\mathbf{x}, t) = \int f(\mathbf{x}, v_z, t) dv_z, \tag{3.7}$$

$$w_1(\mathbf{x}, t) = \frac{1}{n} \int v_z f(\mathbf{x}, v_z, t) dv_z. \tag{3.8}$$

The temporal evolution of the ion density, ion mean velocity and low-frequency content of the electric field are presented in figure 3.5. The high-frequency content of the electric field is presented in figure 3.9. The method to derive the ionization frequency profile from the time-dependent Boltzmann equation is presented in subsection 3.3.4.

3.3.1 Ion density

The ion density is mapped in figure 3.5, as a function of time and position along the discharge channel. Since our LIF bench has not been calibrated, and since we do not possess any collisional-radiative model to infer the ground state dynamics, the density is that of the metastable state, given in arbitrary unit. The raw frequency content below 1 MHz only has been extracted. The time window displays three breathing oscillations, with a broad high-frequency content superimposed, that seems persistent throughout the entire breathing time period.
The ion density does not fluctuate much inside the channel, but an apparent back-and-forth motion of the intense ion density area clearly occurs at the breathing mode frequency, from 2 to 6 mm. From a geometrical viewpoint, the ionization front propagates at ~ 200 $\mathrm{m/s}$, which is on the order of magnitude of the channel neutral gas velocity.

3.3.2 Ion velocity

The ion mean velocity diminishes locally, concomitantly with the forward movement of the ionization area. This spatial oscillation is at the origin of the intermittent low-frequency slow ion group that appear in figure 3.3. However, the final mean velocity is conserved, meaning the potential distribution in the acceleration area is modified, so that the potential difference between the cathode and the anode is conserved.

3.3.3 Electric field

Low-frequency oscillation

The temporal evolution of the electric field both inside and outside the discharge channel of the PPI is shown at the bottom of figure 3.5. The two-peak structure of the electric field profile with alumina ceramics in $2S_0$ geometry has been presented and discussed in subsection 2.2.3. The oscillation amplitude inside the channel is weak compared to the oscillation amplitude of the second peak. Since the discharge voltage is constant, the outside electric field distribution broadens when diminishing to satisfy

$$U_{\text{acc}} = \int_{channel} E_z(\mathbf{x}, t)dz = \text{ constant } \forall t. \tag{3.9}$$

It has been verified that $U_{acc} = 140$ V at each instant in time. This potential is lower than the applied discharge voltage since one must consider the cathode potential relative to the ground, the cathode and anode sheaths and losses in the system like the radial ion velocity component and charge-exchange collisions.

The maxima of the electric fields are separated by 43 μs. This delay suggests the propagation of an electric field front at 250 $\mathrm{m/s}$, which is close to the velocity of the neutrals, and echoes that observed in the density map. The shift between the peaks is almost π. It is therefore impossible to say whether this front is propagating towards the anode or towards the outside of the thruster. Mazouffre and Bourgeois described the first oscillation cycles after the ignition of the plasma[21]. Their paper describes an electric field front propagating towards the anode at the speed of the neutrals. Assuming the existence of a propagating front, the characteristics observed resemble those described by Mazouffre[21]. However, several experimental differences exist. Firstly, a geometrical effect is to be considered since a larger h/d ratio is used here instead of the standard ratio. Secondly, the temporal coherence is obtained here through an active modulation of the discharge current that does not modify the thruster mean behaviour[22], while in the study of Mazouffre and Bourgeois, a fast power switch was used to induce strong oscillations[21]. The system used by Mazouffre and Bourgeois has been shown to dramatically change the temporally-averaged characteristics of the discharge. The wave that is described could have been generated by strong discharge current oscillations as the thruster is close to an igniting regime at each cycle. A wave has indeed been shown to propagate during ignition due to a plasma homogeneity in the first breathing oscillation time period[23]. In contrast, the modulation system induces a very low level of oscillation amplitude.

The evolution of the electric field has been plotted against the distance from the exit plane in figure 3.6 at four different instants during a breathing oscillation. The discharge current oscillation is also shown for clarity sake. The internal electric field peak does not move in space and changes slightly in amplitude, while the external one varies from 43 $\mathrm{V/cm}$ at 4 mm to 55 $\mathrm{V/cm}$ at 7 mm downstream the exit plane.

As we have seen, the characteristic feature of the breathing oscillation is the-back and-forth motion of the ionization zone. This leads to a periodic increase in ion density

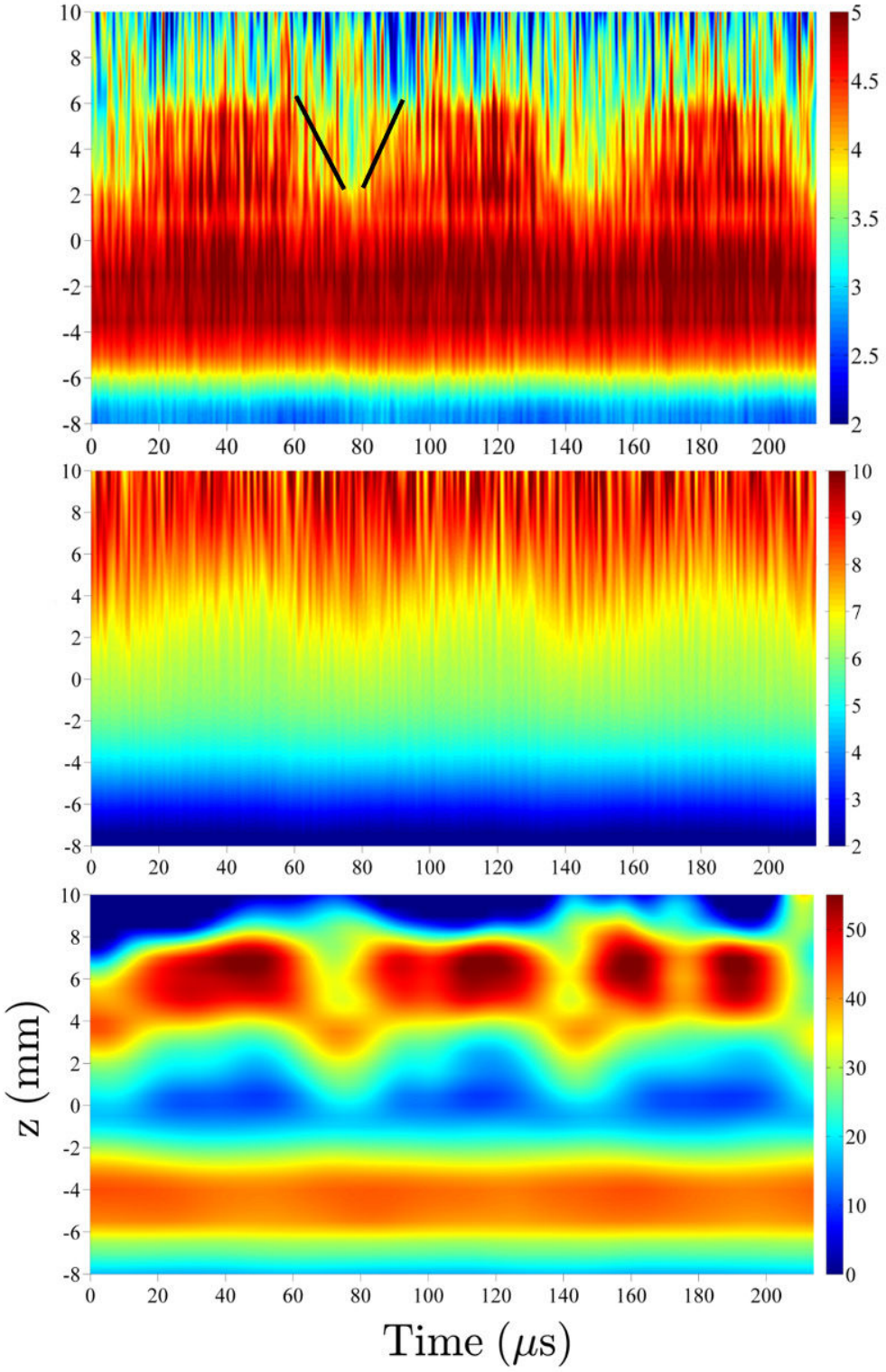

Figure 3.5: Temporal evolution of the ion density (top, arbitrary unit), ion mean velocity (middle, $\mathrm{km/s}$), and low-frequency oscillations of the electric field (bottom, $\mathrm{V/cm}$). The propagation of the ionization front is represented by the black lines on the density map. The density and velocity oscillations ranging from 0 to 1 MHz are shown, while only the electric field fluctuations below 100 kHz are shown. The high frequency regime is shown in figure 3.9.

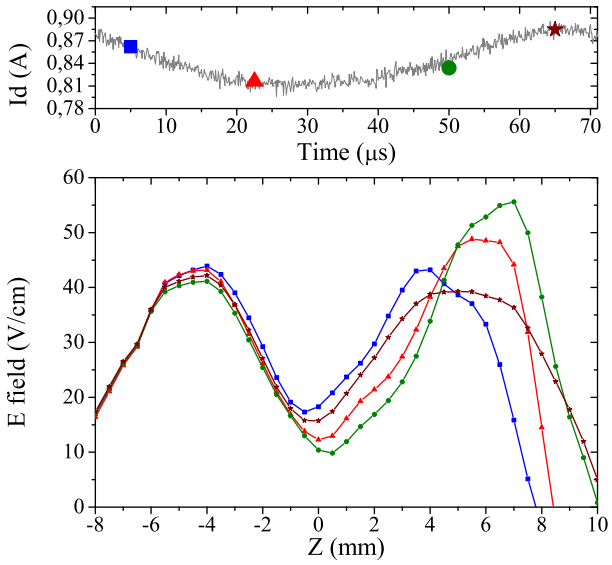

Figure 3.6: Time evolution of the electric field along the discharge channel at t=5 µs, 22 µs, 50 µs and 65 µs.

outside the discharge channel. The concomitant electric field can be computed from these variations. Quasi-neutrality can be assumed since the characteristic length of the density gradients is much above the Debye length. We also assume a purely radial magnetic field along the discharge channel axis between $z = 0\,\mathrm{mm}$ and $z = 10\,\mathrm{mm}$. Collisions are neglected since the various mean free paths are much larger than the characteristic lengths at stake in the measurements, see table 2.1. The linearized equation of motion for the magnetized electrons therefore reads

$$m_e \frac{\partial v_z}{\partial t} = -eE_z - \frac{\nabla p_e}{n} + ev_\theta B_r. \tag{3.10}$$

The left-hand side term of (3.10) can be neglected owing to the low electron mass. Thus the axial electric field is given by

$$E_z = v_\theta B_r - \frac{k_B T_e}{e}\frac{\nabla n}{n}. \tag{3.11}$$

The corresponding electric field is shown in figure 3.7. The electric field computed by this approach is in good agreement with the electric field directly inferred from the measurements, with $v_\theta = 400\ \mathrm{km/s}$, $B_r = 0.015\ \mathrm{T}$ and $T_e = 25\ \mathrm{eV}$. B_r and T_e have been measured experimentally, while v_θ is a free parameter used to fit the electric field amplitude. The chosen value of v_θ appears to be reasonable since it is on the same order of magnitude as drift velocities typically measured, e.g., in the paper of Frias et al[24]. The outside peak of the electric field is therefore attributed to electron density fluctuations generated by the back-and-forth motion of the ionization zone. The stability of the electric field inside the channel indicate that the ionization zone does not strongly oscillate at the breathing mode in this area.

The Boltzmann 1D1V time-dependent equation has been used to compute the electric field temporal evolution. However, the computation, differentiation and division of high order moments of the IVDF is intricate due to the experimental signal-to-noise ratio. A previous attempt in computing the electric field from the non-stationary Boltzmann equation did not allow the observation of comparable structures as in the fluid case[25]. The

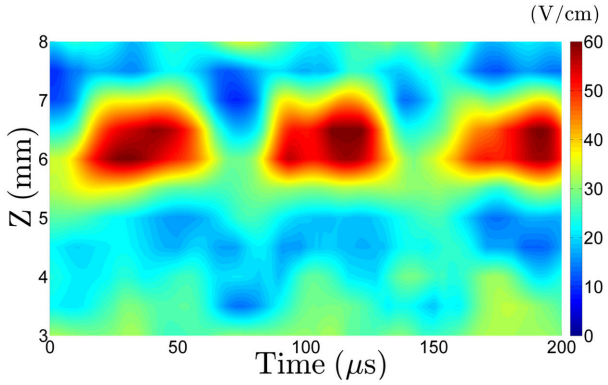

Figure 3.7: Time evolution of the electric field inferred from the density fluctuations (to be compared with figure 3.5).

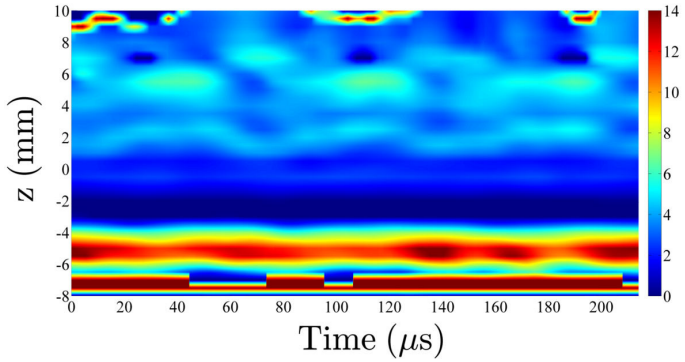

Figure 3.8: Temporal evolution of the electric field computed by the Boltzmann 1D1V non-stationary equation.

electric field evolution is presented in figure 3.8. Structures that resemble those of the fluid computation can be distinguished, but the amplitude is not high enough to correlate with the discharge voltage.

High-frequency oscillation

Coherent structures above the discharge modulation resonant frequency have been observed and briefly described in 3.2.2. Oscillations ranging from 100 kHz to 1 MHz have been observed on every velocity group time series.

Among all the quantities that can be derived from the TR-LIF data, the electric field temporal evolution is quite interesting, and can be compared with previous numerical works in the same frequency band[9]. The [100 kHz;1 MHz] content of the accelerating field has been extracted from the rest of the spectrum and is presented in figure 3.9. The figure spans a 18 $\mathrm{mm}\times$15 $\mu\mathrm{s}$ window. The two peak structure still exists in this regime of oscillation, and strong oscillations are observed outside the channel.
A remarkable feature that is displayed in figure 3.9 is the propagation of an electric field oscillation. The electric field oscillates at 400 kHz, and the scale equals that of the acceleration area. This front is persistent over the breathing mode period, and propagates towards the anode, two peculiarities which contrasts with the simulations of Coche et Garrigues who have developed a (r,θ) particle-in-cell model of a Hall thruster discharge[9]. Their simulation domain, B field and discharge properties are consistent with those of a SPT100 operating at nominal operating point (300 V and 5 $\mathrm{mg/s}$ at anode). Breath-

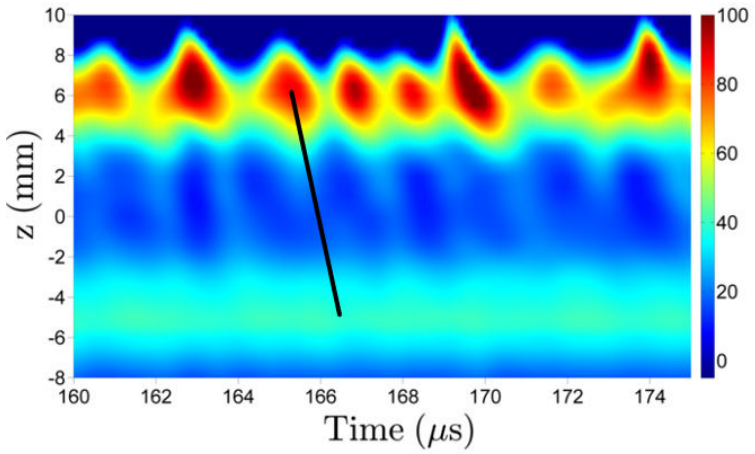

Figure 3.9: Axial electric field oscillations in the [100 kHz;1 MHz] band. The most noticeable feature is the propagation of an electric field front towards the anode at 400 kHz whose scale equals the length of the acceleration zone.

ing, transit time and azimuthal electron-cyclotron instabilities have developed during the computation. An electric field oscillation oriented towards the channel exhaust has been shown to exist at 400 kHz during the decreasing phases of the discharge current. Likewise, our measurements have revealed the propagation of a front at 400 kHz, yet persistent and in opposite direction. Additionally, ions that gain more kinetic energy than theoretically possible have been observed both numerically[9,26] and experimentally[27] in mid-scale Hall thrusters but none in the PPI. As we shall see in section 3.4, difference between the simulation and the various experiments are understandable when considering the strong dependence of the transit time instability to the magnetic field profile.
Future works could aim at observing the impact of these electric field oscillations on the electron-cyclotron azimuthal drift temporal properties, and on their consequence on electron transport. Should the turbulent transport decrease, another unstable mode might develop concomitantly to ensure the conservation of current.

3.3.4 Ionization frequency

The temporal evolution of the ionization frequency profile can be computed using the Boltzmann equation. The process is relatively straightforward: once the electric field time series has been obtained, the source term of the Boltzmann equation is computed from the time-resolved IVDFs. Assuming the neutral distribution images a Dirac delta function and the sole ionization process for collisions, the ionization frequency profile is known. Large uncertainties arise due to the finite signal-to-noise ratio of the experimental data, and the subsequent difficulties in computing the acceleration term. The ionization frequency is presented in figure 3.10 as a function of the position inside the channel and time, over 3 breathing oscillations. The colorbar is given in MHz. The computation at the beginning of the space domain is intricate, due to the high-order moments of the IVDFs that have been evaluated to infer the electric field profile, and that carried the experimental noise.
The time-averaged ionization frequency spatial evolution is presented in figure 3.11. The time-averaged and time-resolved LIF data set yield similar profiles, though the time-averaged LIF is believed to provide a more accurate profile of the ionization frequency, owing to easier calculations.

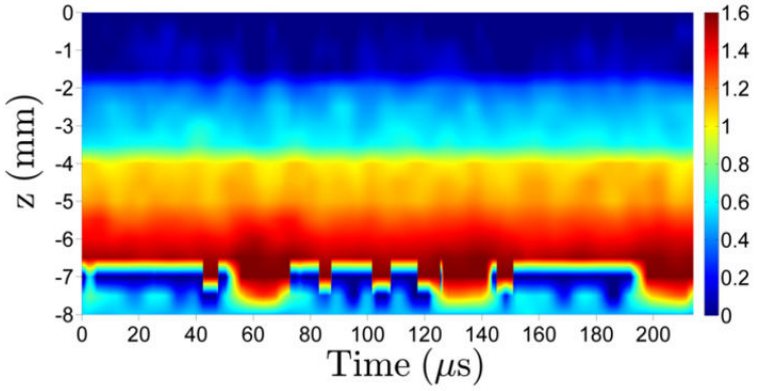

Figure 3.10: Ionization frequency oscillations in the [0;100] kHz band. The colorbar is expressed in MHz. The computation at the domain edge is difficult due to the intricate expressions that are used.

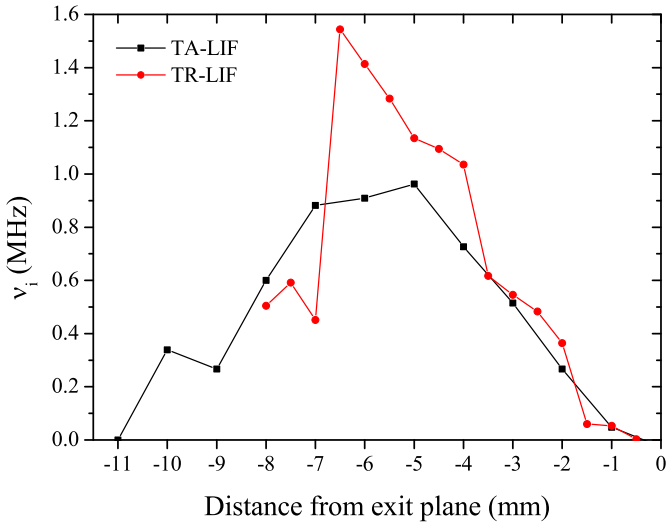

Figure 3.11: Comparison of the time-averaged ionization frequency profiles inferred from time-resolved and time-averaged LIF measurements. The profile deduced from the time-averaged LIF data set is more accurate since its computation is less complicated than that computed from the time-resolved data.

3.4 Investigation of the ion transit time instability

While the low frequency oscillations are well-understood, the transit time instability description has not progressed much from an experimental viewpoint since the early work of Esipchuk and Morozov in 1973[11], rendering the comparison with fluid models impossible. Observations of the floating plasma potential reported at that time an instability, occurring at a frequency corresponding to the reciprocal ion time-of-flight through the acceleration zone, $f \approx v_z/L$, with a wide spread in frequency so that $\Delta f \approx f$.
The marginal spectrum of the time-resolved ion mean velocity (first order moment of the IVDF) has been computed at each measurement location, which allows to detect the existence of the instability, and ultimately to compute its frequency content. In order to extract more information from the measured IVDF, we correlate the experimental observations to a linearized one-dimensional two-fluid model of the plasma, and determine the plasma parameters which influence the instability.
The model is described in subsection 3.4.1, and additional information can be found in Appendix A. The dispersion relation for axial modes is presented in subsection 3.4.2, and some clues as to the ion transit time properties are provided and compared to experimental results. Finally, the possibility for a fraction of the ion population to gain more energy than that applied is examined and discussed in light of past experiments.

3.4.1 Model

The plasma is assumed to be composed of cold unmagnetized ions and cold magnetized electrons. The magnetic field is assumed to be purely radial, which is a reasonable approximation on the cavity axis. We study the case of quasineutral perturbations, and dissipative and ionization processes are neglected. For the sake of simplicity, and for allowing the comparison of the theoretical results with the LIF data set, the model is one-dimensional. The electric field profile along the chamber axis has been obtained using the LIF measurements and a fluid computation[28]. Finally, we consider that the typical transit time frequency ω is much lower than the electron cyclotron frequency ω_{Be}, so that $\omega << \omega_{Be}$. We assume that the plasma density, ion velocity and potential can be written as the sum of a background, unperturbed quantity, and a perturbation labelled by a tilde superscript: $n \rightarrow n + \tilde{n}$, $v_z \rightarrow v_z + \tilde{v}_z$, $\Phi \rightarrow \Phi + \tilde{\Phi}$. Under these assumptions, the continuity equation and the momentum conservation equation for both the ions and the electrons are linearized and read

$$\begin{cases} \dfrac{\partial \tilde{n}}{\partial t} + n\dfrac{\partial \tilde{v}_z}{\partial z} + v_z\dfrac{\partial \tilde{n}}{\partial z} + \tilde{v}_z\dfrac{\partial n}{\partial z} + \tilde{n}\dfrac{\partial v_z}{\partial z} = 0, \\ \dfrac{\partial \tilde{v}_z}{\partial t} + v_z\dfrac{\partial \tilde{v}_z}{\partial z} + \tilde{v}_z\dfrac{\partial v_z}{\partial z} = -\dfrac{e}{m_i}\dfrac{\partial \tilde{\Phi}}{\partial z}, \\ \dfrac{\partial \tilde{n}}{\partial t} + n\dfrac{\partial \tilde{u}_z}{\partial z} + \tilde{u}_z\dfrac{\partial n}{\partial z} = 0, \\ \dfrac{\partial \tilde{u}_\theta}{\partial t} = \dfrac{e}{m_e}\tilde{u}_z B_r, \\ \dfrac{\partial \tilde{u}_z}{\partial t} = \dfrac{e}{m_e}\left(\dfrac{\partial \tilde{\Phi}}{\partial z} - \tilde{u}_\theta B_r\right), \end{cases} \tag{3.12}$$

where the subscripts r, θ and z refer to the cylindrical coordinates, v and u are the ion and electron velocities respectively, n is the plasma density, Φ the accelerating potential, e the ion charge, m_i the ion mass, m_e the electron mass and B_r the magnetic field. Perturbed quantities are labelled by a tilde superscript.

3.4.2 Relation of dispersion

We look for the solution of system (3.12) in Fourier form $\exp\left[i\left(kz - \omega t\right)\right]$, where $\mathbf{k} = (0, 0, k)$ is the perturbation wave vector.
After a few manipulations, detailed in Appendix A, the dispersion relation is obtained in the form of (3.13), in which $\omega_{_{Bi}}$ is the ion cyclotron frequency. Equation (3.13) has two complex roots. Only one of them has a positive real part and is therefore considered as the physical solution. The solution of the dispersion relation is given by (3.14).

$$\left(\frac{1}{v_z}\frac{\partial v_z}{\partial z} + \frac{2}{B_r}\frac{\partial B_r}{\partial z} - ik\right)\left(\frac{1}{v_z}\left[i\omega - \frac{\partial v_z}{\partial z}\right] - ik\right)^2 + \frac{\omega_{_{Be}}\omega_{_{Bi}}}{v_z^2}\left(\frac{1}{v_z}\frac{\partial v_z}{\partial z} - ik\right) = 0. \tag{3.13}$$

$$\omega = v_z k - i\left\{\frac{\partial v_z}{\partial z} + \left[\frac{\omega_{_{Be}}\omega_{_{Bi}}\left(ik - \frac{1}{v_z}\frac{\partial v_z}{\partial z}\right)}{\frac{1}{v_z}\frac{\partial v_z}{\partial z} + \frac{2}{B_r}\frac{\partial B_r}{\partial z} - ik}\right]^{\frac{1}{2}}\right\}. \tag{3.14}$$

The growth rate of the instability is mapped in Fig. 3.12, in MHz, as a function of the mode wavenumber and axial position along the cavity axis. Regions in which the growth rate is positive, and where unstable modes are therefore likely to appear, extend downstream the source exit plane, for $z > 1\ \mathrm{mm}$ and $k < 1000\ \mathrm{m}^{-1}$. The corresponding wavelength is on the order of the width of the electric field distribution outside the cavity. The growth rate becomes negative for higher wavenumbers between $z = 4$ to $9\ \mathrm{mm}$, which is the location of the high electric field region. It is worth noting that the growth rate is negative for any wavenumber in regions where $z < 1\ \mathrm{mm}$, i.e. inside the cavity. Expanding the dispersion relation and factorizing by the powers of the growth rate, it can be seen that, in our operating conditions, the sign of the latter is determined by the opposite sign of $\frac{\partial v_z}{\partial z} + 2\frac{v_z}{B_r}\frac{\partial B_r}{\partial z}$. Owing to the strong axial electric field, $\frac{\partial v_z}{\partial z} > 0$ at each location, and therefore the instability triggering is primarily determined by the magnetic field profile.

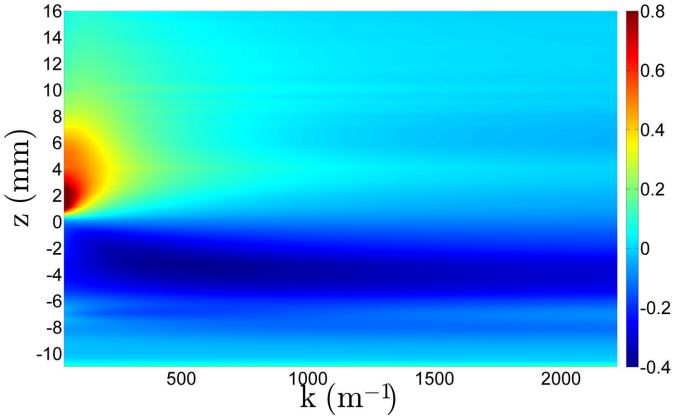

Figure 3.12: Growth rate mapping as a function of the mode wavenumber and axial position along the cavity axis. The colorbar is expressed in MHz.

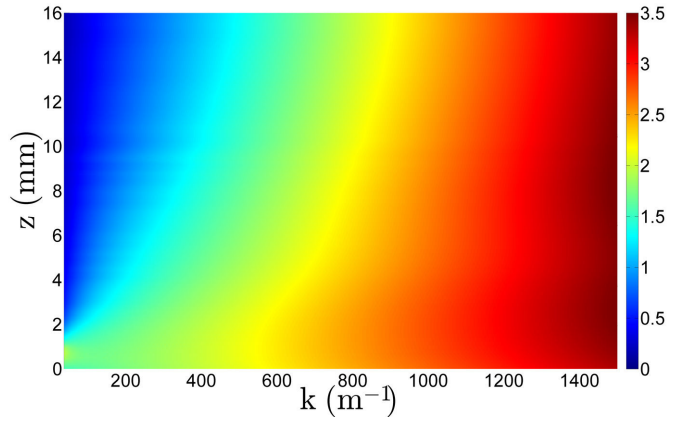

Figure 3.13: Colormap of the mode frequency as a function of wavenumber and axial location. The colorbar is expressed in MHz.

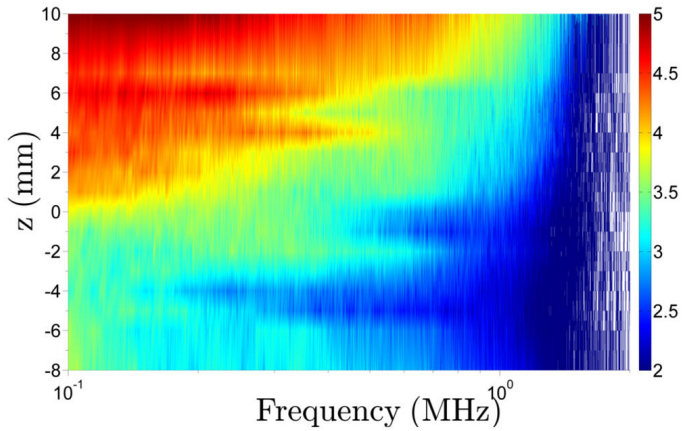

Figure 3.14: Experimental marginal spectra of the ion mean velocity as a function of z. The colorbar is expressed in arbitrary units.

The mode frequencies are mapped in Fig. 3.13, in MHz, in the area of positive growth rate, as a function of the mode wavenumber and axial position along the cavity axis. The instability is more likely to occur at low wavenumbers, which scale with the length of the acceleration zone, on the order of $1\ \mathrm{cm}$. In this region, frequencies range from $150\ \mathrm{kHz}$ to $1.2\ \mathrm{MHz}$, which is on the order of magnitude of the reciprocal ion time-of-flight through the acceleration area $\sim v_z/L$.
The experimental marginal spectra of the ion mean velocity temporal evolution are presented in Fig. 3.14, as a function of the axial position along the cavity axis. The colorbar is expressed in arbitrary units. Agreement can be found between the experimental and the analytical results. The order of magnitude of the mode frequency indeed appears to be similar, ranging in the $100\ \mathrm{kHz}$-$1.1\ \mathrm{MHz}$ band. Notice that the experimental results confirm the turbulent nature of the instability first reported by Esipchuk and Morozov[11], i.e. the frequency spread is on the same order of magnitude as the frequency scale: $\Delta f \approx f$.
A noticeable feature can be found in Fig. 3.14. The amplitude of the unstable mode increases rapidly outside the cavity. This picture is in agreement with the growth rate profile analyzed previously, which indicates that the magnetic field profile may indeed be a key element for describing the instability occurrence. Additionally, oscillations at $400\ \mathrm{kHz}$ were still observed with the PPI operating in wall-less mode, see Chapter 6. In these experiments, the anode was located at the thruster exit plane, so that the B field gradient was negative in the acceleration region. Oscillations at $100\ \mathrm{kHz}$ have however been suppressed, but this range of frequency may be linked to other phenomena[1].

3.4.3 Waveriders

In this subsection, the initial system of equations is rewritten in linear homogeneous matrix form to investigate its eigenmodes. Details of the calculations can be found in Appendix A. The time-resolved LIF measurements performed in the PPI, and past time-averaged LIF acquisitions in the plume of the SPT100-ML and PPS®X000-ML Hall thrusters[27], have shown some remarkable features of the ion flow. We propose to look further at the model description, to gain some insight into the processes that can contribute to generate a fraction of fast-moving ions.

Prerequisites: matrix form and pseudospectrum

Matrix form The system (3.12) can be rewritten

$$\frac{\partial \mathbf{X}}{\partial z} = M\mathbf{X},\ \mathbf{X} = \left(\tilde{v}_z, \tilde{n}, \tilde{\Phi}, \partial\tilde{\Phi}/\partial z\right), \tag{3.15}$$

where

$$M = \begin{pmatrix} \frac{1}{v_z}\left(i\omega - \frac{\partial v_z}{\partial z}\right) & 0 & 0 & -\frac{e}{m_i v_z} \\ \frac{n}{v_z^2}\left(2\frac{\partial v_z}{\partial z} - i\omega\right) & \frac{1}{v_z}\left(i\omega - \frac{\partial v_z}{\partial z}\right) & 0 & \frac{ne}{m_i v_z^2} \\ 0 & 0 & 0 & 1 \\ 0 & -\frac{m_e\omega_{Be}^2}{en} & 0 & \frac{1}{v_z}\frac{\partial v_z}{\partial z} + \frac{2}{B_r}\frac{\partial B_r}{\partial z} \end{pmatrix}. \tag{3.16}$$

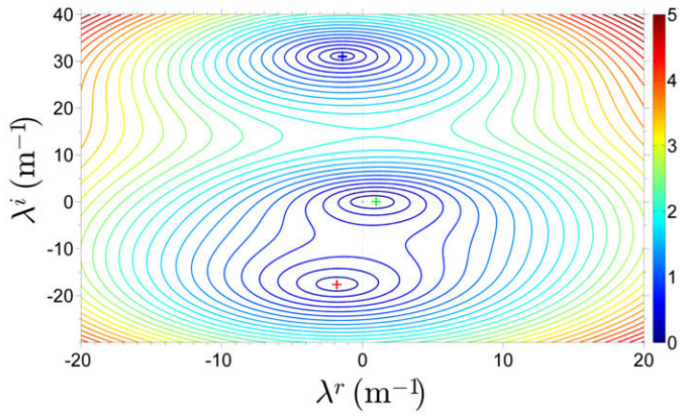

Figure 3.15: Pseudospectrum of M, at the exit plane of the PPI Hall thruster, for ω=400 kHz. The colorbar is expressed in fraction of perturbation level, i.e. the fraction of perturbation that each element of M must be subjected to in order to relocate the eigenvalues. The eigenvalue ssociated to the electric field fluctuations is represented in green crosses. It is located near the $(0, 0)$ crossing of the four quadrants of the complex plane, and therefore it may change sign easily when modifying the thruster parameters.

At each location, M possesses 4 eigenvalues, which are of prime interest to describe the propagation of a perturbation along z. While the analytical solution exists, the final expression is so intricate that its interest is limited. Instead, we have used Matlab to obtain the eigenvalues of M. The solution of equation 3.15 is proportional to $\mathrm{e}^{\Lambda z}\,\mathbf{X_0}$, where $\Lambda = (\lambda_i \delta_{ij})_{1 \leqslant i,j \leqslant 4}$ is the diagonal matrix containing the eigenvalues of M, δ_{ij} is Kronecker's delta, and $\mathbf{X_0}$ is the vector of initial conditions. The eigenvalues of M are written $\lambda_l = \lambda_l^r + i\lambda_l^i$ for $l = 1..4$, where the superscripts r and i stand for the real and imaginary parts of the eigenvalue, respectively.

Pseudospectrum The pseudospectrum of a matrix is an extension of the natural idea of a spectrum. The eigenvalue behavior, i.e. whether a small fluctuation on the matrix elements can change the sign of the real and imaginary parts of the eigenvalue, is assessed by computing the pseudo-eigenvalues of the perturbed matrix. The pseudospectrum of M is defined as

$$P_\varepsilon(M) = \left\{ z \in \mathbb{C}, \| (zI - M)^{-1} \| \geq \varepsilon^{-1} \right\} \tag{3.17}$$

where I is the identity matrix. Therefore, the pseudospectrum of M is closed and composed of poles, of which the centers are the eigenvalues. The computation of the pseudospectrum is equivalent to the determination of the smallest singular value of $zI - M$. The pseudospectrum of M is given in figure 3.15, at the exit plane of the PPI thruster, for ω=400 kHz. The colorbar illustrates the perturbation level of M that is necessary to drive the eigenvalues out of their wells. The blue cross represents λ_2, the red cross stand for λ_3 and the green cross represents λ_4. In this case, $\lambda_1 = 0\ \mathrm{m}^{-1}$. In this example, the Λ matrix is

$$\Lambda = \mathrm{diag}(0, -1.4 + 31i, -1.8 - 17i, 0.9 + 0.2i) \tag{3.18}$$

In the following of this analysis, we will limit the scope of the study to λ_4, which describes the fluctuations of the electric field. This eigenvalue is of prime interest since it is located near the $(0, 0)$ crossing of the four quadrants of the complex plane, and therefore its location may change when the thruster parameters are modified.

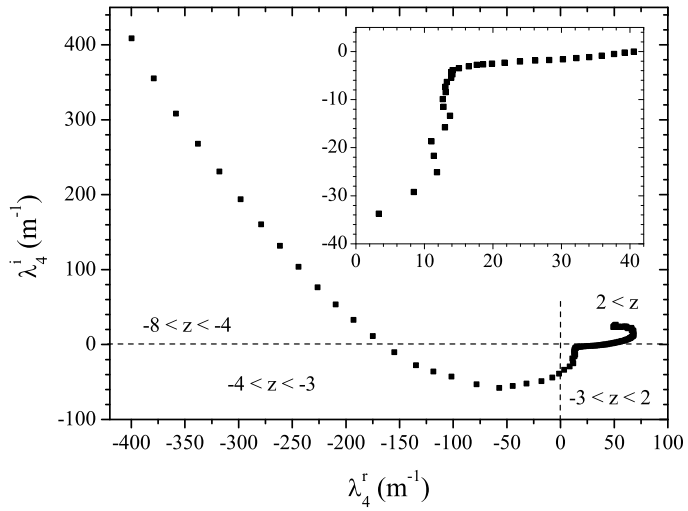

Figure 3.16: Spatial evolution of λ_4 at $\omega = 400$ kHz. Unstable modes are observed for $z > -3$ mm, in qualitative agreement with the TR-LIF measurements.

Model validation

The fluid computation, from the LIF data, of the electric field temporal evolution, has demonstrated the propagation of a front towards the anode at 400 kHz, see figure 3.9. Naturally, this precludes the development of a high-velocity ion population such as that described by Hagelaar[26] on the axial IVDF. However, this is the first time, to our knowledge, that an electric field front is experimentally shown to propagate towards the anode at this frequency. This is an experimental point to be investigated by numerical simulations, in order to validate computer codes.
The profile of λ_4 has been represented in figure 3.16. Each quadrant of the figure corresponds to an interval of locations along the discharge channel ($z = 0$ mm stands for the exit plane). Regions where $\lambda_4^r < 0$ correspond to stable regimes in which oscillations are damped. The regions of interest are that for which $\lambda_4^r > 0$, from -3 mm to the domain outer edge. An electric field oscillation which scales with approximately 5 times the length of the area of high electric field amplitude is shown to propagate towards the anode. One would however expect a propagation at the scale of the acceleration area. The model's simplicity (fluid, one-dimensional) may be the reason for this behavior. Therefore, the model outcomes are to be taken with caution. Still, the most interesting point is that this description is able to predict the electric field front occurrence that has been observed in figure 3.9.

Experiments with the SPT100-ML and PPS®X000-ML Hall thrusters[3]

Past LIF experiments performed in the SPT100-ML and PPS®X000-ML Hall thrusters near-field plume have revealed the presence of ions travelling at a velocity exceeding that theoretically achievable by singly-charged ions[27]. This phenomenon was first observed and reported by Hagelaar and his co-workers in numerical simulations[26]. This process could correspond to the ion Landau damping, which appropriately and inherently permits the exchange of energy in collisionless mediums. Ions that travel at a velocity close to the phase velocity of the wave will benefit, at the end of the acceleration zone, from a higher or lower potential energy than those in the bulk of the IVDF, thus

[3]The experimental results presented in this paragraph have been extracted from the PhD thesis of D. Gawron[27].

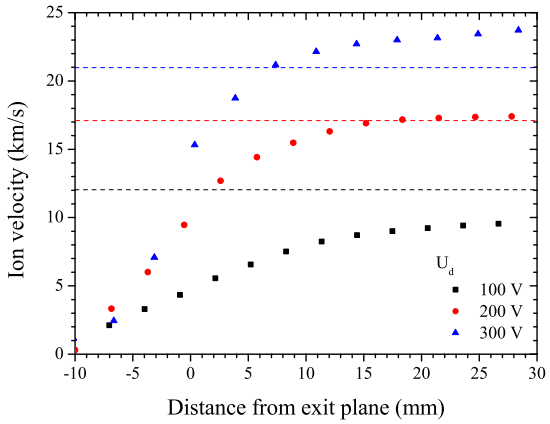

3.17.1: Ion axial velocity along the SPT100-ML channel.

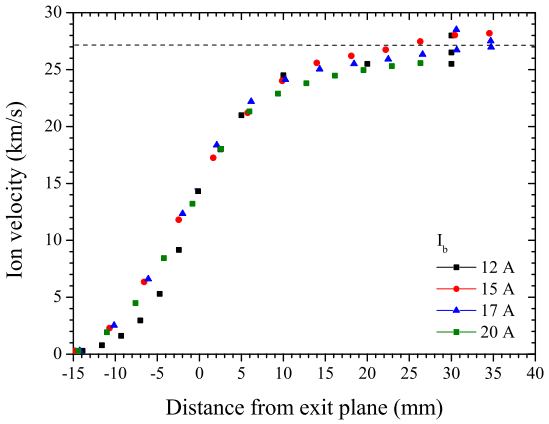

3.17.2: Ion axial velocity along the PPS®X000-ML channel.

Figure 3.17: Axial velocity of ions that represent 10 % of the axial IVDF high-velocity tail population. The dashed bars represent the maximum velocity singly-charged ions can achieve (eU_d). Reproduced from D. Gawron thesis[27].

the appellation of waveriding ions. Ions periodically experience the hill and the well of the oscillation, so that energy is conserved. The kinetic nature of this effect cannot be described with a fluid model. This part intends to obtain orders of magnitude, to evaluate the physical coherence of the figures derived from the model and to present some clues as to the ion super acceleration (and thus deceleration) process, if feasible.

The axial velocity of ions that represent 10 % of the axial IVDF high-velocity tail population has been represented in figure 3.17.1 along the SPT100-ML channel, for three different discharge voltages. The anode flow rate is 5 $\mathrm{mg/s}$ and the coil current is 4.5 A. The maximum velocity achievable by the ions is represented by dashed bars. Likewise, the ion velocity measured in the discharge of the PPS®X000-ML is represented in figure 3.17.2, for four different magnetic field configurations. The discharge voltage is 500 V and the anode flow rate is 6 $\mathrm{mg/s}$. Super-fast ions are observed in both thrusters, meaning their occurrence depends at least on the discharge voltage value and magnetic field configuration. The presence of high-velocity ions is obvious in case of the SPT100-ML, but appears more disputable in the PPS®X000-ML discharge, given the velocity profiles.

The evolution of λ_4 is presented in figures 3.18.1 and 3.18.2 in case of the SPT100-ML and PPS®X000-ML, respectively. Unstable modes are found to propagate towards the channel exhaust, which qualitatively agrees with the existence of fast-moving ions. However, this ion population is not observed experimentally at 100 V of discharge voltage in the SPT100-ML, and for $I_b = 20$ A in case of the PPS®X000-ML. Actually, an effective transfer of energy between the wave and the particles is conditioned by the gap amplitude between the phase velocity of the wave and the velocity of the ions. The ratio of the phase velocity deduced from λ_4^i, to the ion velocity, is presented in figures 3.19.1 and 3.19.2. A qualitative agreement with the experiments can be found: while unstable modes are predicted for the both thrusters in every operating condition that is presented, the phase velocity is closer to the ion velocity when very-fast ions are observed, compared to the cases where no fast population is distinguished (SPT100-ML at 100 V and PPS®X000-ML at 20 A). The agreement is much more seeable in the SPT100-ML case. The most effective transfer of energy would occur for a velocity ratio of 1. Yet the simplicity of the model we have used cannot provide more than just orders of magnitude, and finding a qualitative agreement with experiments is deemed satisfying enough.

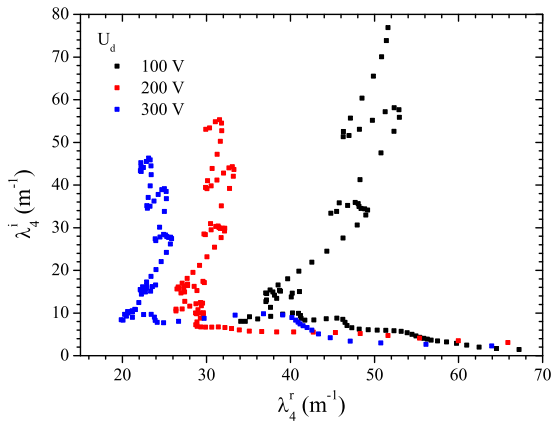

3.18.1: Profiles of λ_4 for U_d =100, 200 and 300 V in the SPT100-ML.

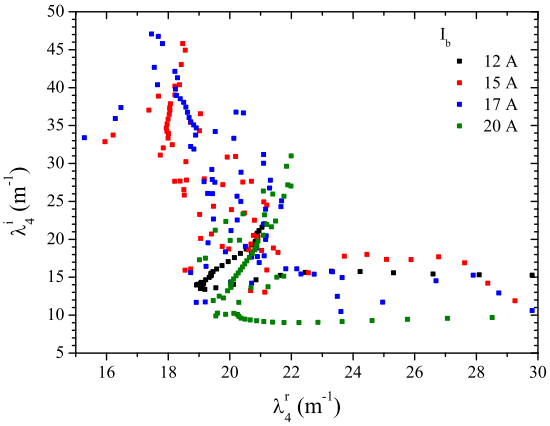

3.18.2: Profiles of λ_4 for I_b =12, 15, 17 and 20 A in the PPS®X000-ML.

Figure 3.18: Spatial evolution of λ_4 at $\omega = 400$ kHz in the SPT100-ML and PPS®X000-ML discharges. Each square represents a location along the channel axis. λ_4^i increases with the distance from the anode. Unstable modes are observed at each location along the channels.

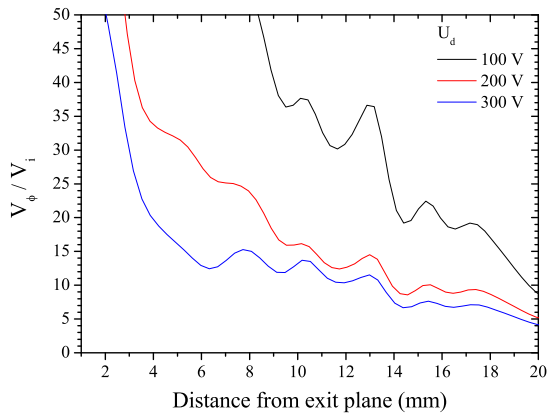

3.19.1: Ratio of the phase velocity to the ion velocity for the SPT100-ML.

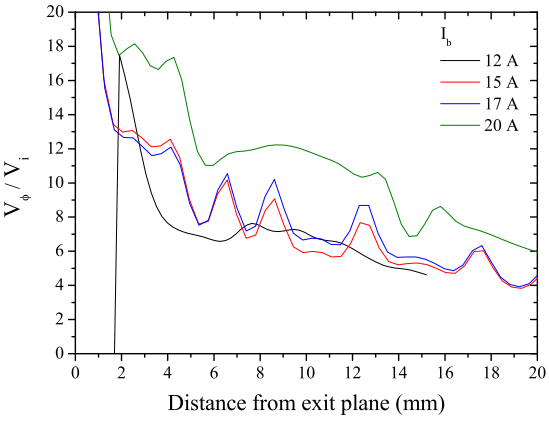

3.19.2: Ratio of the phase velocity to the ion velocity for the PPS®X000-ML.

Figure 3.19: Ratio of the phase velocity to the ion velocity along the discharge channels of the SPT100-ML and PPS®X000-ML Hall thrusters. The ratio diminishes when fast ion populations are observed by means of LIF, which is a qualitative argument in favor of a Landau-damping-like mechanism.

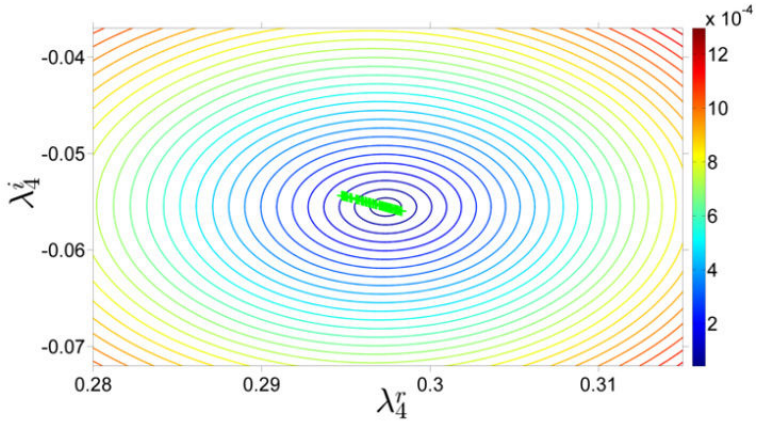

Figure 3.20: Pseudospectrum of M when the ion velocity is perturbed by $\pm$ 60 m/s. The measurement uncertainty does not relocate λ_4 in another quadrant of the complex plane, and has thus no impact on the conclusions of the analysis.

Sensitivity analysis of M

We have seen in subsection 3.4.2 that the magnetic field profile has a crucial impact on the ion transit time instability triggering. Does the magnetic field profile influence λ_4? Does it determine the existence of high-velocity ions?
Before tackling those issues, it is worth evaluating the influence of the measurement uncertainties on the computation outcome. More precisely, how the uncertainty on the ion velocity is transmitted to the phase velocity? The pseudospectrum of M can be used to assess this effect. Let $v_z = v_z^0 + \varepsilon \delta v_z$, where v_z^0 is the ion mean velocity inferred from the LIF measurements, δv_z the velocity uncertainty (prominently determined by the wavelength meter resolution), and ε a random number between -1 and 1. This quantity is injected into M. The perturbed matrix is randomly generated N times, and the pseudo-eigenvalues are computed at each iteration. The influence of the measurement uncertainty on λ_4 can be evaluated for a sufficient number of draws.
The pseudospectrum of $M + \delta M$ is presented in figure 3.20, for $N = 100$ and $\delta v_z = 60$ m/s. The pseudospectrum has been obtained at the exit plane of the PPI operating under nominal conditions, with $\omega = 400$ kHz. It is obvious from this computation that the measurement uncertainty on the ion velocity cannot change the complex plane quadrant in which λ_4 is located, thus the conclusion of the analysis. The same behavior has been observed at each location along the PPI, SPT100-ML and PPS®X000-ML channels.

The influence of the magnetic field profile can be assessed in a similar manner. However, we assume that modifications to the magnetic field do not influence the electric field profile.[4] Let us write $B_r = \Psi B_r^0$, where B_r^0 is the magnetic field profile of the SPT100-ML, and Ψ a random number. Then the only coefficient of M which is modified is that of the 4th line, 2nd column, denoted F. We study the perturbation of F by computing the pseudo-eigenvalues of M, in which $F \rightarrow F + dF/d\Psi$. Since $F \propto B_r^2$, $dF/d\Psi = 2F/\Psi$. Thus, $F + dF/d\Psi = F\,(1 + 2/\Psi)$.
The evolution of λ_4 is presented in the pseudospectrum of M in figure 3.21. The spectrum is obtained at 1 mm downstream the SPT100-ML exit plane, for $\omega = 400$ kHz. The elements of M containing the ion velocity, and F, have been perturbed. The veloc-

[4]This assumption cannot be substantiated by any physical argument since it is fundamentally not true. However, measurements with the PPS®X000-ML have shown that the electric field profile does not change dramatically between the 15 A and 20 A configurations.

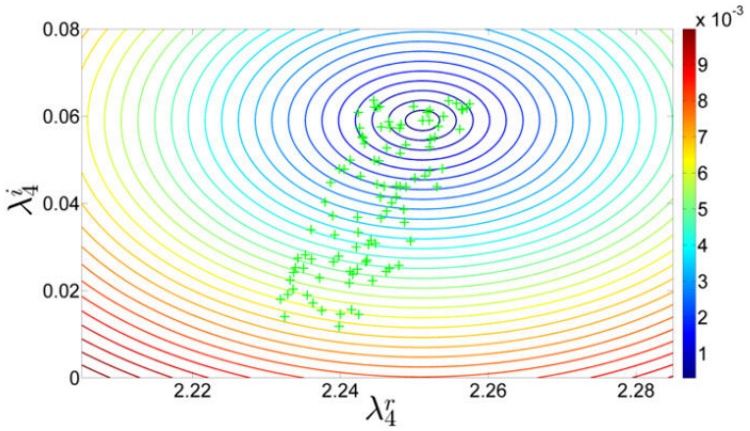

Figure 3.21: Pseudospectrum of M when the ion velocity and F are perturbed. The velocity perturbation is $\pm$ 60 m/s. Ψ has been varied between 0.2 and 2. The perturbation of M does not relocate λ_4 in another quadrant of the complex plane, but modifies the amplitude of the phase velocity.

ity perturbation is 60 $\mathrm{m/s}$. Ψ has been varied between 0.2 and 2. While the sign of the real and imaginary parts of λ_4 is not influenced by the perturbation, the amplitude of λ_4^i ranges from 0.1 to 0.7. The consequent modification in the phase velocity could modify the energy transfer to the ion population, thus conditioning the existence of a super-fast ion population.

3.5 Conclusion

In this chapter, we have used the Hilbert-Huang signal processing technique to investigate the time-resolved properties of the PPI discharge, under nominal operating conditions. The TR-LIF measurements have been associated to a modulation apparatus which has stabilized the discharge and allowed a time-coherent regime of oscillation. Resonance has been reached with the plasma parameters by driving the cathode at the breathing mode frequency. The electric field appears to possess two peaks with alumina walls in $2S_0$ geometry, even though a clarification is still required as to which physical processes would be responsible for such an uncommon profile. The results show strong electric field oscillations outside the channel, while internal electric field oscillations are almost absent. The minimum of the electric field is located at the channel exit plane in the region of high magnetic field. The location of this minimum may be attributed to the modification in plasma/wall interactions induced by the use of an enlarged channel compared to the standard geometry.
The density fluctuations may reveal the propagation of an ionization front at the speed of the neutrals, as in the previous study by Mazouffre[21]. However, in that case, the time coherence was reached by periodically igniting the discharge, which produced strong oscillations as well as important modifications of the discharge mean behavior compared to a stabilized operating regime. It is believed that such a technique may be at the origin of the wave front observed. The different discharge properties between the two studies may also result from a geometrical effect since a larger channel width has been used in the present work. The breathing mode phase-lock mechanism induced by the modulation system may also result in discrepancies between the natural and the observed oscillations of the electric field.

The experimental properties of the ion mean velocity have been compared with a one-dimensional two-fluid model of the plasma flow. The ion transit time oscillation appears only in the region of negative magnetic field gradient both analytically and experimentally. Additionally, its wavelength appears to be similar to the electric field distribution extent outside the cavity.
A theoretical description of the ion wave-riding mechanism as been proposed. The analysis of the matrix M has shown the ability of the model to qualitatively corroborate the experimental data obtained on the PPI. Once validated, the model has provided some clues as to the discharge properties of the SPT100-ML and PPS®X000-ML Hall thrusters that can generate fast-moving ions. A satisfying agreement was found between the time-averaged LIF measurements performed a few years ago and the model predictions.

The TR-LIF measurement campaign took approximately 2 months, and 307 hours of thruster operation. Twenty IVDFs, composed of 15 velocity groups each, yielded 300 photon time series. Each signal has been decomposed into 14 IMFs, and the Hilbert spectral analysis generates 3 times series for each IMF (instantaneous frequency, phase and amplitude). Even though this technique is well-suited to our signals, 13,200 files to be processed have been generated. LIF measurements alone cannot account for the physical complexity and richness of the outcomes, which much be corroborated to other diagnostic tools. Additionally, this is the challenge of processing so many files, with so many unknown quantities, that gave us the idea of using the ion mean velocity, therefore reducing the number of parameters of the problem. The statistical nature of the marginal spectrum has proven difficult to handle, but ultimately we hope the results we provide can serve to better understand the non-stationary nature of the ion flow. To close with Huang et al.[13]: "We've only begun to explore the fully physical interpretations of the Hilbert spectra for any complicated data series."

References

[1] EY. Choueiri. Plasma Oscillations in Hall Thrusters. *Phys. Plasmas*, 8:1411, 2001.

[2] V. V. Zhurin, H. R. Kaufman, and R. S. Robinson. Physics of closed drift thrusters. *Plasma Sources Sci. Technol.*, 8:R1, 1999.

[3] C. L. Ellison, Y. Raitses, N. J. Fisch. Cross-field electron transport induced by a rotating spoke in a cylindrical Hall thruster. *Phys. Plasmas*, 19(013503), 2012.

[4] S Tsikata, C Honoré and D Grésillon. Collective Thomson scattering for studying plasma instabilities in electric thrusters. *Journal of Instrumentation*, 8(10):C10012, 2013.

[5] J. P. Boeuf and L. Garrigues. Low frequency oscillations in a stationary plasma thruster. *J. Appl. Phys.*, 84(7):3541, 1998.

[6] N. Brenning, D. Lundin, T. Minea, C Costin, C. Vitelaru. Spokes and charged particle transport in HiPIMS magnetrons. *J. Phys. D: Appl. Phys.*, 46(084005), 2013.

[7] S Barral, K. Makowski, Z. Peradzyński, M. Dudeck. Transit-time instability in Hall thrusters. *Phys. Plasmas*, 12(073504), 2005.

[8] A. Kapulkin, E. Behar, Y. Raitses. Ion Beam Instability in Hall Thrusters. In Proceedings of the 33rd International Electric Propulsion Conference, Washington, D.C., USA, 2013.

[9] P. Coche and L. Garrigues. A two-dimensional (azimuthal-axial) particle-in-cell model of a Hall thruster. *Phys. Plasmas*, 21(023503), 2014.

[10] S. Tsikata, N. Lemoine, V. Pisarev, and D. M. Gresillon. Dispersion relations of electron density fluctuations in a Hall thruster plasma, observed by collective light scattering. *Phys. Plasmas*, 16(033506), 2009.

[11] Yu. B. Esipchuk, A.I. Morozov, G.N. Tilnin, A.V. Trofimov. Plasma oscillations in closed-drift accelerators with an extended acceleration zone. *Zh. Tekh. Fiz.*, 43:1466–1473, 1973.

[12] S. Barral and E. Ahedo. Low-frequency model of breathing oscillations in Hall discharges. *Phys. Rev. E*, 79(046401), 2009.

[13] N.E. Huang, Z. Shen, S.R. Long, M.L. Wu, H.H. Shih, Q. Zheng, N.C. Yen, C.C. Tung and H.H. Liu. The empirical mode decomposition and Hilbert spectrum for nonlinear and non-stationary time series analysis. Proceedings of the Royal Society of London A: Mathematical, Physical and Engineering Sciences 454, 903-995, 1998.

[14] G. Rilling. *Décompositions Modales Empiriques : Contributions à la théorie, l'algorithmie et l'analyse de performances*. PhD thesis, Université de Lyon, 2007.

[15] T. Schlurmann. Spectral Analysis of Nonlinear Water Waves Based on the Hilbert-Huang Transformation. *J. Offshore Mech. Arct. Eng.*, 124(1):22–27, 2001.

[16] J. Terradas, R. Oliver, and J. L. Ballester. Application of Statistical Techniques to the Analysis of Solar Coronal Oscillations. *Astrophys. J.*, 614:435, 2004.

[17] J. Kurzyna, S. Mazouffre, A. Lazurenko, L. Albarède, G. Bonhomme, K. Makowski, M. Dudeck and Z. Peradzynski. Spectral analysis of Hall-effect thruster plasma oscillations based on the empirical mode decomposition. *Phys. Plasmas*, 12(123506), 2005.

[18] P. Flandrin, P. Goncalves, G. Rilling. Detrending and denoising with empirical mode decompositions. Proceedings of EUSIPCO-04, Vienna, Austria, pp. 1581-1584., 2004.

[19] E.C. Titchmarsh. *Introduction to the theory of Fourier integrals*. 1948.

[20] J. Vaudolon, B. Khiar, S. Mazouffre. Time evolution of the electric field in a Hall thruster. *Plasma Sources Sci. Technol.*, 23(022002), 2014.

[21] S. Mazouffre and G. Bourgeois. Spatio-temporal characteristics of ion velocity in a Hall thruster discharge. *Plasma Sources Sci. Technol.*, 19(065018):9, 2010.

[22] J. Vaudolon, L. Balika, and S. Mazouffre. Photon counting technique applied to time-resolved laser-induced fluorescence measurements on a stabilized discharge. *Rev. Sci. Instrum.*, 84(073512), 2013.

[23] C. L. Ellison, Y. Raitses, and N. J. Fisch. Fast Camera Imaging of Hall Thruster Ignition. *IEEE Trans. Plasma Sci.*, 39:2950–2951, 2011.

[24] W.Frias, A.I. Smolyakov, Y. Raitses and I. D. Kaganovich. Gradient drift instability in Hall plasma devices. IEPC 2013-175, 33rd International Electric Propulsion Conference, The George Washington University, Washington, D.C., USA, 2013.

[25] G. Bourgeois. *Influence de la topologie magnétique, de la cathode et de la section du canal sur l'accélération des ions dans un propulseur à effet Hall*. PhD thesis, Université d'Orléans, 2012.

[26] G. J. M. Hagelaar, J. Bareilles, L. Garrigues and J.P. Boeuf. Role of anomalous electron transport in a stationary plasma thruster simulation. *J. Appl. Phys.*, 93:67, 2003.

[27] D. Gawron. *Phénomènes de transport ionique dans le plasma d'un propulseur à effet Hall à forte puissance : étude par spectroscopie laser*. PhD thesis, Université d'Orléans, 2007.

[28] J. Vaudolon and S. Mazouffre. Indirect determination of the electric field in plasma discharges using laser-induced fluorescence spectroscopy. *Phys. Plasmas*, 21:093505, 2014.

Chapter 4

Probe measurements in the plume of Hall thrusters

Contents

ACCURATE current measurements in the plume of Hall thrusters (in that of any plasma source for that matter), are mandatory for better understanding the physics. Diagnostic tools are manifold, and so are their outcomes. For instance, Faraday probes allow the evaluation of the total ion beam current and to compute the beam divergence angle in Hall thrusters, Langmuir and emissive probes are used to infer the electron properties, retarding potential analyzers and E×B probes are filters that select species according to their energy and velocity, respectively, to yield distributions.
Ground-testing conditions have been known to depart from those met in orbit for far too

many years, considering that the performance of various thrusters, which are competing for similar applications, are crudely compared while being operated in different test facilities. Efforts in standardizing the measurement procedures have been undertaken in Europe and the United States to mitigate specific influences, such as that of the residual pressure[1–3]. It has been checked, with the PPS-Flex, during this research, that the vessel background pressure generates an additional thrust by ionizing a fraction of neutral gas that is ingested into the discharge channel[4]. A notable influence on the ion current density profile was also observed. Other effects, such as the Earth's gravitational field impact on the sputtered materials, are still ill-understood. Likewise, specific issues appear in flight, and cannot be simulated easily in vacuum chambers.
Unfortunately, on top of this, probes are subjected to uncertainties. Some are thought to be theoretically evaluated. Others might not be evaluated without resorting to computer simulations or testing. A test campaign at the European Space Agency Propulsion Laboratory, with the PPS-Flex, intended to evaluate some of the Langmuir probe, Faraday probe, repulsing potential analyzer and E×B probe measurement uncertainties. A summary of this research is proposed in Sec. 4.1. Since most of the probe studies of this dissertation are concerned with planar probes, Sec. 4.2 and 4.3 examine two particularly important matters, namely the effect of background pressure on the ion beam, and the proper computation of the ion beam divergence angle. Aside from the theoretical investigation, the design, construction and operation of planar probes are reported in Sec. 4.4 and Sec. 4.6. These preliminary experiments aimed at characterizing the probes and to vary the measurement conditions, prior to undertake the study of the magnetic topology with the PPI-Mag, reported in Chapter 5. A rotating mechanical assembly, a data acquisition system and an electric circuit have been developed to perform measurements in the NExET vacuum chamber. The systems are presented in Sec. 4.5. Concluding remarks are given in 4.7.

4.1 Probe error sources

4.1.1 Common probes used in electric propulsion that have been considered

In this part, a short description of the working principles of some of the most common probes used for EP testing is made. The Retarding Potential Analyzer, Langmuir, Faraday and E×B probes are described.
Plume measurements are vital for qualification of EP devices since low energy ions emitted by a thruster are capable of damaging sensitive spacecraft surfaces. The damage may consist of erosion due to sputtering, deposition of previously sputtered materials, and/or arcing due to the presence of free charges from the ionized plume. The onboard electronic equipment may be perturbed due to the spacecraft charging. Plume measurements can also provide many important insights into the physics at stake inside the discharge.

Retarding Potential Analyzer

A Retarding Potential Analyzer (RPA), also known as a Retarding Field Electrostatic Analyzer (RFEA), is a gridded probe that uses electric fields to act as an energy filter. A RPA is typically used to determine the ion energy distribution function (IEDF). The probe acts as a high-pass filter: only ions with energies greater than the repelling grid voltage can pass the filter and reach the collector electrode. The potential of the ion retarding grid is varied while monitoring the ion current incident on the collector. A I versus V curve is hence obtained, the so-called I-V characteristic. The basic layout of a

four-grid RPA, and a typical I-V curve are shown in figure 4.1. The first derivative of the I-V curve is then directly proportional to the IEDF[5]. A RPA is usually composed of four grids:

- The first grid at the entrance serves to shield the plasma from the field inside the analyzer in order to minimize disturbance. The mesh size must be on the order of the plasma Debye length. A common practice is either to let this grid floating or to ground it. The latter case presents the advantage to know exactly the potential applied on the grid.
- The second grid is polarized negatively in order to repel electrons so that only ions enter the measurement device.
- The third grid acts as an ion repeller. A variable positive potential is applied to this grid. By adjusting the grid potential the ion energy distribution is scanned. Ions with energies below the grid potential are repelled and cannot be detected.
- The fourth grid is biased negatively to prevent secondary electrons emitted by the collector from escaping.
- The collector is made of a material presenting a low secondary electron emission coefficient, such as tungsten or molybdenum.

Since a RPA distinguishes ion species according to their energy, a RPA is usually not able to separate the different ion charge states in an electrostatic acceleration. Charge separation is however possible when time-of-flight measurements are performed. The profile of the time-resolved current collected by the RPA is in this case composed of different plateaus, ions of different charge states being accelerated according to the square root of their charge, and therefore reaching the collector at different instants in time (true for ion engines and a good first approximation for Hall thrusters). A RPA measures the ion energy with respect to the ground. Comparison of the RPA IEDF with the IVDF obtained by LIF is possible, provided the local plasma potential is measured (a RPA measures the ion energy while LIF measures the ion velocity[6]).

Langmuir probe

Basically, one way to measure in situ the plume ion current is to employ a biased conducting object inserted into the plasma, and connected through some electrical circuit to the outside of the test chamber. In other words, one needs a Langmuir probe. Such an instrument is widely used in the field of plasma physics, and a large number of reviews on the topic, which cover probe theories, operating principles and models, are available in the literature[7–10].

There are several probe sizes, shapes (planar disk, cylinder, sphere), architectures (single, double, emissive) and associated electric circuits. Nevertheless, all the designs rest on the same working principle, which depends on the plasma sheath extent with respect to the probe dimension[7,11,12]. A typical current-voltage probe characteristic is presented in figure 4.2. The curve can be divided into three distinct parts:

- $V < V_p$, where V_p is the plasma potential. The instrument collects mainly positive ions. This part corresponds to the ion saturation regime. It is the domain of interest to measure the ion current in the beam of a Hall thruster.
- $V \approx V_p$: the probe collects ions and electrons. At the floating potential V_f, the ion and electron currents are equal. At $V = V_p$, the curve exhibits a knee as the potential changes its character from attracting ions to repelling ions.

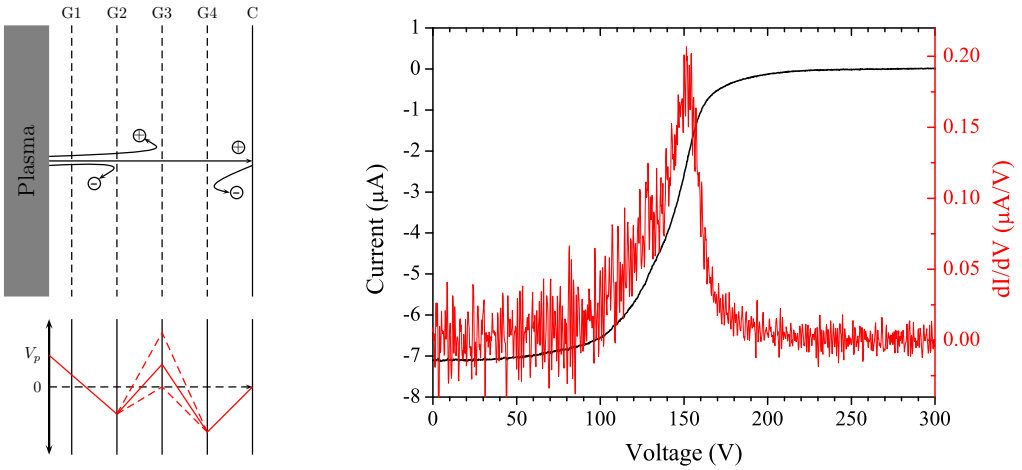

Figure 4.1: (Left) Layout of a four-grid RPA design. The potential distribution within the analyzer is represented. (Right) Four-grid RPA I-V characteristic measured in the plume of the PPI operating at 200 V and 1.0 $\mathrm{mg/s}$ of xenon (black) ; First derivative of the I-V characteristic computed using centered finite differences (red).

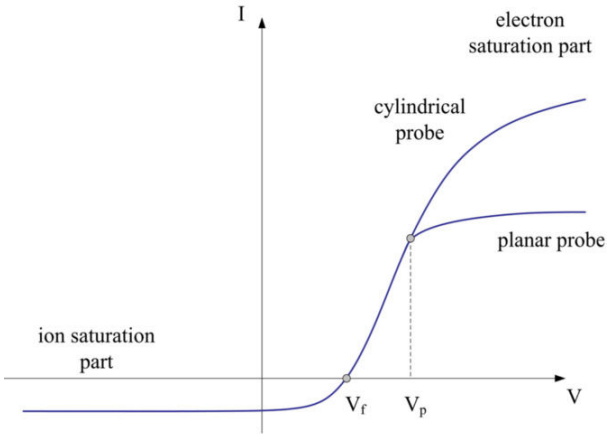

Figure 4.2: Typical I-V characteristics for planar and cylindrical Langmuir probes.

- $V > V_p$: the probe solely captures electrons. It is the electron saturation regime.

Because a magnetic field reduces the transverse flux available to the probe, the electron saturation current becomes a function of the magnetic field in a magnetized plasma. Therefore, the electron saturation current cannot be used to obtain an accurate estimation of the electron number density. Instead, the ion saturation current must be used to determine electron number density. For the plasma conditions in the near-field plume of an EP device, the ion motion is not appreciably influenced by the magnetic field. Furthermore, the ion Larmor radius is large compared with the probe dimensions. For these reasons, magnetic field effects are not expected to significantly impact the density measurements when the ion saturation current branch is used.

Faraday probe

A Faraday probe is, in its simplest design, a planar Langmuir probe. The planar sheath that develops makes the collection theory, however, much simpler than that of the

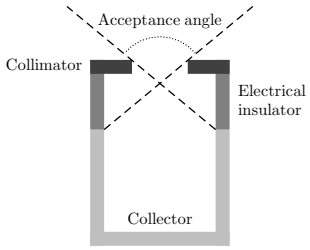

Figure 4.3: Layout of a collimated Faraday probe. Only ions located in the acceptance cone, and which possess the proper velocity vector, can enter the probe and be collected.

cylindrical Langmuir probe. The probe is biased much below the plasma potential, so that the probe operates in the ion saturation regime. The probe current is usually divided by the probe surface to infer the ion current density. There are several types of Faraday probes including nude, guarded, cupped, collimated, gridded (i.e. RPA), and magnetically filtered probes[13–15]. A collimated Faraday probe is a nude probe, encased in a long drift tube with a hole in the collection end, see layout in figure 4.3. The encasement only allows the ions that possess a specific velocity vector to reach the nude Faraday probe. The small acceptance solid angle of the probe theoretically acts as a filter for the low-energy, random ions. The collimator and the collector are electrically separated, so that the current collected by the collimator is not considered in the analysis. The Faraday cup design is similar, except that the collimator is linked to the collector. The collected current is higher since low-energy ions can be collected. Magnetically-filtered probes work in a similar way except that a strong transverse magnetic field is applied to deflect low-energy ions and to prevent secondary electrons to escape.

Faraday probes are widely used on rotating arms to measure ion current density 2D profiles. From these measurements, the total ion current, the ionization efficiency and the ion beam divergence can be inferred. A 3D profile can be obtained with several probes located along a semi-circular arm that is moved across the plume.

E×B probe

An E×B probe, also known as a Wien filter, is a simple example of a mass spectrometry device. As shown in figure 4.4, an E×B probe utilizes perpendicular electric and magnetic fields to filter ions according to their velocity. The magnetic field diverts ions away from a straight trajectory, while the electric field provides an opposing force to push the ions back to their original path. The net force $\mathbf{F}$ experienced by an ion moving at a velocity $\mathbf{v}$ is given by

$$\mathbf{F} = q\left(\mathbf{E} + \mathbf{v}\times\mathbf{B}\right), \tag{4.1}$$

where q is the ion charge, $\mathbf{E}$ and $\mathbf{B}$ are the electric and magnetic fields. The Wien filter selects ions by balancing $\mathbf{E}$ and $\mathbf{B}$ such that the opposing forces exerted by the two fields cancel out each other, and that there is a null net force on the charged particle. For perpendicular $\mathbf{E}$ and $\mathbf{B}$ fields appropriately oriented, equation 4.1 becomes

$$F = q\left(E - vB\right). \tag{4.2}$$

In practice, a constant magnetic field is applied with magnets and a tunable electric field is established between two parallel plates, biased to a potential $\pm V/2$ and separated by a distance d. The condition for an ion to pass throughout the E×B cavity, and to reach the detector, becomes

$$v = \frac{V}{dB}. \tag{4.3}$$

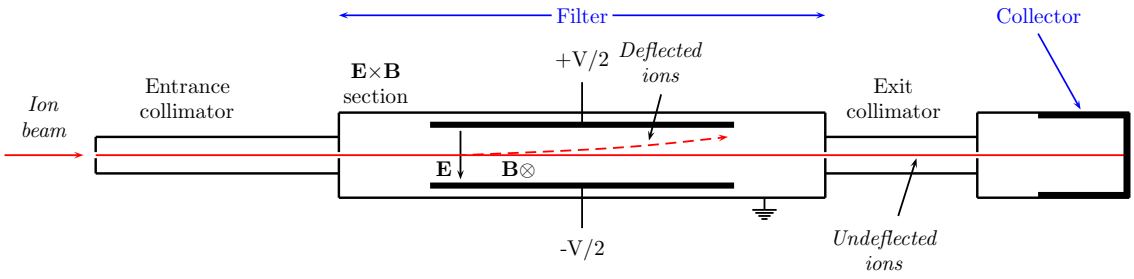

Figure 4.4: Schematic view of an E×B probe.

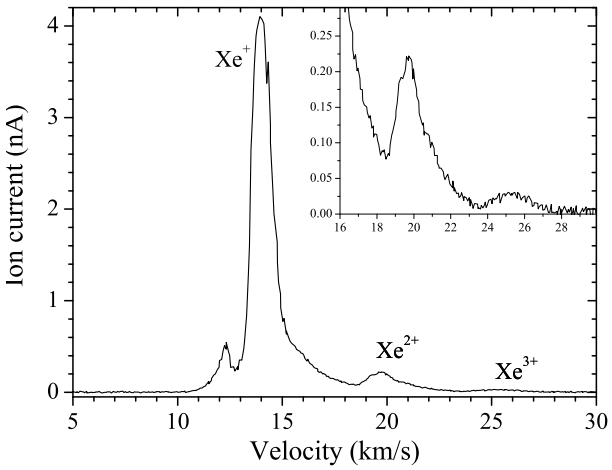

Figure 4.5: E×B probe measurement 40 cm downstream of the PPI exit plane, under operation at 200 V and 1.0 mg/s of xenon. A small extra hump is seen before the main Xe^+ peak, and cannot be explained as of yet. This structure was also observed in previous works[16].

Note that the charge state of the ions is absent from the selection equation. However, charge separation is possible when using an E×B probe for electric propulsion testing, since ions are accelerated according to the square root of their charge state.
A typical spectrum is shown in figure 4.5. The multiply-charged ions are seen. The origin of the small bump before the main Xe^+ peak is unknown, but was previously observed by Kim with a different probe[16]. Kim relates this peak to charge exchange collisions within the plume. The velocity ratio between the Xe^{2+} and Xe^{3+} ions to the Xe^+ ion are 1.41 and 1.73, respectively, demonstrating that the vision of a collisionless electrostatic acceleration is a reasonable approximation in the discharge of a Hall thruster. It also demonstrates that the multiply-charged ions are created in a similar region than their singly-charged brethren.

An E×B probe is therefore a reliable instrument to accurately measure the ion energy distribution function in a well-defined direction. Unlike the RPA technique, the E×B probe does not require the differentiation of the raw current trace to obtain the distribution, a process that is known to impart noise on the data.
Note that the current density must be divided by the charge state to provide the velocity distribution, which requires the identification of the species on each spectrum. The propellant used in electric thrusters are usually of Xe, Kr and Ar which are non reactive. The almost electrostatic acceleration then allows a clear distinction between the different ions. The problem is possibly more intricate in reactive gases, such as that of PEGASES[17].

4.1.2 Identification of the measurement uncertainties

Because there is no possible perfect measurement under the best conditions, errors are generated. These errors introduce uncertainty in the measurements. Uncertainties fall into two different categories: random (referred to as type A) and systematic (type B). More details can be found in a detailed study[2]. The error sources that arise during an electric propulsion testing are listed herein.

- The measuring instrument, δ_{instr}. Instruments can suffer from errors including bias, changes due to ageing, wear, or other kinds of drift, poor readability, noise (for electrical instruments) and many other problems. These features are unpredictable and make δ_{instr} of type A. The regularity of the calibration is to be defined by the instrument manufacturer. The uncertainty can be estimated by repeating measurements. In principle, for random errors, the more measurements you make, and then average, the better estimate you generally can expect to get. It is generally assumed that 10 repetitions is a good number[18]. Mean measurement values and standard deviations can be inferred from these measurements, which are used in the uncertainty budget.

- The thruster behavior, $\delta_{thruster}$, which may not be stable (imagine trying to measure the temperature of a ceramic which is warming-up). The uncertainty depends on each operating conditions and is therefore of type A. In order to minimize $\delta_{thruster}$, the measurements must be made during steady state operation. The transient behavior of an EP device is mainly a thermal effect. While gridded ion engines need a few minutes to stabilize, Hall thrusters require several hours. In practical operation, 30 minutes are generally allowed for a Hall thruster stabilization and makes this uncertainty negligible. Finally, the thruster behavior must be free of mode-hops and hot spots for this error source to be negligible.

- The measurement process, $\delta_{process}$. The measurement itself may be difficult to make. For example measuring the IVDF using an E×B probe may take several minutes. During that time the measurement is subjected to different kind of perturbations. This perturbation is of type A. The measurement process error sources comprise all the errors linked to the diagnostic tools. A detailed review of the error sources specific to the Faraday, Langmuir, RPA and E×B probes has been made and delivered to ESA[2,3,19]. More than 15 uncertainties have been found to lie into $\delta_{process}$.

- 'Imported' uncertainties, $\delta_{calibration}$. Calibration of your instrument has an uncertainty which is then built into the uncertainty of the measurements you make (but remember that the uncertainty due to not calibrating would be much worse). The calibration of the instrument makes $\delta_{calibration}$ of type B. All the measurement and data acquisition equipment should be calibrated to internationally recognised standards. The known assumptions and corrections, such as may be found on calibration certificates, should be described and an uncertainty analysis performed in each case. The calibration certificate often provides the coverage factor k of the distribution associated with the device. The standard deviation to consider for the uncertainty budget analysis is therefore $\delta_{calibration}/k$.

- Operator skill, $\delta_{operator}$. Some measurements depend on the skill and judgement of the operator. One person may be better than another at the delicate work of setting up a measurement, or at reading fine detail by eye. The use of an instrument such as a stopwatch depends on the reaction time of the operator (but gross mistakes are a different matter and are not to be accounted for as uncertainties.) Visual alignment

is for instance an operator skill. The random nature of this error source implies that $\delta_{operator}$ sides with type A. When an operator is required to assess the physical meaning of a measurement, the procedure used to extract the uncertainty $\delta_{operator}$ is similar to that of δ_{instr}. A number of repeated measurements will provide the standard deviation to be used for the computation of the total uncertainty.

- Sampling issues, δ_{sample}. The measurements you make must be properly representative of the process you are trying to assess. If you are choosing samples from a production line for measurement, don't always take the first ten made on a Monday morning. This process is inherently of type A. EP devices can exhibit different behavior during a measurement depending on their previous history. The ceramic of a Hall thruster may require several hours of firing before releasing all the air molecules gathered while being at ambient pressure. It is therefore necessary to repeat the measurements at different periods to determine δ_{sample}.

- The measurement environment, δ_{env}. Facility size, background pressure, boundary conditions and many other conditions can affect the measuring instrument or the item being measured. Where the size and effect of an error are known (e.g. from a calibration certificate), a correction can be applied to the measurement result. But, in general, uncertainties from each of these sources, and from other sources, would be individual inputs contributing to the overall uncertainty in the measurement. δ_{env} is defined as a type B uncertainty. It is believed that the main error source when dealing with the measuring environment is due to the background pressure effects, namely: the neutral gas and the CEX collisions which can occur inside and outside the analyzers. A sufficient amount of measurements at different pressures are needed in order to characterize the pressure dependency of a particular physical parameter. An experimental law may be derived to account for the pressure effects and to determine δ_{env}.

- Data analysis and treatment, $\delta_{analysis}$. Post-process of the experimental data can introduce noise in the computed quantities. For instance differentiating an I-V characteristic is inherently noisy, smoothing often lowers the local amplitude of a maximum and modifies the moments of a distribution, the ion current density profiles obtained with Faraday probes are sometimes approximated by Gaussian functions ... $\delta_{analysis}$ is of type A.

- Cables, δ_{cables}. Since the cables linking the diagnostic tool to the data acquisition system have a small resistance, a potential drop occurs in the line and must be accounted for when analyzing the data.

4.1.3 Uncertainty budget

The accurate determination of the uncertainty budget for the measurement of plasma currents in the plume of an EP device is a difficult task. The total measurement uncertainty of the current to be measured using a given diagnostic tool can be written in the simple form

$$\delta I = \left(\sum_{i \in A} \delta_i^2 \right)^{1/2}, \tag{4.4}$$

where A is the family of the uncertainties and δ_i is the standard uncertainty of the mean[3,18] associated to the i$^{\text{th}}$ error source. In this case, all the error sources are assumed to be independent from one another. However, a more rigorous treatment may be needed for

determining the total uncertainty δI, as processes taken into account in equation (4.4) may be interrelated. The current is then a complex function of many processes, i.e. a function of many variables x_i: $I_i = f(x_1...x_n)$. In that case, δI is not simply the sum of all errors. It can be expressed as

$$\delta I = \sum_{i \in A} \left(\frac{\partial I_i}{\partial x_i} \right) \delta x_i. \tag{4.5}$$

The error sources which appear during EP testing have been listed and described in other works[2,3,19]. A detailed analysis of the uncertainties associated to each diagnostic has been made. The evaluation of the cross-correlation factors between different error sources cannot be done easily and require detailed computer simulations of the thruster discharge. Any attempt to derive an analytical calculation of these terms would require an oversimplified model. Neglecting the correlations potentially introduces less error than trying to analytically evaluate them. Correlations have therefore been neglected in this study.

4.2 Influence of the background pressure

Vacuum facility's background pressure has been shown to affect Hall thruster discharge and plume properties[1,20]. Test campaigns have occurred with the PPS-Flex, a 1.5 kW Hall thruster designed to vary the magnetic topology in a large extent, and with the PPI-Mag, a 200 W thruster which intends to test magnetic configurations optimized for krypton, see the general introduction of this dissertation. Experiments with the PPS-Flex and PPI-Mag have revealed the prime importance of the residual pressure and of the potential far-field condition imposed by the vessel (usually the ground). This section reports part of the testing that occurred with the PPS-Flex at the PIVOINE-2g facility. Theoretical elements as to the consequences of firing a thruster in a vacuum chamber are given in Appendix B.
The background pressure was modified through a combination of varying the number of active cryopumps and by injecting excess xenon. The xenon port was near the base of the chamber at approximately 1 m downstream of the thruster exit plane. The background pressure level was varied from $4.6{\times}10^{-6}$ mbar-Xe to $5{\times}10^{-5}$ mbar-Xe. The pressure gauge was located on top of the vessel, at about 1 m downstream of the thruster exit plane.

Discharge current

Figure 4.6 portrays the effect of background pressure on the discharge current mean value. The discharge current follows a quadratic law with the logarithm of the background pressure.

Thrust

Apart from the generation of low-velocity ions, the residual pressure of a vessel has a significant impact on the thrust level. The current due to the ionization of the residual gas can be estimated using

$$I_{res} = \frac{1}{4} e n_n v_{th} S, \tag{4.6}$$

where n_n is the neutral density, v_{th} the neutral speed and S the channel section. Assuming the sole presence of singly-charged ions, the increment of thrust ΔT imparted by the

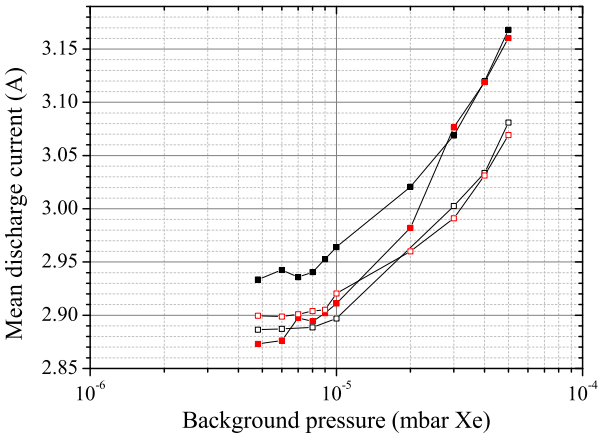

Figure 4.6: Influence of the background pressure on the discharge current mean value, for the PPS-Flex operating at various conditions. The discharge current plateaus below 7×10^{-6} mbar-Xe.

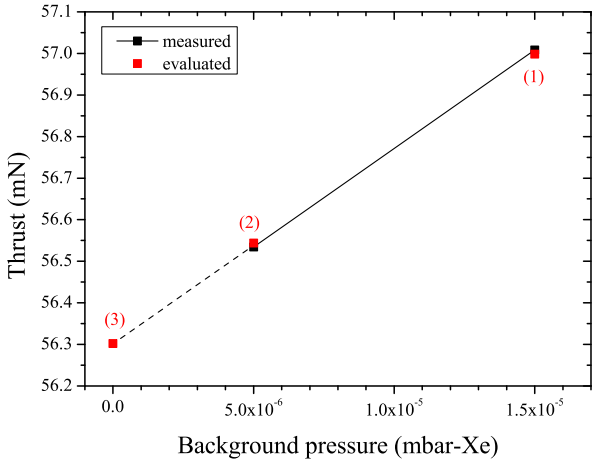

Figure 4.7: Influence of the background pressure on thrust. Relation (4.7) was used to infer the thrust at different pressure levels (red squares) from the measurements (black squares). The thrust measured at 5×10^{-6} mbar-Xe has been extrapolated to that expected at zero background pressure.

residual pressure p_{res} is estimated to

$$\Delta T = \frac{m_n v_i}{e} I_{res} = \frac{m_n v_i v_{th} S}{4kT_n} p_{res}. \tag{4.7}$$

Testing with the PPS-Flex has revealed that equation (4.7) predicts a ΔT in agreement with the thrust measurements at various p_{res}. The thrust developed by the PPS-Flex is shown in figure 4.7 at two different background pressure levels (black squares). The thrust has been estimated at 5×10^{-6} mbar-Xe (respectively at 1.5×10^{-5} mbar-Xe), from that measured at 1.5×10^{-5} mbar-Xe (respectively at 5×10^{-6} mbar-Xe), considering the additional thrust imparted by the residual gas, see the red square labelled (2) (respectively (1)). There is a close match between the measurement and the computation in our operating conditions. The thrust that would result from a null background pressure has been extrapolated, and is labelled (3). It is worth mentioning that the delta between the two extreme values presented in figure 4.7 lies within the thrust stand error bar, which was estimated during the test campaign to be $\pm$ 1.1 mN.

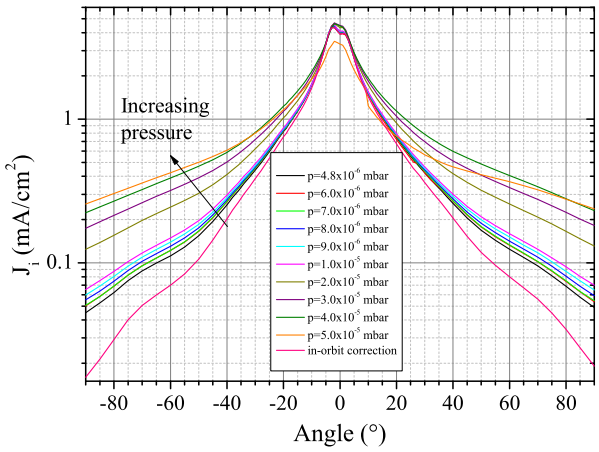

Figure 4.8: Influence of the background pressure on the ion current density, for the PPS-Flex operating at various conditions. Observations similar to Azziz's[21] are made, such as the linear relationship between the ion current density and the background pressure.

Ion current density

The ion current density profile in the plume of the PPS-Flex has been measured at various pressure levels. Figure 4.8 shows that the central hump of the profile remains almost unaffected by the pressure increase, except at 5.10^{-5} mbar-Xe for which the profile appears distorted. The increase in background pressure raises the wings of the current density distribution by 525 %, while the current on the thruster axis is increased by only 14 %. Charge-exchange ions are believed to be the main contributors for the current density amplitude at large angles.
The ion current density has been shown to scale linearly with the pressure level at all angles. This observation is similar to that of Azziz[21], and suggests that this relation does not depend on the thruster, nor the vessel dimensions. Based on this characteristic, the ion current density profile can be extrapolated to zero background pressure: this is the in-orbit condition presented in figure 4.8.

4.3 Computation of the beam divergence half-angle

4.3.1 Definition

We use the notation of figure 4.9, in which the thruster is assumed to be a point source. This representation is commonly used. A more sophisticated approach can be found in the work of Brown[13]. The beam divergence is often defined as a domain which contains 90 % of the ion beam current. This portion of sphere is characterized by two angles that set its boundaries, namely ϕ_{div} and θ_{div}, which are called the ion beam divergence half-angles. While it is not mentioned in any work, every study assumes that

$$\phi_{div} = \theta_{div}, \tag{4.8}$$

even though measurements are made with multiple probes distributed along co-latitudes mounted on a rotating arm moving longitudinally (since usually the ion current along θ is interpolated on the rotating arm angular position vector along ϕ). This assumption appears legitimate, as long as the thruster centerline blends with the vessel axis.

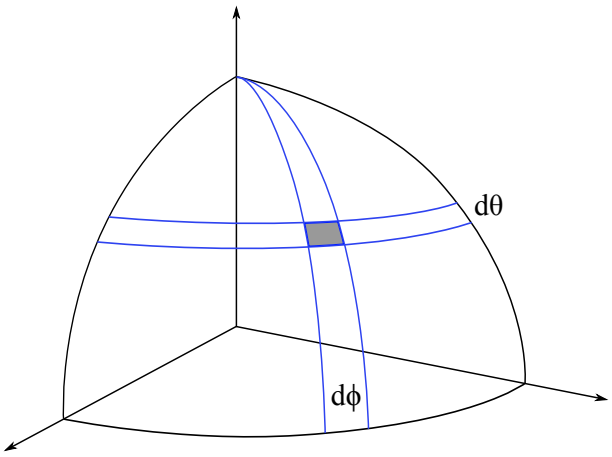

Figure 4.9: Definition of a spherical surface element at a fixed distance from the thruster. The plasma is assumed to originate from a point source.

4.3.2 Some things to beware of

Ion beam current

The ion beam current I_b is equal to the integral of the ion current density j_i over the co-latitude and longitude angles which define an elementary surface, in spherical coordinates, at a fixed distance R

$$I_b = R^2 \int_0^{\pi} \int_0^{\pi} j_i(\theta, \phi) \sin(\theta)\, d\theta d\phi. \tag{4.9}$$

Some studies[22] report only about measurements with a single probe, located on the equatorial plane at $\theta = \pi/2$. A reasoning shortcut is then to consider that j_i must be integrated along a line and not over a surface element, so that equation (4.9) becomes

$$I_b = \pi R^2 \int_0^{\pi} j_i(\phi)\, d\phi. \tag{4.10}$$

This approach can provide coherent results on a physical viewpoint. Yet it is WRONG! Equation (4.10) expresses the integration of the current density over a cylindrical element, which is not a proper coordinate representation of the plume. The Gaussian-like shape of the ion current density profile becomes a cylinder, see figure 4.10. Equation (4.9) must be used in any case, even if a single probe is used. A 2D profile must be constructed assuming symmetry between elevation and inclination: $j_i(\theta, \phi) = j_i^0 j_i(\theta)\, j_i(\phi)$, in which $j_i(\theta) = j_i(\phi)$.

Domain of integration

It is mandatory to integrate j_i over a half-sphere. Some domains are limited to the region of high current density and neglect the profile wings. It is normally not possible to neglect the current densities at large angles in Hall thruster plumes. Table 4.1 shows the consequence of reducing the integration domain on I_b and θ_{div}, for the PPI-Mag operating in xenon, at 200 V and 1.0 $\mathrm{mg/s}$ of anode mass flow rate.

Probe size and angular step

The current density is the ratio of the current collected by the probe to the probe collection area. Since the sheath distribution is unknown, the probe surface is often used

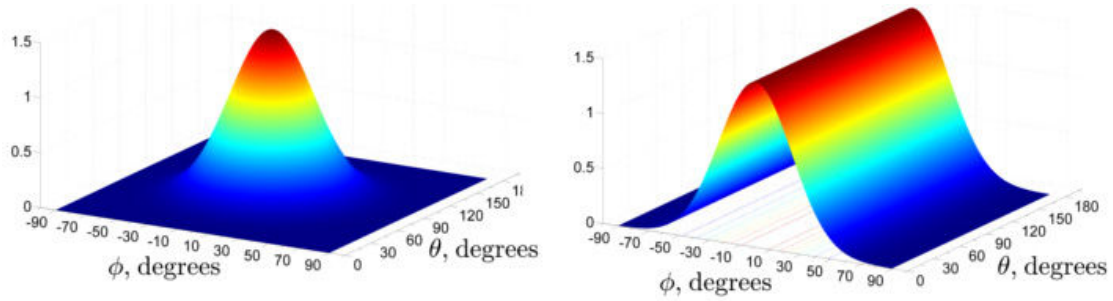

Figure 4.10: Ion current density profiles along θ and ϕ. The change in representation in equation (4.10) assumes the profile to mimic a cylindrical form (right), while the correct profile is somewhat similar to a Gaussian shape (left).

Table 4.1: Diminution in the ion beam current and beam divergence half-angle when shrinking the integration domain of j_i, for the PPI-Mag operating at 200 V and 1.0 $\mathrm{mg/s}$ of xenon. The coverage factor of the reported uncertainty is $k = 1$, providing a confidence level of about 68 %.

	Domain [-90°;90°]×[0°;180°]	**Domain [-60°;60°]×[30°;150°]**
I_b, A	0.493 ± 0.015	0.476 ± 0.015
θ_{div}, °	42 ± 3	37 ± 2

in the literature, instead of the true collection surface. We assume, by this process, that the ion current density is constant on the probe surface, hence small probes are needed to reveal gradients.
This imposes minimal angular steps for the probe distribution and arm rotation. For a cylindrical probe surface with a diameter D,

$$\begin{cases} Rd\theta \geqslant D, \\ R\sin(\theta)\, d\phi \geqslant D. \end{cases} \tag{4.11}$$

Whether these conditions are fulfilled does not modify the result of integral 4.9, but the reasoning is rigorous only if they are. Let us assume that conditions (4.11) are not satisfied. In this case, a fraction of the probe surface covers the same area during two successive measurements, see figure 4.11.2. Since our technique assumes that j_i is constant over the probe surface, $j_i^A = j_i^B$. Thus, $j_i^B = j_i^C$, where C is the next location, and so on for every measurement. In the end, what we assume is that the ion current density is constant everywhere in the plume, which is false of course.

Finally, one must be cautious when designing a rotating arm. Figure 4.11.1 shows that, in order for each probe of a rotating arm to stay within one spherical element at a time, the probe surface must decrease when moving at high co-latitudes, i.e. towards the poles of the domain. On the contrary, the probe diameter tends to increase with the co-latitude angle in most test benches, in order to compensate for the low current that is collected at high angles. This goes against a rigorous determination of j_i (overlapping of the probe) and I_b (integration path).

4.11.1: Surface elements of a spherical domain.

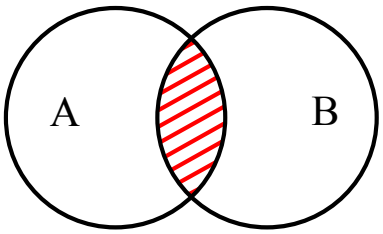

4.11.2: Case in which the angular step is too small.

Figure 4.11: Surface elements of a spherical domain (left). Each probe is supposed to fit inside an element, at every measurement location, which implies to lower the probe diameter at large angles. If condition (4.11) is not met, the probe does not move more than a diameter in between two measurements (right), which implicitely assumes the ion current density to be constant everywhere in the plasma.

4.4 Design and construction of Faraday probes

4.4.1 Faraday probes

This section outlines the process that was followed to design the Faraday probes used for studying the influence of the magnetic barrier extent on the performance of the PPI-Mag, which is described in the introduction. Constraints have been imposed to ensure an adequate design:

- **Probe dimensions.** The probe must be small to mitigate the level of thruster perturbation. Yet, a minimum size is required, in order for the current to be readable by the measurement device (notably at large angles). Finally, the probe must be small enough to reveal gradients while fulfilling conditions (4.11).
  Previous measurements with the PPI operating at nominal operating point have shown that, typically, $j_i^{PPI} = 0.1\ \mathrm{mA.cm^{-2}}$ on the thruster axis, at $R_1 = 70\ \mathrm{cm}$ downstream of the exit plane. Constraints imposed by the vessel size have delimited the probe measurements not farther than $R_2 = 34\ \mathrm{cm}$ downstream of the source. At this distance, the ion flux has been estimated to lie around $j_i^{PPI} R_1^2/R_2^2 \approx 0.4\ \mathrm{mA.cm^{-2}}$. Since currents on the order of magnitude of 100 μA can be measured efficiently, the collector diameter was set to 5.6 mm. It has been checked that the design is compliant with the flux conditions expected off-axis for proper readings.

- **Distance between the collector and the guard ring.** The sheath in front of the collector should be flat and uniform, in order to limit edge effects and deviance from the planar ion collection assumption. The spacing between the two electrodes should therefore be inferior to the sheath size at the measurement location. This gap is 100 $\mu\mathrm{m}$, which equals twice the estimated Debye length in front of the thruster (region of highest plasma density). A kind of worst case scenario has been considered in this budget: the plasma density equals $10^{17}\ \mathrm{m^{-3}}$, and the electron temperature is 5 eV. Off-axis conditions massively depart from these conditions, and make this point open to criticism, see 4.6.3.

- **Material of the probe.** The probe should be made of a conducting material with a high melting point, and a low secondary electron emission coefficient. The lack of experimental data for low energy Xe^+ ion beams makes it difficult to relevantly choose the proper material. Instead, we have decided to make the manufacturing more convenient. Stainless steel and molybdenum materials can be machined using

Figure 4.12: The five Faraday probes that have been characterized in the plume of the PPI-Mag. Four are made of stainless steel. A fifth probe is made of molybdenum (far-right) to evaluate the influence of the probe material on the current that is measured. The guard ring can be removed if necessary, in order to obtain a nude Faraday probe.

standard tools. However, meeting the tolerances imposed on the final dimensions has proven to be a daunting task with our equipment. These two materials have been compared in the plume of the PPI-Mag, see 4.6.5.

- **Potential bias.** The bias must repel all electrons. However, an excessively negative value would modify the potential distribution in the sheath, which in turn would alter ion trajectories in the vicinity of the probe. Such a matter is discussed in 4.6.3.
- **Maintenance operations.** It is mandatory, when designing a product, to allow and specify maintenance operation cycles that ensure a long lifespan. One of the concerns when designing such a diagnostic, composed of tiny inner parts, is to avoid any short-circuit by deposition of sputtered conducting materials. Each probe is composed of small and inexpensive parts made of Teflon, which are to be replaced at regular time intervals to ensure insulation between the two electrodes.

The Faraday probes are shown in figure 4.12. Four probes are made of stainless steel 304, and one of molybdenum. Spare parts for an additional molybdenum probe are available. The guard rings can be removed to obtain nude Faraday probes.

4.4.2 The voltage-follower circuit

Measuring I-V characteristics with a sourcemeter and a Langmuir probe is very simple. Measuring the characteristic of a planar probe equipped with a guard ring, with only one sourcemeter is more intricate since the ring and the collector must be biased simultaneously at exactly the same potential. To this end, I have designed a specific circuit. The diagram is provided in figure 4.13. The sourcemeter is connected directly to the probe collector, but also to the non-inverting input of an OPA454 operational amplifier. The inverting input is connected to the amplifier output to create a follower circuit. Therefore, the guard ring is biased by the sourcemeter, but the current isn't collected by the latter (the input impedance of the amplifier is $10^{13}\ \Omega$, while at our frequency the output is close to $10^2\ \Omega$[23], which insulates the output from the source). Instead, two diodes allow the current to reach the ground for protecting the amplifier. The amplifier is powered by a symmetrical -50/+50 VDC TTI EX752M power supply.
This circuit has a strong transfer function, and low currents (inferior to 0.1 mA) are difficult to measure. Therefore, several measurements with and without the plasma must be made for averaging. The current collected with the plasma off can then be subtracted

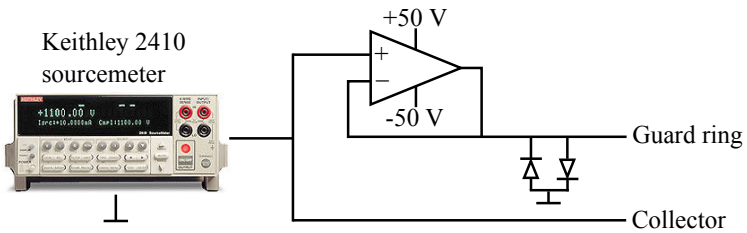

Figure 4.13: Schematics of the voltage follower circuit.

from that with the plasma on. No doubt this circuit can be improved. However, this design has already allowed to observe some of the plasma features, such as the electron energy distribution function isotropy in the far-field plume, see 4.6.8.

4.5 Development of a rotating arm for the NExET vacuum chamber

This section briefly describes the mechanics of the rotating arm and the characteristics of the data acquisition system that I have developed from scratch to perform the measurements presented in 4.6.

4.5.1 Mechanical engineering

The rotating arm designed for NExET is shown in figure 4.14. This rotating arm can be equipped with a maximum of 5 planar probes. However, using Langmuir probes or other devices is possible with a dedicated mechanical interface. The rotating arm and the probes have been designed with respect to the PPI-Mag and vessel characteristics, so that the alignment with the thruster equatorial plane $\theta = \pi/2$ is made automatically. The arm is equipped with different probe holders, which are able to orientate the probes in different directions in the spherical coordinate system:

- The probe located in position 1 collects j_ϕ.
- The probe located in position 2 collects j_θ.
- 2 probes face the thruster (steel- and Mo-made probes can be mounted and tested simultaneously without switching off the thruster). These probes collect the radial flux, j_r, and are located in positions 3 and 4, see figure 4.14.
- The probe located in position 5 collects $j_{-\phi}$.

Notice that the holders are interchangeable, and that they can be put upside down. Such a design allows diverse measurements to be made, within minute, without switching off the thruster and accessing the vessel for modifications.
The angle between to adjacent probes is equal to 15°. All the components of the rotating arm are shown in figure 4.15. A Newport SMC100 rotation stage has been used to move the assembly. The controller has been interfaced with a tailored computer program described in the next paragraph.

4.5.2 Development of the data acquisition system

The current collected by the probes is measured by a sourcemeter Keithley 2410. The collector line is polarized by the sourcemeter, while an external power supply TTI EX752M is used to bias the guard ring of the Faraday probes.

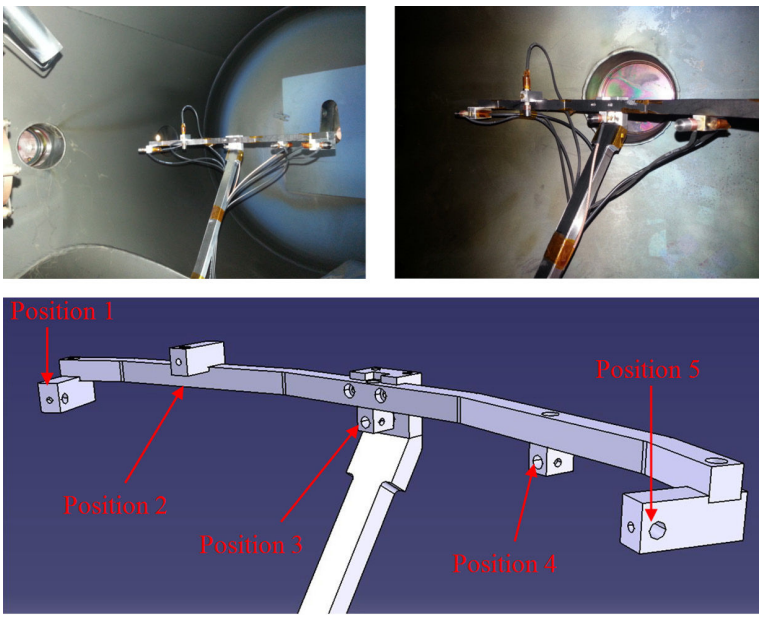

Figure 4.14: Design of the rotating arm for the NExET vacuum chamber. The probes can be oriented in every spherical direction by using the appropriate holder. The arm has been covered with graphite foil to lower secondary electron emission and sputtering yield.

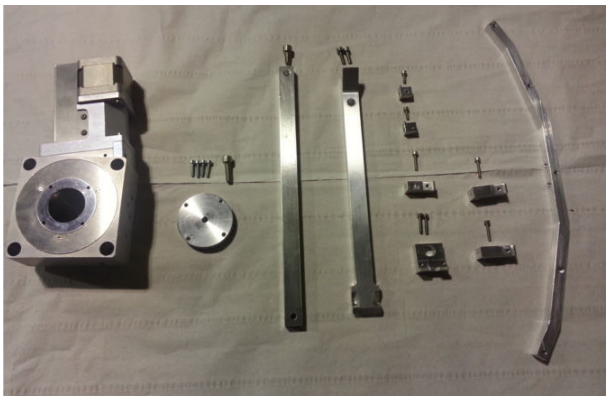

Figure 4.15: Parts that compose the rotating arm. From left to right: rotation stage, mechanical interface, horizontal and angled beams, beam/arch interface and probe holders, arch.

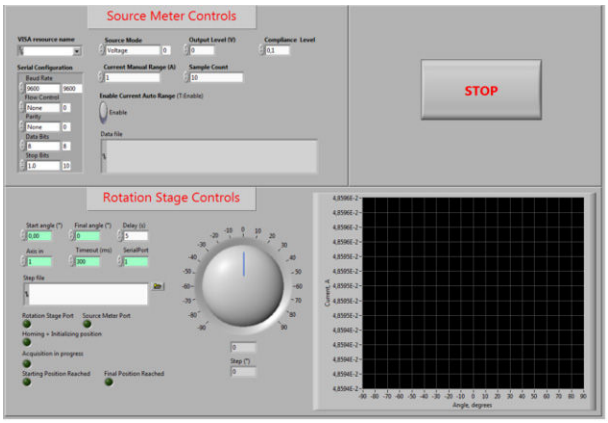

Figure 4.16: Front view of the Labview program for the probe measurements. The program controls the rotation stage and the measurement process, so that both act coherently which each other. The programme creates datafiles for postprocessing.

The sourcemeter has been interfaced with a user-friendly Labview computer program whose front view is shown in figure 4.16. A user manual has been written[24]. This program biases the collector line to the required potential, reads the current measured by the sourcemeter, saves the data and in parallel moves the hardware to the next location. The angular step profile is provided by the user, so that the motion is not constraint in the software and can be adapted to suit one's needs. Several parameters of both the sourcemeter and rotation stage can be changed within the program. A second version has been developed, in which a sweep in potential can be made with the sourcemeter, at each angular position. This version was used to measure Langmuir probe characteristics. Measuring planar probe characteristics is more intricate, since

1. the guard ring and the collector must be biased simultaneously,
2. but that only the collector current is desired,
3. and we have only one sourcemeter (yet perfectly synchronizing two devices would also be intricate).

Therefore, the voltage-follower circuit was designed.

4.6 Measurements in the plume of the PPI-Mag

4.6.1 Test procedures

A standard procedure has been followed for each measurement. The different steps are given in table 4.2. The discharge was deemed stable when the thruster was ignited for more than 30 min, and when the discharge current mean value did not change more than 100 mA during 5 min. Thermal imagery has shown that this criterion corresponds to a ceramic heating rate lower than $1°\mathrm{C/min}$. The anode has been cleaned after each series of experiments, in order to reach reproducible measurement conditions.
The rotation of the arm has always been the same, i.e. the angular steps of each probe has been similar through all the measurements. The angular step profile is given in table 4.3. A Faraday probe measurement from -90°, up to 90°, took approximately 4 min with 10 current measurements at each location. A Langmuir probe scan took about 20 min for scanning the [-30 V;10 V] range at all the positions. The probe distance from the thruster inner pole is constant and equal to 34 cm.

Table 4.2: Standard procedure for the probe measurements in the plume of the PPI-Mag. The discharge was deemed stable when the thruster was ignited for more than 30 min, and when the discharge current mean value did not change more than 100 mA during 5 min. Thermal imagery has shown that this criterion corresponds to a ceramic heating rate lower than $1°\mathrm{C/min}$.

Step	Duration	Description
1	T_0-15 min	cathode heating
2	T_0	thruster ignition, $U_d = 200$ V ; $\phi_a = 1.0$ $\mathrm{mg/s}$
3	T_0+15 min	Setting of the first operating point
4	T_0+30 min	Waiting for the discharge current to stabilize at least 5 min
5	to be adapted	measurement
6	to be adapted	set the next operating point
7	to be adapted	wait for stabilization
8	to be adapted	measurement
9	to be adapted	repeat steps 6 to 8 if necessary

Table 4.3: Rotation step profile for the probe measurements, as a function of the probe angular position. The position 0° corresponds to the thruster centerline. The step is small near the thruster axis to resolve gradients. It has been increased when moving away from the central position in order to keep the measurement time small.

Position	Angular step
-90° → -40°	5°
-40° → -20°	2°
-20° → 20°	1°
20° → 40°	2°
40° → 90°	5°

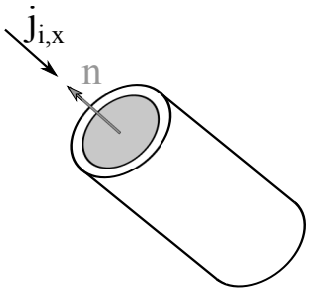

Figure 4.17: Illustration of the directional collection of a Faraday probe.

4.6.2 Computation of physical quantities

This subsection defines some of the quantities that will be used in the following of this chapter, as well as in Chapter 5.

Ion properties

The collection of a current I, by a planar Faraday probe with a collector surface S, whose normal $\mathbf{n}$ is oriented towards $-\mathbf{x}$, allows the determination of the local ion current density $j_{i,x}$

$$j_{i,x} = \frac{I}{S}. \tag{4.12}$$

The ion beam current is computed according to equation (4.9). This quantity allows the computation of the ion current fraction ξ_i, i.e. the fraction of discharge current I_d that comes from the ion contribution, and the ionization efficiency η_i, also termed propellant utilization

$$\xi_i = \frac{I_b}{I_d}, \tag{4.13}$$

$$\eta_i = \frac{m_i I_b}{e\phi_a}, \tag{4.14}$$

where m_i is the ion mass and e the elementary charge. In this work, the discharge is assumed to be composed of singly-charged ions only, so that the raw ion current density profile can be integrated to yield I_b. An E×B probe could be used in order to compensate for multiply-charged species, but the measurement becomes requiring, since the probe needs to rotate around its collimator along two angles in order to compute the local Xe^{n+} fraction. Therefore, the ion current density is overestimated, as Xe^{n+}, $n > 1$, are present in the plume.

Electron properties

The potential sweep of an electrostatic probe allows the computation of several plasma quantities:

- **Plasma potential, V_p.** The plasma potential corresponds to the inflexion point on the I-V characteristic
$$V_p = V\left(\max\left(\frac{dI}{dV}\right)\right). \tag{4.15}$$

- **EEDF, f.** The Electron Energy Distribution Function (EEDF) can be computed from the I-V characteristic. For any probe of convex shape, the EEDF is proportional to the second derivative of the electron current I_e
$$f(\varepsilon) = \frac{2\sqrt{2m_e\varepsilon}}{e^3 S}\frac{d^2 I_e}{dV^2}, \tag{4.16}$$
where ε is the electron energy $e(V_p - V)$, S is the probe surface and m_e is the electron mass. Relation (4.16) is valid for any isotropic distribution. The computation of the second derivative is possible, but difficult. In anisotropic conditions, the EEDF along a direction x can be computed from a planar probe characteristic, which only requires the computation of the first derivative of the electron current[25]
$$f_x(\varepsilon) = \frac{1}{e^3 S}\sqrt{\frac{m_e}{2\varepsilon}}\frac{dI_e}{dV}. \tag{4.17}$$
A deconvolution process must then be made to isolate the beam contribution from the isotropic background, using equation (4.16). The main issue is to properly extract I_e from the total current of the I-V curve. Several techniques can be used, like OML, ABR…[25] Since the precise determination of the electron properties is not crucial in the frame of this research, we have chosen the simplest approach, which is to assume that the ion current that is collected is constant far below the floating potential.

- **Electron density and temperature.** The plasma density and electron temperature can be inferred from the EEDF
$$\begin{cases} n_e = \int f(\varepsilon)d\varepsilon, \\ T_e = \dfrac{2k_B}{3n_e}\int \varepsilon f(\varepsilon)d\varepsilon, \end{cases} \tag{4.18}$$
where k_B is the Boltzmann constant.

- **Debye length.** These quantities can then be used to infer the plasma Debye length
$$\lambda_D = \sqrt{\frac{ek_B T_e}{n_e e^2}}. \tag{4.19}$$

Performance

Several performance indicators can be deduced from the Faraday and Langmuir probe measurements.

- **Thrust** The thrust T depends on the ion mass flow rate ϕ_i and on the ion velocity v_i. The ion velocity cannot be known exactly without LIF or RPA measurements (we have measured the plasma potential in the far-field with a Langmuir probe, which can be used to obtain the local ion velocity from a RPA acquisition). An estimate can be obtained, considering that the maximum velocity theoretically achievable by the ions is governed by the discharge voltage U_d, the cathode potential relative to the ground V_{CRP}, the far-field plasma potential $V_{p,\infty}$ and ionization losses E_i. This seems to be a reasonable assumption considering that the Langmuir probe measurements have been made 34 cm downstream of the PPI-Mag exit plane, where the electric and magnetic fields have vanished. Thus, the thrust can be written

$$T = \phi_i v_i = \frac{m_i I_b}{e}\sqrt{\frac{2e\left(U_d - |V_{CRP}| - V_{p,\infty} - E_i\right)}{m_i}}. \tag{4.20}$$

  Note however that this expression must be taken with great care, since it does not consider a distribution of the ion velocity vector. The interpretation must therefore be criticized.

- **Acceleration efficiency** The acceleration efficiency is the ratio of the kinetic energy to the electric energy

$$\eta_{acc} = \frac{U_d - |V_{CRP}| - V_{p,\infty} - E_i}{U_d} \tag{4.21}$$

- **Anode efficiency** The anode efficiency η_a is determined from the thrust and the discharge current mean value

$$\eta_a = \frac{T^2}{2\phi_a U_d I_d} \tag{4.22}$$

- **Divergence angle** The determination of the beam divergence half-angle has been detailed in section 4.3.

4.6.3 I-V characteristics

A few I-V characteristics have been acquired "manually", i.e. by varying the guard ring bias by hand for each measurement point. The I-V curve of the molybdenum probe, placed in position 1, and equipped with its guard ring, is presented in figure 4.18.1, at 5 different angles with respect to the thruster axis. The PPI-Mag was fired at 200 V and 1.0 $\mathrm{mg/s}$ of xenon. As discussed in 4.6.5, there is no clear difference between the stainless steel and molybdenum probe measurements, even in front of the thruster where the ion energy is the highest, meaning that the probe material does not significantly contribute to the outcome, at least at low ion energy. The conclusions of this paragraph are thus thought not to depend on the probe material.
It is interesting to note that the current does not saturate below a few tens of volt, which should occur given the probe design. It is believed that the sheath might extend so far around the collector that it eventually encompasses the entire probe, diverting ion trajectories and collecting current from other directions than the probe normal. This effect would

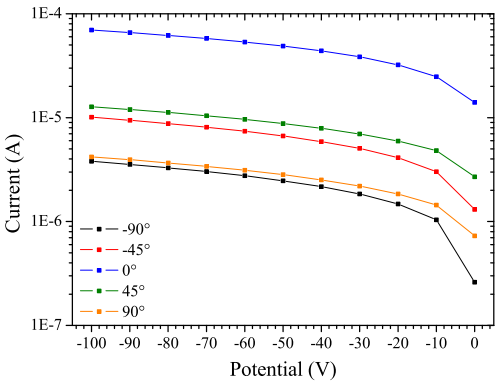

4.18.1: I-V characteristic of the molybdenum probe.

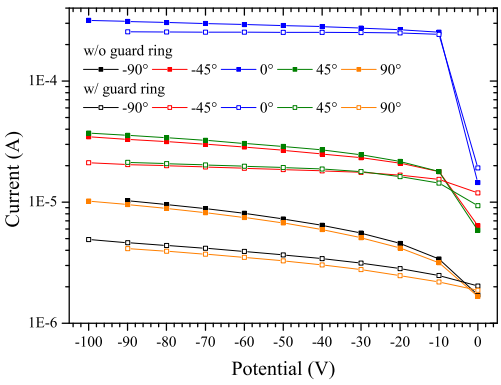

4.18.2: I-V characteristics of nude and guarded Faraday probes.

Figure 4.18: I-V characteristics of the guarded molybdenum probe, perpendicular to the beam (left), and of the stainless steel nude and guarded Faraday probes which face the thruster (right). The PPI-Mag was fired at 200 V and 1.0 $\mathrm{mg/s}$ of xenon.

increase with the probe voltage and angle with respect to the thruster axis, in agreement with figure 4.18.1. This picture is supported by the Debye length amplitude, see 4.6.8.

The I-V characteristics of the stainless steel probes located in positions 3 and 4 (the probes face the thruster) have also been acquired with the same thruster and measurement parameters, and are presented in figure 4.18.2. The probe located in position 3 is nude (without its guard ring), while the other is guarded. The current collected by the nude probe follows the same trend than that in position 1, possibly for similar reasons. The level of current is that expected in the simple approach of section 4.4. The current of the guarded probe saturates rapidly when it is placed on the thruster axis, which validates the guard ring design. The sheath topology is probably planar, and it extends along the collector surface normal vector without altering ions passing close by. The level of the saturation however decreases when moving away from the thruster centerline. This suggests that the probe design is not optimized anymore at these locations. The basic designing rule reported in section 4.4 was valid on the thruster axis. Since the plasma parameters have changed at large angles, the probe design should be reassessed. In order to limit the error level, the bias potential has been set to -30 V for the angular scans in the [-90°;+90°] interval.

This leads to the important conclusion that a guarded Faraday probe, and by extension any electrostatic probe, is designed and optimized for specific plasma parameters. Therefore, rotating arms that are used to infer the beam divergence half-angle, a key figure for the thruster manufacturer and for the satellite prime, must be equipped with many probes that are suitable for the local plasma characteristics. Ultimately, each surface element of figure 4.11.1 must contain a dedicated probe. This approach suffers two drawbacks. Firstly, the plasma parameters must be known prior to undertake the measurement. This problem is encountered with Langmuir probes, whose collection theory depends on the probe size with respect to the Debye length. Secondly, such an assembly is inconceivable, since it would result in large sputtering. This additional matter would contribute to the discharge, therefore perturbing the thruster behavior, and change the thruster environment considerably.

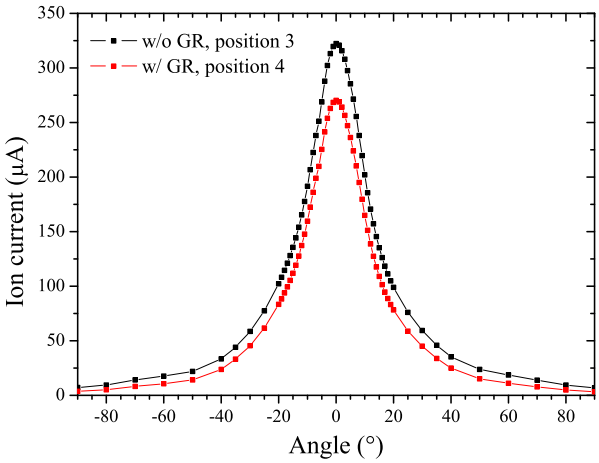

Figure 4.19: Influence of the guard ring on the current collected by nude and guarded probes.

Table 4.4: Influence of the guard ring on the thruster performance at nominal operating point ($U_d = 200$ V, $\phi_a = 1.0$ mg/s). The performance level is greatly influenced by the presence of the guard ring. The coverage factor of the reported uncertainty is $k = 1$, thus a confidence level of about 68 %.

	Guarded Faraday probe	**Nude Faraday probe**
I_b, A	0.46 ± 0.014	0.61 ± 0.019
ξ_i	0.51 ± 0.016	0.68 ± 0.021
η_i	0.63 ± 0.020	0.83 ± 0.026
θ_{div}	49 ± 3	55 ± 3

4.6.4 Influence of the guard ring

Aside from the I-V curve, the impact of the guard ring on the current profile can be assessed during a full angular sweep (i.e. which follows the motion step profile described in table 4.3). The current distribution is shown in the plume of the PPI-Mag at standard operating point in figure 4.19. The measurements have been made with the nude and guarded probes characterized in the previous subsection.
While the influence of the guard ring is obvious, and that the conclusion may seem straightforward, figure 4.19 highlights a serious and unresolved matter: how to determine the ion current density of the nude probe? The increase in current collected by the nude probe likely originates from the sheath distribution. Since the true collection area cannot be known without resorting to computer simulations, the ion current density is deduced by dividing the current from both probes by the same surface, which is that of the collector front. This is one of the reasons for the computation of ion beam currents that often exceed the discharge current[21].

The ion beam current, the ion current fraction, the ionization efficiency and the beam divergence half-angle have been computed with the nude and guarded Faraday probe profiles. The results are presented in table 4.4. Clearly the probe design impacts the performance level that is deduced from the measurements. More results have been inferred from the 2015 test campaign with the PPS-Flex[26].

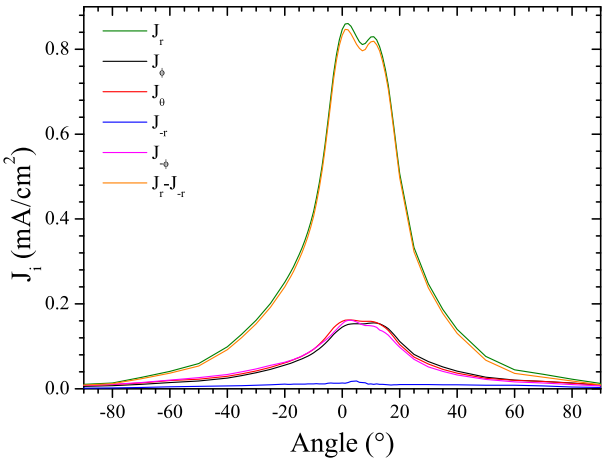

Figure 4.20: Components of current in the plume of the PPI-Mag. The components of current perpendicular to the beam are isotropic. A non-zero current is shown to exist in a direction opposite to the jet, which limits the performance level.

4.6.5 Probe material

The influence of the probe material is discussed in figures 5.9.1 and 5.9.2. There is no clear difference between the ion current density profiles obtained with stainless steel and molybdenum probes. It is believed that the ion beam energy may be below the secondary electron emission threshold. These measurements should be repeated with a larger thruster, in the class of a few kW.

4.6.6 Current components in the plume

Various current components have been measured in the plume of the PPI-Mag with the guarded stainless steel probes. Ion currents I_r, I_θ and I_ϕ have been measured, then the probes have been oriented to end the measurement series. The thruster has been operated at 150, 200 and 250 V ; 1.0 $\mathrm{mg/s}$ of xenon flow rate, and 0.8, 1.0 and 1.2 $\mathrm{mg/s}$; 200 V. Similar features have been observed at each operating point. Figure 4.20 presents the ion current density components. As expected, the probe which faces the thruster collects more current than the others. The probes perpendicular to the beam reveal a similar current profile, the small deviances between the measurements being probably linked to uncertainties in probe alignment. The probe oriented along the beam collects a current density close to 0.01 $\mathrm{mA.cm^{-2}}$. This contribution is thermal, and does not participate in the thruster performance. The performance can be obtained through the resulting ion current density (in orange). The impact of the probe wake could be assessed for further understanding the origin of this thermal component.

The influence of the thermal component on the thruster performance is presented in table 4.5. The performance has been assessed by subtracting the thermal ion current density profile from that measured in front of the thruster. The current components perpendicular to the beam compensate each other and do not contribute to the overall performance. The thermal component decreases the ion current by 4 %, the ion current fraction by 6 %, the ionization efficiency and the thrust by 5 % and the anode efficiency by 10 %. The impact is clear on the PPI-Mag. It should also be evaluated on a larger thruster.

Table 4.5: Influence of the thermal current on the thruster performance at nominal operating point ($U_d = 200$ V, $\phi_a = 1.0$ mg/s). The performance decreases when the thermal current is subtracted from the profile of the probe which faces the thruster. The coverage factor of the reported uncertainty is $k = 1$, providing a confidence level of about 68 %.

	$\mathbf{U_d} = 200$ V						$\phi_a = 1.0$ mg/s			
	$\phi_a = 0.8$ mg/s		$\phi_a = 1.0$ mg/s		$\phi_a = 1.2$ mg/s		$\mathbf{U_d} = 150$ V		$\mathbf{U_d} = 250$ V	
	j_r	$j_r - j_{-r}$	j_r	$j_r - j_{-r}$	j_r	$j_r - j_{-r}$	j_r	$j_r - j_{-r}$	j_r	$j_r - j_{-r}$
I_b, A	0.41 ± 0.013	0.39 ± 0.012	0.54 ± 0.017	0.52 ± 0.016	0.72 ± 0.023	0.71 ± 0.022	0.56 ± 0.018	0.53 ± 0.017	0.54 ± 0.017	0.52 ± 0.016
ξ_i	0.57 ± 0.018	0.55 ± 0.017	0.48 ± 0.015	0.45 ± 0.014	0.50 ± 0.016	0.49 ± 0.015	0.56 ± 0.018	0.53 ± 0.017	0.48 ± 0.015	0.45 ± 0.014
η_i	0.70 ± 0.022	0.67 ± 0.021	0.74 ± 0.023	0.70 ± 0.022	0.81 ± 0.025	0.80 ± 0.025	0.76 ± 0.024	0.71 ± 0.022	0.74 ± 0.023	0.70 ± 0.022
θ_{div}, °	48 ± 3	48 ± 3	50 ± 3	48 ± 3	49 ± 3	49 ± 3	57 ± 3	56 ± 3	50 ± 3	48 ± 3
F, mN	8.9 ± 0.28	8.5 ± 0.27	11.7 ± 0.37	11.1 ± 0.35	15.3 ± 0.48	15.1 ± 0.48	9.9 ± 0.31	9.3 ± 0.29	11.7 ± 0.37	11.1 ± 0.35
η_a	0.34 ± 0.020	0.32 ± 0.021	0.30 ± 0.019	0.27 ± 0.017	0.34 ± 0.021	0.33 ± 0.021	0.33 ± 0.021	0.29 ± 0.018	0.30 ± 0.019	0.27 ± 0.017

Table 4.6: Ion plume properties at R_1 and R_2. The current is conserved between these locations, but the beam divergence increases. The coverage factor of the reported uncertainty is $k = 1$, providing a confidence level of about 68 %.

	$\mathbf{U_d} = 200$ V						$\phi_a = 1.0$ mg/s			
	$\phi_a = 0.8$ mg/s		$\phi_a = 1.0$ mg/s		$\phi_a = 1.2$ mg/s		$\mathbf{U_d} = 150$ V		$\mathbf{U_d} = 250$ V	
	R_1	R_2	R_1	R_2	R_1	R_2	R_1	R_2	R_1	R_2
I_b, A	0.33 ± 0.010	0.33 ± 0.010	0.45 ± 0.014	0.46 ± 0.014	0.57 ± 0.018	0.58 ± 0.018	0.44 ± 0.014	0.43 ± 0.013	0.46 ± 0.014	0.47 ± 0.015
ξ_i	0.52 ± 0.016	0.53 ± 0.017	0.53 ± 0.017	0.54 ± 0.017	0.53 ± 0.017	0.53 ± 0.017	0.53 ± 0.017	0.53 ± 0.017	0.50 ± 0.016	0.51 ± 0.016
η_i	0.56 ± 0.018	0.57 ± 0.018	0.62 ± 0.019	0.62 ± 0.019	0.64 ± 0.020	0.65 ± 0.020	0.59 ± 0.018	0.59 ± 0.018	0.63 ± 0.020	0.64 ± 0.020
θ_{div}, °	47 ± 3	50 ± 3	43 ± 3	47 ± 3	41 ± 2	45 ± 3	56 ± 3	58 ± 3	47 ± 3	50 ± 3

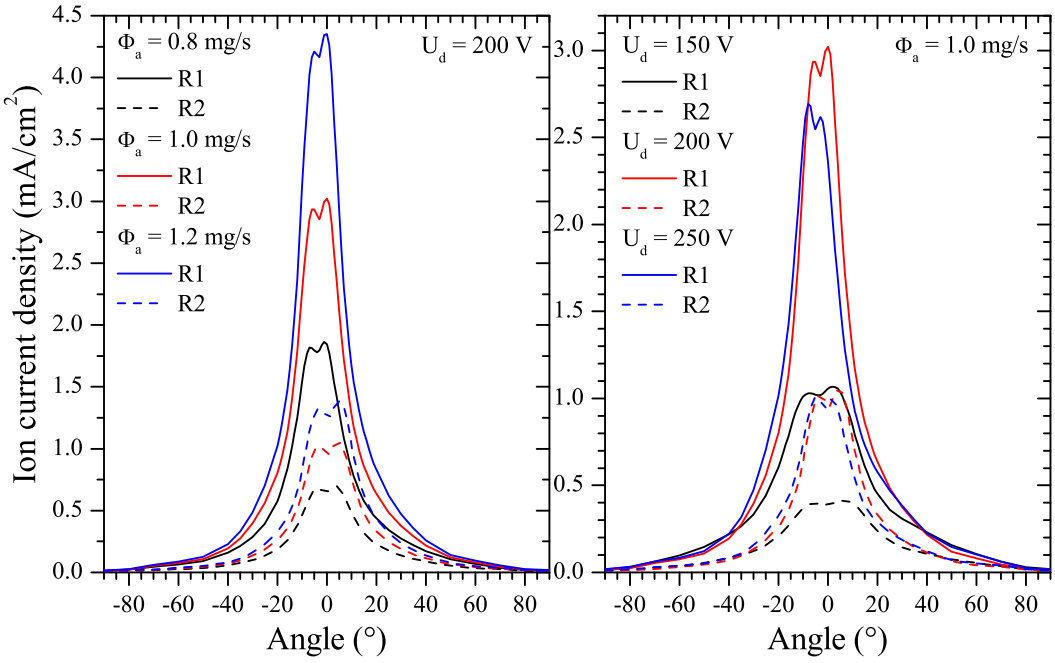

Figure 4.21: Ion current density distributions at $R_1 = 22.8$ cm and $R_2 = 34$ cm downstream of the PPI-Mag exit plane. The thruster operates at various operating points. Similar shapes in ion current density profiles are observed.

4.6.7 Conservation of current

The ion beam current deduced from Faraday measurements may exceed the discharge current, which is non-physical. Due to the large collision mean-free paths, the plume of Hall thrusters is considered mostly collisionless. Charge-exchange collisions are known to occur though[27]. The assumption of ion current conservation throughout the expanding jet is always made, but never demonstrated. The rotating arm has been modified in order to position a guarded stainless steel probe at $R_1 = 22.8$ cm from the thruster inner pole (6 times the mean diameter of the channel), while a similar probe is placed at $R_2 = 34$ cm from the inner pole (9 times the channel mean diameter).
The I-V characteristic of the probe placed at R_1 has been measured at 150, 200 and 250 V ; 1.0 mg/s of xenon flow rate, and 0.8, 1.0 and 1.2 mg/s ; 200 V. The ion branch has been found to saturate at -20 V. Therefore, the potential bias used for the previous measurements, -30 V, has been applied to this probe.
The angular distributions of the ion current density are shown in figure 4.21, at various operating points of the PPI-Mag. It is no surprise that the ion current density increases with the discharge voltage and the anode mass flow rate. It is however surprising to observe similar shapes between R_1 and R_2, such as the central double hump.

Some integral quantities of the discharge are given in table 4.6. The ion current is conserved in our operating conditions (background pressure, electric reference) between R_1 and R_2. However, the ion beam divergence angle increases. Two reasons may be invoked:

1. The potential distribution of the plume is likely to cause radial electric fields that accelerate ions towards the facility walls.

2. Since the vessel is grounded, a radial electric field exists and accelerates ions accordingly.

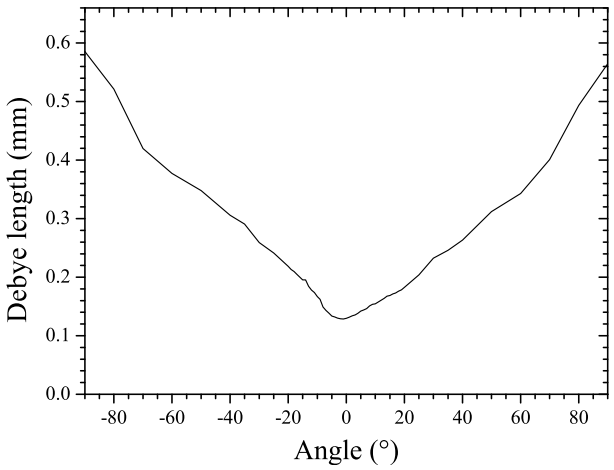

Figure 4.22: Angular profile of the Debye length at 34 cm downstream of the PPI-Mag operating at nominal operating point. The Debye length on the thruster axis is close to that evaluated during the probe development stage, and justifies the design.

4.6.8 Electron properties

Langmuir probe measurements

The electron properties have been measured at 34 cm away from the thruster exit plane. The probe tip is made of a 5 mm long, 0.8 mm in diameter pure tantale wire, inserted into a 2 mm in diameter alumina tube. The core of a 50 Ω coaxial cable is connected to the tantale wire with a terminal block. The connection is insulated with kapton. The cable is 3 m long. The probe tip has shown no sign of ablation during testing. The potential has been swept from -10 V to 10 V to yield the I-V characteristic.

The angular profile of the Debye length is shown in figure 4.22 at the PPI-Mag nominal operating point. The estimate of the Debye length given in 4.4 is close to that effectively computed, on the thruster axis. This is why the ion branch saturates quickly on the thruster centerline in figure 4.18.2. The Debye length is found to increase when going off-axis, owing to the decrease in plasma density. As previously explained, the conditions for a proper operation of the Faraday probes are not met at large angles.

Faraday probe measurements

The purpose of the voltage-follower circuit presented in figure 4.13 is to access the electron energy distribution function with a guarded Faraday probe. A potential sweep waveform is generated by the sourcemeter, and the current collected by the collector electrode is measured. First, the circuit must be validated. Figures 4.23.1 and 4.23.2 show the I-V characteristics of a guarded stainless steel probe at three angular positions, in the plume of the PPI-Mag at nominal operating point. A few points have been measured manually, that is by adjusting the guard ring bias with an external power supply (square symbols), without the circuit. The sweep potential step is 0.2 V for the measurements with the voltage-follower apparatus, which results in the continuous lines. This circuitry is able to retrieve the characteristics that are measured "by hand". Limitations of the amplifier make the ion saturation branch noisy, but the mean current value agrees with the characteristic measured without the circuit. Enhancing the system performance is only a matter of changing the amplifier, and internally switching from one calibre to the other during an acquisition.

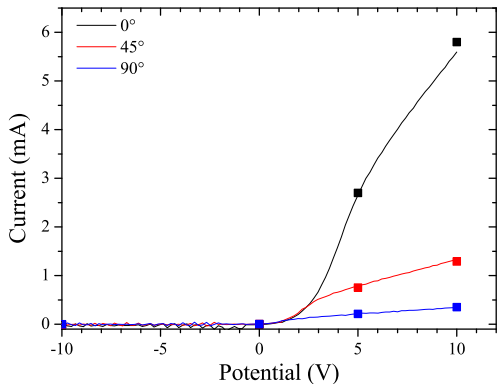

4.23.1: I-V characteristics measured with the voltage-follower circuit.

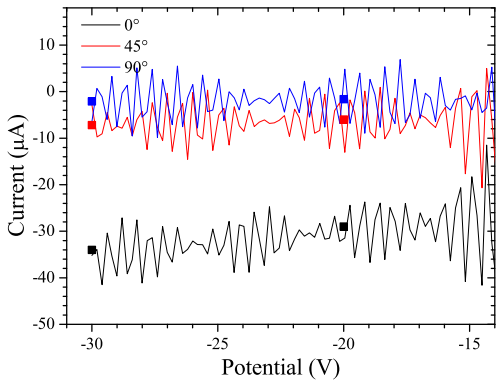

4.23.2: Focus on the ion branch of the I-V characteristic.

Figure 4.23: Faraday probe I-V characteristics measured with the voltage-follower circuit, at the PPI-Mag nominal operating point. The position 0° blends with the thruster axis. The voltage-follower apparatus is able to reproduce the I-V curve measured "by hand" (squares), i.e. without the circuit. The ion saturation branch measured by the voltage-follower circuit appears noisy (notice the current is approximately 100 times lower in this region of the characteristic compared to that in the electron saturation branch). The amplifier could be replaced for this portion of the curve, but the current mean value seems to agree with the manual measurements.

The electron energy distributions along the radial, inclination (θ) and elevation (ϕ) directions have been computed using equation (4.17), at the PPI-Mag nominal operating point. Figure 4.24 shows the that electron energy is maximum on the thruster axis, that the EEDF is isotropic in the far-field plume, and that every distribution is composed of a bump, whose energy depends on the angular position of the probe. Assessing whether this peak is artificially generated by the circuit, or is a physical electron population, is out the scope of this research and will be treated in another work at ICARE.

4.7 Conclusions

A summary of the measurement uncertainties that arise when using Faraday, Langmuir, RPA and E×B probes has been made. More details about the quantitative evaluation of some of the errors has been made during a test campaign with the PPS-Flex at EPL. The measurement procedures that must be followed to infer the uncertainties and the results have been presented in several technical notes[2,3,19].

The influence of the background pressure has been assessed with the PPS-Flex, and a small part of the results has been reported in this chapter. However, a much more detailed analysis has been made, but is excluded from this dissertation for confidentiality reasons. Additionally, elements for properly determining the beam divergence half-angle have been presented.

Based on these preliminaries, the plume of the PPI-Mag has been diagnosed with tailored Faraday probes, a unique rotating arm design and a dedicated computer interface. An electronic circuit has been proposed to go into further analysis. These developments are important for the EP team at ICARE, since a novel and flexible diagnostic apparatus is available for plume studies. This system has been shown to operate as expected.

Among the most important results, the currents perpendicular to the beam do not seem to play any role in the thruster performance, but a thermal component that does impact the performance has been shown to exist along the beam direction. The ion current conservation assumption, which is usually made but never demonstrated, has been verified. The

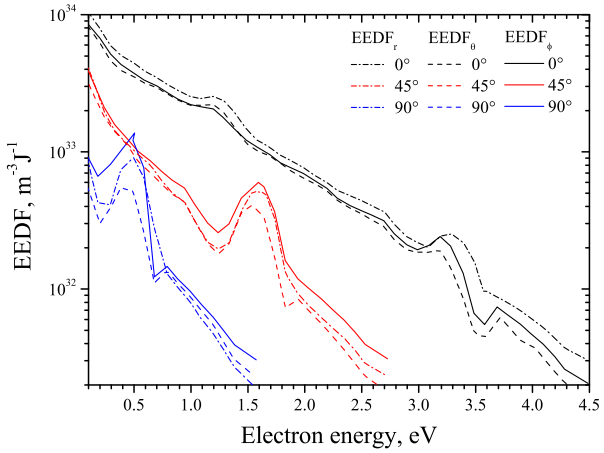

Figure 4.24: The electron energy distribution functions along the radial, inclination (θ) and elevation (ϕ) directions, measured in the plume of the PPI-Mag by means of three guarded stainless steel Faraday probes. The measurements have been performed at 3 angular positions, and show the isotropy of the EEDF in the far-field.

plume characterization using Faraday probes is simple and first order. More precisely, a detailed test campaign must be dedicated to studying the influence of the probe geometry on the performance that is inferred.

This study was preliminary to the characterization of the PPI-Mag, which has been developed to study the influence of the magnetic barrier extent on the thruster performance. This is a part of the magnetic topology activities that I have been involved into during my research, which are now being described in Chapter 5.

References

[1] K.D. Diamant, R. Liang and R.L. Corey. The effect of background pressure on SPT-100 Hall thruster performance. In proceedings of the 50th AIAA/ASME/SAE/ASEE Joint Propulsion Conference, 28-30 July 2014, Cleveland, Ohio, USA, AIAA-2014-3710, 2014.

[2] J. Vaudolon and S. Mazouffre. Description of electric propulsion diagnostic tools used for qualification testing, error sources and possible calibration techniques. Technical report, PE-R-03-2014, ICARE, CNRS, 2014.

[3] J. Vaudolon and S. Mazouffre. Test procedures for determining the uncertainty budgets when using electric propulsion diagnostic tools during qualification testing. Technical report, PE-R-04-2014, ICARE, CNRS, 2014.

[4] J. Vaudolon and S. Mazouffre. Influence de la topologie magnétique et des conditions expérimentales sur les performances du propulseur PPS-FLEX. Technical report, PE-R-02-2014, ICARE, CNRS, 2014.

[5] C. Bohm and J. Perrin. Retarding-field analyzer for measurements of ion energy distributions and secondary electron emission coefficients in low-pressure radio frequency discharges. *Rev. Sci. Instrum.*, 64(1), 1993.

[6] S. Mazouffre et al. Calibration of a RPA by means of LIF: feasibility study. Technical report, PE-R-07-2011, ICARE, CNRS, 2011.

[7] F. F. Chen. *Introduction to plasma physics*. Plenum, New York, 1976.

[8] I. H. Hutchinson. *Principles of plasma diagnostics*. Cambridge University Press, New York, 1987.

[9] P. L Chung, L.Talbot, K. J. Touryan. *Electric probes in stationary and flowing plasma*. Berlin, 1975.

[10] V. I. Demidov, S. V. Ratynskaia, K. Rypdal. Electric probe for plasmas: The link between theory and instrument. *Rev. Sci. Instrum.*, 73(3409), 2002.

[11] M. A. Lieberman, A. J. Lichtenberg. *Principles of plasma discharges and materials processing*. John Wiely & Sons, New York, 1994.

[12] V. E. Golant, A. P. Zhilinski, S. A. Sakharov. *Fundamentals of plasma physics*. Wiley, New York, 1980.

[13] D.L. Brown. *Investigation of low discharge voltage Hall thruster characteristics and evaluation of loss mechanisms*. PhD thesis, University of Michigan, 2009.

[14] J.L. Rovey, M.L.R. Walker, A.D. Gallimore and P.Y. Peterson. Magnetically filtered Faraday probe for measuring the ion current density profile of a Hall thruster. *Rev. Sci. Instrum.*, 77(013503), 2006.

[15] M.L.R. Walker, R.R. Hofer and A.D. Gallimore. The Effects of Nude Faraday Probe Design and Vacuum Facility Backpressure on the Measured Ion Current Density Profile of Hall Thruster Plumes. In proceedings of the 38th AIAA/ASME/SAE/ASEE Joint Propulsion Conference & Exhibit, 7-10 July 2002, Indianapolis, Indiana, USA, 2002.

[16] S.W. Kim. *Experimental investigation of plasma parameters and species-dependent ion energy distribution in the plasma exhaust plume of a Hall thruster*. PhD thesis, University of Michigan, 1999.

[17] D. Renaud, S. Mazouffre and A. Aanesland. Plasma composition and ion acceleration in the PEGASES thruster. In proceedings of the 4th Space Propulsion Conference, Cologne, Germany, paper 2969109, 2014.

[18] R. Blott, S. Gabriel and D. Robinson. Draft Handbook for Electric Propulsion Verification by Test. Technical report, SEP/ESA/P05401000591/2012, ESA, 2012.

[19] J. Vaudolon and S. Mazouffre. Data and performance analysis of EPL diagnostic tools for their use in qualification testing. Technical report, PE-R-10-2014, ICARE, CNRS, 2014.

[20] W. Huang, H. Kamhawi and T. Haag. Effect of background pressure on the performance and plume of the HiVHAc Hall thruster. In proceedings of the 33rd Internation Electric Propulsion Conference, Washington, D.C., USA, IEPC-2013-058, 2013.

[21] Y. Azziz. *Experimental and Theoretical Characterization of a Hall Thruster Plume*. PhD thesis, Massachussetts Institute of Technology, 2007.

[22] D.L. Brown and A.D. Gallimore. Evaluation of plume divergence and facility effects on far-field faraday probe current density profiles. In proceedings of the 31st Internation Electric Propulsion Conference, Ann Arbor, Michigan, USA, IEPC-2009-030, 2009.

[23] Texas Instruments. OPA454 datasheet. Technical report, Texas Instruments, 2008.

[24] J. Vaudolon. NExET rotating arm and data acquisition system user's manual. Technical report, ICARE, CNRS, 2015.

[25] *Plasmas froids: Génération, caractérisation et technologies*. Université de Saint-Etienne, 2004.

[26] J. Vaudolon and S. Mazouffre. Optimisation de la topologie du PPS-FLEX en mode sans-parois - influence de la géométrie d'une sonde de Faraday sur le courant mesuré et les grandeurs déduites. Technical report, PE-2015, ICARE, CNRS, 2015.

[27] J. Vaudolon, S. Mazouffre, D. Harribey, C. Henaux, A. Rossi. Influence de la topologie magnétique et des conditions expérimentales sur les performances du propulseur PPS-FLEX. Technical report, PE-R-02-2014, ICARE, CNRS, 2014.

Chapter 5

Influence of the magnetic topology on the performance of Hall thrusters[1]

Contents

THE magnetic structure of a conventional Hall thruster comprises two main elements: a series of coils or magnets to produce the magnetic flux, and a conducting circuit to guide the flux and to shape the B field. The circuit, which is made of a ferromagnetic material like iron or iron-cobalt alloy, has typically two pole pieces. Magnetic screens can be added if necessary. The usual configuration is composed of one central coil, and coils around the outer channel wall. The two parts are not necessarily electrically connected in series. With a standard configuration, the B field is the highest at the channel exhaust with a positive gradient inside the channel, when following the ion flow direction. An example of B field distribution along the channel axis is shown in figure 5.1. The magnetic field lines form an ion lens that is symmetrical about the channel axis[1,2]. The lens tends to focus the ions out of the channel into a well-defined beam. As previously explained, the magnetic field plays a major role in a Hall thruster as it controls to a large extent both the ionization of the neutral gas and the acceleration of the ions. Additionally, the curvature of the magnetic field lines, and the lens inclination influence the ion beam properties. Therefore, it appears necessary to optimize the magnetic topology in order to reach a high performance level.

The influence of the magnetic topology on the performance and discharge characteristics

[1] Adapted from:
S. Mazouffre, G. Bourgeois, J. Vaudolon et al. *J. Propul. Power*, **31**, 4 (2015)

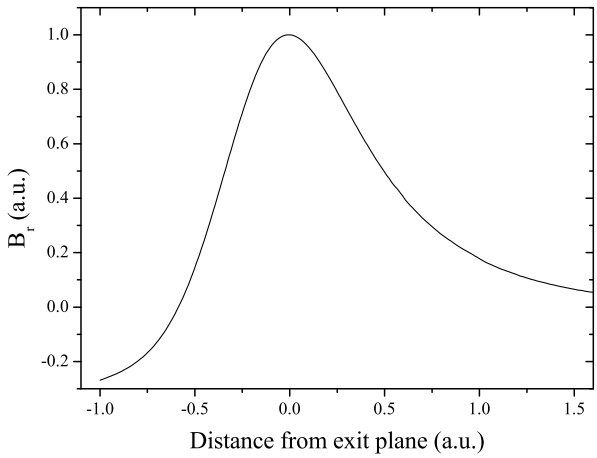

Figure 5.1: Distribution of the radial magnetic field strength along the channel axis for a conventional Hall thruster magnetic design.

Table 5.1: Macro characteristics of the four PPS-Flex test campaigns. The test campaign 2014 at ESA was split in two parts. The magnetic exploration sequence lasted 2 weeks, while the other 6 were dedicated to other purposes.

	2012	**2013**	**2014**	**2015**
Hours of operation	18	39	49	6
Number of magnetic configurations	14	62	65	8
Residual pressure (mbar-Xe)	3×10^{-5}	4.5×10^{-6} - 5×10^{-5}	2×10^{-5}	1.5×10^{-5}
Test duration (weeks)	2	7	8 (2)	2

of a Hall thruster has been studied in the past using a conventional magnetic architecture, from experimental as well as numerical viewpoints[3–7]. For instance, Hofer and co-workers extensively examined the influence of the magnetic topology on the performance of the 5 kW-class NASA-173M v2 Hall thruster[3,4]. For that purpose they added two trim coils to the original magnetic structure in order to obtain additional control of the magnetic topology. A first trim coil was placed behind the anode to increase the B field gradient inside the channel. A second trim coil was located outside the channel. When energized, the magnetic topology downstream the thruster channel exit plane changes, especially the inclination of the ion lens. Despite the use of additional trim coils, modifying one characteristic parameter of the magnetic topology induces a change in other characteristics. In other words, the use of a standard magnetic circuit does not allow to vary one parameter while keeping all others fixed. This aspect makes any precise study on the B field impact very complicated. The PPS-Flex has been designed with the prospect of controlling the B field parameters in independent, versatile and broad manners.
A summary of the four test campaigns that have occurred with the PPS-Flex is made in Sec. 5.1. The influence of the magnetic field on the discharge properties when changing the propellant gas has been examined with the PPI-Mag, whose testing is reported in Sec. 5.2. Finally, conclusions are given in Sec. 5.3.

5.1 Performance analysis of the PPS-FLEX

The PPS-Flex thruster was fired with xenon as a propellant gas. The thruster was equipped with BN-SiO_2 walls for the straight channel as well as the conic section. A cold hollow cathode was used as a beam neutralizer during the first test campaign. A heated hollow cathode similar to that employed with the PPI and PPI-Mag was used for the three other campaigns. Key figures of the PPS-Flex campaigns are given in table 5.1.
For confidentiality reasons, most of the results of the PPS-Flex test campaigns are absent from the manuscript. The analysis and the conclusions have been given in the test reports:

- G. Bourgeois and co-workers, *Influence de la topologie magnétique sur les performances et la divergence du propulseur PPS-FLEX*, 37 pp, P02-2012, ICARE, CNRS (2012).
- J. Vaudolon and co-workers, *Influence de la topologie magnétique et des conditions expérimentales sur les performances du propulseur PPS-FLEX*, 127 pp, PE-R-02-2014, ICARE, CNRS (2014).
- J. Vaudolon and co-workers, *Tuning of the PPS-FLEX magnetic field at EPL*, 90 pp, PE-R-03-2015, ICARE, CNRS (2015).
- J. Vaudolon and co-workers, *Optimisation de la topologie du PPS-FLEX en mode sans-parois - influence de la géométrie d'une sonde de Faraday sur le courant mesuré et les grandeurs déduites*, 50 pp, PE-2015, ICARE, CNRS (2015).

5.1.1 First test campaign in the LIC facility - Snecma, Vernon, France[2]

The first experiments with the PPS-Flex were dedicated to testing the prototype, and verification of the magnetic flexibility. The test campaign occurred in the LIC vacuum vessel at Snecma, Vernon, France. The thruster was operated at a fixed discharge current value of 4.28 A, that means the xenon mass flow rate automatically adjusts itself. The discharge voltage was varied between 200 V and 350 V. The input power never exceeded 1,500 W to limit the thermal load. The vacuum chamber background pressure was typically 2.10^{-5} mbar-Xe. The thruster was mounted onto a calibrated thrust balance to determine the thrust level and the specific impulse. A rotating arm equipped with 15 Faraday probes was used to measure the ion current density profile in the ion beam far-field.

5.1.2 The PIVOINE-2g test campaign 2013 - CNRS, Orléans, France

The second test campaign with the PPS-Flex occurred at PIVOINE-2g ground test facility, at the fall of 2013. The purpose of this campaign was to measure the performance of the PPS-Flex in terms of thrust, beam divergence angle and anode efficiency (the total efficiency of the PPS-Flex cannot be compared to that of a flight model, owing to the large number of coils to power). The performance has been measured at various operating points, the anode power spanning the 500 W - 1,500 W range.
The magnetic topology has been tuned to a large extent. The gradients both inside and outside the chamber, the plasma lens inclination, the field lines curvature, the position of maximum B field and its amplitude have been varied as the performance was constantly recorded. Numerous results concerning the influence of the magnetic field parameters on

[2] Although I have participated to this test campaign, it is G. Bourgeois who investigated the influence of B on the performance[8].

the thruster performance have been obtained. Conclusions together with recommendations for future works have been made in the test report[9]. Note that a visual evidence of magnetic shielding has been obtained, a first version of this topology that pave the way for future research, see Chapter 6.
The influence of the background pressure on the performance parameters, such as the ion current density profile in the far-field plume, has been investigated, see Chapter 4. The research included the measure of performance when changing the thruster and cathode potential reference.

5.1.3 Measurements in CORONA - ESA, Noordwijk, the Netherlands

The objectives of the test campaign 2014 at the ESA Propulsion Laboratory (EPL) were:

- To test a series of plasma plume diagnostics in a standard magnetic configuration. Faraday, Langmuir, ExB and RPA probes have been used.
- To produce test procedures and advices for using such diagnostics during a qualification test campaign.
- To list possible sources of error and inaccuracy and to provide the uncertainty associated with each measurement performed with the diagnostics.
- To measure the performance of the PPS-FLEX for several magnetic field configurations.

This campaign has been the maiden testing of a mid-power class Hall thruster in the wall-less mode. The PPS-Flex is a unique and crucial tool to optimize the magnetic topology of the wall-less concept. In this design, the anode is placed at the thruster exit plane. Recent studies on the PPI have revealed that the plasma bulk is then located outside the discharge channel[10]. Since the wall material does not interact with the plasma anymore, the plasma is solely confined by the magnetic field. A section of Chapter 6 reports the first results obtained with the PPI and with the PPS-Flex.
The PPS-Flex operation has been nominal during the entire test campaign at EPL. The PPS-Flex has been equipped with a heat-dissipator circuit, made in copper, wrapped around the channel and presented in figures 5.2.1 and 5.2.2. The outer coil temperature did not exceed $140^{\circ}\mathrm{C}$ during the tests (this has been a matter of concern during the first two test campaigns as it exceeded $350^{\circ}\mathrm{C}$). The inner coil temperature, however, increased rapidly during operation since there was no heat drain. Cool down cycles were therefore necessary to prevent them from damage.

5.1.4 The PIVOINE-2g test campaign 2015 - CNRS, Orléans, France

Because of hardware and facility issues during the test campaign 2014, the outcomes of the test campaign at EPL have not brought as much scope as those obtained in 2013 for shaping advanced thruster concepts. A fourth campaign has therefore been conducted at PIVOINE-2g ground-test facility at the ICARE Laboratory, in Orléans, France, during spring 2015.
During two weeks, the wall-less design has been extensively studied. The design of the anode has been optimized, and the magnetic topology finely adjusted to maximize the performance level, given the capabilities of the PPS-Flex for shaping such requiring topologies. Details can be found in Chapter 6. The wall-less concept has notably been shown to

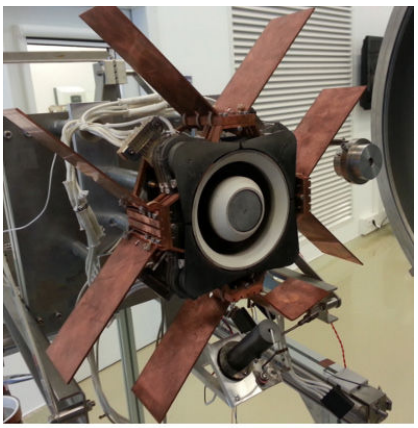

5.2.1: PPS-Flex Hall thruster fitted with thermal radiator and cathode.

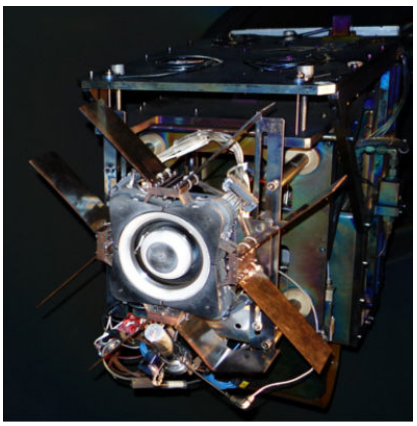

5.2.2: The PPS-Flex in PIVOINE-2g ground-test facility vacuum vessel.

Figure 5.2: The PPS-Flex has been fitted with radiators to limit the thermal load on the outer coils. Such an arrangement has been implemented after the test campaign 2013. The PPS-Flex is shown at EPL during the test campaign 2014 (left), and mounted on the thrust balance at PIVOINE-2g ground-test facility vacuum vessel during alignment of the Faraday probes (right). A RPA provided by ICARE is visible in figure 5.2.1 to perform measurements in the thruster backflow.

Table 5.2: Description of the 13 magnetic configurations tested during the first test campaign.

PPS-Flex magnetic configurations			
Label	**Characteristic**	**Label**	**Characteristic**
1	PPS®1350-ML (reference)	5	Shift of B inside the channel
2	SPT100	6-10	Positive and negative lens inclination
3, 4	Steep gradient inside the channel	11-13	Moving of the zero B-field region

be operable for standard periods of time (the thruster has been operated 1 h at 850 W during a stability test), and seems promising to bridge the gap between a high thrust / low I_{SP} and a low thrust / high I_{SP} throttling capability.
A preliminary study to characterize the influence of the probe geometry on the ion current density profile collected in the plume has also been made. The conclusions have been given in the test report[11].

5.1.5 Examples of relationship between magnetic configuration and performance

In this part, we give a few elements as to the PPS-Flex performance, for various magnetic configurations. The results presented herein have been obtained during the first test campaign, in 2012. As a reminder, the anode flow rate was regulated, in order to operate the thruster at a fixed discharge current of 4.28 A.
The PPS-Flex capability of generating different magnetic configurations is here exemplified through 13 magnetic topologies, which are summarized in table 5.2. The latter also gives the identification label for the remainder of this section. The topologies include standard configurations such as PPS®1350-ML-type and SPT100-type B fields. For configurations (3) and (4), the positive B field gradient inside the channel is increased compared to (1) and (2) by moving downstream the zero field region. The maximum of the radial magnetic field component has been located inside for the configuration (5), all

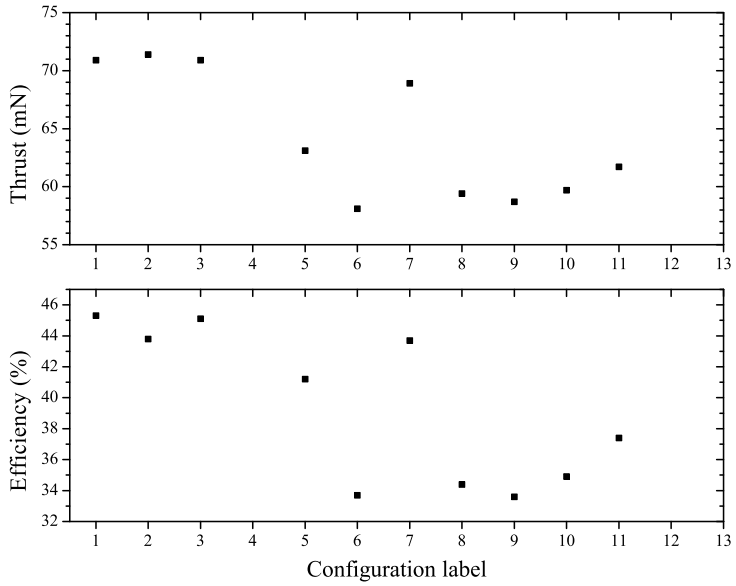

Figure 5.3: Thrust and total efficiency of the PPS-Flex thruster, at 250 V applied voltage and 1,070 W input power, for various magnetic configurations (see table 5.2).

other parameters being unchanged. The lens inclination at the straight channel exit plane for configurations (6) to (10) are 0°, 6°, -6°, -19° and 19°, respectively. Here a negative angle corresponds to a lens directed towards the thruster centerline. Configuration (11) is similar to (5), except that a zero field region is created downstream the thruster exit plane. The configuration (12) has two zero-field regions: one inside and one outside the channel. Configuration (13) corresponds to (12), with a lower magnetic field amplitude. The 22 coils together with 10 power units are needed to generate the aforementioned family of topologies.

The measured thrust level is given in figure 5.3 for the 13 magnetic configurations previously described. Figure 5.3 also displays the total efficiency η, which accounts for the cathode gas flow rate. Measurements have been carried out for a discharge voltage of 250 V. The power furnished to the discharge is 1,070 W. Configurations labeled (4), (12) and (13) were not stable for these operating conditions. Current oscillations were large and the discharge was switched-off after a short time span. The highest thrust level and the largest efficiency are reached for the first three configurations, which can be considered as standard. The magnetic configuration labeled (7), which exhibits a negative lens inclination, leads to relatively good performance. However, due to the inclination angle, the temperature of the channel inner ceramic wall is high, meaning the erosion rate is certainly large, with direct consequence on the thruster lifetime. The reference configuration, labeled (1), gives discharge current, thrust, specific impulse and efficiency values that are very close to those of the PPS®1350-ML Hall thruster, whatever the discharge voltage. Firstly, it indicates the PPS-Flex magnetic circuit can accurately reproduce the normal PPS®1350-ML magnetic field map. Secondly, it shows the weak effect of the additional conic section on the discharge and plume properties. As can be seen in figure 5.3, the PPS®1350-type magnetic configuration (1) delivers a performance above the SPT100-type configuration (2). However, the ordering depends on the background pressure, and on the cathode electrical wiring.

Figure 5.4 shows the anode xenon mass flow rate, ϕ_a, that is necessary to maintain the

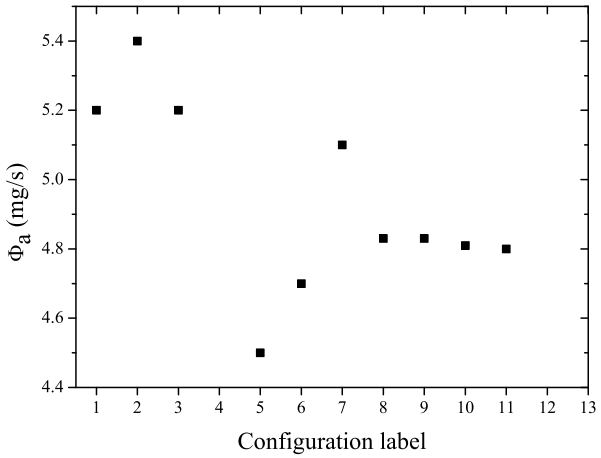

Figure 5.4: Xenon anode mass flow rate at 250 V applied voltage needed to maintain the discharge current at 4.28 A for various magnetic configurations (see table 5.2).

Table 5.3: Performance data of the PPS-Flex thruster for several magnetic configurations.

Label	**Thrust** (mN)	$\phi_{\mathbf{a}}$ (mg/s)	α	η	$\mathbf{I_{sp}}$ (s)	$\theta_{\mathbf{div}}$ (°)
1	70.9	5.20	0.72	0.45	1,446	36.7
2	71.4	5.40	0.71	0.44	1,379	35.5
3	70.9	5.20	0.74	0.45	1,367	35.6
5	63.1	4.50	-	0.41	1,410	-
6	58.0	4.70	0.57	0.34	1,258	40.5
7	68.9	5.10	0.73	0.44	1,371	38.6
8	59.4	4.85	0.59	0.34	1,254	39.0
9	58.7	4.85	0.61	0.33	1,237	40.7
10	59.7	4.80	0.58	0.35	1,267	40.1
11	61.7	4.80	0.65	0.37	1,310	39.8

discharge current at 4.28 A for the 13 magnetic configurations of the PPS-Flex. In that case, the mass flow rate gives information about the ionization efficiency. ϕ_a is relatively high for the PPS®1350-ML topology. The lowest xenon mass flow rate is obtained with the configuration labeled (5), i.e. when moving the peak of the magnetic field axial profile upstream. But the thrust and the efficiency are low with this configuration, as shown in figure 5.3, due to an increase in wall losses.
The set of experimental data is summarized in table 5.3, for a discharge voltage of 250 V and a current discharge of 4.28 A. The specific impulse is computed from the thrust level. The quantity denoted α is the ionization efficiency, or propellant utilization, and θ_{div} is the beam divergence half-angle. The largest specific impulse is reached with the PPS®1350-ML configuration, which also gives a low beam divergence. The propellant utilization is slightly increased when the gradient inside the cavity is steepen.

5.2 Impact of the magnetic barrier extent on the performance of a krypton-fueled Hall thruster

Xenon is conventionally used in Hall thrusters due to its low ionization potential and its high atomic mass. Unlike metal propellants such as bismuth, or mercury, its inert nature is a major advantage since it eliminates safety concerns. Xenon will likely remain the standard propellant for future short and mid term missions. However, its scarcity and the large price swings that occur on the rare gas market constitute black spots that make relevant the study of alternative propellants. Furthermore, the growing delta-V demand requires increasing amounts of propellant and costs savings might be of concern at some point.
In search for solutions, a variety of alternatives can be proposed[12–14]. The simplest solution is to substitute another rare gas for xenon, since it would not change the overall architecture of the propulsion system radically. Notice however that bismuth has already been demonstrated as a viable option for Hall thrusters[15], but several drawbacks and technological issues when dealing with metals constitute barriers for their application, the main one being the metal vaporization. Setting radon aside for safety reasons, krypton is therefore the next logical choice after xenon in the rare gas family. The performance penalty incurred by utilizing helium, neon or argon would be more significant than with krypton, due to higher ionization energy, among other things. It is about 13 times more prevalent than xenon in the air and can currently be produced at a cost fraction of one-tenth that of xenon. The cost benefit is likely to be even greater during spikes in the demand of xenon. These spikes may occur more frequently in the future since xenon is now used by different industries for fast growing markets, such as the lighting manufacture, electronic chips and its application as an anaesthetic. Besides, only a hundred air separation units in the world are big enough and configured for extracting rare gases efficiently, and this number might not increase as fast as the demand[16,17].
Despite krypton's inherently lower performance, it could conceivably fulfil the propulsion requirements of some missions. The thruster would potentially be operated at higher power and/or with a longer cumulative firing time. Erosion of the channel walls and the performance output are therefore the two main concerns when using krypton. Missions such as GEO communication satellites north-south station keeping could benefit from the additional specific impulse offered by krypton. For missions such as orbit raising, the use of krypton would, however, increase the trip time because of the corresponding diminution of the thrust-to-power ratio. The use of krypton might nonetheless be advantageous considering that solar electric power systems specific power increases.

5.2.1 Design of the PPI-Mag

Faraday probe, RPA, thrust and LIF measurements have been performed with the PPI, in ESA's and ICARE's test facilities in 2011 and 2012. Results have revealed that the acceleration efficiency is not fundamentally altered when using krypton instead of xenon[18]. The higher ionization potential, however, lowers the ionization efficiency of the krypton-fueled discharge. Based on the results of the first attempts made with krypton, the ICARE Laboratory has devoted a significant effort in the past two years in designing the PPI-Mag, a Hall thruster optimized for krypton. The thruster is shown in figure 5.5, operating in the NExET vacuum facility at the ICARE Laboratory. The channel geometry of the PPI-Mag is similar to that of the PPI and is based on a $2S_0$ configuration[19].

One might think that lengthen the channel could offer larger ionization rates by increasing the residence time of the atoms, and therefore their probability for experiencing

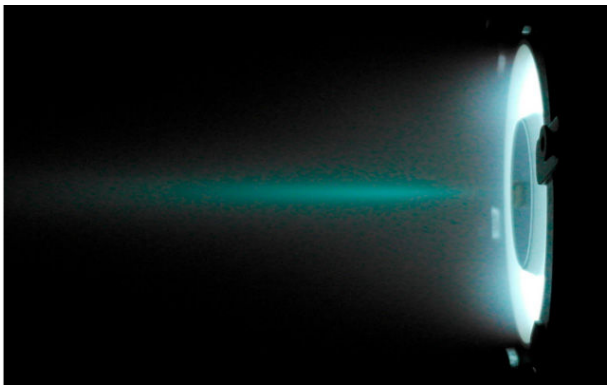

Figure 5.5: The PPI-Mag operating in the NExET chamber at 200 V and 1.0 $\mathrm{mg/s}$ of xenon flow rate.

an ionizing collision. This is not likely to offer any benefit, since the ionization area will not be extended as much. Besides, the overall system mass would be increased. When looking for ionization probabilities, one might however fulfil

$$\lambda_i << L_i, \tag{5.1}$$

where λ_i is the ionization mean free path and L_i the length of the ionization zone. Ionization occurs in a zone where the atomic density is high and in which electrons are trapped by the magnetic field. Therefore, there is a link between the length of the ionization zone, L_i, and the length of the magnetized area, L_B. In this work, we have taken L_B to be the width at half maximum of the radial magnetic field profile along the channel axis. Assuming that the link between L_B and L_i is linear, the residence time of an atom in the magnetized area is written

$$\tau = \frac{L_i}{v_n} \propto \frac{L_B}{v_n} \propto L_B \sqrt{\frac{m_i}{T_g}}, \tag{5.2}$$

where v_n is the neutral speed, m_i the ion mass and T_g the gas temperature. We also assume that the temperature of the atoms does not strongly depend on the nature of the gas. The ratio of the residence times for xenon and krypton atoms can then be obtained

$$\frac{\tau_{Xe}}{\tau_{Kr}} = \frac{L_B \sqrt{m_{Xe} T_{Kr}}}{L_B \sqrt{m_{Kr} T_{Xe}}} \approx \sqrt{\frac{m_{Xe}}{m_{Kr}}} \approx 1.25. \tag{5.3}$$

Therefore, it appears that extending the magnetized area may increase the ionization efficiency of the discharge. This argument has guided the design of the PPI-Mag.
Sets of permanent magnets can be wrapped around the channel of the PPI-Mag and inserted into the central pole to shape magnetic field profiles, without changing the channel geometry nor the anode. Three topologies have been tested. The magnetic field maximum, the location of the maximum and the gradients at half maximum have been kept unchanged between the configurations. However, L_B is modified. Configuration 1 is that of the PPI to allow comparison with the results of the previous test campaigns at ESA and ICARE. Configurations 2 and 3 progressively increase L_B. In other words, the length of the magnetized area of configuration 3 is larger than that of configuration 1. The basic idea was to achieve a similar ionization rate with krypton in configuration 3 than with xenon in configuration 1.

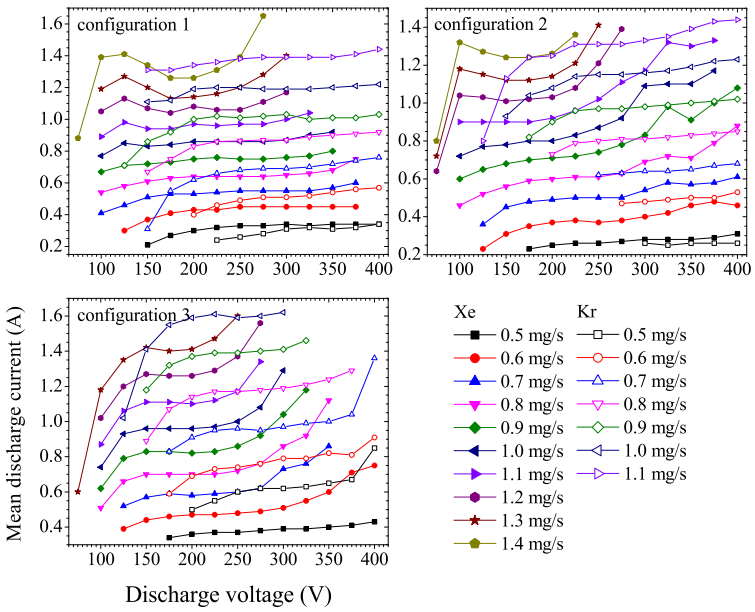

Figure 5.6: $U_d - I_d$ characteristics of the PPI-Mag, in xenon and krypton, for the three magnetic configurations (L_B increasing from left to right, and from top to bottom).

5.2.2 Characterization of the PPI-Mag

The discharge voltage / discharge current characteristics of the PPI-Mag are presented in figure 5.6. The thruster has been operated in xenon and krypton, and the three magnetic configurations are presented. The anode flow rate ranges from 0.5 $\mathrm{mg/s}$ to 1.4 $\mathrm{mg/s}$ by a 0.1 $\mathrm{mg/s}$ step. The discharge voltage ranges between 75 V and 400 V. For each mass flow rate, the discharge voltage was set to 400 V, then decreased by 25 V steps until extinction.

The krypton characteristics plateau for the three configurations, except at low discharge voltages. A similar plateau is observed for configuration 1 operated in xenon. Configurations 2 and 3 show an increase in discharge current with the discharge voltage, when operated with xenon, an inflexion point being located at 200 V. The mean discharge current values do not change much, with krypton, for configurations 1 and 2, but increase significantly in configuration 3.

The standard deviation of the discharge current oscillations has been computed according to equation (5.4), in which N is the number of samples, $I_{d,i}$ is the discharge current for sample i, and $\overline{I_d}$ is the mean discharge current value on the observation window.

$$\sigma_{I_d} = \sqrt{\frac{\sum_{i=1}^{N} \left(I_{d,i} - \overline{I_d}\right)^2}{N}}. \tag{5.4}$$

The oscillations of the discharge current, represented in figure 5.7, show similar trends between operating points, propellant and magnetic configurations. The oscillation is lower than 200 mA, except in one, possibly two, areas where it can increase up to 800 mA (configuration 3, krypton). The two unstable zones of configuration 1 are located at 150 V and 250 V. These zones shift to 200 V and 350 V for configuration 2. Then a single zone, larger than the others of configurations 1 and 2, is observed between 250 V and 400 V for the third configuration.

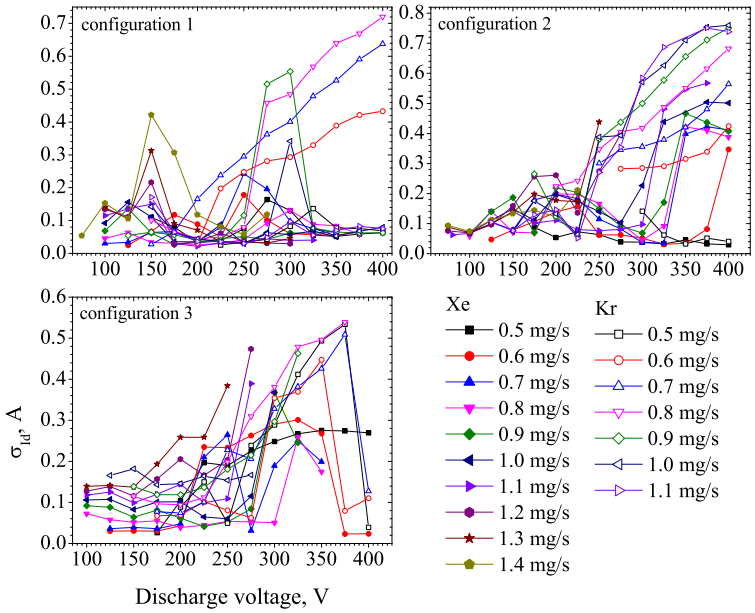

Figure 5.7: Standard deviation of the discharge current oscillations, presented for the PPI-Mag operating in xenon and krypton. Unstable areas relocate when changing the magnetic configuration.

The discharge is stable in configuration 1, both in xenon and krypton, in terms of mean discharge current level and oscillations. This configuration is close to that of the PPI, which is optimized for xenon. It allows a stable operation on a wide range of operating points. The stability regions of configurations 2 and 3 are narrower. Switching from xenon to krypton, without changing the thruster design, is thus possible without modifying the discharge characteristic dramatically.

5.2.3 Properties of the far-field plume

In this part, the ion properties in the far-field plume are presented. Faraday probe measurements have been made at 34 cm downstream of the thruster exit plane. The PPI-Mag has been operated at five operating points: 150, 200 and 250 V at 1.0 $\mathrm{mg/s}$ of propellant flow rate, and 0.8, 1.2 $\mathrm{mg/s}$ at 200 V. Xenon and krypton have been used. Three magnetic configurations have been tested. Note that there have been no measurements at 200 V, 1.2 $\mathrm{mg/s}$ and 250 V, 1.0 $\mathrm{mg/s}$ for configuration 3, in krypton, the anode power of 400 W having been deemed too stressful.

Current density components normal to the beam

The ion current density along inclination and elevation directions are given in figures 5.8.1 and 5.8.2. Generally, the ion current density increases with the anode flow rate. This is obvious for configurations 1 and 3, and disputable for configuration 2. The thruster was unstable when operated with configuration 2, which has made the measurements difficult to perform. The extension of L_B may not be the reason for such a behavior, given that configurations 1 and 3 demonstrated stable regimes. As highlighted with the PPS-Flex, the entire magnetic topology should be considered when discussing the discharge properties.
The current density profiles in the two directions are almost identical at each operating point. Assuming $j_{-\theta} = j_{\theta}$ and $j_{-\phi} = j_{\phi}$, the currents perpendicular to the beam cancel out each other, which makes their consideration useless when computing the thruster

performance. The discussion is still ongoing though. Our previous statement lead us to ignore the currents perpendicular to the beam for computing key thruster characteristics, such as the ionization efficiency. Yet ions have been collected, and therefore do exist and should somehow be accounted for. Similarly, the observation of currents perpendicular to the beam should force the EP community to define some parameters more precisely, such as the divergence angle: do we deal with a plasma divergence angle, a beam divergence angle, both? In this work, the beam divergence angle was considered. But keep in mind that the ions travelling perpendicularly are those which can impact surfaces, like solar panels.
The discharge voltage series, in figure 5.8.1, is more complex than figure 5.8.2. Configuration 1 has a standard behavior with xenon and krypton, i.e. the ion current density increases with the discharge voltage, that is the ion energy. In this configuration, the plasma did not appear in a jet mode, but rather looked like in a ball, at 150 V and 1.0 $\mathrm{mg/s}$, in xenon, hence a different shape. The current density increases from 150 V to 200 V, but stagnates or even diminishes at 250 V. This feature was not observed for the beam current density.

Ion beam current density

The radial ion current density profiles have been measured at the same time than those perpendicular to the beam[3]. The current density profiles acquired with guarded stainless steel and molybdenum probes are presented in figures 5.9.1 and 5.9.2. The discharge voltage and anode flow rates series have been constructed similarly to the previous figures. The ion beam current density increases with discharge voltage and anode mass flow rate for both propellants.
There is no conclusive difference between the profiles obtained with the stainless steel and molybdenum probes. We have not been able to find any precise data regarding the secondary emission coefficients at our energies. Besides, these depend on the incoming species, on the target material, surface finishing and temperature. General knowledge nonetheless allows to assume that the secondary emission of molybdenum is lower than that of steel[20]. The level of current that is collected is, however, similar for the two materials. Therefore, in this case, correction for the secondary emission current does not seem to be a matter of concern. These observation contradict those of Walker, Hofer and Gallimore, who observed a clear difference between steel and tungsten[21]. Notice, however, that the secondary emission coefficient of tungsten is probably lower than that of molybdenum, and that the incoming flux was higher in their experiments (NASA-173Mv1 Hall thruster operating at 300 V, 5.0 $\mathrm{mg/s}$ and 9.7 $\mathrm{mg/s}$ of xenon).

5.2.4 Influence of the magnetic barrier extent on the thruster performance

Integral quantities

The thruster performance has been computed using equations of paragraph 4.6.2 of Chapter 4. The error bars for such quantities have been estimated during the PPS-Flex test campaign 2014[22]. The uncertainties depend on the thruster operating point. Table 5.4 gives the average uncertainty of some quantities. This general information can be used to evaluate the uncertainty level on the PPI-Mag performance. However, a precise determination of these uncertainties requires a dedicated test campaign, as other measurements must be made to evaluate diverse contributions (probe design, background pressure level,

[3]Since we possess only one sourcemeter, the acquisitions are not simultaneous, but separated by a few minutes. The point is that the thruster is not switched off, nor its regime is modified in between two measurements.

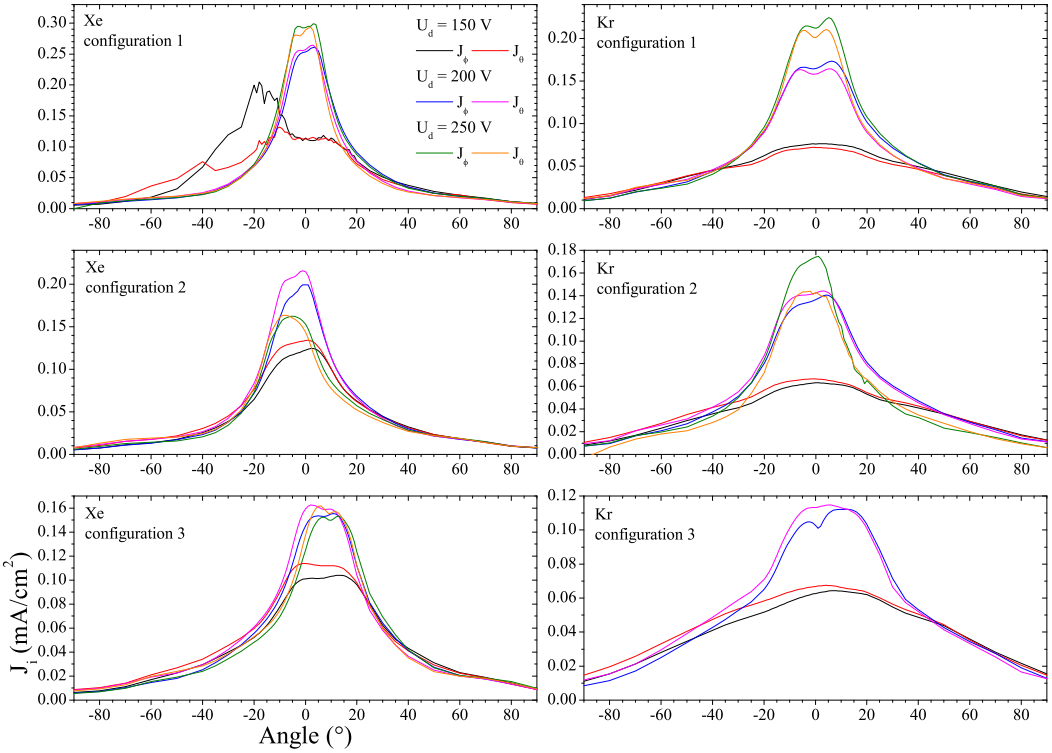

5.8.1: Ion current density profiles - discharge voltage series.

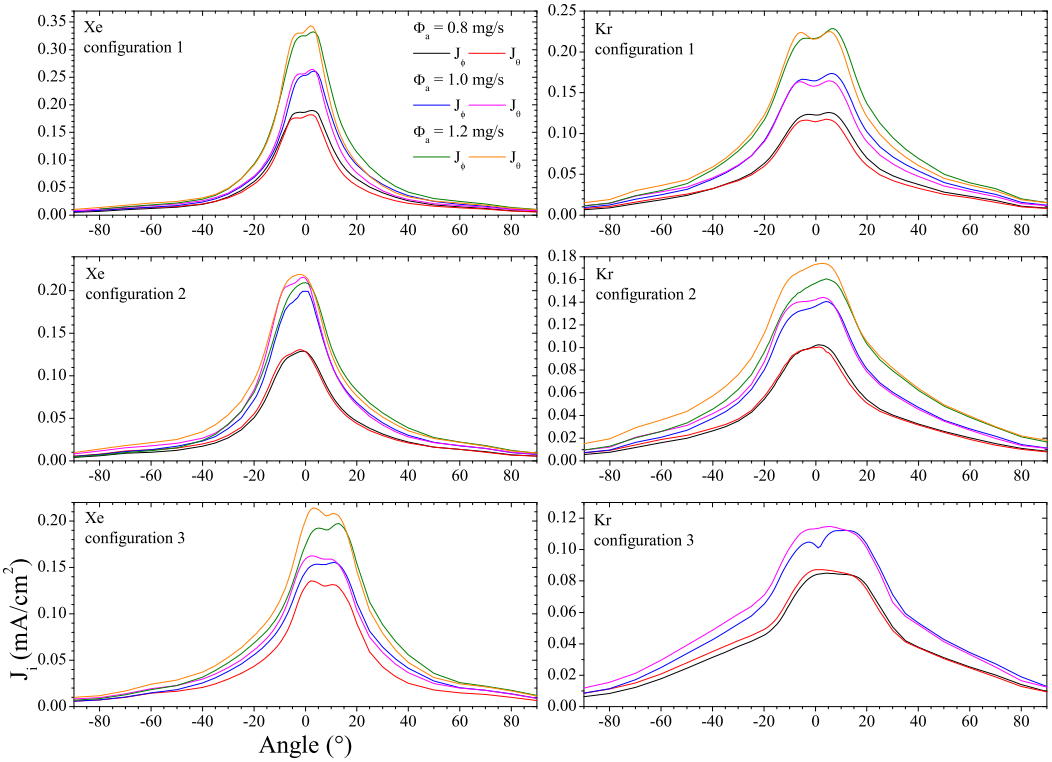

5.8.2: Ion current density profiles - anode flow rate series.

Figure 5.8: Distribution of ion current density profiles normal to the beam of the PPI-Mag, operated in xenon (left column) and krypton (right column). The three magnetic configurations have been examined (configuration 1 to 3, respectively from top to bottom of each figure). The current density increases with the discharge voltage (top figure) and the mass flow rate (series at bottom). The ion current density amplitude decreases when L_B increases.

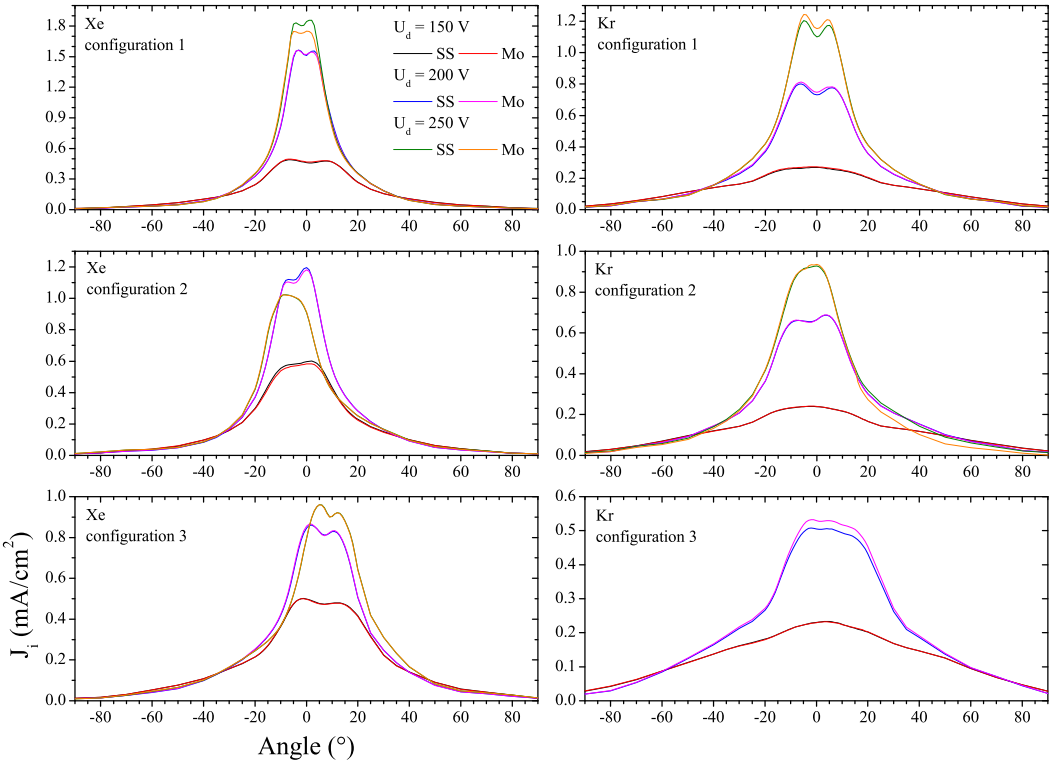

5.9.1: Ion beam current density profiles - discharge voltage series.

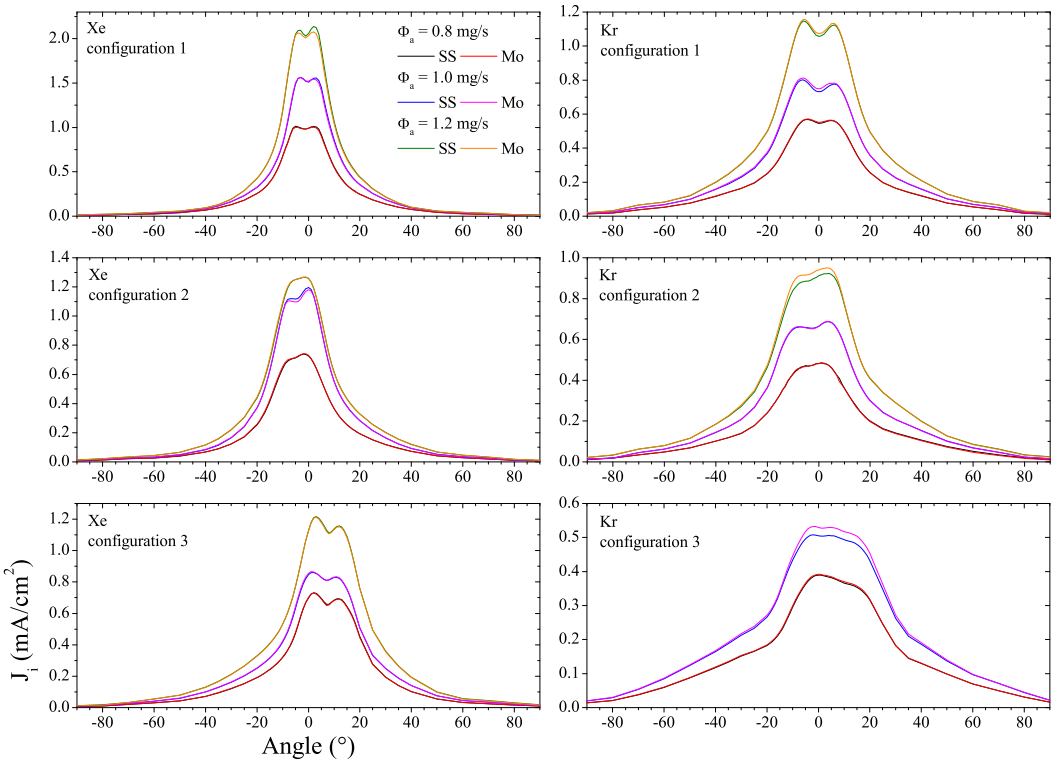

5.9.2: Ion beam current density profiles - anode flow rate series.

Figure 5.9: Ion beam current density profiles of the PPI-Mag, with the stainless steel (SS) and molybdenum (Mo), guarded, Faraday probes. The thruster has been operated with xenon (left column) and krypton (right column). The current density increases with the discharge voltage (top) and the mass flow rate (series at bottom). There is no conclusive difference between the two materials at these energies.

Table 5.4: Evaluation of uncertainties on Faraday probe measurements with the PPS-Flex, during the test campaign 2014. The uncertainty is provided with a coverage factor k=1.

Quantity	I_b	ξ_i	η_i	θ_{div}
Uncertainty	3 %	3 %	5 %	10 %

electric reference, acquisition chain...).

The ion current, ion current fraction and ionization efficiency are presented in figure 5.10.1. While the ion currents increase from configuration 1 to configuration 3, the ion current fractions decrease, due to a higher discharge current mean value. The current fraction is maximum at the thruster nominal operating point. The ionization efficiency profile is remarkable. It increases by 8 % from configuration 1 to configuration 3, which validates the design of the PPI-Mag. However, singly-charged ions have been considered only, and a more detailed analysis should consider a fraction of multiply-charged ions to conclude more precisely. Yet, it seems unlikely that a significant portion of doubly-charged ions appear at these energies. The unstable behavior of the thruster, when operated with configuration 2 as a magnetic topology, was previously highlighted, and results in the lowest performance.

Figure 5.10.2 portrays the beam divergence half-angle, the thrust and the anode efficiency. The jet diverges more in krypton than in xenon, and yet the thrust is not impacted. This is in clear opposition with physics, but understandable when considering the simple nature of equation (4.20). This model does not illustrates the inherently integral characteristic of this quantity. One could think of two different thrusters: the first one with a large divergence angle and an almost uniform ion current density distribution, the other having a narrow and focused beam, with an intense ion current density peak. Although the ion beam currents are similar, the thrust levels differ massively. Therefore, the anode efficiency that is provided certainly possesses a large uncertainty.

Thermal imaging

The thermal imaging measurement procedure is similar to that of the Faraday probe measurements, see table 4.2. Another constraint has been added: the thruster operating point can be changed when the largest ceramic thermal gradient drops below $1°\mathrm{C}/\mathrm{min}$ in xenon, and $2°\mathrm{C}/\mathrm{min}$ in krypton.

The temperatures of the PPI-Mag inner and outer ceramics are shown in figures 5.11.1 and 5.11.2, in xenon and krypton, for discharge voltage and anode flow rate series. The temperature is taken as that of the ceramic hottest point, which locates $2\ \mathrm{mm}$ before the exit plane with the three configurations. The wall losses are always higher with krypton. The temperature of the inner ceramic remains constant, while that of the outer ceramic soars with L_B. This cannot be explained by the magnetic lens angle, which is equal to 7.5° for configuration 1, and to 3.2° for configuration 3 (a positive angle indicates an inclination towards the thruster centerline).

The behavior at $150\ \mathrm{V}$ and $1.0\ \mathrm{mg/s}$, in krypton, is different than the others, since the temperatures decrease in configuration 3. This difference cannot be explained with the data we have. Some assumptions can however be made as to the localization of the ionization and potential drop areas along the channel axis of configuration 3, that could shift downstream that of configurations 1 and 2. This picture is supported by the profile of the beam divergence half-angle.

The results suggest that the ion energy at the exit plane increases with L_B. This is in

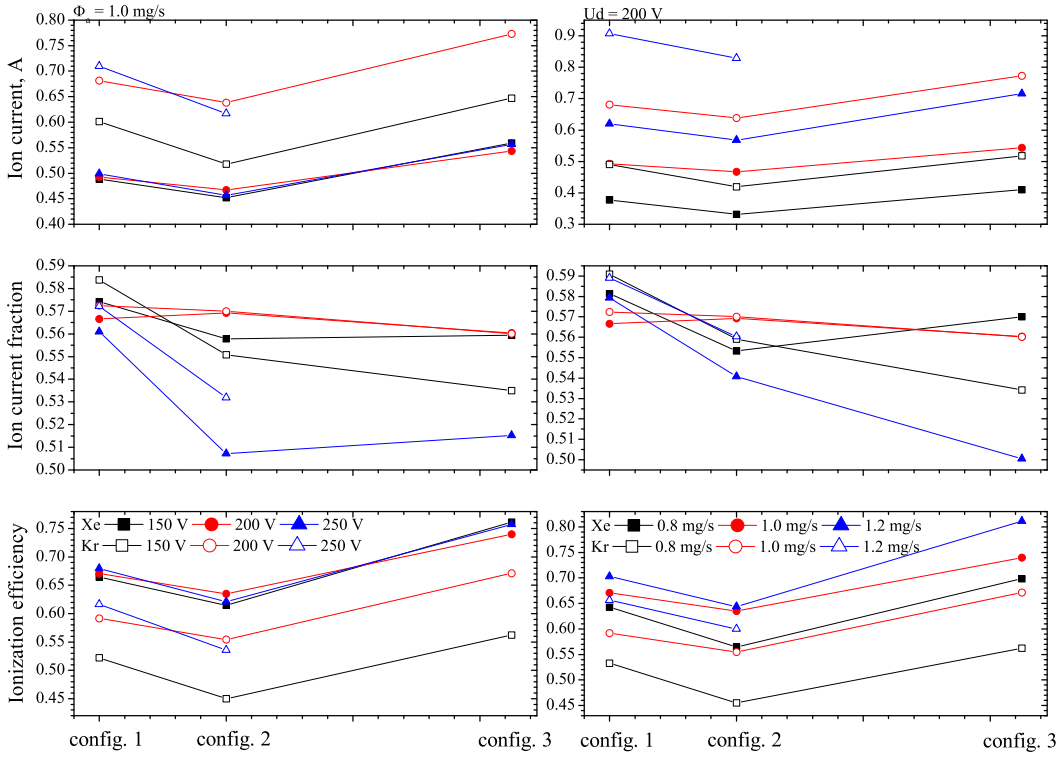

5.10.1: Thruster performance as a function of L_B - ion quantities.

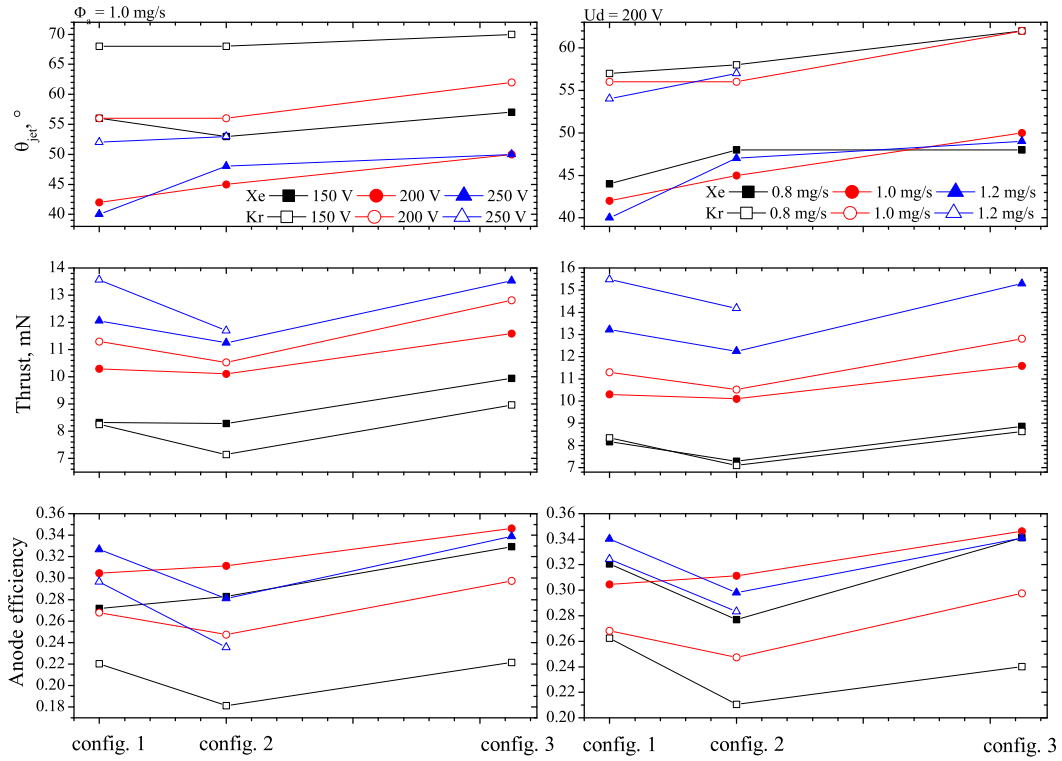

5.10.2: Thruster performance as a function of L_B - thrust & efficiency.

Figure 5.10: Thruster performance as a function of L_B. Left (right) columns represent the discharge voltage (respectively anode flow rate) series. The performance is presented in xenon and krypton. Every performance parameter has been deduced from the Faraday probe measurements, using the equations presented in section 4.6.2, in Chapter 4. This study assumes the sole presence of singly-charged ions.

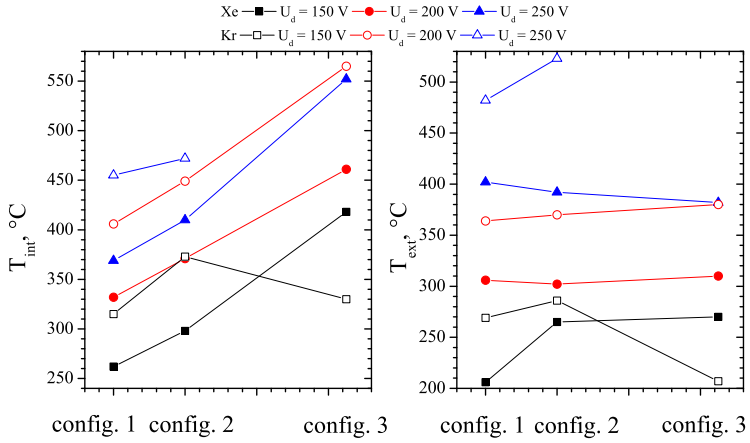

5.11.1: Temperature of the PPI-Mag ceramics - discharge voltage series.

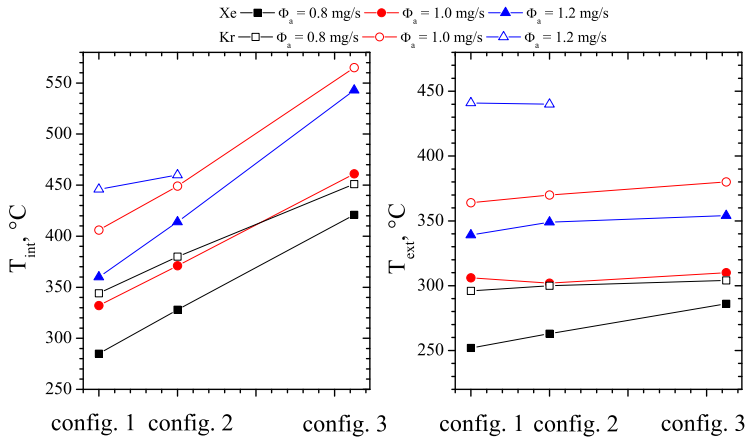

5.11.2: Temperature of the PPI-Mag ceramics - anode flow rate series.

Figure 5.11: Temperature of the PPI-Mag ceramics as a function of L_B. Left (right) quadrants represent the temperature of the inner ceramic (respectively outer ceramic). The temperature is taken at that of the ceramic hottest point. The temperature of the inner ceramic does not fluctuate much, while that of the outer ceramic increases rapidly with L_B.

qualitative agreement with the description of Garrigues and co-workers[5], who numerically studied a similar case. A SPT100-type Hall thruster was considered with a two-dimensional hybrid code. Their simulations have revealed that the potential drop relocates upstream of the ion flow when extending the magnetized area. Ions therefore possess a higher energy at the exit plane, which leads to a higher flux to dissipate. We cannot infer more from the comparison of these works, since the simulation and experimental conditions depart (the magnetic topologies are different, there is a scale effect, the operating points are not similar...).

5.3 Conclusions

The recently developed 1.5 kW class PPS-Flex Hall thruster has been tested and validated. The PPS-Flex is an unique Hall thruster prototype because it offers the possibility to separately control all the magnetic parameters. The number of magnetic topologies that can be achieved is vast. Configurations range from the classical SPT100 to the magnetic shielding and include tilted lenses and zero-field maps. A large amount of topologies have been characterized in terms of related performances and discharge properties (149 to date).

The objectives of the works involving the PPS-Flex are twofold: to improve the performance of standard Hall thrusters and to validate topologies for stable operation at high voltage (high specific impulse) and over long periods of time. In order to achieve these goals, a first step consists in acquiring macroscopic quantities such as thrust and discharge current for a large number of magnetic configurations. A second, more fundamental step is, however, necessary. Advanced diagnostic techniques such as laser induced fluorescence spectroscopy and coherent Thomson scattering must be combined with modelling and numerical simulations to capture the complex relationship between the magnetic field, the discharge properties and the overall performance.

The PPI-Mag has been tested both with xenon and krypton propellants. A set of planar probes, a mechanical assembly and a dedicated acquisition chain have been developed to characterize the far-field plume. The thruster operation in krypton, in configuration 1, does not reveal any sign of an unusual behavior, which shows that a switching from xenon to krypton on a standard architecture is feasible without deep modifications of the discharge properties.

The thruster performance has been evaluated from the ion current density profiles. Among the most important results, the ionization efficiency with configuration 3, in krypton, equals that of configuration 1, in xenon. Yet the thruster behavior is controlled by the whole topology, as demonstrated by the unstable behavior of configuration 2. The basic rules that have guided the design of the magnetic circuit seem to be validated. However, LIF measurements could be performed to evaluate the extent of the ionization zone, thus providing the coupling between L_i and L_B. Additionally, E×B probe measurements would help addressing the impact of multiply-charged ions on the performance level that is inferred, even though their fraction is believed to be small at these discharge voltages. Finally, some parameters such as thrust could be measured, instead of being computed, and would require the development of a thrust stand for NExET. Experiments are also possible in the vacuum chamber at PIVOINE-2g facility, at very low pressure.

References

[1] V. V. Zhurin, H. R. Kaufman, and R. S. Robinson. Physics of closed drift thrusters. *Plasma Sources Sci. Technol.*, 8:R1, 1999.

[2] V. Kim. Main physical features and processes determining the performance of stationary plasma thrusters. *J. Propul. Power*, 14:736–743, 1998.

[3] R.R. Hofer, R.S. Jankovsky, and A.D. Gallimore. High-specific impulse Hall thrusters, part 1: influence of current density and magnetic field. *J. Propul. Power*, 22:721–731, 2006.

[4] R.R. Hofer and A.D. Gallimore. High-specific impulse Hall thrusters, part 2: efficiency analysis. *J. Propul. Power*, 22:732–740, 2006.

[5] L. Garrigues, G.J.M. Hagelaar, J. Bareilles, C. Boniface and J.P. Bœuf. Model study of the influence of the magnetic field configuration on the performance and lifetime of a Hall thruster. *Phys. Plasmas*, 10:4886–4892, 2003.

[6] E. Ahedo and D. Escobar. Influence of design and operation parameters on Hall thruster performances. *J. Appl. Phys.*, 96:983–992, 2004.

[7] D. Gawron, S. Mazouffre, N. Sadeghi and A. Héron. Influence of magnetic field and discharge voltage on the acceleration layer features in a Hall effect thruster. *Plasma Sources Sci. Technol.*, 17(025001), 2008.

[8] G. Bourgeois, S. Mazouffre, J. Vaudolon, R. Vilamot, D. Harribey, C. Henaux, D. Le Mehauté, A. Lorand, T. Chesneau, J. Gueniffey, T. Moulin. Influence de la topologie magnétique sur les performances et la divergence du propulseur PPS-FLEX. Technical report, P02-2012, ICARE, CNRS, 2012.

[9] J. Vaudolon, S. Mazouffre, D. Harribey, C. Henaux, A. Rossi. Influence de la topologie magnétique et des conditions expérimentales sur les performances du propulseur PPS-FLEX. Technical report, PE-R-02-2014, ICARE, CNRS, 2014.

[10] S. Mazouffre, S. Tsikata, and J. Vaudolon. Development and experimental characterization of a wall-less Hall thruster. *J. Appl. Phys.*, 116(243302), 2014.

[11] J. Vaudolon and S. Mazouffre. Optimisation de la topologie du PPS-FLEX en mode sans-parois - influence de la géométrie d'une sonde de Faraday sur le courant mesuré et les grandeurs déduites. Technical report, PE-2015, ICARE, CNRS, 2015.

[12] R.A. Dressler. Propellant alternatives for Ion and Hall effect thrusters. 38th Aerospace Sciences Meeting & exhibit, Reno, NV, AIAA 2000-0602, 2000.

[13] A. Kieckhafer, L.B. King. Energetics of propellants option for high-power Hall thruster. *J. Propul. Power*, 23(1), 2007.

[14] J. Szabo, B. Pote, S. Paintal, M. Robin, A. Hillier, R.D. Branam, R. Huffman. Performance evaluation of an iodine-vapor hall thruster. *J. Propul. Power*, 28(4), 2012.

[15] S. Tverdokhlebov, A. Semenkin, J. Polk. Bismuth propellant option for very high power TAL thruster. In 40th AIAA Aerospace Sciences Meeting & Exhibit. American Institute of Aeronautics and Astronautics, AIAA-2002-0348, 2002.

[16] R. Betzendahl. Ever Changing Rare Gas Market. *CryoGas International*, 2013.

[17] R. Welle. Xenon and Krypton Availability for Electric Propulsion: An Updated Assessment. Proceedings of the AIAA/SAE/ASME/ASEE 29th Joint Propulsion Conference and Exhibit, AIAA 1993-2401, 1993.

[18] S. Mazouffre, K. Dannenmayer, G. bourgeois, A. Lejeune. Performances of a variable channel width hall thruster operating with xenon and krypton. In Proceedings of the 3rd Space Propulsion Conference, Bordeaux, France, 2012.

[19] S. Mazouffre, G. Bourgeois, K. Dannenmayer, A. Lejeune. Ionization and acceleration processes in a small, variable channel width, permanent-magnet Hall thruster. *J. Phys. D: Appl. Physics*, 45(185203), 2012.

[20] C.E. Carlston, G.D. Magnuson and P. Mahadevan. Electron ejection from single crystals due to 1- to 10-keV noble-gas ion bombardment. *Phys. Rev.*, 139(3A), 1965.

[21] M.L.R. Walker, R.R. Hofer, A.D. Gallimore. Ion collection in Hall thruster plumes. *J. Propul. Power*, 22(1):205, 2005.

[22] J. Vaudolon and S. Mazouffre. Data and performance analysis of EPL diagnostic tools for their use in qualification testing. Technical report, PE-R-10-2014, ICARE, CNRS, 2014.

Chapter 6

Hall thruster advanced designs[1]

Contents

THE main drawback of conventional Hall thrusters is their relatively short operational lifetime. The primary factor that limits the lifetime is the erosion of the dielectric annular channel walls due to high-energy ion bombardment. In addition, plasma-wall interaction also generates power losses and thermal stress on the structure components. The large particle flux toward the walls is a direct consequence of the magnetic topology.
In a HT, the accelerating electric field originates in a decrease of the electron mobility at the channel exit. An efficient barrier necessitates a radial magnetic field of which the lines intersect the walls. Recently, an original approach to significantly reduce the erosion rate, thereby prolonging the thruster lifetime, was proposed and validated. This approach is termed magnetic shielding (MS)[1,2]. MS consists in preventing the magnetic field lines from crossing the walls in the acceleration region. Instead, the lines remain parallel to the wall of the downstream channel section and extend to the anode region to collect cold electrons. Such a topology strongly reduces the radial electric field component magnitude, thus decreasing wall material sputtering.
There is another, more drastic alternative, to limiting the interaction between plasma and surfaces in a HT. The principle is to entirely shift the ionization and acceleration regions outside the cavity. This unconventional design is named here a Wall-Less Hall Thruster, or WL-HT in short. Such an unusual configuration was in fact first explored during the 90's in Russia by Kapulkin et al[3,4]. At that time, the concept was introduced as a Hall thruster with an external electric field. However, due to a presumed ion current limitation linked to plasma instabilities, researchers moved from a standard one-stage architecture to a two-stage architecture. The design and operation of the latter are more complicated, making

[1] Adapted from:
S. Mazouffre, S. Tsikata and J. Vaudolon *J. Appl. Phys.*, **116**, 243302 (2014)
S. Mazouffre, J. Vaudolon et al. *IEEE Transactions on plasma science*, **42**, 2668 (2014)

the concept somewhat less attractive. In this research, the WL-HT concept has been considered, firstly with the PPI for preliminary characterization. Then, the PPS-Flex was used as proving ground for the anode and magnetic topology optimization.
A visual evidence of magnetic shielding has been obtained with the PPS-Flex during the test campaign 2013. Based on these first experiments, a 200 W magnetically-shielded Hall thruster, termed PPI-MS, has been designed. The testing of the PPS-Flex, and the PPI-MS development are discussed in Sec. 6.1. The wall-less design is presented in Sec. 6.2, in which the first experimental results with the PPI and the PPS-Flex are presented. Conclusions are given in Sec. 6.3.

6.1 Magnetically-shielded Hall thruster

6.1.1 Magnetic shielding background and theory

Background

In 2010, Aerojet and Lockheed Martin Space Systems successfully extended the qualification test of BPT-4000 beyond 10,400 h[5]. The data from the test indicated no measurable erosion of the channel ceramic walls between 5,600 h and 10,400 h. The simulation of the BPT-4000 discharge has shown that the particular magnetic topology of this thruster, near the inner and outer walls having receded to a geometry coherent with a 5,600 h of operation, had three consequences which led to significantly reduce the erosion rate:

- the reduction of the electric field perpendicular to the wall, prohibiting ions from acquiring a significant impact energy,
- the reduction in potential fall in the sheath along the ceramic, lowering the maximum kinetic energy ions could gain before striking the material,
- the decrease in ion number density, thereby in ion flux at the wall.

The ceramics appeared shielded from any significant ion bombardment. A topology such as that of the BPT-4000 in steady-state configuration was thus appropriately termed "magnetic shielding". The first principles of magnetic shielding were then validated on the H6 Hall thruster at the Jet Propulsion Laboratory, after its magnetic field and channel geometry were modified from a standard, unshielded topology[6]. The thruster performance was maintained (the efficiency slightly decreased by 1 %, which is within the measurement uncertainty), the erosion rate is reported to be 100 to 1,000 times lower than conventional early-of-life channel designs and operation up to 800 V is possible[6,7]. The magnetic shielding developments in the U.S. now span the power level from 300 W to 20 kW[8–10].

Theory

In a Hall thruster, the self-magnetic field produced by the azimuthal electron current has a magnitude of only a few Gauss[11]. Therefore, it is fair to assume that the magnetic field is stationary, so that the Maxwell-Faraday equation is written

$$\nabla \times \mathbf{E} = 0, \text{ and therefore } \mathbf{E} = -\nabla\phi, \tag{6.1}$$

where ϕ is the plasma potential. Additionally, considering that the electron mass is small enough to neglect inertia, and that resistive terms along a magnetic field line are small[12], the electron momentum equation along the lines of force reduces to

$$E_{/\!/} = -\frac{\nabla_{/\!/}\mathbf{P_e}}{en_e}, \tag{6.2}$$

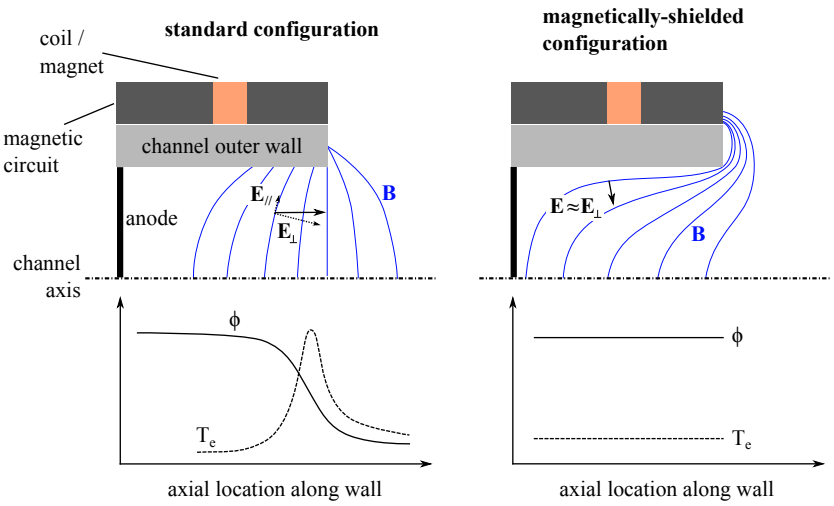

Figure 6.1: Schematics of the magnetic field lines in standard (left) and shielded (right) configurations. The typical profiles for ϕ and T_e along the channel wall are represented at the bottom.

with $/\!/$ denoting parallel components in the frame of reference of the magnetic field, $\mathbf{P_e}$ the electron pressure tensor and n_e the electron number density. The same arguments apply to the electron energy equation[13], which leads to the isothermalization of the lines of force first reported by Morozov[12]

$$\begin{cases} \nabla_{/\!/} T_e \approx 0, \\ E_{/\!/} \approx -\dfrac{k_B T_e}{e} \dfrac{\nabla_{/\!/} n_e}{n_e}. \end{cases} \tag{6.3}$$

Therefore, though each line is isothermal, ϕ varies due to electron pressure (T_e is never zero), which allows the existence of a non-zero electric field parallel to the magnetic field. Ion can thus be accelerated towards the channel walls if the magnetic field lines cross the surface of the material. Figure 6.1 (left) shows typical field lines in a single-stage Hall thruster. Since the lines are nearly radial, the evolution of T_e and ϕ along the wall resembles that along the channel centerline. A large ion flux is driven by the elevated T_e and $E_{/\!/}$. In the magnetic shielding approach, the field lines are curved towards the anode, in a way that sustains near the channel walls a ϕ as close as possible to the anode potential, and a low T_e by capturing the coldest electrons, located in the channel upstream end, see figure 6.1 (right). The ion flux towards the wall is thus marginalized. A proper magnetic topology orientates $\mathbf{E}$ nearly perpendicular to the field lines, in order to accelerate ions away from the walls.

6.1.2 Visual evidence of magnetic shielding with the PPS-Flex

The first realization of magnetic shielding outside the United States has been performed with the PPS-Flex, during the test campaign 2013, in Orléans, France. Figure 6.2 (left) shows a photograph of the PPS-Flex thruster fired at 250 V and 3.5 mg/s of xenon anode flow rate in a standard unshielded magnetic configuration, where the force lines are perpendicular to the $BNSiO_2$ walls at the exit of the channel. Notice the conical section only serves to protect the inner and outer coils of the upper stage. The plasma is concentrated inside the straight section of the channel where it interacts with the walls. Figure 6.2 (right) is a photograph of the PPS-Flex in what is believed to be a magnetic shielding (MS) configuration under similar operating conditions to figure 6.2 (left). In

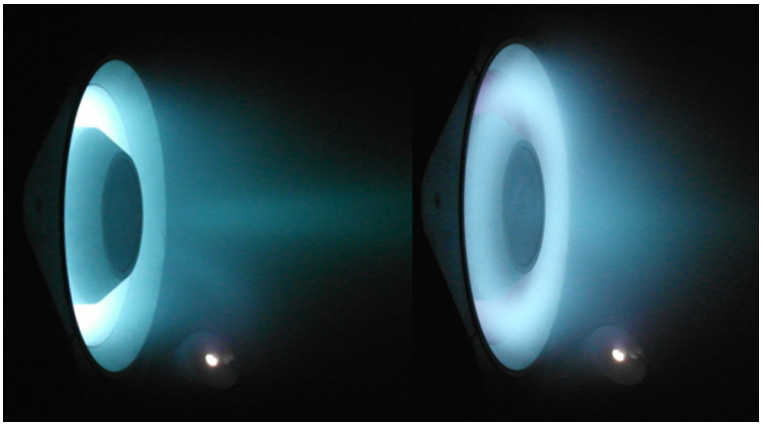

Figure 6.2: Photograph of the PPS-Flex Hall thruster operating with xenon at 250 V and 3.5 mg/s. (Left) Standard unshielded magnetic configuration with the lines perpendicular to the channel walls. The plasma is localized inside the channel (the 45° conical element is used to protect the last coil stage). (Right) MS configuration with the lines parallel to the walls both in the conical section and in the upstream end of the channel. The plasma is mostly localized in front of the channel. As expected, interaction with the walls is reduced as illustrated by the low-light intensity inside the channel and in the vicinity of the cone surface.

figure 6.2 (right), the plasma forms a torus beyond the channel exit. The ionization and acceleration zones are then shifted downstream, which explains the low-light intensity inside the channel. The plasma is also detached from the walls, as illustrated by the presence of a dark area in the conical part between the plasma and the surface. The dark space near the walls, which is due to a local reduction in the electron temperature, is better defined in the figures of Hofer et al.[1]. In their work, visual evidence for MS was observed, and MS was confirmed through direct plasma measurements. The faint boundary seen in our picture originates in the fact that the magnetic field lines do not extend deeply into the channel, preventing the capture of cold electrons. Finally, the ion beam is less dense with MS in the PPS-Flex and the central part of the ion beam is less luminous. This results from the low-maximum magnetic field intensity applied, only 90 G, due to the coil current limit set for this topology. The thrust level is, therefore, much lower than in the unshielded case, 34 mN against 44 mN, contrary to what has been obtained by JPL[1,2]. The ultimate proof of the attainment of MS with this thruster will, nevertheless, necessitate plasma properties measurements at the walls.

6.1.3 Design of a magnetically-shielded low-power HT

The PPI-MS is a 200 W Hall thruster which possesses a magnetic shielding B field configuration[1,2]. The PPI-MS has been designed with the following constraints:

- the anode is the same than that used for the PPI Mag,
- the rear plate is that of the PPI Mag,
- the tightness is ensured using standard fluorocarbon seals,
- the set of ceramics of the standard PPI-Mag stays unchanged,
- the SmCo magnets of the PPI are used instead of the PPI-Mag annular rings. The gap which exists between the magnets can thus be used to pass diagnostics (such as a Langmuir probe), through the assembly, to perform near-wall measurements.

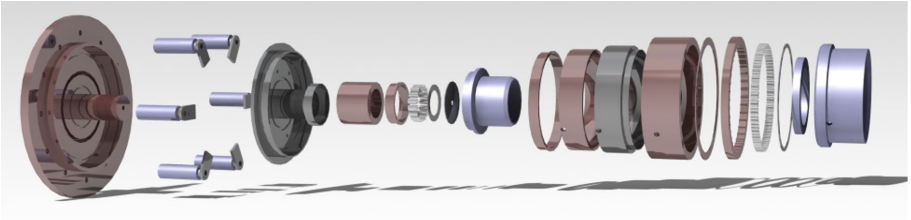

Figure 6.3: Parts that compose the PPI-MS. The PPI-MS magnetic circuit is made of Armco®iron. A large number of copper parts conduct the heat load to the radiator, which is located behind the copper plate interface, at the far-left of the figure.

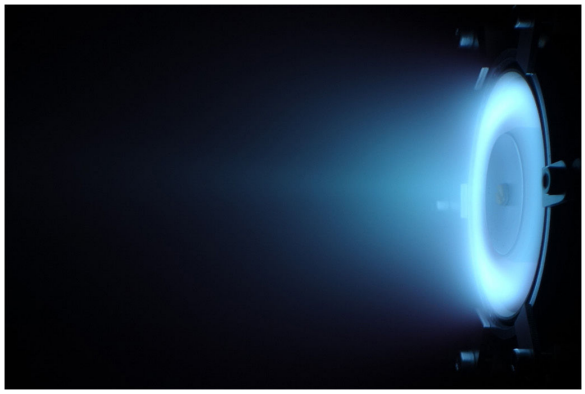

6.4.1: Operation of the PPI-MS in MS configuration.

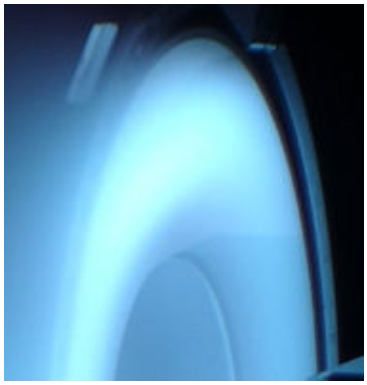

6.4.2: A clear line of sight is visible along the channel wall.

Figure 6.4: The PPI-MS operating in the NExET vacuum chamber in MS configuration.

- The maximum radial component of the magnetic field is close to that measured for the PPI-Mag standard configurations,
- the grazing line must reached the anode region. As defined in the work of Hofer and co-workers[2], this is the line that extends deepest into the channel and runs closest to the wall without crossing it.
- The magnetic circuit manufacture tolerance requirements must be standard (on the order of 0.1 mm),
- the number of iron parts must be minimized in order to limit deviances from the numerically-evaluated magnetic topology, when assembling the circuit.

The parts that compose the thruster are shown in figure 6.3. The Armco®iron pieces that conduct the magnetic flux, and the copper rings that drive the heat loads are presented. A photograph of the PPI-MS is presented in figure 7, in the introduction. An annealing process has been applied to the iron parts after machining to fix their magnetic properties.

The PPI-MS is shown in operation in the NExET vacuum chamber in figures 6.4.1 and 6.4.2. The plasma appears to be detached from the walls, which constitutes a crucial visual evidence that is in favor of an effective shielding of the walls from the plasma. Several experiments are ongoing at the ICARE Lab to confirm the shielding, and to precisely characterize the plasma. At the present time, the PPI-MS is the smallest magnetically-shielded Hall thruster in the world.

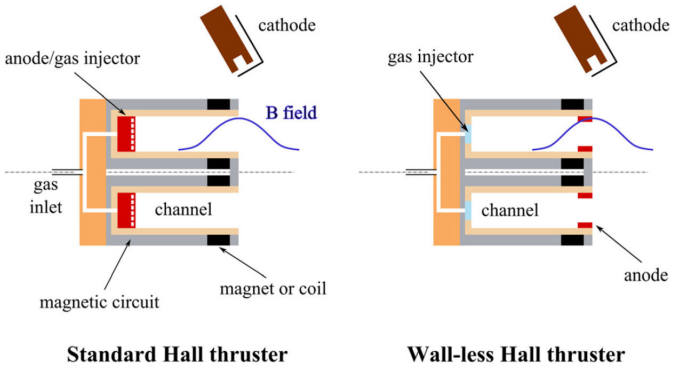

Figure 6.5: (Left) Layout of the configuration of a standard single-stage Hall thruster. The anode is placed at the back of an annular ceramic channel. The magnetic field is maximum at the channel exit plane. (Right) Basic transformation into a wall-less HT. The anode is shifted towards the channel exit plane. The other elements remain unchanged.

6.2 Wall-less design

The standard configuration of a Hall thruster is schematically depicted in figure 6.5. Additional details can be found elsewhere[14–16]. The anode is placed at the back of an annular ceramic channel. In many designs, the anode is also used as a gas injector. The cathode, which produces the electron current for discharge balance and ion beam neutralization, is located outside the channel. To shift both the ionization and the acceleration regions outside the thruster cavity, the simplest way is to move the anode at the channel exit plane, as illustrated in figure 6.5, without other modifications. The thruster shape and size remain unchanged, as do the cavity material and the magnetic topology. This is the basic method for transforming a Hall thruster into a Wall-Less Hall Thruster (WL-HT). However, optimization of the thruster in its new configuration will certainly require other changes. When moving the anode to the exit, one of two conditions must be fulfilled to minimize ion losses inside the channel: the potential drop inside the channel, if any, must be limited, and/or the ion fraction inside the channel must be small.
A Wall-Less Hall thruster is not a Thruster Anode Layer, as there is no guard ring at the cathode potential in front of the anode to localize the potential drop[15,17]. In a WL-HT, the distribution of the plasma potential downstream the exit plane is solely fixed by a balance between ionization and diffusion processes in a magnetized plasma.

6.2.1 First experiments with the PPI

A photograph of the WL-HT prototype constructed in our laboratory is shown in figure 6.6. The prototype is based on the architecture of the PPI, which has been described in the introduction. In this study, the channel dielectric walls of the WL-HT were made of $BNSiO_2$. The channel was in the $2S_0$ configuration. The anode used for the wall-less prototype is a 5 mm-wide stainless steel ring. It is wound around the external wall at the channel exit plane, where the magnetic field amplitude is the highest. Notice that both gridded disk and ring anode shapes have been tested, but the standard magnetic configuration of the PPI, without modification, is in favor of a ring-like anode. Xenon is used as a propellant gas. A heated hollow cathode with a LaB_6 insert was used with a constant xenon flow rate of 0.2 $\mathrm{mg/s}$. The cathode orifice was placed 10 cm below the thruster symmetry axis in radial direction and 3 cm away from the channel exit plane in axial direction. The cathode and the thruster body are floating but unbound.

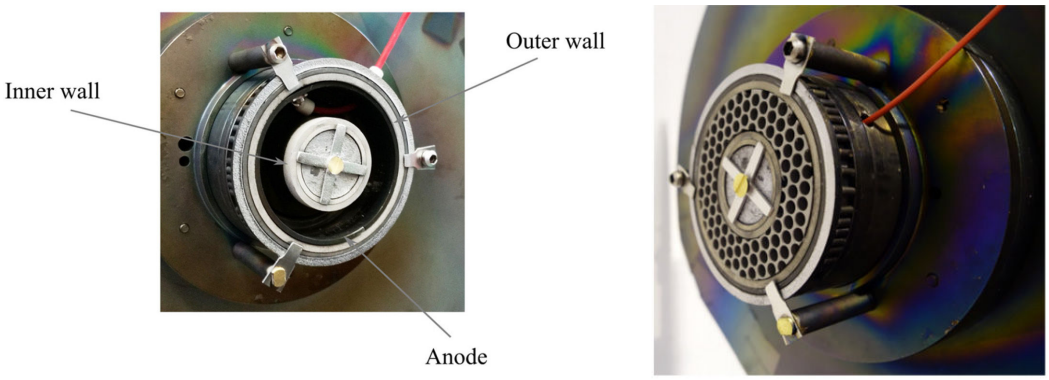

Figure 6.6: Photograph of the 200 W-class WL-HT prototype. Both ring (left) and gridded disk (right) anode shapes have been tested.

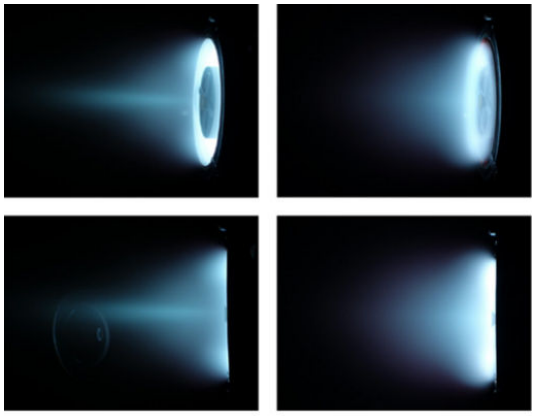

Figure 6.7: (Left) Photographs of the low-power Hall thruster firing with Xe at 200 V and 1 $\mathrm{mg/s}$ in standard configuration. (Right) Photographs of the WL-HT prototype firing with Xe under identical conditions. In the latter case, the anode is a conducting ring located at the channel exit plane around the external wall.

Source operation

Figure 6.7 shows a set of photographs of the low-power ion source firing with Xe in the NExET vacuum chamber, in the standard configuration and in the wall-less configuration, with a ring anode. Pictures were taken with the same camera settings. The discharge voltage was equal to 200 V and the gas mass flow rate to 1 $\mathrm{mg/s}$. The background gas pressure inside the tank was 3.5×10^{-5} mbar-Xe.
The photos show that the plasma discharge is moved outside the dielectric cavity in the wall-less configuration, as illustrated by the strong light intensity in front of the exit plane. It is also interesting to note that the ion beam boundaries are less sharp in the WL configuration. For instance, the brightness of the on-axis, collimated structure that originates from the interaction of elementary beams from opposite sides of the channel, seen in the photographs on the left, is fainter in the WL configuration, which certainly images deteriorated performance. According to the photos, the WL configuration is expected to lead to a larger ion beam divergence angle. As a consequence, the thrust will be lower, and the wear of the external parts like the pole pieces could be increased. In addition, a large beam divergence has a negative impact on the interaction between the plasma and the spacecraft elements.

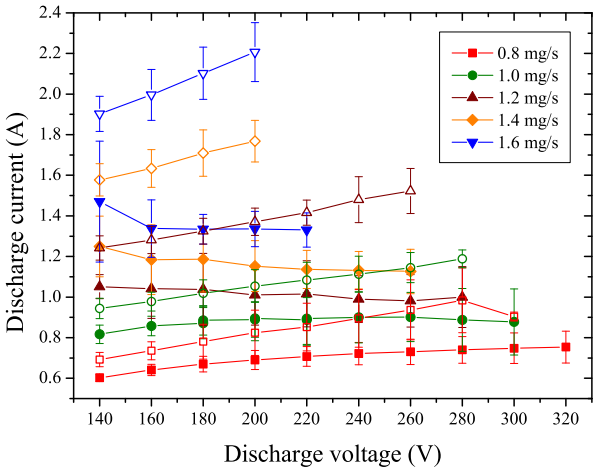

Figure 6.8: Anode discharge current against applied discharge voltage for several xenon mass flow rates in the standard (full symbols) and WL-HT configurations (open symbols). Error bars indicate the current standard deviation.

Current-voltage characteristics

The graph in figure 6.8 shows the anode discharge current as a function of the applied voltage for various xenon gas mass flow rates. The current-mass flow rate envelope is similar for the two configurations, i.e. the thruster can operate with the same parameters. However, the discharge current is higher in the case of the WL-HT whatever the voltage-flow rate couple. The difference increases with the gas flow rate and the applied voltage. Moreover, the rate of change in I_d with U_d is positive in WL, whereas it is negative in standard mode for most flow rates. As the maximum input power is allowed to exceed 300 W only for a short time to prevent damage to the device, the WL mode is limited in voltage at large mass flow rate. As can be seen in figure 6.8, at 200 V, the current increases from 1.34 A to 2.21 A when the configuration is switched from a standard to a WL-HT mode (an increase of 65 %). Such an increase cannot be attributed to an improved gas ionization. The large discharge current in the WL mode is due to a larger diffusion of the electrons, in other words a less efficient electron confinement, in the region of strong magnetic field. With the non-optimized WL-HT thruster design, the electron resistivity is reduced in front of the thruster, see figure 6.5. With a classical topology, magnetic field lines are perpendicular to the walls at the channel exhaust. Therefore many lines intersect the anode in WL mode, making the passage of hot electrons coming from the outside plasma to the anode easier. The fact that electrons cannot transfer a large fraction of their energy to the gas in this WL design implies a lower ionization degree.
Figure 6.8 also shows that the discharge current standard deviation is not greatly affected when the anode is moved towards the channel exit plane. This confirms the oscillation level of the breathing mode does not depend on the configuration, see figure 6.9. This fact reveals that the ionization and acceleration mechanisms do not change overall. In other words, the underlying physics remains unchanged at the macroscopic level.

Discharge current waveform

The discharge current waveforms measured on the anode line at 200 V and 260 V and 1 $\mathrm{mg/s}$ are presented in figure 6.9 for the two thruster configurations. The current was measured with a calibrated Tektronix TCP202 DC coupled current-probe (DC to 50MHz

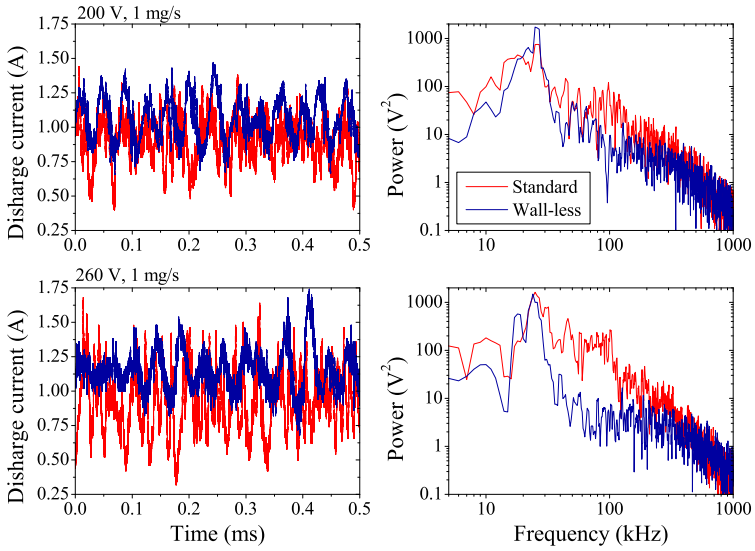

Figure 6.9: (Left) Discharge current waveforms of the thruster in the standard configuration and in the wall-less configuration for two different applied voltages. (Right) Corresponding power spectra computed using a FFT algorithm.

bandwidth). The mean value of the discharge current is always larger in the WL-HT. At 200 V and 260 V, it is, respectively, 1.05 A and 1.14 A for the WL-HT. At 200 V and 260 V, the current is, respectively, 0.89 A and 0.90 A in the standard thruster. On the contrary, the standard deviation of the discharge current is lower is wall-less mode. At 200 V and 260 V, it is, respectively, 0.16 A and 0.15 A for the WL-HT. At 200 V and 260 V, the dispersion is, respectively, 0.17 A and 0.24 A for the standard thruster. As in a conventional Hall thruster, the current trace of a thruster with an external discharge exhibits low-frequency oscillations in the 10-30 kHz range, which corresponds to the well-known breathing mode[18]. Such oscillations, which find their origin in an ionization instability, can be interpreted in terms of a predator-prey mechanism between atoms and ions[19,20].

Also shown in figure 6.9 are the power spectra associated with the discharge current time series. The power spectra were computed using a FFT algorithm. In figure 6.9, the breathing oscillation frequency is between 20 kHz and 25 kHz. The breathing frequency is not influenced by the thruster design, an indication that the main physical processes that govern ionization in the cross-field discharge remain unchanged. The power spectrum also shows strong oscillations around 100 kHz in the standard configuration. These oscillations encompass phenomena such as rotating instabilities and ion transit time instabilities[18]. These oscillatory phenomena are absent, or at least much weaker, in the WL-HT, whatever the operating conditions.

The discharge current is a macroscopic quantity that includes oscillatory contributions from many physical processes. This quantity determines part of the thruster performance, and its oscillations represent one of the major concerns for power processing units. Recently, Coche and Garrigues have developed a (r,θ) particle-in-cell model of a Hall thruster[21]. The simulation of a SPT100 Hall thruster at nominal operating point has shown a bimodal discharge current, which looks like the pattern in figure 3.1[21]. A high-frequency oscillation is superimposed to the breathing oscillations, only on the decreasing portions of the discharge current. The discharge current waveform of the PPI, operating in the wall-less mode, at 200 V and 0.9 mg/s of xenon, is presented in figure 6.10. An agree-

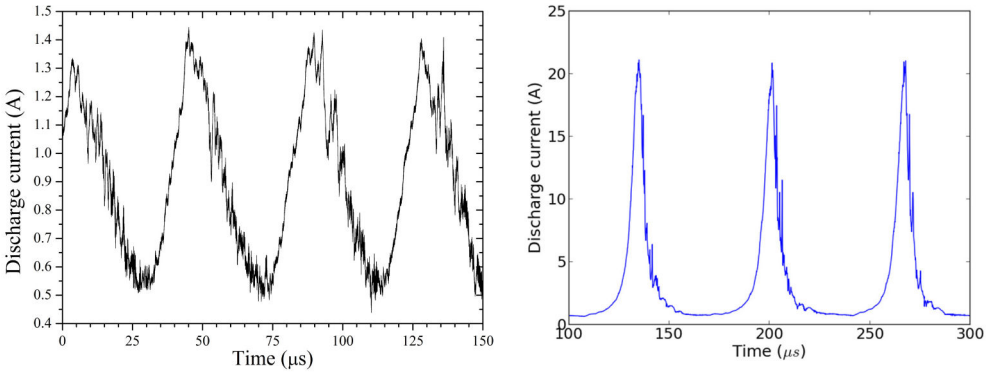

Figure 6.10: (Left) Discharge current waveform of the PPI in wall-less mode operation, at 200 V and 0.9 mg/s of xenon flow rate. (Right) Discharge current pattern computed by Coche and Garrigues, for a SPT100 HT operated at 300 V and 5 mg/s of xenon anode flow rate (reproduced from the paper of Coche and Garrigues[21]).

ment is found between the shapes of the experimental and numerical waveforms. It can be assumed that the WL-HT is a tool of strong interest to distinguish between the channel wall and plasma instabilities contribution to the discharge properties. It is believed that the absence of interaction with the ceramics in the WL mode has made it possible to match the (r,θ) simulation, which cannot account for interaction with the channel walls, even though the simulation domain does not reflect the PPI dimensions. More comparisons are required between simulations and experiments, with similar geometry and operating points.

Ion velocity and electric field distribution

The time-averaged distribution of the axial velocity component of metastable Xe^+ ions was measured along the channel axis of the PPI, by means of laser induced fluorescence spectroscopy, at 834.72 nm, for the two configurations. Details about the LIF technique and the experimental arrangement can be found in Chapter 1. In figure 6.11, the most probable ion velocity, i.e. the velocity for which the ion velocity distribution function (IVDF) is the highest, is plotted as a function of the position along the channel axis, for a discharge voltage of 200 V and a gas flow rate of 1 mg/s. The position 0 mm refers to the channel exit plane. With a standard design, the ion acceleration process starts upstream of the exit plane. At 0 mm, the ion velocity is already 5,200 m/s. Beyond the exit plane, the ion velocity increases over a short distance of about 20 mm and reaches a maximum of 15,200 m/s. With the wall-less prototype, the acceleration region is entirely shifted outside the channel. The velocity is typically 150 m/s inside the channel. This value is close to the thermal speed for xenon atoms at 300 K. The maximum velocity is 13,510 m/s. It is worth noting that the atom velocity is typically 500 m/s at the channel exhaust in the standard configuration[22,23]. This large atom velocity, well above the thermal speed, can only be explained by taking into account ion recombination at the walls to form fast neutrals[23]. The very low ion axial velocity inside the cavity of a WL-HT source is therefore an indirect proof that plasma-surface interaction has been strongly reduced.
The accelerating potential, V_b, also called the beam energy, corresponds to the potential drop experienced by the ions. It is directly computed from the velocity. In the standard configuration, V_b is 160 eV, whereas it is only 120 eV in the WL-HT. The low final ion axial velocity, i.e. the low beam energy, in WL configuration indicates a poor energy conversion efficiency in the axial direction. Energy losses may originate in the strong

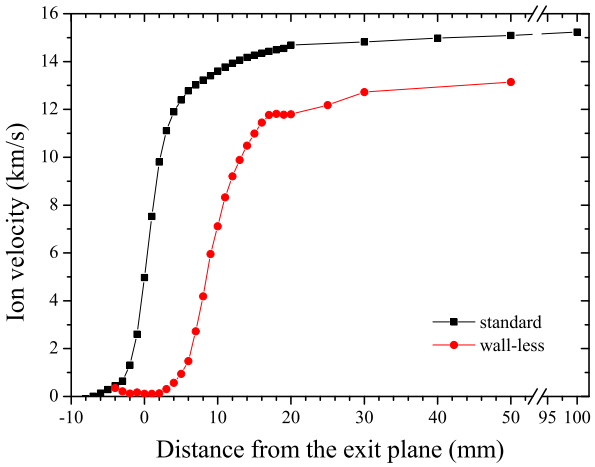

Figure 6.11: Most probable Xe^+ ion velocity along the channel axis of the ion source in standard (square) and WL-HT (circle) configurations (200 V, 1 mg/s).

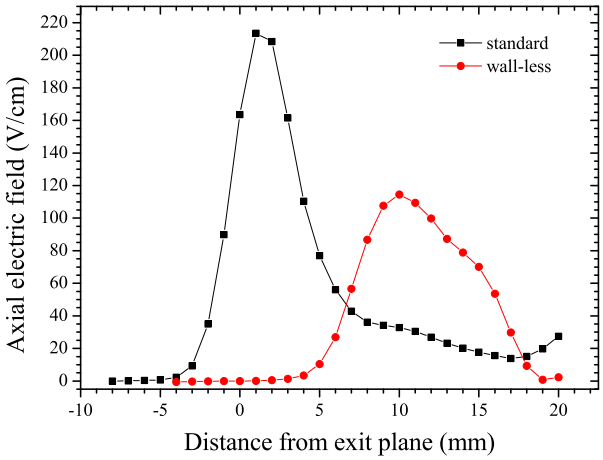

Figure 6.12: Accelerating electric field distribution along the channel axis of the ion source in the standard (square) and WL-HT (circle) configurations (200 V, 1 mg/s).

curvature of the magnetic field lines in the acceleration region, which makes the ion beam diverge, as suggested by figure 6.7. The low beam energy indicates that the WL configuration must be improved and optimized. Possible ways are discussed further.

In steady-state conditions, the accelerating electric field profile can be directly inferred from the profile of the ion velocity axial component using the energy conservation equation[22,24]. The electric field distribution along the channel axis of the WL-HT is shown in figure 6.12 for 200 V and 1 mg/s. The electric field profile measured in the conventional configuration is also shown in figure 6.12 for comparison. As expected, the electric field is situated outside the cavity in the WL-HT. The length of the acceleration region is about 15 mm, similar to the size observed with the standard configuration. The shift of the electric field towards the exterior has been observed for other experimental parameters: 150 V and 0.8 mg/s ; and 85 V and 1.3 mg/s[25]. The wall-less condition is only driven by the anode position, but the electric field shape depends on the operating parameters.

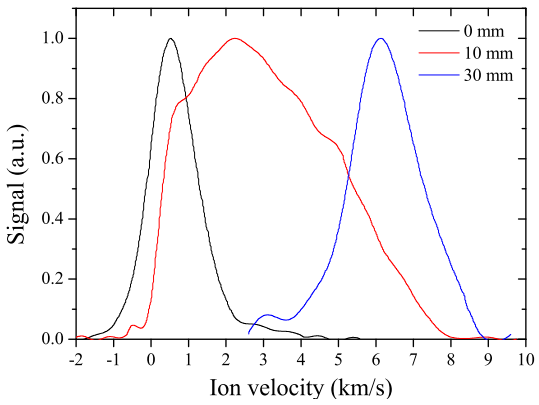

Figure 6.13: Xe^+ IVDF at 3 positions along the channel axis of the wall-less HT (85 V, 1.3 mg/s). The position 0 mm refers to the exit plane.

Ionization

A direct measurement of the spatial extent of the ionization region, e.g. by means of a Langmuir probe, is not yet available. We have, however, indirect evidence that a large fraction of ions are produced outside the channel. Figure 6.13 shows three normalized Xe^+ IVDF measured by near-infrared LIF along the channel centerline of the WL-HT, at 85 V and 1.3 mg/s. The width, or dispersion, of the IVDF is observed to change with axial position. The IVDF is relatively narrow at the exit plane as well as far downstream. In contrast, the IVDF is very broad a few millimeters behind the exhaust. In a Hall thruster discharge, the ion velocity dispersion is mostly determined by the overlap between the ionization region and the acceleration region[22]. Moreover, the largest dispersion indicates the end of the ionization region[22,26]. With a standard design, the ionization layer ends at the exit plane. The shape of the IVDF in figure 6.13 shows that a large part of the ionization process occurs outside the channel of the wall-less Hall thruster, as the highest dispersion is reached beyond 10 mm.

Erosion and thermal state

Visual observation of the thruster prototype while firing, and measurements of various quantities, indicate that a non-optimized WL configuration leads to a high plume divergence angle and to a large discharge current, with possible consequences for the erosion level and thruster heating. There was no visible sign of accelerated erosion of pole pieces or other elements after several tens of hours of operation. Similarly, we did not observe deposit formation inside the ceramic channel. However, more precise erosion measurements and longer-term endurance testing will be necessary to confirm these preliminary observations.
The temperature of the WL-HT components was not recorded during the campaign. However, at large gas mass flow rates, i.e. when the discharge current is large (see figure 6.8), hot zones appeared on the anode ring and the thruster could only be operated for a few minutes, an indirect evidence that the thermal load of a WL-HT is large compared to a standard configuration. Despite the shifting of the acceleration region beyond the exit plane, the particle flux to the walls at the location of the anode is considerable. Optimization of the magnetic topology should limit this flux.

First conclusions

In summary, the discharge can be ignited and it is stable in wall-less configuration. The electric field profile and the ionization zone are shifted outwards the channel, as expected. The electric field exists in a region with no physical boundary in the radial direction and where the magnetic field gradient is negative. The interaction between high energy ions and ceramic surfaces is therefore negligible in a WL Hall thruster. This aspect is obviously of great relevance for allowing high-voltage operation and for prolonging the lifetime of the device. Moreover, the low-frequency oscillations of the discharge current are not modified in a WL configuration, which warrants the conservation of the physical mechanisms at the origin of the thrust.
However, measurements show that the discharge current is much higher in the wall-less mode. The thermal load experienced by the thruster is also large, and the beam energy is low. The efficiency of the device is therefore limited. The first low-power thruster prototype was intended for demonstrating the validity of the wall-less concept, and for obtaining some insights into the discharge and ion beam properties. Although the WL-HT concept has proven to be valid, experimental outcomes nevertheless reveal that the design must be optimized, in order to reach an acceptable performance level.

6.2.2 Optimization of the wall-less design

Anode geometry and magnetic topology

Figure 6.14 (left) illustrates the interaction between the anode and the magnetic field lines in the basic configuration of the first WL Hall thruster prototype. As previously explained, the B field lines are perpendicular to the thruster axis with a standard magnetic topology and they intercept the anode that is placed at the channel exhaust. The magnetic confinement therefore becomes much less efficient. A large fraction of hot electrons originating from the external cathode and trapped along B field lines are directly lost at the anode. The discharge current is therefore high and the ionization degree decreases.
In order to prevent electron losses at the anode, the magnetic barrier must be restored. The basic idea is to make the magnetic field lines parallel to the anode surface. The anode could be rotated at 90° without changing the magnetic topology. This design is, however, not efficient for two reasons, namely: (i) a large fraction of the magnetic flux is injected into the channel and it does not play any role in the electron trapping and thrust production and (ii) the magnetized region, where ionization and acceleration take place, is short, i.e. the number of electron-atom collision events is rather low. Figure 6.14 (right) exemplifies a more suitable design. The magnetic barrier is located in front of the channel exit plane by injecting the magnetic flux in the axial direction. The maximum of the B field magnitude is then shifted outside the cavity. The anode is still placed at the channel exhaust, but its shape is curved to avoid any interaction with the magnetic field lines: the lines never cross the anode surface. The optimized WL magnetic topology resembles the magnetic shielding (MS) topology[13,27]. There is nevertheless one main difference: the magnetic field lines do not have to extend deep into the channel to capture cold electrons. This difference makes easier the generation of a WL topology, compared to a MS topology.

Experimental campaigns with the PPS-Flex Hall thruster

The optimization of the wall-less design has been investigated with the second version of the PPS-Flex Hall thruster[28,29]. This new version is fitted with additional heat pipes and with 8 large external radiators to reach a high input power level, without damaging the magnetizing coils and the circuit. The thruster has been fired up to 2 kW without

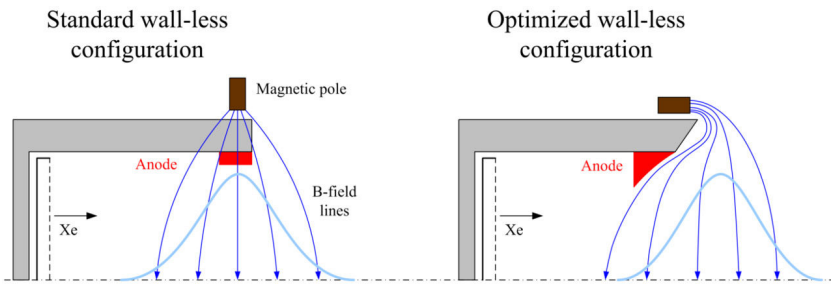

Figure 6.14: (Left) Basic configuration of a wall-less Hall thruster: The anode is simply moved at the channel exit plane. The magnetic field lines intercept the anode. (Right) Optimized wall-less design: The magnetic field lines are parallel to the anode.

troubles. Figure 6.15.1 shows a photograph of the PPS-Flex Hall thruster in WL configuration mounted on the thrust stand of the PIVOINE-2g test facility vacuum vessel in Orléans.
In the WL configuration, the PPS-Flex is equipped with a curved anode split in two parts, as can be seen in figure 6.15.1. The inner and outer rings are located at the exit plane of the straight section of the $BNSiO_2$ channel, and are connected to one another. Note that the straight cavity corresponds to the cavity of the PPS ®1350 thruster. The conical section is used to protect the last magnetic stage[28]. The magnetic topology has been changed and optimized during the experiments. The typical topology is given in figure 6.14. Two experimental campaigns were performed:

- The optimization procedure was first tested at the ESA Propulsion Laboratory (ESA-ESTEC), in the Netherlands, in October 2014. The PPS-Flex in WL mode was fired in the CORONA vacuum chamber. Preliminary testing validated the optimization approach for the topology. The discharge current drastically decreased when switching from a standard magnetic map to a WL map, as expected.

- A second campaign was conducted at ICARE, in the PIVOINE-2g facility vacuum chamber, in April 2015. The anode geometry and the magnetic map have been further optimized to reach a high thrust efficiency. Several quantities have been acquired: the thrust, the discharge current time series, the ion current density profile and the thruster component temperature by means of calibrated infrared thermal imaging[30,31]. During this campaign, the thruster was operated over of broad range of parameters: $U_d = [200\text{-}500]$ V, $\phi_a = [2\text{-}3.5]$ mg/s, power $= [400\text{-}1,500]$ W.

A heated hollow cathode with a LaB_6 insert was used with a constant mass flow rate of 0.4 mg/s during the two campaigns. The cathode and the thruster body were floating but unbound.
A picture of the PPS-Flex thruster in WL configuration firing with Xe in the PIVOINE-2g chamber is displayed in figure 6.15.2. This photograph must be compared with the picture of the first WL prototype displayed in figure 6.7 (right). When optimizing the design, the contrast ratio is high, boundaries are sharp, and the plume structure is well-defined, as it is the case with a high-efficiency Hall thruster. The discharge is bright inside the conical channel and a spike of plasma extends far downstream along the channel centerline. The plume is in the so-called "spike mode" in figure 6.15.2.

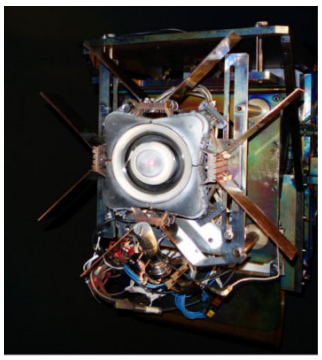

6.15.1: PPS-Flex Hall thruster in WL configuration.

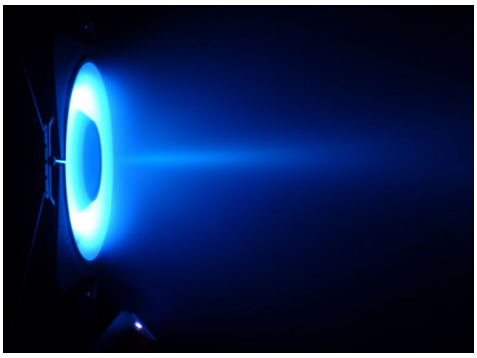

6.15.2: Wall-less PPS-Flex operating with xenon.

Figure 6.15: (Left) Photograph of the PPS-Flex Hall thruster in WL configuration mounted onto the thrust balance of the PIVOINE-2g test bench. (Right) Photograph of the PPS-Flex in WL configuration, operating with xenon ($U_d = 350$ V, $\phi_a = 2.5$ mg/s).

Current measurements

The discharge current was measured as a function of the applied voltage for several magnetic topologies. Figure 6.16.1 illustrates the results obtained at the EPL with the PPS-Flex. The anode geometry was not optimized in this case. As can been seen, the current decreases drastically when switching from a standard-like to a wall-less-like magnetic topology. A similar trend was observed with larger xenon anode mass flow rates.
During the campaign at EPL, the ion current density was measured by means of a Faraday cup on the thruster centerline. Results are shown in 6.16.2 for several applied voltages and for 3 magnetic topologies, with $\phi_a = 3.5$ mg/s. Here MS refers to a Magnetic Shielding-type topology. With the anode placed at the exit plane, the ion current density is the highest for a WL magnetic configuration, whatever the voltage. The on-axis value reaches 1 $\mathrm{mA.cm^{-2}}$ at 300 V, which is typical at this distance (70 cm) for a well-designed Hall thruster.
The experimental outcomes therefore confirm (i) the increase in discharge current observed with the first prototype is due to the electron fluid (ii) the magnetic confinement can be restored with a well-defined B field and (iii) the ion current can be large with an optimized magnetic field map for a WL configuration.

The anode geometry and the magnetic topology have been optimized prior to testing the PPS-Flex in the PIVOINE-2g facility vacuum vessel, in April 2015. As illustrated in 6.2.2, the interaction between the anode and the magnetic field lines in the basic configuration of the first WL Hall thruster prototype have imposed considerable thermal stress on the anode, and prevented a long operation. Once the anode and B field optimized, the PPS-Flex could be operated for standard periods of time. Figure 6.17 shows the evolution of the discharge current mean value, and oscillation standard deviation, during a stability test. The PPS-Flex was operated at 300 V and 3.0 mg/s of xenon flow rate, for 1 h. The discharge current reached a steady state at 2.75 A with a standard deviation of 0.4 A after 30 min. During the first half an hour, the discharge current increased up to 2.83 A with a standard deviation of 1.0 A before decreasing towards a constant value, see figure 6.17. The curved anode was able to sustain the thermal load. We did not observe the formation of hot zones.

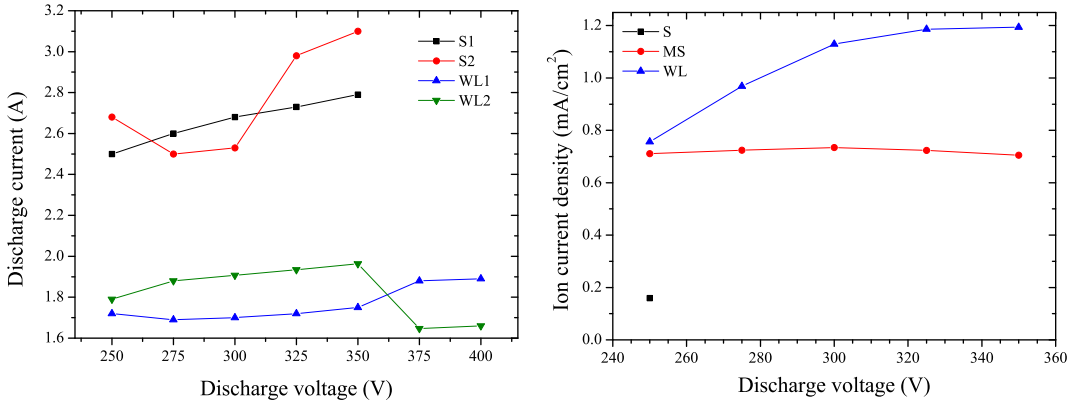

6.16.1: Current-voltage plots, for the PPS-Flex operating in WL mode.

6.16.2: Ion current density in the plume of the PPS-Flex in WL mode.

Figure 6.16: (Left) Current-voltage plots in standard (S) and wall-less (WL) configuration, obtained with the PPS-Flex, at $\phi_a = 2$ mg/s. (Right) Ion current density on the thruster axis, against discharge voltage in standard (S), magnetic shielding (MS) and wall-less (WL) modes, at $\phi_a = 3.5$ mg/s.

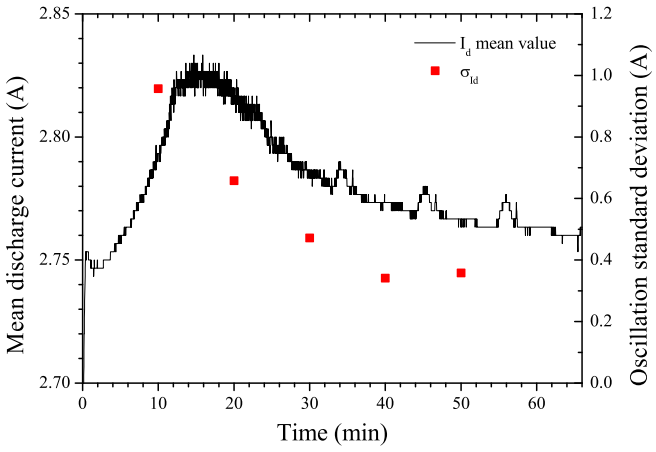

Figure 6.17: Evolution of the discharge current over a 1 h time span. The PPS-Flex was operated in WL mode, at 300 V and 3.0 mg/s, in the vacuum chamber in Orléans.

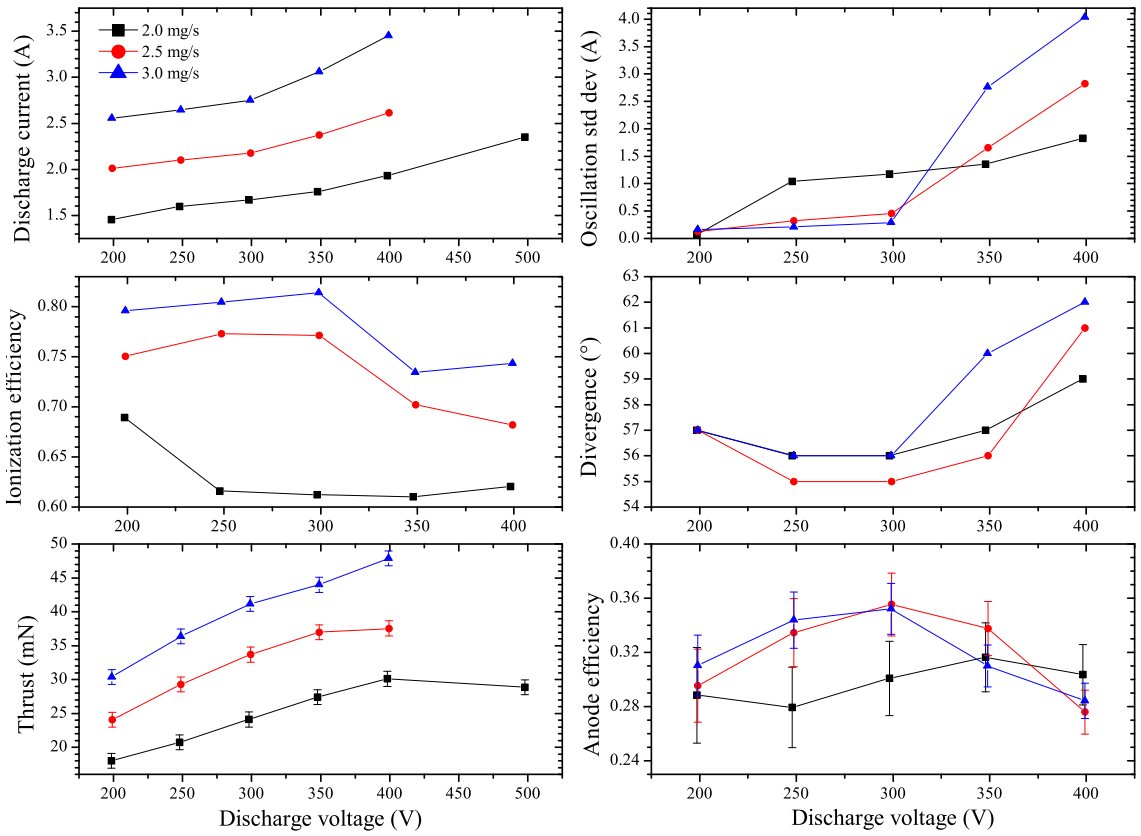

Figure 6.18: Performance of the PPS-Flex in WL mode, at various operating points. From left to right, and top to bottom: discharge current mean value, standard deviation of the discharge current oscillation, ionization efficiency, beam divergence half-angle, thrust and anode efficiency. The error bars on the anode efficiency have been estimated considering the thrust uncertainty only.

PPS-Flex performance in WL mode

The thrust level and far-field ion properties have been measured in the PIVOINE-2g test-bench. One of the stainless steel guarded Faraday probes presented in Chapter 4 has been used to characterize the ion beam. The probe was biased at - 30 V. Both the anode geometry and the magnetic topology were optimized for these experiments, see previous section. Some results are presented in figure 6.18, for various xenon mass flow rates and applied voltages. The quantities are in fact not far from standard values for a high-efficiency 1.5 kW-class Hall thruster, yet some differences appear and can be explained, see below. The anode efficiency is computed using relation (4.22). The specific impulse is given by

$$I_{sp} = \frac{F}{g_0 \phi_a}, \tag{6.4}$$

where F is the thrust, g_0 is the gravity of Earth at sea level, and ϕ_a the anode flow rate. As can be seen in figure 6.18, the discharge current agrees with the injected mass flow rate. However, it does not plateau, which is probably due to an increase in electron current with the discharge voltage. This may likely originate from the low amplitude of the magnetic field, which peaks at 70 G, therefore limiting the electron confinement. It is also probable that the proximity of the anode with the magnetic field maximum (about 10 mm) does not allow electrons to cool down before reaching the anode. The low magnetic field strength in MS and WL configuration originates from the actual design of the PPS-Flex thruster

magnetic circuit. Therefore, a third version of the PPS-Flex thruster, able to provide a high B field magnitude, whatever the topology, is currently under development. For similar reasons, the beam divergence half-angle and the anode efficiency are respectively higher, and lower, than flight models. The ionization efficiency and thrust level already appear satisfying, considering the WL design has only been studied in our team for a year, and that the margin for improvement is still large.

6.3 Conclusions

The first European realization of magnetic shielding has been proposed with the PPS-Flex. While this visual evidence is yet to be confirmed with near-wall measurements, it demonstrates the capabilities of the PPS-Flex in terms of magnetic flexibility. The knowledge gained during this first testing has served the development of the PPI-MS, a 200 W permanent magnets Hall thruster, based on the PPI and PPI-Mag.

An alternative Hall thruster architecture that shifts the ionization and acceleration regions outside the cavity has been developed, tested, and characterized. The objectives of this work were multiple: (i) to verify the possibility of moving the ionization zone and the electric field entirely outside the cavity, while still ensuring thruster operation, (ii) to evaluate the potential of the design with benefits and drawbacks, and (iii) to propose an optimization strategy.

First experimental results with the PPI, using this design, concerning thruster operation, discharge oscillations, electric field distribution, and the ionization zone indicate that the magnetized discharge can be moved outside the cavity without significantly compromising the ion production and acceleration. The discharge is stable, although magnetic field gradients are negative. This study also reveals the deterioration of the performance as well as drawbacks in the wall-less configuration: the beam energy is low, the divergence is large, the discharge current is high, and the interaction of the plasma with the thruster poles is probably increased. Further optimization of several parameters were therefore necessary to recover a high efficiency.

The second series of experiments have involved the PPS-Flex at the ESA Propulsion Laboratory, in 2014, and at PIVOINE-2g ground-test facility, in 2015. The PPS-Flex was a proving ground to test optimization strategies. In the end, the thruster performance is acceptable, considering the prototype is a modified version of a standard single-stage Hall thruster, given the standard magnetic architecture, and the current TRL level.

A high-efficiency Hall thruster in the WL configuration with an external electric field would offer significant benefits for spacecraft propulsion in terms of integration, operating envelope, lifetime, and fuel options. As the thrust is generated outside, the dielectric channel can be considerably shortened, leading to economies in mass and volume. Plasma interaction with the walls will have been significantly reduced. The cavity material will therefore have less influence on the thruster performance, and more importantly, operation at high voltage is presumably possible and lifetime can be extended. Furthermore, reduction in plasma-wall interactions could lead to the achievement of larger electron temperature, a positive point for an efficient ionization of atomic fuels like krypton and argon. The absence of cavity would possibly make the vectorization of the thrust achievable, without resulting in an asymmetrical erosion of the thruster components. On the other hand, plume-spacecraft interaction might represent a critical issue if the plume divergence angle remains large for a WL-HT, and the erosion rate of the magnetic poles is yet to be determined.

References

[1] I. G. Mikellides, I. Katz, R. R. Hofer, and D. M. Goebel. Magnetic shielding of walls from the unmagnetized ion beam in a Hall thruster. *Appl. Phys. Lett.*, 102(2):023509–1–023509–5, 2013.

[2] R. R. Hofer, D. M. Goebel, I. G. Mikellides, and I. Katz. Magnetic shielding of a laboratory Hall thruster. II. Experiments. *J. Appl. Phys.*, 115(4):043304, 2014.

[3] A. M. Kapulkin, A. D. Grishkevich, and V. F. Prisnyakov. Outside electric field thruster. In proceedings of the 45th IAF Congress; Space Technol., Pergamon, UK, Vol. 15, pp. 391-394, 1995.

[4] V. F. Prisnyakov, A. N. Petrenko, A. M. Kapulkin, I. N. Statsenko, A. I. Kondratiev, and S. N. Kulagin. The review of the works on electrical propulsion thrusters development and investigation carried out at the Dnepropetrovsk State University. In Proceedings 24th International Electric Propulsion Conference, Moscow, Russia, IEPC Paper 95-12, 1995.

[5] K.H. De Grys, A. Mathers, B. Welander and V. Khayms. Demonstration of >10,400 hours of operation on 4.5 kW qualification model Hall thruster. AIAA Paper 10-6698, 2010.

[6] R.R. Hofer, D.M. Goebel, I.G. Mikellides, I. Katz. Magnetic shielding of a laboratory Hall thruster. II. Experiments. *J. Appl. Phys.*, 115(043304), 2014.

[7] R.R. Hofer, B.A. Jorns, J.E. Polk, I.G. Mikellides and J.S. Snyder. Wear test of a magnetically shielded Hall thruster at 3000 seconds specific impulse. In proceedings of the 33rd International Electric Propulsion Conference, Washington, D.C., IEPC paper 2013-033, 2013.

[8] R.W. Conversano, D.M. Goebel, R.R. Hofer, T.S. Matlock and R.E. Wirz. Magnetically shielded miniature Hall thruster: development and initial testing. In proceedings of the 33rd International Electric Propulsion Conference, Paper 2013-201, 2013.

[9] R.W. Conversano, D.M. Goebel, I.G. Mikellides, R.R. Hofer, T.S. Matlock and R.E. Wirz. Magnetically Shielded Miniature Hall Thruster: Performance Assessment and Status Update. in Proceedings 50th Joint-Propulsion Conference, Cleveland, Ohio, AIAA Paper 2014-3896, 2014.

[10] H. Kamhawi, W. Huang, T. Haag, R. Shastry, G. Soulas, T. Smith, I.G. Mikellides and R.R. Hofer. Performance and Thermal Characterization of the NASA-300MS 20 kW Hall Effect Thruster. 2013.

[11] J.M. Haas and A.D. Gallimore. Considerations on the role of the Hall current in a laboratory-model thruster. *IEEE Transactions on Plasma Science*, 30(2), 2002.

[12] A. I. Morozov. Focusing of Cold Quasineutral Beams in Electromagnetic Fields. *Soviet Physics - Doklady*, 10:8, 1966.

[13] I.G. Mikellides, I. Katz, R.R. Hofer, D.M. Goebel and K. deGrys. Magnetic shielding of the channel walls in a Hall plasma accelerator. *Phys. Plasmas*, 18(033501), 2011.

[14] D. M. Goebel and I. Katz. *Fundamentals of Electric Propulsion*. Wiley, Hoboken, 2008.

[15] V. V. Zhurin, H. R. Kaufmann, and R. S. Robinson. Physics of closed drift thrusters. *Plasma Sources Sci. Technol.*, 8:R1, 1999.

[16] K. Dannenmayer and S. Mazouffre. Elementary scaling relations for Hall effect thrusters. *J. Propul. Power*, 27:236, 2011.

[17] M. Keidar, Y. Choi, and I. D. Boyd. Modeling a two-stage high-power anode layer thruster and its plume. *J. Propul. Power*, 23:500, 2007.

[18] EY. Choueiri. Plasma Oscillations in Hall Thrusters. *Phys. Plasmas*, 8:1411, 2001.

[19] S. Barral and E. Ahedo. Low-frequency model of breathing oscillations in Hall discharges. *Phys. Rev. E*, 79(046401), 2009.

[20] J. P. Boeuf and L. Garrigues. Low frequency oscillations in a stationary plasma thruster. *J. Appl. Phys.*, 84(7):3541, 1998.

[21] P. Coche and L. Garrigues. A two-dimensional (azimuthal-axial) particle-in-cell model of a Hall thruster. *Phys. Plasmas*, 21(023503), 2014.

[22] S. Mazouffre. Laser-induced fluorescence diagnostics of the cross-field discharge of Hall thrusters. *Plasma Sources Sci. Technol.*, 22(013001), 2013.

[23] S. Mazouffre, G. Bourgeois, L. Garrigues, and E. Pawelec. A comprehensive study on the atom flow in the cross-field discharge of a Hall thruster. *J. Phys. D: Appl. Phys.*, 44(105203), 2011.

[24] J. Vaudolon and S. Mazouffre. Indirect determination of the electric field in plasma discharges using laser-induced fluorescence spectroscopy. *Phys. Plasmas*, 21:093505, 2014.

[25] S. Mazouffre, S. Tsikata, and J. Vaudolon. Development and characterization of a wall-less Hall thruster. in Proceedings 50th Joint-Propulsion Conference, Cleveland, Ohio, AIAA Paper 2014-3513, 2014.

[26] D. Gawron, S. Mazouffre, N. Sadeghi, and A. Héron. Influence of magnetic field and discharge voltage on the acceleration layer features in a Hall effect thruster. *Plasma Sources Sci. Technol.*, 17(025001), 2008.

[27] D.M. Goebel, R.R. Hofer, I.G. Mikellides, I. Katz, J.E. Polk and B. Dotson. Conducting wall Hall thrusters. In proceedings of the 33rd International Electric Propulsion Conference, Washington, D.C., IEPC paper 13-276, 2013.

[28] S. Mazouffre, G. Bourgeois, J. Vaudolon, L. Garrigues, C. Hénaux, D. Harribey, R. Vilamot, A. Rossi, S. Zurbach and D. Le Méhauté. Development and testing of Hall thruster with flexible magnetic field configuration. *J. Propul. Power*, 31:1167–1174, 2015.

[29] L. Garrigues, S. Mazouffre, C. Hénaux, R. Vilamot, A. Rossi, D. Harribey, G. Bourgeois, J. Vaudolon and S. Zurbach. Design and first test campaign results with a new flexible magnetic circuit for a Hall thruster. In proceedings of the 33rd International Electric Propulsion Conference, Paper 2013-250, 2013.

[30] S. Mazouffre, P. Echegut and M. Dudeck. A calibrated infrared imaging study on the steady state thermal behavior of Hall effect thrusters. *Plasma Sources Sci. Technol.*, 16:13–22, 2007.

[31] S. Mazouffre, K. Dannenmayer and C. Blank. Impact of discharge voltage on wall-losses in a Hall thruster. *Phys. Plasmas*, 18(064501), 2011.

Conclusions

THIS dissertation has been concerned with the physics, and the performance, of Hall thrusters. This technology represents prime economic and technical assets on the communication satellite market. Plasma propulsion will likely be used in the future to propel spacecrafts, both in Earth orbit and to destinations in deep space. This research was motivated by better understanding the physics of these devices, and by enhancing the performance, so that the gap between research and development may be bridged.

The research work has been divided into laser-induced fluorescence measurements on the PPI, probe measurements in the plumes of the PPI-Mag and PPS-Flex, and performance characterization while varying the magnetic topology of these two thrusters.

Laser-induced fluorescence measurements have been performed in the plume of the PPI, as well as, marginally, in that of the SPT100-ML Hall thrusters. The methods for deriving the time-averaged plasma properties (ion velocity, electric field, ionization frequency, electron temperature...) have been analyzed and discussed. The possible ways for precisely determining the electric field have especially been investigated, through energy, fluid and kinetic approaches. The fluid approach appears to be of little interest in a very low-pressure experimental work when ionization occurs locally (the model's simplicity is counterbalanced by the experimental requirements), but has been able to describe the intermediate ion flow regime of the discharge. The energy and Boltzmann equations can be used, provided special experimental and numerical care are taken.

A novel technique to perform time-resolved measurements has been proposed. This technique associates a photon-counting method with a discharge stabilization apparatus, which ensures time-coherence. The discharge oscillating pattern is phase-locked at the breathing mode frequency, which allows reproducible measurement conditions, those being mandatory to accumulate fluorescence photons over time.
The Hilbert-Huang signal processing technique has been successfully applied to the photon time series obtained through TR-LIF measurements. The large number of data that resulted from the spectral analysis, added to the complexity of the ion velocity distribution temporal dynamics, has proven challenging to handle. Therefore, the properties of the ion mean velocity have been used, instead of considering each ion group individually. The low- and high-frequency temporal characteristics of the axial electric field in the discharge of the PPI have been described. The ion transit time instability has notably been examined. The experimental analysis has been complemented by a two-fluid theoretical description of the discharge, which has shed light on the prime importance of the magnetic field profile regarding the instability occurrence. Some concomitance has been found with previous measurements, and particle-in-cell simulations.

A thorough investigation of the error sources that arise when using probes in the plume of electric propulsion devices has been made, and delivered to the European Space

Agency. Among other things, the technical notes describe the method, and measurement procedures, to compute some of the uncertainties that have been identified. A two-months test campaign with the PPS-Flex has allowed figures to be obtained, and constitute a first determination of the uncertainties on particularly important thruster characteristics, such as the ion beam current, the beam divergence angle, and the electron properties. For instance, the results show that today's diagnostic tools and vacuum chambers cannot provide an accurate estimation of the divergence angle, which would make the comparisons of the various thrusters satisfying and trustworthy.
Based on these observations, a set of planar probes, a rotating arm, a data acquisition system and an electronic system have been developed. The probe design and bias, the ion and electron properties, have been examined in the plume of the PPI-Mag. The existence of isotropic ion currents perpendicular to the thruster jet has been shown.
The probe and rotating arm assembly have been used to study the influence of the magnetic barrier extent on the performance of the PPI-Mag. Basically, operating with krypton a Hall thruster optimized for xenon does not change the overall characteristics of the discharge, but lowers its performance. Among the most important results, the ionization efficiency with magnetic configuration 3, in krypton, equals that of configuration 1, in xenon. Yet the thruster behavior is controlled by the whole topology, as demonstrated by the unstable behavior of configuration 2. The basic rules that have guided the design of the magnetic circuit seem to be validated, i.e. extending the width of the radial B field profile along the channel axis has an impact on how efficiently the neutral gas is converted into ions that participate in useful thrust.

The optimization of the magnetic topology was the main concern of this dissertation, although 99 % of the results obtained with the PPS-Flex are presented in confidential test reports. The 149 different magnetic configurations tested so far have allowed to show links between magnetic features (B field gradients, lens inclination...) and performance. Additionally, the influence of the discharge electric reference and background pressure on the performance have been investigated, for several magnetic topologies.

The wall-less design of Hall thrusters has been presented, and preliminary experiments undertaken. A wall-less ion source provides an ideal platform for the study of cross-field discharge configurations with sophisticated tools like Thomson scattering (coherent and incoherent) and LIF spectroscopy. The access it provides to key regions of the plasma facilitates a thorough investigation of plasma instabilities, discharge oscillations, and small-scale turbulence for a better understanding of the discharge physics, anomalous electron transport and the influence of secondary electron emission. The wall-less source also represents a good test-case for physical modelling and associated numerical simulations of the discharge due to the greatly simplified boundary conditions.
A high-efficiency Hall thruster in the wall-less configuration with an external electric field would offer significant benefits for spacecraft propulsion in terms of integration, operating envelope, lifetime, and fuel options. As the thrust is generated outside, the dielectric channel can be considerably shortened, leading to economies in mass and volume. Operation at high voltage is presumably possible, and lifetime may be extended compared to a classical design.

Future activities

Based on this research, several future activities can be suggested for understanding the physics, and the performance, of Hall thrusters.
Concerning LIF measurements:

- The energy conservation model has been used to analyze various electric field profiles in the plume of the PPI Hall thruster, inferred from LIF measurements. The influence of the wall material, and channel geometry, have been briefly discussed. The research shows the complex nature of the electric field shape, that is not determined only by the magnetic field profile. The two-peak structure that has been observed with alumina ceramics, in the $2S_0$ channel geometry, is particularly interesting. This work has been complemented, and confirmed, by probe measurements. While it is true that probes are invasive, measurements can be quite fast. A consequent number of operating conditions is therefore explored in a matter of days. A better understanding of the plasma instabilities, which may participate in electron transport, of the near-wall conductivity, and of secondary emission, could complement the LIF data.

- The LIF signal-to-noise ratio could be improved by working in a strongly saturated regime, or by enlarging the core diameter of the fluorescence collection optical fiber. This improvement in signal resolution could allow the efficient use of the non-stationary Boltzmann 1D1V equation for time-resolved analysis. Alternatively, for time-averaged measurements, the lock-in integration constant can be increased, at the expense of the measurement time though.

- The description of the ion transit time instability could be refined, by taking into account the various ion velocity groups of the velocity distributions. Various oscillating patterns are observed inside each distribution. This analysis would greatly benefit from a particle-in-cell model of the PPI. Besides, to our knowledge, TR-LIF data with such a high temporal resolution are unique in the field of plasma propulsion, and could conceivably help in validating computer simulations.

Concerning probe measurements:

- The evaluation of the measurement uncertainties could be improved by evaluating more terms. This would, however, require the development of simulations, and to adapt the measurement procedures. Details are given in the technical notes delivered to ESA.

- The influence of the probe geometry on the measurements remains to be studied. While the nude and guarded Faraday probes have been compared, a more general research and development effort is to be done. The optimum size for the guard ring, and the comparison with the Faraday cup design rank among the top priorities.

- The influence of the vacuum chamber conditions depart from that encountered in flight. Amid various effects, a preliminary study of the background pressure impact on the thruster performance has been performed with the PPS-Flex. Further investigation is necessary, and should be made in cooperation with the satellite primes and suppliers.

- The existence of ion currents perpendicular to the thruster jet implies that the thruster performance analysis should somehow account for such currents. The discussion

as to how to integrate these data into the analysis is still ongoing, since a better understanding of the probe wake is mandatory. Particle-in-cell simulations would help addressing this matter.

Regarding the magnetic topology:

- The PPS-Flex has brought considerable knowledge concerning the relationship between the magnetic topology and the thruster performance. The majority of the studies conducted so far have considered only the modification of the radial magnetic field profile along the channel axis. The influence of the near-wall magnetic field amplitude, gradients and field lines orientation must be assessed.
- Among the vast set of magnetic topologies that has been tested, two configurations have developed a performance slightly above that of current designs. Future activities involving the PPS-Flex should operate these topologies at a broader range of operating points, and evaluate other quantities which are key for the thruster performance, such as the erosion rate and stability over long periods of time. More details and outlooks are given in the test reports.
- The PPI-Mag has been tested both with xenon and krypton propellants. The basic rules that have guided the design of the magnetic circuit seem to be validated. However, LIF measurements could be performed to evaluate the extent of the ionization zone, thus providing the coupling between L_i and $L_{_B}$. Additionally, E$\times$B probe measurements would help in addressing the impact of multiply-charged ions on the performance level that is inferred, even though their fraction is believed to be small at these discharge voltages. Finally, some parameters, such as thrust, could be measured, instead of being computed.
- The PPI-MS, a 200 W permanent magnets Hall thruster based on the PPI and PPI-Mag, has been designed to operate in magnetic shielding. A tremendous research is to be performed, which include: the characterization of the thruster envelope, near-wall probe measurements to assess whether the walls are shielded from the plasma, axial and radial LIF measurements inside the discharge channel to examine the distribution of the electric field and to evaluate the acceleration efficiency, the measurement of the thrust level to determine the anode efficiency, far-field measurements of the ion current density to obtain the ionization efficiency and the beam divergence angle. All that for a broad range of operating conditions.

Finally, the wall-less Hall thruster seems promising. On a physical standpoint, countless experiments will benefit from this design, which may help in understanding fundamental matters, such as the relationship between plasma instabilities and electron transport. On an engineering viewpoint, this design offers a compact and light thruster, with the hope of allowing a dual-mode operation (high thrust or high specific impulse), a thrust vectorization capability and an extended lifespan, among others. The next step is to scale the design, at least up to the 1.5 kW class, to fully determine its capabilities.

Appendix A

Relation of dispersion for the ion transit time oscillation

The plasma is assumed to be composed of cold unmagnetized ions and cold magnetized electrons. The magnetic field is assumed to be purely radial, which is a reasonable approximation on the cavity axis. We study the case of quasineutral perturbations, and dissipative and ionization processes are neglected. For the sake of simplicity, and for allowing the comparison of the theoretical results with the LIF data set, the model is one-dimensional. Finally, we consider that the typical transit time frequency ω is much lower than the electron cyclotron frequency ω_{Be}, so that $\omega << \omega_{Be}$. Under these assumptions, the continuity equation and the momentum conservation equation for both the ions and the electrons are linearized and read

$$\begin{cases} \dfrac{\partial \tilde{n}}{\partial t} + n\dfrac{\partial \tilde{v}_z}{\partial z} + v_z\dfrac{\partial \tilde{n}}{\partial z} + \tilde{v}_z\dfrac{\partial n}{\partial z} + \tilde{n}\dfrac{\partial v_z}{\partial z} = 0, \\ \dfrac{\partial \tilde{v}_z}{\partial t} + v_z\dfrac{\partial \tilde{v}_z}{\partial z} + \tilde{v}_z\dfrac{\partial v_z}{\partial z} = -\dfrac{e}{m_i}\dfrac{\partial \tilde{\Phi}}{\partial z}, \\ \dfrac{\partial \tilde{n}}{\partial t} + n\dfrac{\partial \tilde{u}_z}{\partial z} + \tilde{u}_z\dfrac{\partial n}{\partial z} = 0, \\ \dfrac{\partial \tilde{u}_\theta}{\partial t} = \dfrac{e}{m_e}\tilde{u}_z B_r, \\ \dfrac{\partial \tilde{u}_z}{\partial t} = \dfrac{e}{m_e}\left(\dfrac{\partial \tilde{\Phi}}{\partial z} - \tilde{u}_\theta B_r\right), \end{cases} \tag{A.1}$$

where the subscripts r, θ and z refer to the cylindrical coordinates, v and u are the ion and electron velocities respectively, n is the plasma density, Φ the accelerating potential, e the ion charge, m_i the ion mass, m_e the electron mass and B_r the magnetic field. Perturbed quantities are labelled by a tilde superscript.

It is useful to notice that

$$\begin{cases} v_z = \left(\dfrac{2e\Phi}{m_i}\right)^{1/2} \rightarrow \dfrac{\partial v_z}{\partial z} = \dfrac{1}{2}\left(\dfrac{2e\Phi}{m_i}\right)^{-1/2}\dfrac{2e}{m_i}\dfrac{\partial \Phi}{\partial z} = \dfrac{e}{m_i v_z}\dfrac{\partial \Phi}{\partial z}, \\ nv_z = n(z=0)v_z(z=0) \rightarrow \dfrac{\partial n}{\partial z} = -\dfrac{n(z=0)v_z(z=0)}{v_z^2}\dfrac{\partial v_z}{\partial z} = -\dfrac{n}{v_z}\dfrac{\partial v_z}{\partial z}. \end{cases}$$

A.1 Linear system in matrix form

We look for the solution in Fourier form, $\exp\left[i\left(kz-\omega t\right)\right]$, where $\mathbf{k}=(0,0,k)$ is the perturbation wave vector.

A.1.1 Ion momentum equation

The ion momentum equation of system (A.1) reads

$$-i\omega\tilde{v}_z + v_z\frac{\partial\tilde{v}_z}{\partial z} + \tilde{v}_z\frac{\partial v_z}{\partial z} = -\frac{e}{m_i}\frac{\partial\tilde{\Phi}}{\partial z}. \tag{A.2}$$

Therefore, the velocity perturbation is given by

$$\frac{\partial\tilde{v}_z}{\partial z} = \frac{1}{v_z}\left[\left(i\omega - \frac{\partial v_z}{\partial z}\right)\tilde{v}_z - \frac{e}{m_i}\frac{\partial\tilde{\Phi}}{\partial z}\right]. \tag{A.3}$$

A.1.2 Ion continuity equation

The ion continuity equation of system (A.1) reads

$$-i\omega\tilde{n} + n\frac{\partial\tilde{v}_z}{\partial z} + v_z\frac{\partial\tilde{n}}{\partial z} + \tilde{v}_z\frac{\partial n}{\partial z} + \tilde{n}\frac{\partial v_z}{\partial z} = 0. \tag{A.4}$$

By inserting equation (A.3), the density perturbation is described by

$$\frac{\partial\tilde{n}}{\partial z} = \frac{n}{v_z^2}\left(2\frac{\partial v_z}{\partial z} - i\omega\right)\tilde{v}_z + \frac{1}{v_z}\left(i\omega - \frac{\partial v_z}{\partial z}\right)\tilde{n} + \frac{ne}{m_i v_z^2}\frac{\partial\tilde{\Phi}}{\partial z}. \tag{A.5}$$

A.1.3 Electron continuity and momentum conservation equations

The electron system reads

$$\begin{cases} -i\omega\tilde{u}_\theta = \dfrac{e}{m_e}\tilde{u}_z B_r, \\ -i\omega\tilde{u}_z = \dfrac{e}{m_e}\left(\dfrac{\partial\tilde{\Phi}}{\partial z} - \tilde{u}_\theta B_r\right), \\ -i\omega\tilde{n} + n\dfrac{\partial\tilde{u}_z}{\partial z} + \tilde{u}_z\dfrac{\partial n}{\partial z} = 0. \end{cases} \tag{A.6}$$

The first and second equations provide $\tilde{u}_z$:

$$-i\omega\tilde{u}_z = \frac{e}{m_e}\frac{\partial\tilde{\Phi}}{\partial z} - i\frac{\omega_{Be}^2}{\omega}\tilde{u}_z, \tag{A.7}$$

where $\omega_{Be} = eB_r/m_e$ is the electron cyclotron pulsation. Thus,

$$\tilde{u}_z = i\frac{e}{m_e\omega}\frac{1}{1-\left(\dfrac{\omega_{Be}}{\omega}\right)^2}\frac{\partial\tilde{\Phi}}{\partial z} \approx -i\frac{e}{m_e\omega}\left(\frac{\omega}{\omega_{Be}}\right)^2\frac{\partial\tilde{\Phi}}{\partial z}. \tag{A.8}$$

This relation can be differentiated to provide

$$\frac{\partial\tilde{u}_z}{\partial z} = -\frac{2}{B_r}\frac{\partial B_r}{\partial z}\tilde{u}_z - i\frac{e\omega}{m_e\omega_{Be}^2}\frac{\partial^2\tilde{\Phi}}{\partial z^2}. \tag{A.9}$$

We can now use the last equation of system (A.6) to obtain the potential perturbation

$$\begin{aligned}
&-i\omega\tilde{n} - n\left(\frac{2}{B_r}\frac{\partial B_r}{\partial z}\tilde{u}_z + i\frac{e\omega}{m_e\omega_{Be}^2}\frac{\partial^2\tilde{\Phi}}{\partial z^2}\right) + i\frac{e}{m_e\omega}\left(\frac{\omega}{\omega_{Be}}\right)^2\frac{\partial\tilde{\Phi}}{\partial z}\frac{n}{v_z}\frac{\partial v_z}{\partial z} = 0,\\
&-i\frac{\partial^2\tilde{\Phi}}{\partial z^2} + i\frac{1}{v_z}\frac{\partial v_z}{\partial z}\frac{\partial\tilde{\Phi}}{\partial z} - \frac{2\omega_{Be}}{\omega}\frac{\partial B_r}{\partial z}\tilde{u}_z - i\frac{m_e\omega_{Be}^2}{en}\tilde{n} = 0,\\
&\frac{\partial^2\tilde{\Phi}}{\partial z^2} = \frac{1}{v_z}\frac{\partial v_z}{\partial z}\frac{\partial\tilde{\Phi}}{\partial z} + i\frac{2\omega_{Be}}{\omega}\frac{\partial B_r}{\partial z}\tilde{u}_z - \frac{m_e\omega_{Be}^2}{en}\tilde{n},\\
&\frac{\partial^2\tilde{\Phi}}{\partial z^2} = \frac{1}{v_z}\frac{\partial v_z}{\partial z}\frac{\partial\tilde{\Phi}}{\partial z} + \frac{2\omega_{Be}}{\omega}\frac{\partial B_r}{\partial z}\frac{e}{m_e\omega}\left(\frac{\omega}{\omega_{Be}}\right)^2\frac{\partial\tilde{\Phi}}{\partial z} - \frac{m_e\omega_{Be}^2}{en}\tilde{n}.
\end{aligned} \tag{A.10}$$

Hence the potential perturbation equation

$$\frac{\partial^2\tilde{\Phi}}{\partial z^2} = \left(\frac{1}{v_z}\frac{\partial v_z}{\partial z} + \frac{2}{B_r}\frac{\partial B_r}{\partial z}\right)\frac{\partial\tilde{\Phi}}{\partial z} - \frac{m_e\omega_{Be}^2}{en}\tilde{n}. \tag{A.11}$$

A.1.4 Expression of the linear system to solve

Equations (A.3), (A.5) and (A.11) are gathered to describe the matrix M of the linear system

$$\frac{\partial\mathbf{X}}{\partial z} = M\mathbf{X},\ \mathbf{X} = \left(\tilde{v}_z, \tilde{n}, \tilde{\Phi}, \partial\tilde{\Phi}/\partial z\right), \tag{A.12}$$

where

$$M = \begin{pmatrix}
\frac{1}{v_z}\left(i\omega - \frac{\partial v_z}{\partial z}\right) & 0 & 0 & -\frac{e}{m_i v_z}\\
\frac{n}{v_z^2}\left(2\frac{\partial v_z}{\partial z} - i\omega\right) & \frac{1}{v_z}\left(i\omega - \frac{\partial v_z}{\partial z}\right) & 0 & \frac{ne}{m_i v_z^2}\\
0 & 0 & 0 & 1\\
0 & -\frac{m_e\omega_{Be}^2}{en} & 0 & \frac{1}{v_z}\frac{\partial v_z}{\partial z} + \frac{2}{B_r}\frac{\partial B_r}{\partial z}
\end{pmatrix}.$$

A.2 Relation of dispersion

The solutions of the linear system (A.12) are searched in the form of e^{ikz} where $k = 2\pi/\lambda$. Thus,

$$\frac{\partial \mathbf{X}}{\partial z} = ik\mathbf{X} = M\mathbf{X}. \tag{A.13}$$

The dispersion relation is then given by

$$\begin{vmatrix} \frac{1}{v_z}\left(i\omega - \frac{\partial v_z}{\partial z}\right) - ik & 0 & 0 & -\frac{e}{m_i v_z} \\ \frac{n}{v_z^2}\left(2\frac{\partial v_z}{\partial z} - i\omega\right) & \frac{1}{v_z}\left(i\omega - \frac{\partial v_z}{\partial z}\right) - ik & 0 & \frac{ne}{m_i v_z^2} \\ 0 & 0 & -ik & 1 \\ 0 & -\frac{m_e\omega_{Be}^2}{en} & 0 & \frac{1}{v_z}\frac{\partial v_z}{\partial z} + \frac{2}{B_r}\frac{\partial B_r}{\partial z} - ik \end{vmatrix} = 0. \tag{A.14}$$

We develop the determinant along the third column, which leads to

$$-ik \begin{vmatrix} \frac{1}{v_z}\left(i\omega - \frac{\partial v_z}{\partial z}\right) - ik & 0 & -\frac{e}{m_i v_z} \\ \frac{n}{v_z^2}\left(2\frac{\partial v_z}{\partial z} - i\omega\right) & \frac{1}{v_z}\left(i\omega - \frac{\partial v_z}{\partial z}\right) - ik & \frac{ne}{m_i v_z^2} \\ 0 & -\frac{m_e\omega_{Be}^2}{en} & \frac{1}{v_z}\frac{\partial v_z}{\partial z} + \frac{2}{B_r}\frac{\partial B_r}{\partial z} - ik \end{vmatrix} = 0. \tag{A.15}$$

The trivial solution $k = 0$ is omitted. Development along the third line provides

$$\begin{aligned} \left(\frac{1}{v_z}\frac{\partial v_z}{\partial z} + \frac{2}{B_r}\frac{\partial B_r}{\partial z} - ik\right) & \begin{vmatrix} \frac{1}{v_z}\left(i\omega - \frac{\partial v_z}{\partial z}\right) - ik & 0 \\ \frac{n}{v_z^2}\left(2\frac{\partial v_z}{\partial z} - i\omega\right) & \frac{1}{v_z}\left(i\omega - \frac{\partial v_z}{\partial z}\right) - ik \end{vmatrix} \\ + \frac{m_e\omega_{Be}^2}{en} & \begin{vmatrix} \frac{1}{v_z}\left(i\omega - \frac{\partial v_z}{\partial z}\right) - ik & -\frac{e}{m_i v_z} \\ \frac{n}{v_z^2}\left(2\frac{\partial v_z}{\partial z} - i\omega\right) & \frac{ne}{m_i v_z^2} \end{vmatrix} = 0. \end{aligned} \tag{A.16}$$

The dispersion relation can then be written

$$\left(\frac{1}{v_z}\frac{\partial v_z}{\partial z} + \frac{2}{B_r}\frac{\partial B_r}{\partial z} - ik\right)\left(\frac{1}{v_z}\left(i\omega - \frac{\partial v_z}{\partial z}\right) - ik\right)^2 + \frac{\omega_{Be}\omega_{Bi}}{v_z^2}\left(\frac{1}{v_z}\frac{\partial v_z}{\partial z} - ik\right) = 0. \tag{A.17}$$

The solution of the dispersion relation is

$$\omega = v_z k - i\left\{\frac{\partial v_z}{\partial z} + \left[\frac{\omega_{Be}\omega_{Bi}\left(ik - \frac{1}{v_z}\frac{\partial v_z}{\partial z}\right)}{\frac{1}{v_z}\frac{\partial v_z}{\partial z} + \frac{2}{B_r}\frac{\partial B_r}{\partial z} - ik}\right]^{\frac{1}{2}}\right\}. \tag{A.18}$$

Appendix B

Particle-in-cell model of the PPI-Mag plume in the NExET vacuum chamber

In order to understand in more details some of the results obtained with the PPI-Mag and the PPS-Flex, a (r, z) particle-in-cell (PIC) model of the PPI-Mag plume has been developed. The goals of the study are to assess the impact of the backpressure level on the ion current density profile in the plume far-field. The conservation of current in the plume is also examined by computing key ion properties at different locations.

B.1 Description of the model

B.1.1 Computational domain

The plasma is assumed to be composed of xenon atoms and Xe^+ ions coming from the thruster. Since this study is first order, and that we do not compute the discharge, the cathode is not considered in the simulation. The simulation domain is shown, not to scale, in figure B.1. The domain extends from the thruster centerline to the vacuum chamber wall. As we shall see, there is no need to resolve the Debye length in this simulation, so that the true physical dimensions of the system can be considered. The thruster axis is placed at 39 cm away from the chamber wall (which equals NExET radius). The left-hand side of the domain contains the thruster exit plane (1 cm in width, such as that of the PPI-Mag, or that of the PPI in $2S_0$ channel geometry for that matter). We assume that particles are fully accelerated, and that there are no electric nor magnetic fields that comes from the discharge.

The boundaries at the left, right and bottom of the domain are open, which means that particles can leave the domain. In this case, new particles are added at the injection plane. The flux normal to the upper boundary is zero, since ions leaving the domain from this side are replaced by those coming from the opposite channel (not simulated). The electric fields on lateral faces are imposed to zero, while it is the potential which is constrained on the upper and lower boundaries. The beam potential V_b is imposed to 5 V, while the chamber wall is set to the ground.

B.1.2 Treatment of species

The model employs a PIC treatment of the ions, and considers the atom and electron populations as uniform backgrounds. Each macroparticle represents $\sim 10^6$ particles. Collisions are treated by means of the Monte-Carlo technique. Only charge-exchange collisions with the residual neutral gas are considered. At regular time intervals, the prob-

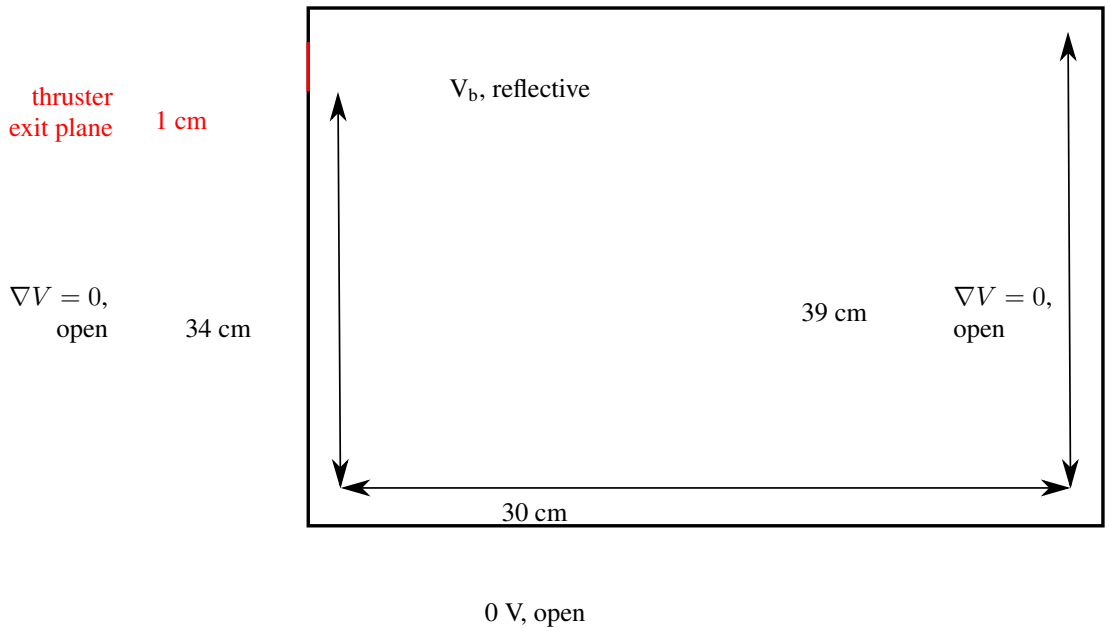

Figure B.1: The simulation region, not to scale in this figure, extends from the thruster exit plane (left, in red) to the far-field (right), and from the thruster centerline (top) to NExET vacuum chamber wall (bottom).

ability for a collision to occur is computed and compared to a random number. The probability is given by

$$P = 1 - \exp\left(-n_n \sigma \Delta V \Delta t\right), \tag{B.1}$$

where n_n is the density of the residual gas, σ the collision cross-section, ΔV the relative velocity between the ion and the neutral target, and Δt the time step between collision checks. In this work, Δt is five times the time step of the computation, to improve the code performance.

Inlet conditions Ions are injected at the thruster exit plane. Their transverse location, denoted y_p, is sampled from a Maxwellian distribution. The initial velocity distribution must comply with three requirements:

1. $(v_x, v_y) = (v_b + v_{th}, v_{th})$ on the channel axis,
2. $(v_x, v_y) = (v_{th}, v_{th})$ on the channel edges,
3. The initial beam divergence angle and ion current must be compatible with those of a 200 W-class Hall thruster.

Given the dimensions of the thruster and its location inside the vessel, it is easily inferred that the initial field (B.2) satisfies the conditions (1) and (2) above. The factor A and the Maxwellian shape were found to comply with condition (3).

$$\begin{cases} v_x = v_b \exp\left(-A\left[y_p - 0.34\right]^2\right) \cos\left(2\arctan\left[\dfrac{y_p - 0.34}{0.005}\right]\right) + v_{th}, \\ v_y = v_b \exp\left(-A\left[y_p - 0.34\right]^2\right) \sin\left(2\arctan\left[\dfrac{y_p - 0.34}{0.005}\right]\right) + v_{th}, \\ A = \dfrac{\ln\left[\dfrac{v_b}{v_{th}}\right]}{25 \times 10^{-6}}, \end{cases} \tag{B.2}$$

where v_b is the beam velocity, and v_{th} is the thermal velocity of Xe^+ ions sampled from a Maxwellian distribution (laser-induced measurements have evaluated the ion temperature to lie within 0.3 eV). In this work, $v_b = 10$ km/s.

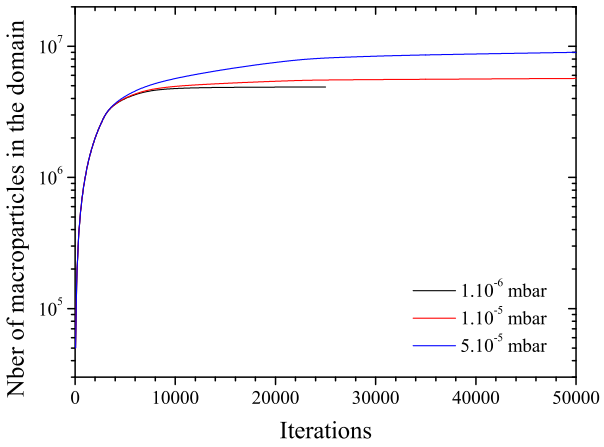

Figure B.2: Number of macroparticles in the computational domain as a function of time steps. Each time step is equal to 10 ns. The computations were stopped when the number of particles was deemed stabilized.

B.1.3 Numerical approach

Poisson's equation is not solved, which is physically disputable, but this is at the advantage of the computation time, since the plasma Debye length and the electron plasma frequency are not the quantities that impose the time and spatial steps anymore. The evolution of the ion population is considered only, so that there is no need to mesh the domain. Therefore, the equation of motion is integrated and there is no need, in principle, for minimum spatial and time steps. However, the particles must be located inside the computational domain, and $n_n \sigma \Delta V \Delta t$ largely inferior to 1. Given v_b, the residual pressure levels and the domain extent, a time step of 10 ns was found to be suitable.
Note that energy is not conserved. Fast neutrals generated during the charge-exchange collisions are not considered in the simulation (the neutral gas is a uniform background at ambient temperature). However, the modification in the velocity vector of the incoming ions is considered obviously.

B.2 Results

Since the purpose of this code is to relate the observations in the plume of the PPI-Mag and PPS-Flex to numerical analysis, simulations have been conducted at three different background pressures: 10^{-6}, 10^{-5} and 5×10^{-5} mbar-Xe. All other input parameters were kept unchanged, namely the neutral temperature and the inlet conditions. The simulations were halted when the number of particles inside the domain was constant (more precisely the outward ion flux is exactly compensated by that injected at the thruster exit plane). The number of particles inside the domain is displayed in figure B.2, as a function of the number of time steps. It took 8 days to complete each of the simulations, on 2 processors.

B.2.1 Position and velocity distributions of the particles

The locations and velocities of the ions are presented in figures B.3.1 and B.3.2, for a residual pressure of 10^{-6} mbar-Xe. Ions that have not experienced a CEX collision are tagged by a blue circle, why the slow-moving, CEX ions, are labelled by a red circle. Large fractions of CEX collisions occur on the channel axis owing to the large plasma

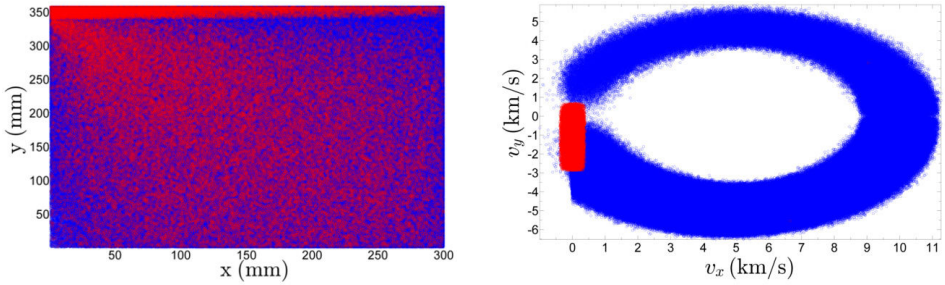

B.3.1: Particle locations.

B.3.2: Particle velocities.

Figure B.3: Distribution of the particles location (left) and velocity (right) in the phase space. Blue circles represent the ions which evolve unperturbed, while the red circles tag the slow ions generated by CEX collisions. The influence of the grounded wall appears clearly on the CEX particle velocity distribution.

density. This can be surprising at first glance, since the collision probability only depends on the target species density, i.e. the neutrals. Yet, the more particles you have in a region of space, the more likely some of them may have experienced a CEX collision somewhere. Even more surprising is the localization of a significant number of particles in the region across the domain, i.e. at $\approx 45°$ from the channel axis. Why does this structure appear is unknown, but it is clearly related to the inlet conditions. **The initial distributions of the particles' locations and velocities have been sampled from Maxwellians, thus depart from those of a Hall thruster. This entails a necessary critical analysis of the conclusions that are drawn from this code.** Notice also that Poisson's equation is not solved, which may impact the repartition of particles.
The (v_x, v_y) distribution illustrates the impact of the grounded wall on the plasma. The transverse ion velocities are mostly negatives, due to the electric field that exists. The average velocity is consistent with that given by an integral picture, $eE_y\Delta t/m_i$.

B.2.2 Ion density and mean velocity

The spatial maps of the ion density and mean velocity (first order moment of the ion velocity distribution) are given in figures B.4.1 and B.4.2. The background pressure increases from left to right. The full domain is represented for the velocity mapping. A smaller portion is shown in the density maps, since there is not discernible evolution elsewhere in the plume. Regions with blank squares in velocity correspond to areas without particles, which may seem strange. While there is no mesh for the computation, a grid is used for the post-processing part. Ion velocity distributions are computed in each cell. Macroparticles may not appear in some cells, given the fine grid that has been used (squares of 100 μm side length).
The structure which appears on the thruster centerline, at $y = 38$ cm, looks like the spike which is usually seen when operating a thruster. However, the origin of the experimentally-observed structure on the thruster axis is more likely to originate in Coulomb interactions, which are not considered in this work.

B.2.3 Ion and beam properties

The primary objective of this work was to assess the evolution of the plume current distribution and beam divergence angle with the background pressure and distance from the thruster exit plane. The ion current density has been inferred on a cylindrical contour at several distances R from the thruster axis. Given that only half of the plasma is simulated,

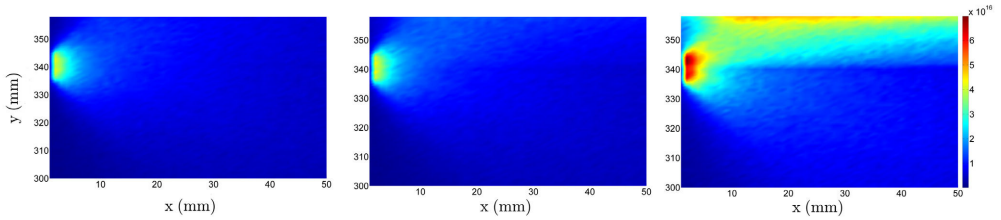

B.4.1: Ion density. The residual pressure increases from left to right. The colorbar is in m^{-3}.

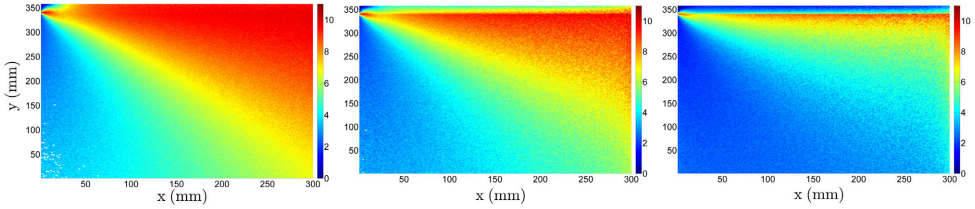

B.4.2: Ion velocity. The residual pressure increases from left to right. The colorbar is expressed in $\mathrm{km/s}$.

Figure B.4: Distribution of the ion density and velocity in the plume. Three different background pressure cases are examined. The structure on the thruster centerline, at $5{\times}10^{-5}$ mbar-Xe, may be the spike usually observed. Coulomb interactions should be considered, and Poisson's equation solved, for a conclusive determination of the plume structures.

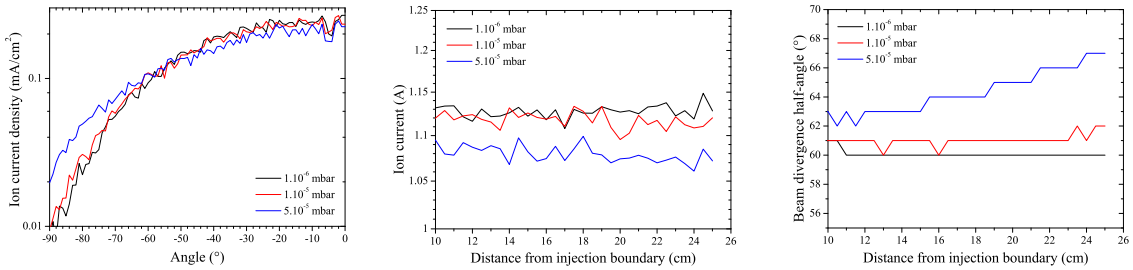

B.5.1: Ion current density.

B.5.2: Ion current.

B.5.3: Divergence angle.

Figure B.5: Properties of the far-field plume: ion current density (left), ion current (middle) and beam divergence half-angle (right). The three quantities are given in case of three distinct background pressure levels. The beam divergence angle evolution is to be compared with that of the PPI-Mag, presented in Chapter 4.

the contour extends from -90° up to 0°.

The ion current density profiles at 25 cm from the injection plane are given in figure B.5.1, for the three different background pressures. Although the profiles are not similar to that of a Hall thruster, possibly due to the specific inlet conditions, the wing current noticeably increases with the background pressure. On the other hand, it diminishes at the center of the profile. One can already guess that the ion current is conserved when increasing the background pressure, which is more precisely reported in figure B.5.2. The current lowers with increasing background pressure, but tends to be constant throughout the plume.

However, the beam divergence angle, delimiting the domain that contains 90 % of the ion current, depends on both the background pressure level and distance from the injection plane. This evolution is in quantitative agreement with that presented in table 4.6. The increase in beam divergence angle, for the larger residual pressure case, precisely equals that observed with the PPI-Mag (between 4° and 6°), in spite of the various assumptions of the model.

B.3 Conclusion

This code certainly will not contribute to ground-breaking discoveries in the field of electric propulsion. Nevertheless, I have had the opportunity of using it as a teething ground tool, to familiarize with the development, writing, operation and post-processing of a PIC code. Being interested as I am in PIC simulation is one thing. Knowing some basic rules to design and write one is another.
In addition to the personal interest, some interesting conclusions can be drawn, always in light of the simplifications from the real experimental life. Most prominently are the evolution of the ion current density and beam divergence angle with the background pressure, and for the latter with the distance from the thruster exit plane. It corroborates part of my work with the PPS-Flex and PPI-Mag, and that was just the aim.

Appendix C

List of publications

Peer-reviewed international journal papers

- J. Vaudolon, S. Mazouffre and A. Lejeune,
Multi-directional measurements of the ion current in the plume of a low-power Hall thruster
Submitted to IEEE Transactions on Plasma Science
- J. Vaudolon, S. Mazouffre, C. Hénaux, D. Harribey and A. Rossi,
Optimization of a wall-less Hall thruster
Accepted for publication in Appl. Phys. Lett. (2015)
- S. Mazouffre, G. Bourgeois, J. Vaudolon, L. Garrigues, C. Hénaux, D. Harribey, R. Vilamot, A. Rossi, S. Zurbach, and D. Le Méhauté,
Development and testing of a Hall thruster with a flexible magnetic field configuration
J. Propul. Power **31**, 4, pp. 1167-1174 (2015)
- J. Vaudolon and S. Mazouffre,
Observation of high-frequency ion instabilities in a cross-field plasma
Plasma Sources Sci. Technol. **24**, 032003 (2015)
- S. Mazouffre, S. Tsikata and J. Vaudolon,
Development and preliminary experimental characterization of a wall-less Hall thruster
J. Appl. Phys. **116**, 243302 (2014)
- S. Mazouffre, J. Vaudolon, G. Largeau, C. Hénaux, A. Rossi and D. Harribey,
Visual Evidence of Magnetic Shielding With the PPS-Flex Hall Thruster
IEEE Transactions on Plasma Science **42**, 0093-3813 (2014)
- J. Vaudolon and S. Mazouffre,
Indirect determination of the electric field in plasma discharges using laser-induced fluorescence spectroscopy
Phys. Plasmas **21**, 093505 (2014)
- J. Vaudolon, B. Khiar and S. Mazouffre,
Time evolution of the electric field in a Hall thruster
Plasma Sources Sci. Technol. **23**, 022002 (2014)

- J. Vaudolon, L. Balika and S. Mazouffre,
Photon counting technique applied to time-resolved laser-induced fluorescence measurements on a stabilized discharge
Rev. Sci. Instrum. **84**, 073512 (2013)

Conference proceedings

- J. Vaudolon and S. Mazouffre,
Impact of the magnetic barrier extent on the performance of a krypton-fuelled Hall thruster
51th AIAA/ASME/SAE/ASEE Joint Propulsion Conference, Orlando, Florida, USA, AIAA-2015-3922 (2015)
- J. Vaudolon and S. Mazouffre,
Investigation of the ion transit time instability in a Hall thruster combining time-resolved LIF spectroscopy and analytical calculations
51th AIAA/ASME/SAE/ASEE Joint Propulsion Conference, Orlando, Florida, USA, AIAA-2015-4004 (2015)
- S. Mazouffre, J. Vaudolon and S. Tsikata, C. Hénaux, D. Harribey, A. Rossi, K. Dannenmayer and J. Del Amo,
Optimization of magnetic field topology and anode geometry for a wall-less Hall thruster
51th AIAA/ASME/SAE/ASEE Joint Propulsion Conference, Orlando, Florida, USA, AIAA-2015-4007 (2015)
- S. Mazouffre, J. Vaudolon, S. Tsikata, C. Hénaux, D. Harribey and A. Rossi,
Optimization of the design of a wall-less Hall thruster
34th International Electric Propulsion Conference, Kobe, Japan, IEPC-2015-182 (2015)
- L. Garrigues, S. Mazouffre, J. Vaudolon and S. Tsikata,
Fully two-dimensional particle-in-cell Monte Carlo collisions model of a wall-less Hall thruster
34th International Electric Propulsion Conference, Kobe, Japan, IEPC-2015-311 (2015)
- J. Vaudolon and S. Mazouffre,
Investigation of the ion transit time instability in a Hall thruster combining time-resolved LIF spectroscopy and analytical calculations
34th International Electric Propulsion Conference, Kobe, Japan, IEPC-2015-400 (2015)
- S. Mazouffre, S. Tsikata and J. Vaudolon,
Development and characterization of a wall-less Hall thruster
50th AIAA/ASME/SAE/ASEE Joint Propulsion Conference, Cleveland, Ohio, USA, AIAA 2014-3513 (2014)
- S. Mazouffre, G. Bourgeois, J. Vaudolon, L. Garrigues, C. Hénaux, D. Harribey, R. Vilamot, A. Rossi, S. Zurbach and D. Le Méhauté,
Performance analysis of a Hall thruster with a highly versatile magnetic circuit
4th Space Propulsion Conference, Cologne, Germany, SP2014-2969094 (2014)

- J. Vaudolon and S. Mazouffre,
Evaluation of different methods for determining the electric field profile in a Hall thruster
4th Space Propulsion Conference, Cologne, Germany, SP2014-2979732 (2014)

- S. Mazouffre, S. Tsikata and J. Vaudolon,
Hall thruster with external electric field
4th Space Propulsion Conference, Cologne, Germany, SP2014-2970604 (2014)

- J. Vaudolon, B. Khiar and S. Mazouffre,
Low and high frequency oscillations of the accelerating electric field in a Hall thruster
33rd International Electric Propulsion Conference, Washington, D.C., USA, IEPC-2013-089 (2013)

- L. Garrigues, S. Mazouffre, C.Hénaux, R. Vilamot, A.Rossi , D. Harribey, G. Bourgeois, J. Vaudolon and S. Zurbach,
Design and first test campaign results with a new flexible magnetic circuit for a Hall thruster
33rd International Electric Propulsion Conference, Washington, D.C., USA, IEPC-2013-250 (2013)

- S. Mazouffre, S. Tsikata, K. Dannenmayer, G. Bourgeois, A. Lejeune, J. Vaudolon, L. Balika and A. Pétin,
Recent progress in understanding the physics of Hall thrusters
31st International Conference on Phenomena in Ionized Gases, Grenada, Spain, paper PS2-110 (2013)

- J. Vaudolon, S. Mazouffre, D. Gerst and S. Tsikata,
Experimental study of acceleration processes in Hall effect thrusters
63rd International Astronautical Congress, Naples, Italy, IAC-12-E2.1.8 (2012)

Appendix D

Version française

D.1 Introduction

Propulsion

Les moteurs aérobies et anaérobies fonctionnent tous selon le même principe, qui consiste à transmettre au véhicule la quantité de mouvement de la fraction de carburant quittant le système. Une force de poussée est générée en retour et permet l'accélération du véhicule. Généralement, l'énergie dégagée lors de la combustion d'un ou plusieurs ergols est convertie en énergie cinétique. Il existe, cependant, une exception : la propulsion électrique, encore appelée propulsion plasma. Cette technologie diffère grandement des autres techniques propulsives, puisque l'énergie générant l'accélération du carburant n'est pas embarquée à bord du véhicule, mais collectée à l'aide de panneaux solaires. Ce point est à l'origine des atouts, mais aussi des inconvénients, de la propulsion électrique.

A ce jour, les systèmes de propulsion spatiale peuvent être rangés dans deux catégories distinctes, selon leur rapport poussée/masse. Les systèmes chimiques, qui sont par exemple utilisés pour permettre le décollage des lanceurs, exhibent de grands rapports poussée/masse. Les bases de la propulsion chimique sont connus et appliqués depuis des millénaires, la première référence à la poudre à canon datant de la dynastie Han, en 206 av. J.-C. En général, deux réactifs sont mélangés dans une chambre de combustion, puis le mélange est allumé (à l'exception du cas d'ergols hypergoliques pour lesquels ces deux étapes sont simultanées). La poussée est générée en détendant les gaz chauds dans une tuyère convergente-divergente.

Les systèmes de propulsion électrique peuvent générer de la poussée de trois manières : en chauffant un gaz, par une accélération électrostatique ou par l'utilisation de la force de Lorentz. Ces systèmes présentent de faibles rapports poussée/masse. Alors que les moteurs chimiques sont souvent qualifiés de limités en énergie, les propulseurs électriques sont principalement limités par la puissance électrique délivrée par l'alimentation. D'autres considérations peuvent intervenir. Par exemple, la poussée maximale d'un moteur ionique à grilles est déterminé par le courant maximum qu'il est possible d'extraire par les orifices des grilles.

La poussée s'exprime rigoureusement de manières différentes pour les systèmes chimiques et électriques. Cependant, un dénominateur commun peut être obtenu, sous la forme de l'équation (D.1),

$$T = \dot{m}_p v_p, \tag{D.1}$$

dans laquelle $\dot{m}_p$ est la masse du carburant, et v_p sa vitesse effective d'éjection. Le moteur chimique mono-chambre à ergols liquides le plus puissant jamais testé, le F-1, générait un débit total de carburant et de comburant environ égal à 3 000 $\mathrm{kg/s}$, une vitesse d'éjection

de 2,5 $\mathrm{km/s}$, et développait 680 tonnes de poussée. Son pendant électrique, le moteur de Hall PPS-20k (le moteur le plus puissant opéré en Europe), possède un nominal à 43 $\mathrm{mg/s}$ de xénon. La vitesse ionique est de 23 $\mathrm{km/s}$ et la poussée approche 1 N. Un ordre de grandeur sépare les vitesses d'éjection des systèmes chimiques et électriques, alors que les débits diffèrent de 10^8 ! Par conséquent, bien que la poussée dépende linéairement de la vitesse d'éjection du carburant, son amplitude est principalement déterminée par le débit.
Cependant, les lois de la mécanique imposent que v_p est le facteur premier à ajuster pour délivrer une fraction massique significative de charge utile à destination. Les modifications de vecteur vitesse ΔV, la fraction massique ξ, et v_p, sont reliés par l'équation de Tsiolkovski (D.2), fondatrice de l'astronautique moderne, dérivée au début du 20ème siècle.

$$\xi = \exp\left(-\frac{\Delta V}{v_p}\right). \tag{D.2}$$

La comparaison des systèmes propulsifs est couramment réalisée à l'aide de (D.3), qui introduit la notion d'impulsion spécifique, ISP. Cette grandeur s'exprime en secondes, et représente la durée pendant laquelle une unité de masse d'ergol produit une poussée équivalente dans le champ gravitationnel terrestre.

$$ISP = \frac{\int T dt}{g_0 \int \dot{m}_p dt}. \tag{D.3}$$

Si la poussée et le débit massique sont constants dans le temps,

$$ISP = \frac{T}{g_0 \dot{m}_p} = \frac{v_p}{g_0}. \tag{D.4}$$

Les équations (D.2) et (D.4) indiquent que v_p est le principal indicateur de performance utilisé pour comparer les systèmes propulsifs entre eux.

La réécriture des relations (D.1) et (D.2) met en lumière deux paramètres clefs d'un propulseur spatial (poussée et impulsion spécifique)

$$\begin{cases} \Delta m_p = m_i \left(1 - \exp\left[-\dfrac{\Delta V}{g_0 I_{sp}}\right]\right), \\ \Delta t = \dfrac{g_0 I_{sp} \Delta m_p}{F}. \end{cases} \tag{D.5}$$

Au bout du compte, la stratégie adoptée, i.e. développer une forte poussée ou une forte ISP, est un choix qui doit être fait au regard de l'ensemble des besoins mission. Un accord doit généralement être trouvé par l'ingénieur ou l'équipe en charge de l'architecture moteur.

Contexte du travail de thèse

Topologie magnétique La géométrie du canal de décharge et la topologie magnétique sont les deux points les plus importants à considérer lors du design d'un propulseur de Hall. Un programme dédié à l'étude de la géométrie du canal a été initié en 2009, dans le cadre du GDR 3161, liant les activités du CNRS, du CNES et de la Snecma. La largeur du canal du propulseur de Hall de 200 W nommé PPI (acronyme pour *Petit Propulseur Innovant*) a été variée, tout en conservant son diamètre moyen. Il a notamment été démontré que les

pertes aux parois diminuaient lorsque le canal était élargi. Cependant, modifier la largeur du canal a également modifié la topologie magnétique. Une étude détaillée, et dédiée à la variation de la topologie magnétique seule, était à conduire.

La compréhension de l'influence de la topologie magnétique sur les performances des propulseurs de Hall a constitué un objectif majeur du travail de thèse. Le champ magnétique confine le plasma, et représente le support qui transmet la poussée au véhicule. Ce travail repose sur deux axes :

- Le rôle de la topologie magnétique a tout d'abord été étudié par G. Bourgeois, sur le PPI et le PPS®1350-ML. Les expériences ont révélé l'impact déterminant de l'amplitude du champ magnétique sur le rendement d'accélération du moteur. L'exploration magnétique était cepedant limitée, en raison du manque de flexibilité des circuits magnétiques standards.
  Une nouvelle structure magnétique, polyvalente, dédiée aux propulseurs de Hall, a été développée par R. Vilamot et ses collaborateurs au laboratoire LAPLACE, à Toulouse. Le prototype a été appelé PPS-Flex pour illustrer sa grande flexibilité magnétique. Les objectifs du programme de recherche impliquant le PPS-Flex sont multiples : mieux comprendre l'influence des paramètres de champ magnétique sur les performances du moteur, tester de nouvelles topologies, et optimiser les caractéristiques du champ pour des opérations à haut rendement et grande durée de vie. Les résultats de ces tests sont présentés dans le Chapitre 5.

- Les topologies de champ actuelles sont optimisées pour le xénon. Cependant, sa rareté et la volatilité de son cours sur le marché des gaz rares sont des points noirs qui justifient l'étude d'ergols alternatifs. Plusieurs solutions peuvent être proposées. La plus simple consiste à remplacer le xénon par un autre gaz rare, afin de conserver les architectures standard déjà développées. Le radon étant mis de côté pour des raisons de sécurité (cet élément est radioactif), le krypton est le prochain candidat. Utiliser de l'hélium, du néon ou de l'argon, pénaliserait davantage la performance du moteur. Le krypton est environ 13 fois plus présent dans notre atmosphère que le xénon, et son prix en est 10 fois plus bas.
  Des expériences préliminaires avec le PPI opéré en krypton ont montré que le rendement d'accélération n'était pas grandement altéré, en comparaison du xénon. Le plus grand potentiel de première ionisation du krypton abaisse cependant le rendement d'ionisation. En se basant sur ces résultats, le laboratoire ICARE a engagé un effort important ces deux dernières années, en développant le PPI-Mag, un moteur optimisé pour le krypton.

Spectroscopie de fluorescence induite par laser Cette thèse a eu pour objectif de mieux comprendre la physique des moteurs de Hall, en plus des études de performance liées au réglage du champ magnétique. Des mesures de fluorescence induite par laser (FIL), sur l'ion Xe II, ont été faites dans le PPI, principalement le long de son axe canal, dans le banc d'essais NExET. La mesure de fonctions de distribution en vitesse moyennes dans le temps permet la comparaison avec les codes PIC, qui malgré leur excellente description de la physique nécessitent des réglages empiriques. La recherche s'est notamment concentrée sur deux points :

- Une nouvelle technique permettant des mesures de FIL résolues en temps a été mise en œuvre. La branche de détection du signal se base sur une technique de comptage de photons. L'accumulation des photons est statistique, et nécessite un comportement temporel cohérent de la décharge sur plusieurs minutes. Dans le passé, cette

cohérence était assurée par une interruption régulière de la décharge, ce qui entrainait un rallumage périodique du moteur. Ce comportement transitoire de la décharge ne reflétait pas une opération standard et stabilisée. Une nouvelle méthode a été utilisée, et consiste à appliquer une oscillation de potentiel sur une électrode proche de l'orifice de la cathode. La fréquence de l'oscillation peut être ajustée afin de trouver une résonance avec la décharge. Cette injection d'énergie est limitée (typiquement 5 %), et permet d'obtenir un comportement quasi-périodique dans le domaine basse fréquence. Le comportement moyen du moteur n'est pas perturbé par cette modulation.
Des mesures de FIL résolue en temps ont été conduites dans la décharge du PPI. Les oscillations de respiration et de temps de transit ont été caractérisées.

- Le champ électrique est une grandeur clef pour caractériser les processus de création et de transport. Sa détermination à partir des données de FIL nécessite cependant l'emploi d'un modèle. Les approches énergétique, fluide et cinétiques ont été comparées et discutées dans la plume du PPI. Le niveau de précision requis lors du calcul est à tempérer par les considérations expérimentales. Des conclusions et des recommandations ont été faites pour un calcul correct du champ électrique.

Organisation du manuscrit

Cette thèse est organisée en deux parties majeures : les Chapitres 1 à 3 étudient la physique des propulseurs de Hall, tandis que les Chapitres 4 à 6 caractérisent les performances des moteurs de Hall.
Le banc de FIL est présenté au Chapitre 1. La nouvelle méthode utilisée pour permettre des mesures résolues en temps est présentée, et validée. Les quantités intéressantes pour ce manuscrit qu'il est possible de déduire de données de FIL sont exposées. Des exemples sont donnés dans la décharge du PPI. Les différentes méthodes de calcul du champ électrique utilisant les mesures de FIL sont analysées au Chapitre 2. Une étude temporelle du champ électrique et des oscillations ioniques est proposée au Chapitre 3.
Les principales considérations qui interviennent lors de mesures de sondes dans la plume des moteurs de Hall sont discutées au Chapitre 4. Le bras rotatif conçu pour la chambre NExET est présenté, et les mesures effectuées dans la plume du PPI-Mag sont analysées. L'influence de la topologie magnétique sur les performances des moteurs de Hall est étudiée au Chapitre 5. Quelques résultats des campagnes d'essais conduites avec le PPI-Mag et le PPS-Flex sont donnés. Le Chapitre 6 discute d'architectures moteurs évoluées. Enfin, les conclusions de ce travail sont données, et de futurs axes de recherche sont proposés.

D.2 Chapitre 1 : Fluorescence induite par laser

Le Chapitre 1 présente le banc de spectroscopie de FIL. Les transitions utilisées pour le xénon et le krypton sont analysées, les longueurs d'onde au repos sont obtenues et servent de référence pour la suite des travaux, aux Chapitres 2 et 3.
La technique de comptage de photons a été validée, à la condition que la décharge puisse être maintenue dans un régime oscillatoire cohérent. Une modulation de potentiel sur une électrode flottante placée près de l'orifice de sortie de la cathode du moteur a permis de stabiliser le comportement basse fréquence de la décharge. La cohérence temporelle a été rendue possible en synchronisant les acquisitions avec le système de modulation.

D.3 Chapitre 2 : Comment calculer le champ électrique à partir des données de FIL ?

Plusieurs méthodes pour calculer le champ électrique du moteur à partir des données de FIL sont présentées au Chapitre 2. L'approche fluide s'est révélée peu intéressante dans le cas où des processus d'ionisation apparaissent. La simplicité du modèle est séduisante, mais est contrebalancée par des besoins expérimentaux similaires à ceux des modèles plus évolués. Le modèle fluide a cependant été capable de reproduire le caractère intermédiaire, i.e. ni totalement fluide ni totalement cinétique, de l'écoulement ionique. Les modèles énergétique et cinétiques sont en revanche privilégiés, ces derniers nécessitant un soin expérimental pour maximiser le rapport signal sur bruit. Plus précisément, le modèle cinétique 1D1V apparait suffisant pour la plupart des études qui visent à déterminer le champ électrique axial du moteur, sur l'axe du canal. L'approche cinétique permet également la détermination du profil spatial de la fréquence d'ionisation. La formulation 2D2V est plus complexe, et les barres d'erreur qui en résultent ne permettent pas son utilisation, pour le moment. Les champs électriques radiaux qui se développent dans le moteur ont également été calculés. Cependant, les barres d'erreur ne permettent pas de conclure sur les résultats des modèles.

La méthode énergétique, peu coûteuse en temps expérimental, a été utilisée pour analyser différents cas opératoires du PPI. L'influence du matériau composant la paroi, et de la géométrie du canal, ont été étudiées. Les résultats montrent la nature complexe des processus physiques au sein du plasma, qui localisent la chute de potentiel. Contrairement à ce qui a longtemps été cru, le champ magnétique n'est pas le seul paramètre guidant la répartition du champ électrique.

D.4 Chapitre 3 : Oscillations d'ionisation et de temps de transit

Dans le Chapitre 3, la méthode de traitement du signal Hilbert-Huang a été utilisée pour analyser les données de FIL résolue en temps obtenues dans la décharge du PPI. Après avoir décrit la nature statistique des spectres fréquentiels obtenus, les propriétés spectrales des oscillations ioniques ont été décrites. Des quantités locales, telles que les oscillations des groupes de vitesse des fonctions de distribution ioniques, ont été présentées. Une description macroscopique a également été entreprise via l'étude temporelle de la vitesse moyenne et du champ électrique. Le profil spatial de ce dernier est particulièrement intéressant dans la géométrie de canal $2S_0$, lorsqu'il est équipé de céramiques en alumine. De nouvelles mesures sont proposées pour pousser l'interprétation plus avant. Les fluctuations de densité ionique ont suggéré la propagation d'un front d'ionisation à la vitesse des atomes de xénon.

Les propriétés spatio-temporelles de la vitesse ionique moyenne ont été analysées et comparées à un modèle fluide du plasma. Les oscillations de temps de transit ont été révélées, et la région de leur déclenchement prédite par le modèle est en accord avec les mesures. La longueur d'onde de l'instabilité correspond à l'extension du champ électrique, ce qui semble cohérent compte tenu de sa nature.
Une description succinte des mécanismes par lesquels des ions supravéloces peuvent être générés a été donnée. L'analyse de la matrice du système linéaire fluide a montré un accord qualitatif avec les données expérimentales du PPI. Cette étape de validation a été suivie par l'étude de données de FIL datant de 2007, et lève une partie du mystère concernant l'apparition, ou non, d'ions supravéloces. Les accords qualitatifs obtenus sont satisfaisants, compte tenu de la nature relativement simple du modèle.

D.5 Chapitre 4 : Mesures de sondes dans la plume des moteurs de Hall

Le Chapitre 4 présente une investigation poussée des incertitudes de mesures dans la plume des moteurs de Hall, pour des outils diagnostics couramment utilisés : sondes de Faraday, de Langmuir, à champ retardeur et en champs croisés. Des évaluations quantitatives ont été faites, grâce à une campagne d'essais de deux mois à l'Agence Spatiale Européenne. Les résultats montrent que certains paramètres physiques des moteurs sont obtenus avec une précision suffisante, tels le courant ionique du faisceau, mais que les paramètres de performance souffrent d'une uncertitude importante. Ce niveau d'incertitude rend impossible une comparaison fine des moteurs entre eux, notamment au travers de l'angle de divergence du jet.

A partir de ces études préliminaires, la plume du PPI-Mag a été diagnostiquée à l'aide d'outils de mesure spécialement conçus. Un jeu de sondes de Faraday équipées d'anneaux de garde a été monté sur un système mécanique rotatif. La rotation, et la mesure des courants d'ions par les sondes, ont été pilotées par une interface développée en interne. Ces développements offrent maintenant à l'équipe de propulsion électrique de l'ICARE un nouveau système de mesure, ce qui complète une panoplie déjà large de moyens d'essais.

L'influence de la présence de l'anneau de garde autour du collecteur de la sonde a été étudiée, ainsi que l'influence de la position de mesure sur la valeur de cette dernière. Des mesures par sonde de Langmuir ont montré que la variation importante de la taille de gaine autour de la sonde nécessite l'emploi d'une sonde par condition plasma. La conservation du courant ionique dans la plume a également été montrée. Une étude plus poussée, étudiant notamment la géométrie dite de "coupe", a été proposée.

D.6 Chapitre 5 : Influence de la topologie magnétique sur les performances des moteurs de Hall

Le Chapitre 5 rapporte les campaignes d'essais du PPS-Flex. Le PPS-Flex est un moteur de 1,5 kW. Ce prototype unique au monde offre la possibilité de varier les paramètres de champ magnétique indépendamment les uns des autres. Le nombre de topologies qu'il est possible de générer est considérable. Les configurations magnétiques s'étendent des modèles classiques, type SPT100, au magnetic shielding, en passant par des configurations exotiques telles que des inclinaisons de lentille magnétique. A ce jour, 149 topologies différentes ont été testées.

Les objectifs des travaux engageant le PPS-Flex sont doubles : améliorer les performances des moteurs actuels, et valider des topologies capables d'opérer à forte tension de décharge pendant de longues périodes. La première étape a consisté à obtenir des quantités macroscopiques, telles que la poussée ou le courant de décharge, pour une vaste gamme de topologies. Une seconde, plus fondamentale, est nécessaire. Elle implique l'emploi d'outils de mesure tels que la spectroscopie de FIL et la diffusion Thomson. Ces expériences doivent être complétées par des simulations numériques pour comprendre les processus qui s'opèrent.

Les caractérisations préliminaires des sondes planes au Chapitre 4 ont permis d'étudier la plume du PPI-Mag au Chapitre 5. Le PPI-Mag a été utilisé en xénon et en krypton. L'opération du moteur en krypton, sous la configuration magnétique standard optimisée pour le xénon, n'a pas révélé de modification majeure de ses caractéristiques. Ce qui implique qu'il est possible de changer d'ergol sans changer la nature des processus

physiques dominants.
La performance du moteur a été étudiée à partir des mesures de sondes planes et de Langmuir dans le champ lointain. Parmi les résultats marquants, le rendement d'ionisation en krypton, sous la configuration magnétique 3, égale celui obtenu en xénon sous la configuration 1, ce qui valide la méthodologie de conception du moteur. Davantage de mesures seront nécessaires pour comprendre le lien entre la largeur de la zone magnétique et l'extension de la zone d'ionisation. Des mesures de sonde en champs croisés permettront également d'évaluer l'impact des ions multichargés sur les performances calculées du moteur.

D.7 Chapitre 6 : Architectures avancées pour les moteurs de Hall

Le Chapitre 6 est consacré à l'étude d'architectures moteurs avancées. Les concepts de magnetic shielding et de moteur sans parois sont notamment rapportés.
La première réalisation européenne du magnetic shielding a été proposée avec le PPS-Flex, à travers une indication visuelle. Des mesures en proche paroi sont toutefois nécessaires pour confirmer l'écrantage des parois. L'expérience retirée la génération de cette cartographie magnétique sur le PPS-Flex a servi de base au développement du PPI-MS, un moteur de 200 W basé sur le PPI et le PPI-Mag, et dédié à l'étude du magnetic shielding.

Une architecture moteur novatrice a été proposée avec le concept sans parois. Un prototype a été testé à partir du PPI, et montre que les zones d'ionisation et d'accélération sont localisées en dehors du canal moteur. Les objectifs étaient triples, à savoir : démontrer que le moteur opère de manière standard, même en sortant les zones d'ionisation et d'accélération, identifier les avantages et les inconvénients du design, et proposer une stratégie d'optimisation moteur.
Les premières études conduites avec le PPI ont montré que les caractéristiques de la décharge, à savoir le courant moyen, ses oscillations, la distribution du champ électrique et de la zone d'ionisation, ne sont pas drastiquement différentes de celles d'une architecture standard. L'optimisation de la géométrie de l'anode et du champ magnétique sont toutefois nécessaires pour améliorer le rendement et la divergence du jet, ces deux paramètres étant en réalité intimement liés.
La seconde série de mesures a été conduite avec le PPS-Flex, au laboratoire de propulsion électrique de l'ESA en 2014, puis dans PIVOINE-2g en 2015. Le PPS-Flex a servi de banc d'essai pour l'optimisation de l'architecture. La stratégie d'optimisation s'est révélée concluante, et nous avons obtenu des performances proches de certains moteurs actuels. Ces résultats sont très encourageants, compte tenu de la marge de progression encore importante qui existe.

Un propulseur sans parois permettrait des gains importants en termes d'intégration, d'enveloppe de fonctionnement, de durée de vie et de choix d'ergol. La poussée étant générée à l'extérieur du moteur, le canal peut être considérablement raccourci, ce qui conduit à des gains de masse et de volume. Les interactions avec les céramiques sont diminuées, voire supprimées, ce qui facilite la comparaison avec les codes de calcul qui ont encore du mal à prendre en compte les propriétés d'émission secondaire et de conductivité pariétale par exemple. Un autre point, capital, est la possiblité d'opérer en dual-mode, i.e. soit à forte poussée, soit à forte impulsion spécifique. Ces points positifs sont à nuancer, du fait d'une divergence de jet légèrement accrue, sur laquelle il reste toutefois possible d'agir à travers de nouvelles étapes d'optimisation.

D.8 Conclusions

Cette thèse s'est attachée à étudier la physique, et la performance, des propulseurs de Hall. Cette technologie représente des atouts techniques et commerciaux majeurs sur le marché des satellites de télécommunication. La propulsion électrique sera sans nul doute utilisée dans le futur pour propulser les satellites en orbite terrestre, mais aussi les sondes (et vaisseaux ?) interplanétaires. Ce travail de recherche a été motivé par mieux comprendre la physique des moteurs de Hall, et par améliorer leurs performances, afin de faire le lien entre recherche et développement.

La recherche a été organisée en plusieurs parties : spectroscopie de fluorescence induite par laser sur le PPI, mesures de sondes dans les plumes du PPI-Mag et du PPS-Flex, et enfin des études de performance pour ces deux derniers moteurs.

Les mesures de FIL ont été conduites sur le PPI, et de manière marginale sur le SPT100-ML. Les techniques d'extraction des principales grandeurs plasma (vitesse ionique, champ électrique, fréquence d'ionisation, température électronique…) ont été explorées. Les méthodes qu'il est possible d'appliquer pour calculer le champ électrique à l'origine de la poussée ont notamment été examinées. L'approche fluide a été écartée en raison de la simplicité du modèle, qui apparaissait contrebalancée par des besoins expérimentaux lourds, à l'avantage des modèles énergétique et cinétiques.

Une nouvelle technique permettant de réaliser des mesures de FIL résolues en temps a été proposée. Cette technique associe une méthode de comptage de photons à un outil de stabilisation de la décharge, ce qui assure la cohérence temporelle. Les oscillations basse fréquence du plasma, dites de respiration, deviennent alors pseudo-périodiques, et des conditions de mesure reproductibles sont obtenues.
Une technique avancée de traitement du signal, dite de Hilbert-Huang, a été appliquée avec succès aux séries temporelles de FIL. Le nombre important de données extraites de l'analyse, ajouté à la complexité de la dynamique ionique, se sont révélés délicats à gérer pour en extraire des informations utiles. Par conséquent, l'étude temporelle a été conduite sur la vitesse moyenne, ce qui réduit le nombre de variables du problème. Les oscillations basse et haute fréquences du champ électrique du PPI ont été décrites. L'instabilité de temps de transit à été analysée, et un lien avec le profil du champ magnétique a été obtenu grâce à un modèle fluide de la décharge. Les résultats du modèle sont en bon accord qualitatif avec les données expérimentales.

Une étude détaillée des sources d'erreur inhérentes aux mesures de sondes dans la plume des moteurs de Hall a été faite, et les conclusions remises à l'ESA. Les notes techniques délivrées décrivent, entre autres, les méthodes et procédures de mesure à suivre afin d'obtenir des incertitudes quantitatives. Les procédures ont été établies pour les sondes de Faraday, de Langmuir, à champ retardateur et en champs croisés. Une campagne d'essais de deux mois avec le PPS-Flex a permis d'extraire des incertitudes chiffrées sur diverses grandeurs, telles que le courant ionique dans la plume, la divergence du faisceau, et les propriétés électroniques. Les résultats montrent par exemple que les designs actuels ne permettent pas de quantifier précisément l'angle de divergence du jet, et qu'il n'est par conséquent pas possible de comparer tels quels des chiffres proches, i.e. séparés de quelques degrés, obtenus dans des installations différentes.
A partir de ces observations, un jeu de sondes planes équipées d'anneaux de garde, un système mécanique rotatif, un logiciel d'acquisition et un boîtier électronique de mesure ont été développés. Diverses caractéristiques de sondes ont été étudiées (matériau, présence de l'anneau de garde), le courant dans la plume a été montré conservé… L'existence de

courants non négligeables, perpendiculairement au faisceau, a notamment été révélée. Ces mesures préliminaires ont été poursuivies par l'étude de l'influence de la largeur de la barrière magnétique du PPI-Mag sur ses performances, en xénon et en krypton, par des mesures dans la plume. On voit que typiquement, opérer en krypton un moteur optimisé pour le xénon ne pose pas de probème majeur. La performance est néanmoins dégradée, et l'objectif prioritaire du PPI-Mag était de restaurer la performance en krypton. La démonstration, sous certaines hypothèses, d'un rendement en krypton, avec la configuration magnétique 3, similaire à celui obtenu en xénon, avec la configuration 1, valide la méthodologie de conception.

L'optimisation de la topologie magnétique a constitué le principal sujet d'étude de cette thèse, bien que 99 % des résultats obtenus avec le PPS-Flex soient contenus dans des rapports d'essais confidentiels. Les 149 configurations magnétiques différentes testées à ce jour ont permis de mettre en lumière des liens directs entre les performances et les paramètres de champ. De plus, l'influence des conditions expérimentales a été évaluée (pression résiduelle, références électriques).

Le design sans parois a été étudié grâce à des expériences préliminaires. Ce type de source apparaît idéal pour étudier la décharge à l'aide d'outils évolués, tels que la spectroscopie de FIL et la diffusion Thomson. L'étude détaillée des instabilités et des oscillations permettra une meilleure compréhension des processus de diffusion à travers la barrière magnétique, et l'émission secondaire électronique, entre autres. Il s'agit également d'un outil adapté aux comparaisons avec les simulations numériques, en raison de la simplification des conditions aux limites.

Perspectives

A partir de ces travaux, plusieurs recommandations et axes de recherches peuvent être proposés. Concernant les mesures de FIL :

- Le modèle énergétique a été utilisé pour déduire des profils de champs électriques dans la décharge du PPI, à partir de données de FIL. Les influences du matériau composant la paroi, et de la géométrie du canal, ont été brièvement discutées. Les études ont montré la nature complexe des processus liés à la répartition de la chute de potentiel, qui n'est pas seulement déterminée par le profil du champ magnétique. La structure à deux maxima observée en alumine, et en géométrie $2S_0$, est particulièrement intéressante. Ces résultats ont été confirmés par des mesures de sonde, qui bien qu'intrusives, fournissent des résultats rapides. Une meilleure compréhension des instabilités et du rôle des parois est nécessaire pour préciser l'organisation des phénomènes de transport et d'émission secondaire.

- Le rapport signal sur bruit des spectres de FIL pourrait être amélioré en travaillant en régime saturé, ou en élargissant le diamètre du cœur de la fibre optique de collection. Cette amélioration permettrait par exemple de calculer le profil temporel du champ électrique par l'équation de Boltzmann instationnaire, au lieu de passer par un modèle fluide. Pour les mesures moyennes en temps, on pourrait également penser à augmenter le temps d'intégration du lock-in, au détriment du temps de mesure.

- La description de l'instabilité de temps de transit pourrait être affinée, en prenant en compte les divers groupes de vitesse au sein d'une fonction de distribution. Différentes caractéristiques spectrales sont observées. L'association de codes PIC serait

bénéfique pour retirer un maximum d'informations. De la même manière, ces données expérimentales sont, à notre connaissance, uniques dans un propulseur de Hall, et permettraient de valider des codes de calcul.

Concernant les mesures de sondes :

- Les modèles utilisés pour déduire les incertitudes de mesure peuvent être améliorés en considérant plus de termes sources. Ceci nécessite cependant le développement de codes de calcul, et l'adaptation des procédures de mesure. Des détails sont donnés dans les notes techniques remises à l'ESA.
- L'influence de la géométrie de la sonde est à étudier. Le Chapitre 4 a comparé les profils de densité de courant ionique avec et sans anneau de garde, mais une étude plus générale est à conduire. Il faut entre autres choses analyser les profils mesurés par une coupe de Faraday.
- Les conditions d'essais rencontrées dans les chambres à vide sont différentes des conditions de vol. Parmi les effets néfastes aux comparaisons directes, les influences de la pression résiduelle et des référencements électriques sur la performance du PPS-Flex ont été étudiées. Une étude plus poussée doit être conduite sur une chaîne de vol, en lien avec les équipementiers et fabricants de plateformes.
- L'existence de courants perpendiculaires au jet implique que l'analyse de performance les considèrent. Cependant, la méthode adaptée n'est pas encore identifiée, et nécessite par exemple de mieux comprendre l'influence du sillage de la sonde.

Concernant la topologie magnétique :

- Le PPS-Flex a apporté un savoir considérable quant aux liens entre performances et paramètres magnétiques. La majorité des études se sont attachées à faire varier le profil axial du champ radial, le long de l'axe du canal moteur. L'influence des modifications de champ en proche paroi devrait maintenant être examinée.
- Parmi l'ensemble des topologies, deux configurations ont montré des performances légèrement supérieures aux configurations actuelles. Les activités futures engageant le PPS-Flex pourront opérer le moteur sur une large gamme de points de fonctionnement, et évaluer des quantités clefs pour l'application, tels que des taux d'érosion et la stabilité de la décharge sur de longues périodes de tir.
- Le PPI-Mag a été testé en xénon et en krypton. Les principes de base qui ont guidé sa conception semblent validés. Cependant, des mesures de FIL pourront être faites pour préciser le couplage entre L_i et L_B. Des mesures de sonde en champs croisés pourront de plus fournir la fraction d'ions multichargés dans la plume, et donc affiner la valeur du rendement d'ionisation. Des mesures directes de la poussée sont également à prévoir.
- Le PPI-MS, un moteur de 200 W à aimants permanents, basé sur le PPI et le PPI-Mag, a été conçu pour opérer en topologie magnetic shielding.

Enfin, le concept sans parois semble prometteur. Du point de vue de la physique, de nombreuses expériences pourront bénéficier de ce design, pour mieux comprendre la relation entre les instabilités et le transport par exemple. Du point de vue de l'ingénierie, cette architecture offre un moteur compact et léger, qui porte l'espoir d'une opération en dual-mode. La prochaine étape est de tester un prototype dédié, d'une puissance au moins égale à 1,5 kW, pour complètement déterminer les potentialités de ce concept.

Julien Vaudolon

Détermination du champ électrique et optimisation de la topologie magnétique dans les propulseurs de Hall

La propulsion électrique est à un tournant de son histoire. La récente mise en œuvre de satellites de télécommunication "tout-électrique" se traduit par l'ouverture d'un nouveau marché, et par une évolution des besoins opérationnels. L'identification de ces nouvelles missions nécessite l'amélioration des performances de nos moteurs.

La première partie de ces travaux rapporte l'utilisation d'un outil de spectroscopie laser destiné à caractériser la distribution en vitesse des ions. Les différentes méthodes de calcul du champ électrique dans les propulseurs de Hall ont été exposées. Deux instabilités ioniques ont été observées et analysées.
Les sources d'erreurs liées aux mesures par sondes électrostatiques ont été analysées, et un exemple de sonde plane étudié.
Une analyse paramétrique de l'influence des paramètres de champ magnétique sur les performances des propulseurs de Hall a été conduite. Le concept de moteur "sans parois" est présenté. L'identification de ce concept constitue une avancée porteuse de promesses pour l'avenir de la propulsion électrique.

Mots clés : propulsion spatiale électrique, propulseur de Hall, champ électrique, champ magnétique, magnetic shielding, fluorescence induite par laser, instabilités, sondes électrostatiques, moteur sans parois

Electric field determination and magnetic topology optimization in Hall thrusters

Electric propulsion is facing new challenges. Recently, the launch of "all-electric" satellites has marked the debut of a new era. Going all-electric now appears as an interesting alternative to conventional systems for telecom operators.

A laser spectroscopy technique was used during this research to investigate the ion velocity distribution dynamics. The different methods for determining the electric field in Hall thrusters were exposed. Two unstable ion regimes were identified and examined.
Measurement uncertainties using electrostatic probes were assessed. Planar probed have been designed and tested.
A thorough investigation of the influence of the magnetic field parameters on the performance of Hall thrusters was performed. The wall-less Hall thruster design was presented, and preliminary experiments have revealed its interest for the electric propulsion community.

Keywords : electric space propulsion, Hall thruster, electric field, magnetic field, magnetic shielding, laser-induced fluorescence, instabilities, electrostatic probes, wall-less thruster

ICARE - CNRS
1C Avenue de la Recherche Scientifique
45071 Orléans Cedex 2, France